The Pennsylvania State University
The Graduate School
Department of Materials Science and Engineering

GRAIN-ORIENTED $Pb(Mg_{1/3}Nb_{2/3})O_3$-$PbTiO_3$ CERAMICS PREPARED BY TEMPLATED GRAIN GROWTH

A Thesis in
Materials Science and Engineering
By

Edward M. Sabolsky

Submitted in Partial Fulfillment
of the Requirements
for the Degree of

Doctor of Philosophy

December 2001

UMI Number: 3036107

ProQuest Information and Learning Company
300 North Zeeb Road
P.O. Box 1346
Ann Arbor, MI 48106-1346

We approve the thesis of Edward M. Sabolsky.

Date of Signature

Gary L. Messing
Professor of Ceramic Science and Engineering
Thesis Co-Advisor
Chair of Committee

Sept 5, 2001

Susan Trolier-McKinstry

Susan Trolier-McKinstry
Associate Professor of Ceramic Science and Engineering
Thesis Co-Advisor

Sept. 11, 2001

Thomas R. Shrout
Professor of Materials and Senior Scientist

Sept 5, 2001

Long Qing Chen

Long-Qing Chen
Associate Professor of Materials Science and Engineering
Coordinator of the Graduate Program
Department of Materials Science and Engineering

Sept. 5, 2001

ABSTRACT

Rhombohedral $Pb(Mg_{1/3}Nb_{2/3})O_3$-$PbTiO_3$ (PMN-PT) single crystals near the morphotropic phase boundary (MPB) show enhanced strain levels combined with exceedingly large piezoelectric and electromechanical coupling coefficients for <001>-oriented and -poled crystal cuts. In principle, <001> fiber-textured PMN-PT ceramics should possess a high fraction of the electromechanical and dielectric properties displayed by their single crystal counterparts. To investigate this, the Templated Grain Growth (TGG) process was used to fiber-texture PMN-PT in the <001> direction. The TGG process involves the growth of multiple oriented template particles into a fine-grained matrix during thermal processing. The texture fraction of the ceramic increases with the increase of template growth, driven by the difference in surface free energies of the template and the matrix grains.

The TGG process is dependent upon the alignment and growth of the template particles within the ceramic matrix. The TGG process requires the template to have a strong epitaxial relationship to the crystal structure of the matrix composition. The template must also show the proper size and aspect ratio, so it may be mechanically aligned and grow at the expense of the fine matrix. This work emphasized the importance of the physical and compositional stability of the template particles at the desired growth temperature and environment. Potential template particles with a layered-perovskite and tungsten-bronze structure ($Bi_4Ti_3O_{12}$, $Sr_3Ti_2O_7$, $KSr_2Nb_5O_{15}$, and $Sr_2Nb_2O_7$) were shown to form a cubic-pyrochlore phase when reacted with the PMN-PT matrix at temperatures >850°C. Some perovskite templates (including forms of $PbTiO_3$,

$SrTiO_3$, and $BaTiO_3$) were shown to dissolve into the PMN-PT matrix or intergranular PbO-phase, minimizing their utility in templating the desired PMN-PT composition. $BaTiO_3$ platelet crystals were found to be suitable templates for the TGG of PMN-PT. The $BaTiO_3$ crystals were stable within the PMN-PT matrix at temperatures >850°C and they were shown to act as proper heteroepitaxial substrates for templated growth of the PMN-PT composition.

The TGG kinetics from {001}-, {110}-, and {111}-$BaTiO_3$ crystals were observed and fitted to a diffusion-controlled model with a non-constant driving force. The crystal growth kinetics were shown to be limited by the decrease in the driving force due to the coarsening and shape change of the matrix grains. The growth kinetics were also shown to be dependent upon the intergranular liquid content and the template orientation. Excess PbO concentration >1 wt% was shown to accelerate the growth of the crystal layer. The <111> crystallographic orientation was found to be the fastest growing direction with the <001>-direction as the slowest.

PMN-32.5PT ceramics were fiber-textured by initially aligning {001}-$BaTiO_3$ platelets (~75-150 μm in diameter) within the matrix by tapecasting. Dense PMN-32.5PT ceramics (1 wt% excess PbO) with a 5 vol% template concentration were <001>-textured to a texture fraction ~0.90 with an annealing time >1 h at 1150°C. The degree of texturing was slightly increased with an increase in annealing time and template concentration (10 vol% templates). The decrease in texturing rate was attributed to the decreasing driving force for growth due to the coarsening and shape change of the matrix. The texturing kinetics was also found to decrease after longer annealing times (>1 h) due to grain impingement and porosity development around the templated grains.

An increase in texture fraction of the {001}-$BaTiO_3$ templated PMN-32.5PT ceramics produced an increase in the piezoelectric, electromechanical coupling, and compliance coefficients over randomly-oriented samples of the same composition. The d_{33} coefficient of highly textured PMN-32.5PT ceramics (~90%-textured) were found to be ~1.2-1.5 times greater than randomly-oriented samples. The unipolar strain-field measurements (<5 kV/cm) of ~90%-textured PMN-32.5PT ceramics produced d_{33} coefficients as high as 1150 pC/N with relatively low piezoelectric hysteresis. Additional PbO was purposely added to the PMN-32.5PT matrix in order to increase the TGG kinetics and drive the samples to full-texture. Regardless of the texture quality, the presence of the intergranular PbO-phase resulted in a low dielectric constant ($\varepsilon_{rr}^{poled}<3000$) for the textured samples, which remained similar to random PMN-32.5PT samples containing excess PbO. The presence of the residual $BaTiO_3$ templates within the templated grains did not alter the transition temperatures of the PMN-32.5PT ceramics. This suggests that $BaTiO_3$ did not dissolve into the matrix, further emphasizing the relative stability of the $BaTiO_3$ template particles. The magnitude of the dielectric and piezoelectric properties were also found to be limited by the presence of misoriented templated-grains, unoriented grains, porosity, and the remnant $BaTiO_3$ templates.

TABLE OF CONTENTS

LIST OF TABLES

Table

Table

LIST OF FIGURES

Figure

Figure

Figure

Figure

Figure

Figure

Figure

Figure

Figure

ACKNOWLEDGEMENTS

I would like to acknowledge Dr. Messing and Dr. McKinstry for their guidance over the past five hard years. With their instruction and assistance, I have matured and grown both personally and professionally. They have taught me a great deal through their words and by their example.

Also, I want to express my gratitude to all the members of Dr. Messing's group, both past (Roger, Scott, Dr. Hong, Dr. Watari, Dr. Oh, Joerg, Matt, Bhaskar, Ender, Paul, Rob, Eric, and Mike) and present (Seongtae, Dr. Lee, Erkin, Aravind, Kristen, Huseyin, and Cihangir). They have become more than just co-workers to me; they have become my brothers and sisters. I would like to thank Bhaskar, Matt, and Ender for being both my friends and my first mentors. They brought a team feeling to the group which made working long nights both fun and stimulating. Thank you to Cihangir (the only one who truly understands me) for putting up with me for all those years. I also want to thank Dr. Adair's group for being part of the processing family. My appreciation goes out to Tim Klinger (my biking partner), Leah (my Penn State mom), and all the staff and faculty at MRL, MRI, and the Department of Materials Science and Engineering at Penn State for their help and companionship.

I would also like to thank all my friends and roommates (past and present). Thanks to Mike, Amy, Crazy, Rich, Ronny, Kristen, Ginger, and Big Paul for being my partners in crime for the past five years. You guys represent almost all the fun I had at Penn State, and I will never forget you. Mike, my Philippine brother, I could never express enough how much your friendship has meant to me. Without you, I would have never made it to this point. We made it under the wall of Shawshank; we're finally free. Thank you to my angel; you were there when I needed you.

Thanks to Bocian and John. Your visits reminded me of who I am and where I came from. For a fraction of time, you made me forget PMN-PT. You guys will be with me, in my mind and heart, forever.

My largest thanks goes out to my family, and especially, my father and mother (who are my biggest fans). They have been supporting and cheering me on for the past five years during my studies, just like they have for all of those baseball, soccer, and hockey games from my youth. I like to thank my father for teaching me the importance of learning and for being the best role model a son could ever have. Everyday, I strive to be one-millionth the man my father is. I want to thank my mother for her unconditional love. My mother brought to me comfort through all the hard times during my life.

Thank you God for walking with me when I was alone in the desert.

Dedicated to

My Father and Mother

Chapter 1

INTRODUCTION

1.1 STATEMENT OF THE PROBLEM

The direct piezoelectric effect of a material gives a dielectric displacement linearly proportional to an applied mechanical stress. The same fundamental property produces the converse piezoelectric effect, which causes the material to strain in proportion to an applied electrical field.(1) A great deal of understanding and development of inorganic piezoelectric crystals and ceramics has occurred since the discovery of the piezoelectric nature of barium titanate ($BaTiO_3$) in 1945. Currently, inorganic piezoelectric crystals and ceramics are applied to a broad variety of applications. These applications can be categorized into four major groups: 1) generators (which converts mechanical into electrical energy), 2) sensors (that converts mechanical force into a electrical signal), 3) sonic and ultrasonic transducers (which converts electrical into mechanical energy), and 4) actuators (that converts electrical signals into a mechanical displacement).(2,3) Therefore, piezoelectric materials can be used to produce high quality igniters, hydrophones, microphones, micro-motors and -pumps, buzzers, loud speakers, micropositioners, delay lines, video head positioners, sonar, medical ultrasound equipment, and multiple other electromechanical devices.

Materials displaying piezoelectric, electrostrictive, piezomagnetic, magnetostrictive, photostrictive, thermoelastic, or shape memory physical characteristics may be applied to actuator applications. Currently, inorganic piezoelectric materials are the most widely used, especially in the case of high performance actuators, due to their high generative force, relatively accurate displacement, and high frequency operation capabilities.

The most widely used piezoelectric single crystal materials are α-quartz (SiO_2), lithium niobate ($LiNbO_3$), and lithium tantalate ($LiTaO_3$). These materials are extensively used in industrial applications as a result of their temperature stability, wide operating temperature range, and ease in processing in which large, defect-free single crystals by conventional growth techniques. The most widely used polycrystalline ceramics for piezoelectric applications are $BaTiO_3$ and $Pb(Zr_x,Ti_{1-x})O_3$ (PZT), which both have the perovskite structure (ABO_3). PZT shows the maximum piezoelectric response at compositions near the morphotropic phase boundary (MPB) between the tetragonal and rhombohedral phases ($Pb(Zr_{0.52}Ti_{0.48})O_3$). Since there are two equally stable phases at this composition, there remains multiple allowable domain orientations which are associated with these phases, allowing for efficient poling. The processing and physical properties for the $BaTiO_3$ and PZT compositions have been thoroughly studied over the past fifty years. The properties and stability of both $BaTiO_3$ and PZT are commonly altered through the substitution of various isovalent or aliovalent ions for either the A or B sites of the perovskite structure.

For a high performance actuator, the piezoelectric material must show high thermal stability, high strain with an applied electric field, low mechanical loss, and thus, low hysteresis.(3) Therefore, piezoelectric materials for actuator applications should possess a high phase transition, or Curie, temperature, a high piezoelectric coefficient (d_{ij}), and in some cases a high mechanical quality factor. In addition to the above mentioned requirements, for high performance medical transducer applications, a high electromechanical coupling coefficient (k_{ij}) is required since the k_{ij} dictates the bandwidth of the transducer.

The next generation of actuators and transducers for the above mentioned applications require a significant increase in some or all of the typical figure of merit coefficients (d_{ij}, k_{ij}, and Q_M) which describe the performance of the piezoelectric materials. The various solid solutions based on PZT ceramics are the most promising for many piezoelectric applications, but the degree of improvement in the PZT compositions has been modest from the 1970's to the late 1990's. The inability to grow single crystals of PZT near the MPB of a usable size and quality has slowed progress towards the next generation of novel high strain piezoelectric materials.

Although large single crystals of PZT at the MPB composition have not been been grown, other Pb-based relaxor ferroelectric-$PbTiO_3$ compositions at their MPB can be grown by conventional high temperature solution growth. This was first shown in the early 1980's.$^{(5,6)}$ The Pb-based relaxor ferroelectric-$PbTiO_3$ compositions also have the basic perovskite structure, like PZT, but the B-sites are occupied by various off-valent ions. Kuwata *et al.*, for single crystal $Pb(Zn_{1/3}Nb_{2/3})O_3$-$PbTiO_3$ (PZN-PT), and later Park and Shrout (1997)$^{(4)}$, for both single crystal PZN-PT and $Pb(Mg_{1/3}Nb_{2/3})O_3$-$PbTiO_3$ (PMN-PT), reported piezoelectric coefficients (d_{33}) between 1500-2500 pC/N and electromechanical coupling coefficients (k_{33}) >0.9 with low hysteresis. It should be noted that the best PZT (PZT-5H)$^{(7,8)}$ shows d_{33} of ~600 pC/N and k_{33} of ~0.70-0.75. PZT-5H is considered a "soft" ferroelectric, since its domain state can be easily altered by a small electric field or mechanical stress. However, under large field drives soft PZT shows undesirably large hysteresis, dielectric and mechanical loss, and heat generation.$^{(4)}$

Acceptor doping the PZT to form a "hard" PZT (PZT-4, PZT-8, PZT-7A) eliminates the large hysteresis under high drive levels, but it also lowers the piezoelectric coefficients (d_{33}<300 pC/N) and the electromechanical coupling coefficients to some degree (k_{33}<0.7). Therefore, the ultrahigh piezoelectric coefficients, electromechanical coupling coefficients, strain levels, and low hysteresis values observed for the PZN-PT and PMN-PT single crystals represent a significant step forward in piezoelectric actuation materials.

The enhanced piezoelectric response and low hysteresis for the rhombohedral PZN-PT and PMN-PT single crystals was observed primarily for <001> crystal cuts. Crystal cuts offset from this orientation displayed lower piezoelectric response and increased hysteresis. The elevated piezoelectric response for the [001] oriented rhombohedral single crystals was credited to the rotation of the polarization vector from the <111> to [001].(4) The low hysteresis in the rhombohedral crystals has been attributed to a stable domain configuration in the <001>. The manipulation of the crystal orientation in order to access a specific stable domain configuration had been termed "domain engineering."

PMN-PT ceramics can not directly benefit from the findings for its single crystal counterpart, since the microstructure of a ceramic usually consists of a broad distribution of randomly oriented crystallites. This broad distribution results in the averaging of the single crystal properties which are anisotropic in nature.

It has been demonstrated that by orienting (texturing) the grain structure of the ceramic, the macroscopic symmetry can reflect that of its single crystal counterpart. The decrease in symmetry from the random polycrystalline ceramis to single crystal state depends on the texture dimensionality (fiber or sheet texture) and the distribution of the grain crystallographic orientation. Multiple piezoelectric compositions have been textured (Table 1.1), and the texturing always leads to an increase in the property anisotropy. When the composition was textured in the polarization direction, there was always an increase in the piezoelectric coefficient over that of the random ceramic due to the increase in poling efficiency. All but one of the piezoelectric compositions textured possess relatively low symmetry, and thus, these compositions show an innate ability to form anisometric grains as well as anisotropic grain growth behavior. This behavior assists in the initial orientation of the grain structure during green processing and the further texture development due to anisotropic grain growth during high temperature treatment. The $BaTiO_3$ and $Bi_{0.5}(Na_{0.35}K_{0.15})_{0.5}TiO_3$ compositions are the only piezoelectric compositions textured from cubic prototype groups reported in literature.(11,15)

The primary objective of the research was to fiber-texture PMN-PT ceramics, especially the PMN-PT compositions near the MPB, in the <001> directions so that the single crystal electromechanical properties observed for <001>-cuts of PMN-PT single crystals can be accessed. A poled <001>-textured ceramic is a close match to the macroscopic symmetry displayed by a fully <001>-poled PMN-PT single crystal. This allows the textured PMN-PT ceramic to benefit from the concept of domain engineering in order to access the low hysteresis and extraordinary high piezoelectric response of the single crystals. In addition to the enhancement in the piezoelectric properties, processing problems encountered during the growth of the single crystal PMN-PT can be circumvented by texturing PMN-PT by conventional ceramic processing techniques. Single crystal growth of PMN-PT is limited by low production efficiency, high

Table 1.1: Effect of texture on piezoelectric ceramics.

Composition	Texture Percentage	Piezoelectric Coefficient	Degree of Enhancement	Reference
$Bi_4Ti_3O_{12}$	>98%	d_{33}= 30 pC/N	77% of xtal	9
$Bi_4Ti_3O_{12}$	>95%	d_{33}= 10 pC/N	26% of xtal	10
$Bi_{0.5}(Na_{0.35}K_{0.15})_{0.5}TiO_3$	~90%	d_{31}=- 63 pC/N	60% >polyxtal	11
$(Pb,K)_{0.4}Ba_{0.6}Nb_2O_6$	>50%	d_{33}= 120 pC/N	50% >polyxtal	12
$CaBi_4Ti_4O_{15}$	83-100%	d_{33}= 45 pC/N	200% >polyxtal	13
$Na_{0.475}Ca_{0.05}Bi_{4.475}Ti_4O_{15}$	86-93%	d_{33}= 44 pC/N	238% >polyxtal	13
$Sr_{0.53}Ba_{0.47}Nb_2O_6$	~90%	d_{33}= 78 pC/N	87% of xtal	14
$BaTiO_3$	~27%	d_{33}= 270 pC/N	70% >polyxtal	15

xtal=single crystal
polyxtal=polycrstalline

production cost, long growth time, small product size, limited shape forming capability, and compositional heterogeneity. Standard ceramic processing techniques which provide the proper shear force to align the ceramic platelet or fiber particles during the green and final processing stages may allow for the formation of low cost, high yield, textured PMN-PT ceramics of various sizes and shapes.

1.2 SCIENTIFIC APPROACH

There are various processing techniques which can be employed to texture the grain structure of a ceramic. These processing routes will be described, compared, and contrasted in the following chapter. The processing route required to produce dense, fully-textured PMN-PT samples must be a relatively low cost process which can be scaled up. The Templated Grain Growth (TGG) process was selected as the most desirable route to texture PMN-PT, since it utilizes conventional ceramic processing techniques to produce highly textured, dense ceramics. TGG entails the mechanical alignment of a relatively small volume fraction of template particles within a ceramic matrix during green processing. With thermal treatment of the green ceramic, the template particles grow at the expense of the finer matrix powder in order to increase the volume fraction of textured material within the ceramic.(16) This work will focus on the use of {001}-$BaTiO_3$ crystallites as the template material in the TGG process to texture the PMN-PT composition in the <001>.

Texturing a bulk ceramic of a highly symmetric composition, like PMN-PT, has not yet been achieved with great consistency. As previously stated, ceramic systems with strong anisotropy are more easily textured. Beyond this challenging materials engineering hurdle are many scientific questions which must be answered relating to both the TGG processing of PMN-PT and the resultant dielectric and electromechanical properties of the textured PMN-PT ceramics. Some of the TGG issues that were addressed in this work include:

- The stability of potential template particles, which display the proper crystal structure, particle shape, and particle size, in the PMN-PT matrix.
- The heteroepitaxial nucleation and growth of oriented single crystal PMN-PT from the potential template particles.
- The processing parameters which affect the kinetics of PMN-PT matrix grain growth and TGG.

The issues that will be addressed relating to the dielectric and piezoelectric response of the <001>-textured PMN-PT ceramics are as follows:

- The effect of texturing PMN-PT on the dielectric permittivity, piezoelectric coefficients and electromechanical coupling coefficients.
- The effect of fiber-texture on the stability of the engineered domain state of the grain-oriented PMN-PT ceramic.
- The effect of a residual intergranular PbO-rich phase on the piezoelectric and dielectric properties of random and textured ceramic PMN-PT.
- The mechanical clamping issues relating to the residual template particles embedded within the textured PMN-PT grain structure.

1.3 ORGANIZATION OF THE THESIS

Chapter 2 introduces a concise review of the definitions of piezoelectricity and ferroelectricity, and the relations of these two phenomena to symmetry. Included in Chapter 2 is a review of: 1) the pertinent processing techniques which have been used to synthesize single crystal, thin film, ceramic, and powder PMN-PT, 2) the dielectric and electromechanical properties of PMN-PT, and 3) the typical processing techniques utilized to texture polycrystalline materials, as well as a description of the TGG process.

The physical and chemical characteristics required for particles to successfully act as templates for the TGG process are presented in Chapter 3. Various particle compositions, which include both whisker and platelet particle morphologies, were investigated as possible template candidates. Four template compositions ($Bi_4Ti_3O_{12}$, $Sr_3Ti_2O_7$, $KSr_2Nb_5O_{15}$, and $Sr_2Nb_2O_7$) are non-perovskites materials, but these compositions have crystal structures which are composed of stacked layers of corner-sharing perovskite-like octahedra. The other four template compositions are perovskite materials ($BaTiO_3$, $SrTiO_3$, and $PbTiO_3$) which all have a low lattice mismatch with PMN-PT. The results of the interaction of these particle compositions with the PMN-PT matrix are reported. The prime template candidates ($BaTiO_3$ and $SrTiO_3$) for the TGG of PMN-PT are identified in Chapter 3.

Chapter 4 describes the relationship between various processing variables on the kinetics of single crystal PMN-PT growth from $BaTiO_3$ template crystals. These variables include temperature, time, excess PbO concentration, and template orientation. The growth kinetics of both the PMN-PT matrix and single crystal were fitted to various diffusion and interface growth models. From these results, a proposed growth mechanism for the TGG of PMN-PT from $BaTiO_3$ template crystals is proposed.

{001}-$BaTiO_3$ template crystals were used to texture PMN-32.5PT ceramics in the <001>. The effect of various processing variables on the quality and degree of <001>-texture is described in Chapter 5. Some of the variables identified were template concentration, excess PbO concentration, density and growth time. The growth kinetics, reported in Chapter 4, were used in a simple space filling model to predict the resultant kinetics of the texture development.

The resultant piezoelectric and dielectric responses of both random and textured PMN-PT ceramics are reported in Chapter 6. The work shows the effect of excess PbO on the properties by affecting both the dielectric response and the degree of growth of the oriented grains. The limitations of domain movement (clamping) in the textured grains, resulting in the piezoelectric and ferroelectric hysteresis, were investigated by *in-situ* optical microscopy with applied fields. These results are also reported in Chapter 6.

1.4 REFERENCES

1) T. Ikeda, *Fundamentals of Piezoelectricity.* Oxford University Press, Oxford, England (1990).

2) J.W. Wanders, *Piezoelectric Ceramics: Properties and Applications.* Philips Components, Eindhoven, The Netherlands (1991).

3) K. Uchino, *Ferroelectric Devices.* Marcel Dekker, Inc., New York (2000).

4) S.-E. Park and T.R. Shrout, "Ultrahigh Strain and Piezoelectric Behavior in Relaxor Based Ferroelectric Single Crystals," *J. Appl. Phys.*, **82** [4] 1804-11 (1997).

5) J. Kuwata, K. Uchino, and S. Nomura, "Phase Transitions in the $Pb(Zn_{1/3}Nb_{2/3})O_3$-$PbTiO_3$ System," *Ferroelectrics*, **37** 579-82 (1981).

6) J. Kuwata, K. Uchino, and S. Nomura, "Dielectric and Piezoelectric Properties of $0.91Pb(Zn_{1/3}Nb_{2/3})O_3$-$0.09PbTiO_3$ Single Crystals," *Jpn. J. Appl. Phys.*, **21** 1298-302 (1982).

7) B. Jaffe, W.R. Cook, and H. Jaffe, *Piezoelectric Ceramics.* Academic Press, New York (1971).

8) U.S. Department of Defense, *Military Standard: Piezoelectric Ceramic Material and Measurements Guidelines for Sonar Transducers, MIL-STD-1376B(SH).* Naval Sea Systems Command, Arlington, VA (1995).

9) S.-H. Hong, "Dielectric and Electromechanical Properties of Textured Niobium-Doped Bismuth Titanate Ceramics," *J. Am. Ceram. Soc.*, **83** [1] 113-18 (2000).

10) S. Swartz, W.A. Schulze, and J.V. Biggers, "Fabrication and Electrical Properties of Grain Oriented $Bi_4Ti_3O_{12}$," *Ferroelectrics*, **38** 765-68 (1981).

11) T. Tani, "Crystalline-oriented Piezoelectric Bulk Ceramics with a Perovskite-type Structure," *J. Kor. Phys. Soc.*, **32** S1217-S1220 (1998).

12) B. Brahmaroutu, *Templated Grain Growth of Textured Strontium Niobate Ceramics.* Ph.D. thesis, Penn State University (1999).

13) T. Takeuchi, T. Tani, and Y. Saito, "Piezoelectric Properties of Bismuth Layer-Structured Ferroelectrics Ceramics with a Preferred Orientation Processed by the Reactive Templated Grain Growth Method," *Jpn. J. Appl. Phys.*, Part 1 [9B] 5553-56 (1999).

14) C. Duran, S. Trolier-McKinstry, and G.L. Messing, "Fabrication and Electrical Properties of Textured $Sr_{0.53}Ba_{0.47}Nb_2O_6$ Ceramics by Templated Grain Growth," *J. Am. Ceram. Soc.*, **83** [9] 2203-13 (2000).

15) Y. Ohara, K. Koumoto, and H. Yanagida, "Barium Titanate Ceramics with High Piezoelectricity Fabricated from Fibrous Particles," *J. Am. Ceram. Soc.*, **68** [4] C108-C109 (1985).

16) M.M. Seabaugh, I.H. Kerscht, and G.L. Messing, "Texture Development by Templated Grain Growth in Liquid-Phase-Sintered α-Alumina," *J. Am. Ceram. Soc.*, **80** [5] 1181-88 (1997).

Chapter 2

BACKGROUND

2.1 EFFECT OF SYMMETRY ON PHYSICAL PROPERTIES

Neumann's Principle can be stated as: *The symmetry elements of any physical property of a crystal must include the symmetry elements of the point group of the crystal.*(1) This postulate is the framework for the relationship between properties and symmetry for all known crystals. Neumann's Principle also implies that physical properties can include more symmetry than is dictated by the point group. By generalizing Neumann's Principle, it can be also stated that: *The symmetry elements of any physical property of a composite must include the symmetry elements of the point group of the composite.*(2) Therefore, the properties demonstrated by composites and polycrystalline materials are limited by the overall symmetry elements of the comprising phases and their geometrical and microstructural arrangements. This idea has been labeled as Curie's principle of symmetry superposition.

By Neumann's Principle, the internal arrangement of the ions in a crystal is reflected in the external properties of the crystal. The symmetry of a crystal can be separated into 7 crystal systems which include in descending symmetry: cubic, hexagonal, trigonal, tetragonal, orthorhombic, monoclinic, and triclinic. These crystal systems can be subdivided into 32 different point groups in which the symmetry is composed of combinations of rotations, mirror planes, and center of symmetry elements. The elements of a specific point group symmetry, when applied to a material property, will display the "allowable response" of a crystal possessing that specific symmetry.

The magnitude and direction of the response will depend on its specific symmetry and the intrinsic capability of the crystal.

2.2 PIEZOELECTRICITY

The piezoelectric effect can be described as follows:

$$D_i = d_{ikl}X_{kl} + \varepsilon^X_{ik}E_k \quad \text{(Direct)} \qquad \text{Eq. 2.1}$$

$$x_{ij} = s^E_{ijkl}X_{kl} + d_{kij}E_k \quad \text{(Converse)} \qquad \text{Eq. 2.2}$$

where D_i is the dielectric displacement, X_{kl} is the applied mechanical stress, ε^X_{ik} is the dielectric permittivity (measured at constant stress), x_{ij} is the induced strain, s^E_{ijkl} is the mechanical compliance (measured at constant field), E_k is the applied electrical field, and d_{ikl} is the piezoelectric coefficient.(3) The direct piezoelectric effect is defined as the linear relation between an applied stress and an induced electrical polarization. The converse effect is where a mechanical strain is proportional to an applied electric field. As seen from Eqns. 2.1 and 2.2, the direct and converse piezelectric effects are linear and reversible, and the magnitude of the response is directly related to the direction and magnitude of the applied stress or electric field. Both equations are expressed in tensor form, but the piezoelectric coefficient is usually simplified to a subscript matrix form where d_{ijk} is reduced to d_{ij} where i=1,2,3 and j=1,...6. The above equations in matrix form describe the piezoelectric effect for different orientations of the material, where 1, 2, and 3 are parallel in direction to the x, y, and z Cartesian axes, except in hexagonal and trigonal systems.(3,4)

Since the piezoelectric effect is a third rank tensor (d_{ijk}), then the application of the symmetry elements of a point group containing a center of symmetry would eliminate the piezoelectric effect. For a noncentrosymmetric crystal, an applied stress would displace both the positive and negative ions with respect to each other, producing a net dipole within the material.

Within the 32 point groups, 11 of the point groups possess a center of symmetry which eliminates the piezoelectric effect for the crystals possessing this symmetry. Of the remaining 21 point groups, the 432 point group is non-centric, but due to the combination of its symmetry elements, the piezoelectric effect is canceled. Therefore, there are 20 crystal point groups which display the piezoelectric effect (Table 2.1).(1,3)

2.3 FERROELECTRICITY

Of the 20 piezoelectric point groups, 10 point groups show a spontaneous polarization (Table 2.1). These materials are termed pyroelectric materials. The magnitude of the dipole varies with a change in temperature, as shown by the linear pyroelectric effect:

$$\Delta P_i = p_i \Delta T \qquad \text{Eq. 2.3}$$

where ΔP_i is a change in the dielectric polarization, ΔT is a change in temperature, and p_i is the pyroelectric coefficient.

A subgroup of the pyroelectric family consists of ferroelectric materials. Ferroelectric materials display a spontaneous polarization, where in the limit of a single crystal, the dipole or dipoles can be reoriented between crystallographically defined equilibrium states by the application of an electric field. This phenomenon can be

Table 2.1: Symmetry classes which exhibit the piezoelectric and pyroelectric effect.(1)

Crystal System	**Piezoelectric Classes**	**Pyroelectric Classes**
Triclinic	1	1
Monoclinic	2, m	2, m
Orthorhombic	222, mm2	mm2
Tetragonal	4, $\bar{4}$, 422, 4mm, $\bar{4}$2m	4, 4mm
Trigonal	3, 32, 3m	3, 3m
Hexagonal	6, $\bar{6}$, 622, 6mm, $\bar{6}$m2	6, 6mm
Cubic	23, $\bar{4}$3m	None

observed by viewing the dielectric polarization as a function of electric field after applying a large amplitude sinusodal electric field across the material (Fig. 2.1). The resultant trend indicates the ability of the dipoles within the material to switch orientation in response to the applied electric field. The magnitude of the coercive field (E_c) is a quantitative indication of the degree of resistance the dipole or dipoles experience during reorientation. The remanent polarization (P_r) represents the macroscopic polarization which remains in the material, parallel to the direction of the applied field, after the field is removed.

The ferroelectric (and pyroelectric) state of a crystal is dependent on temperature. Most ferroelectric materials possess a specific transition temperature below which the crystal structure distorts to a noncentrosymmetric structure. This temperature is termed the Curie temperature (T_c). The phase transition from the ferroelectric to the paraelectric state can occur as a first or second order phase transition for "normal" ferroelectric materials. At the transition temperature, a first order phase transition shows a sudden change in the spontaneous polarization as a function of temperature (Fig. 2.2(a)), where a second order phase transition does not (Fig. 2.2(b)).(3,4) The designation of a "normal" ferroelectric will be described later.

Due to the development of the reorientable dipoles within the crystal below T_c, there develops a localized surface charge density and an accompanying depolarizing field. The energy associated with the localized fields can be minimized by a microstructural twinning mechanism where adjacent regions within the material possess different dipole orientations. The regions where the dipole directions are aligned in the same crystallographic direction are called domains. Domains also nucleate in response to

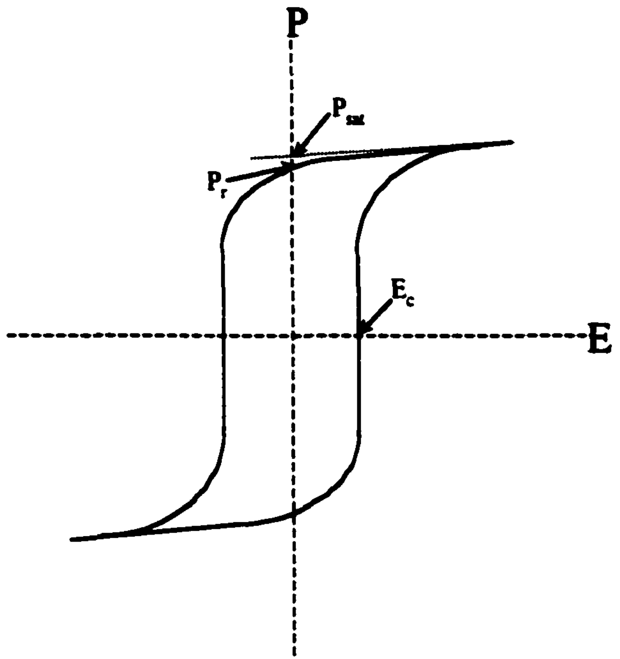

Figure 2.1: Schematic of the dielectric polarization (P) as a function of electric field (E) behavior for a ferroelectric material below its Curie temperature.

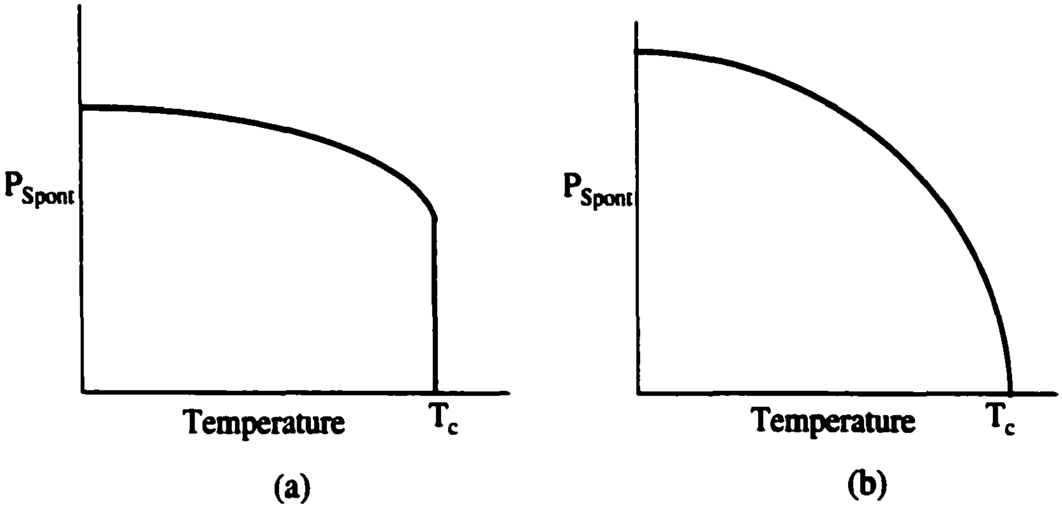

(a)

(b)

Figure 2.2: Schematic of the spontaneous polarization behavior as a function of temperature for a (a) first-order and (b) second-order ferroelectric material.

internal or applied mechanical stresses. Crystals are usually composed of multiple domains unless a field is applied parallel to one of the polar directions. The domains which consist of dipoles aligned in the direction of the applied field will grow at the expense of the misoriented domains. The process of realigning the dipoles with an applied electric field is termed *poling*.(5)

2.4 PIEZOELECTRICITY IN FERROELECTRIC CERAMICS

Ferroelectric ceramics below T_c initially behave as non-polar materials, since the crystallites in the ceramic are randomly oriented. This is a reflection of Curie's principle of symmetry superposition which was previously described (Fig. 2.3). A polycrystalline ceramic can be thought of as a composite material which is composed of multiple single crystals which incidentally are composed of multiple domains of various orientations. Therefore, the macroscopic symmetry of a randomly oriented ferroelectric material, which has never experienced a DC field bias, will show spherical symmetry ($\infty\infty m$ symmetry).(2) This macroscopic symmetry is centrosymmetric, therefore, the unpoled ferroelectric ceramic does not show the piezoelectric effect. By poling the ferroelectric ceramic, some of the dipoles within the randomly oriented grains will reorient, consequently reducing the overall energy of the system under the field. Poling a ferroelectric ceramic alters its macroscopic symmetry from spherical to conical symmetry (∞m symmetry).(2) The conical symmetry is not centrosymmetric, thus, the poled ceramic displays the piezoelectric effect. The effectiveness in maximizing the macroscopic polarization of the ceramic by poling is limited due to the random orientation of the grains within the ceramic.

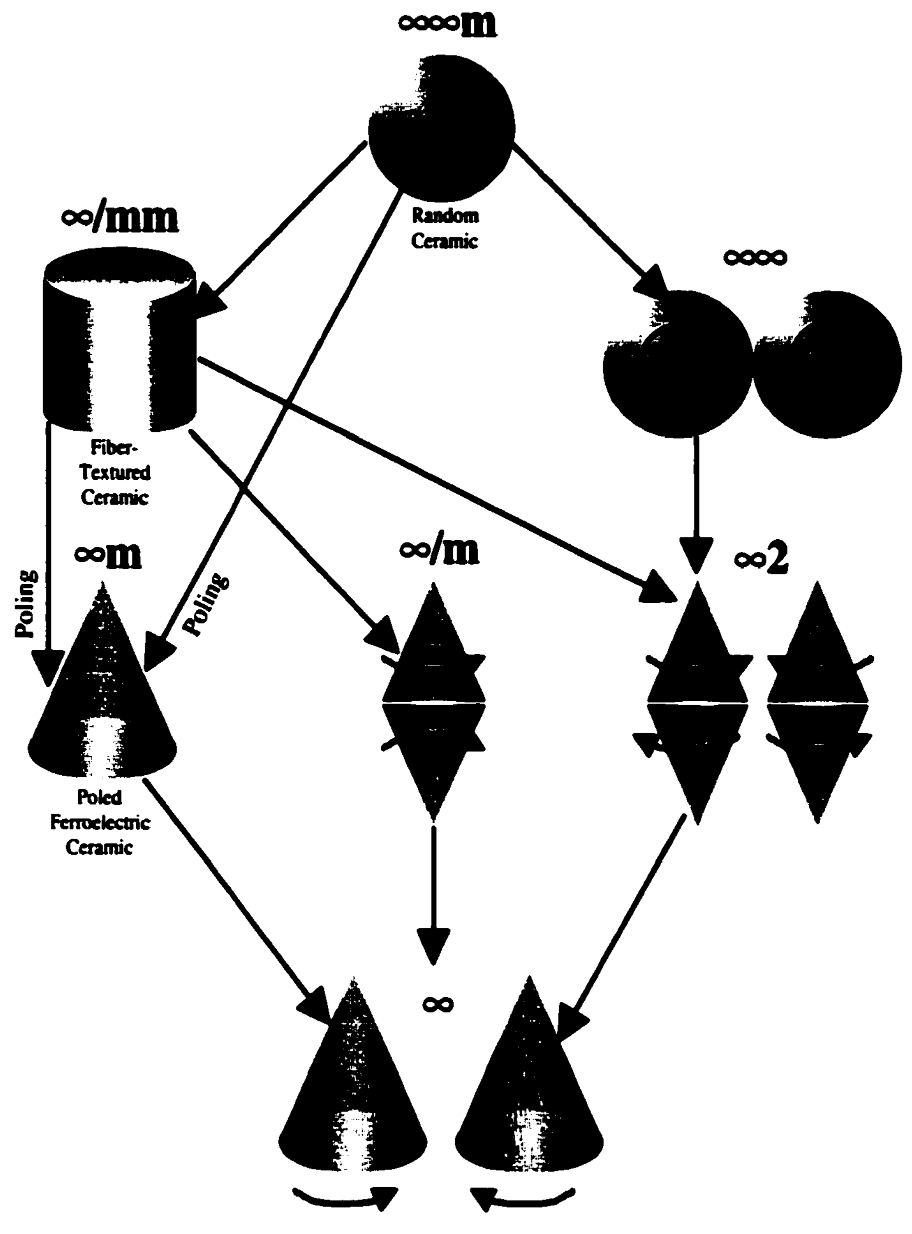

Figure 2.3: Curie symmetry groups composed of various symmetry elements including rotations, mirror planes, and handedness.(2)

Due to the multidomain state of ferroelectric ceramics, there are both intrinsic and extrinsic contributions to the piezoelectric effect.(6) The intrinsic effect refers to the distortion or strain of the unit cell due to the applied electric field. The extrinsic effect represents the ferroelastic response caused by the motion of non-180° domain walls.(6-9) This ferroelastic response is exhibited in the nonlinear and hysteretic nature of the mechanical strain and dielectric polarization with an applied AC field or stress. The piezoelectric response of ferroelectric ceramics, like $BaTiO_3$ and $Pb(Zr,Ti)O_3$ (PZT), is often dominated by the contribution of domain-wall motion at room temperature. Several studies have reported that up to 60-70% of the piezoelectric effect for $BaTiO_3$ and soft PZT ceramics is contributed by the extrinsic sources.(6-9) The effect of grain boundaries, space charge, and defects control the reversible and irreversible nature of the domain-wall motions within the grains, thus controlling the reversible and irreversible changes in the ferroelectric polarization and strain.(10-13)

The measured longitudinal and transverse piezoelectric coefficients of ferroelectric thin films display much lower values than their ceramic counterparts. The reason for the discrepancy has been attributed to the mechanical clamping by the substrate, as well as, limited domain-wall motion in the thin film. Since over half of the observed piezoelectric effect of ceramic compositions like PZT is attributed to extrinsic sources, the piezoelectric coefficients of thin films of these compositions is substantially diminished.(12,13)

2.5 PIEZOELECTRIC PROPERTIES OF FERROELECTRIC CERAMICS

There are many ferroelectric ceramics which display a spectra of different structures and compositions. The perovskite family is the most widely used for piezoelectric ceramics.(14) Perovskites in their idealized form are cubic having the general formula $A^{XII}B^{VI}O_3^{VI}$, where *A* ions occupy the corner sites, *B* ions occupy the center site, and *O* (oxygen) ions occupy all of the faces of the cube (Fig. 2.4).(15) The Roman numerals represent the coordination number. The geometrical structure formed allows for a nearly closed-packed array of *A-O* ions with *B* ions occupying octahedrally coordinated sites between the packed arrays. *A* ions (e.g. Ca, Sr, Ba, Pb, La, Cd, K, Na...) are large and comparable to the size of the oxygen ion. The *B* ions (e.g. Ti, Zr, Mg, Nb, Ta, W, Mn, Zn, Ni, Al, Sc, Sn...) are rather small, since they must fit in the interstices. Below the T_c of a perovskite ferroelectric material, a slight displacement of the *B* ion from the idealized center position of the cube toward either the face, edge, or corner results in the formation of a dipole within the unit cell. This slight displacement and the unit cell distortion from the origin position results in the spontaneous polarization.

The family of ceramic lead-based perovskite ferroelectrics at compositions near their morphotropic phase boundary (MPB) show anomalously high dielectric and piezoelectric properties. The MPB is the compositional phase boundary separating two distinct ferroelectric phases usually appearing as a constant composition over a wide temperature range up to the ferroelectric phase transition temperature (T_c).(16) MPB ceramics show enhanced poling efficiency due to the multiple available dipole directions. At the MPB composition, the structure of both phases are nearly equivalent in energy,

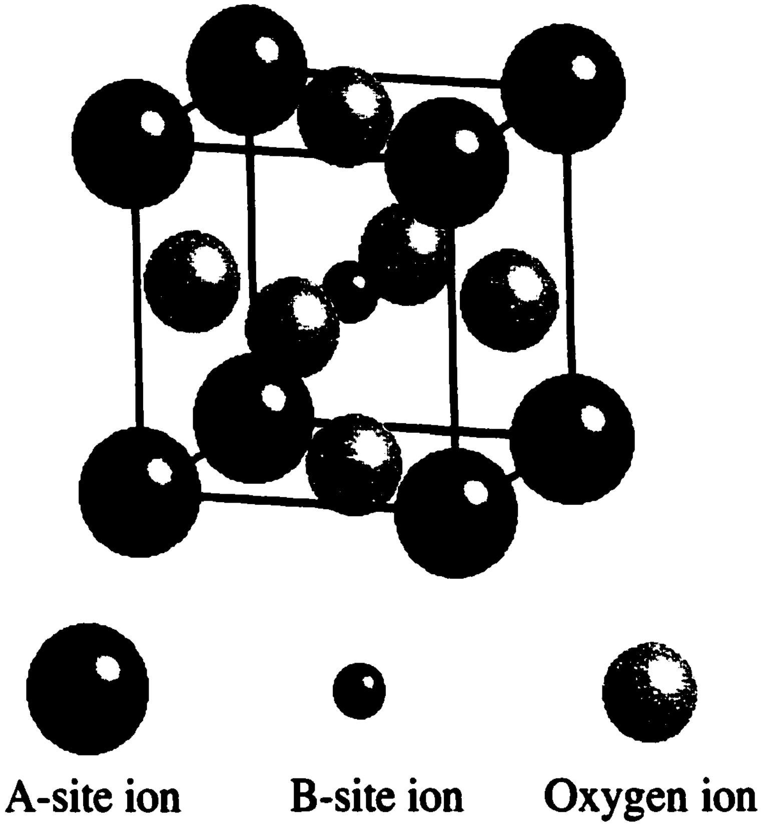

Figure 2.4: Schematic of the prototype perovskite structure (m3m symmetry).

therefore, the material possesses two structural alternatives and multiple stable polar directions. The most notable lead-based ferroelectric MPB perovskite is $Pb(Zr_{0.52}Ti_{0.48})O_3$ (PZT). Table 2.2 compares the properties of some typical ferroelectric ceramic compositions.(14) "Soft" PZT compositions (like PZT-5H and $(Pb_{0.92}La_{0.08})(Zr_{0.65}Ti_{0.35})O_3$) show the highest piezoelectric coefficients (d_{33}≈550-700 pC/N) and electromechanical coupling coefficients (k_{33}≈0.7-0.75). Although these compositions show some of the best electromechanical properties of any ceramics, their utility is limited by the large hysteresis, high dielectric loss, and high mechanical loss which is associated with "soft" ferroelectric materials.

The $0.65Pb(Mg_{1/3}Nb_{2/3})O_3$-$0.35PbTiO_3$ (PMN-35PT) composition, also shown in Table 2.2, displays piezoelectric and dielectric properties similar to that of "soft" PZT. Choi *et al.* systematically investigated the effect of $PbTiO_3$ content in PMN on the dielectric and piezoelectric properties of the solid solution.(17) Choi reported anomalously high dielectric constants and piezoelectric constants at $PbTiO_3$ compositions between 27.5-30 mol% (Table 2.3, Fig. 2.5). The largest dielectric values ($K_{max}^{Unpoled}$= 36,469, K_{max}^{Poled}= 33,289) and piezoelectric values (d_{33}=669 pC/N) were reported for the ~30 mol% $PbTiO_3$ composition, indicating the compositional location of the MPB for the PMN-PT system. A phase diagram of the PMN-PT was then estimated by Choi by plotting the variation in transition temperature as a function of composition at 1 kHz. Zhao *et al.* later reported a PMN-PT phase diagram similar to the one introduced by Choi *et al.* (Fig. 2.6).(18) This phase diagram indicated that the MPB, separating the pseudo-cubic (rhombohedral) and tetragonal phases, was located at a $PbTiO_3$ composition of ~35 mol%. The work by Kelley *et al.* supported the phase diagram reported by Zhao *et al.* by

Table 2.2: Properties of various piezoelectric ceramics. (14)

Composition	Density (g/cm^3)	T_C (°C)	K	tan δ (%)	k_p	k_{33}	d_{33} ($\times 10^{-12}$ C/N)	d_{31} ($\times 10^{-12}$ C/N)
$BaTiO_3$	5.7	115	1700	0.5	0.36	0.5	190	−78
PZT-4	7.5	328	1300	0.4	0.58	0.7	289	−123
PZT-5A	7.8	365	1700	2.0	0.6	0.71	374	−171
PZT-5H	7.5	193	3400	4.0	0.65	0.75	593	−274
PMN–PT (65/35)	7.6	185	3640		0.58	0.70	563	−241
PMN–PT (90/10)	7.6	40	24000	5.5	0	0	0	0
$PbNb_2O_6$	6.0	570	225	1.0	0.07	0.38	85	−9
$(Na_{0.5}K_{0.5})NbO_3$	4.5	420	496	1.4	0.46	0.61	127	−51
PLZT 7/60/40	7.8	160	2590	1.9	0.72		710	−262
PLZT 8/40/60	7.8	245	980	1.2	0.34			
PLZT 12/40/60	7.7	145	1300	1.3	0.47		235	
PLZT 7/65/35	7.8	150	1850	1.8	0.62		400	
PLZT 8/65/35	7.8	110	3400	3.0	0.65		682	

Table 2.3: Dielectric and piezoelectric properties of (1-x)PMN-xPT. [17]

Sample	Unpoled						Poled					
PMN-PT	K(RT)	D(RT)	K_{max}	T_c(°C)	D_{max}	d_{33} (pC/N)	K(RT)	D(RT)	K_{max}	T_c(°C)	D_{max}	T_c(°C)
0.775–0.225	3533	.032	29552	112	.036	297	1695	.022	28688	114	.042	96
0.75–0.25	2778	.031	30192	127	.061	305	2435	.018	28714	130	.070	124
0.725–0.275	2873	.035	33432	136	.045	353	2091	.030	31986	138	.051	130
0.7–0.3	3782	.034	36469	139	.035	669	4936	.027	33289	143	.057	136
0.675–0.325	4170	.029	33350	155	.029	663	5260	.018	30048	159	.049	156
0.65–0.35	3190	.013	30623	177	.098	456	3119	.006	29020	182	.069	230
0.625–0.375	2434	.015	28524	190	.018	405	2781	.011	28126	198	.038	191
0.6–0.4	2097	.016	27156	202	.030	323	2371	.010	25189	207	.044	204

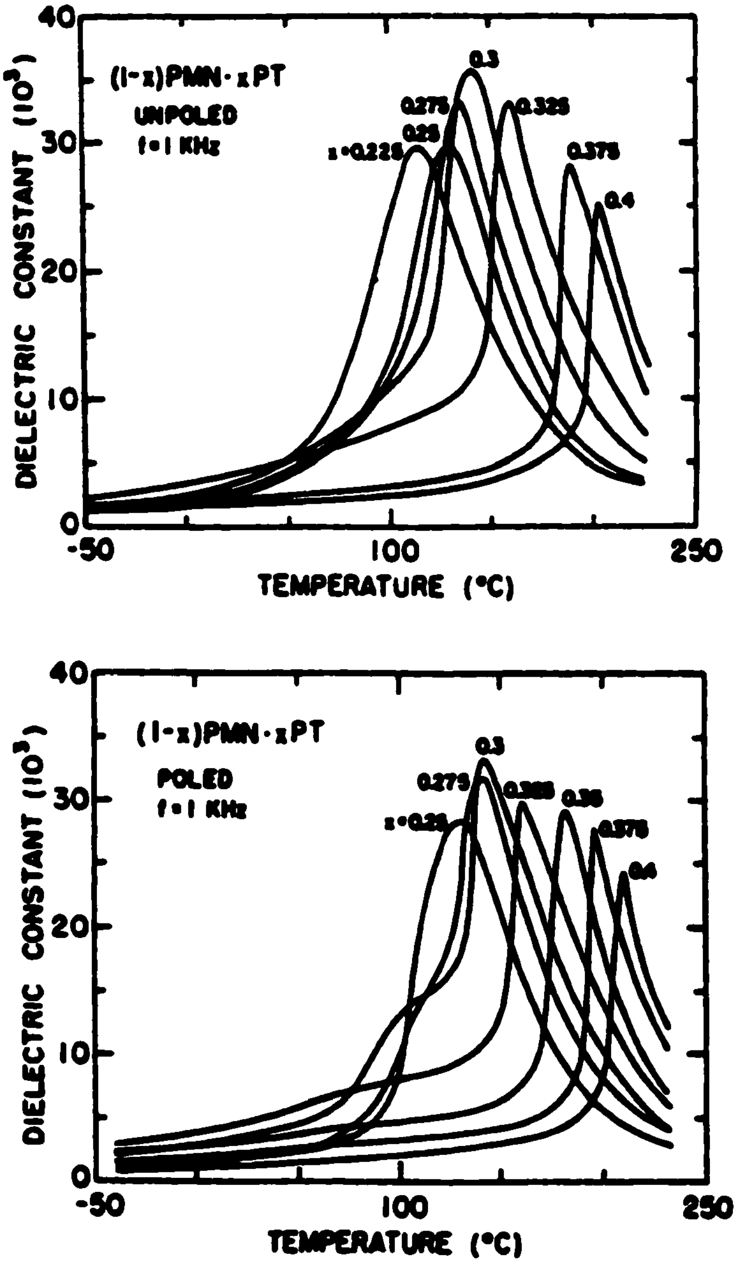

Figure 2.5: Dielectric behavior of (1-x)PMN-xPT ceramics as a function of temperature measured at 1 kHz (Choi *et al*.).(17)

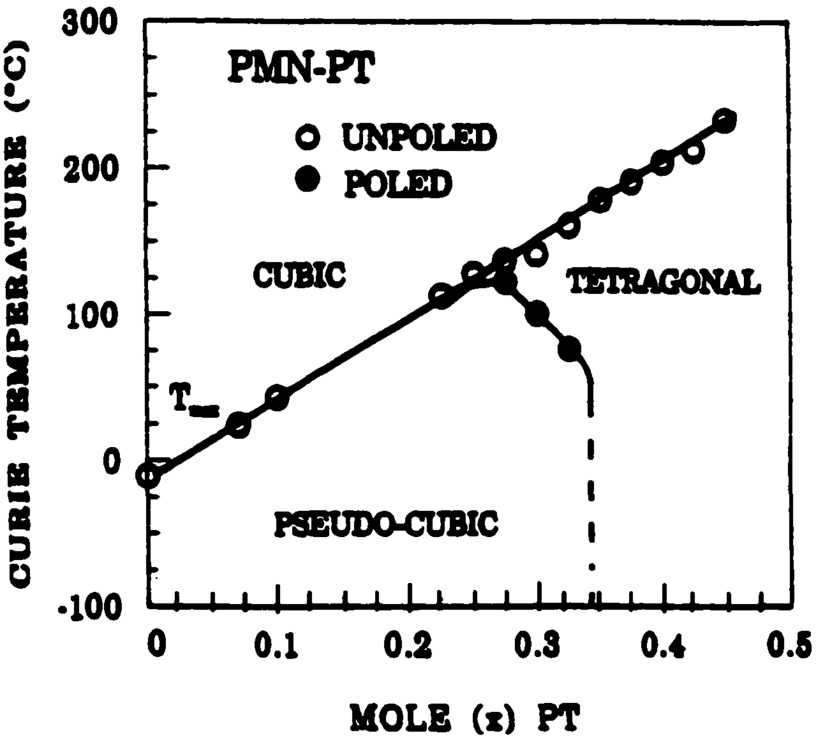

Figure 2.6: Phase diagram of the (1-x)PMN-xPT system (Zhao *et al*).(18)

further refining the effect of $PbTiO_3$ composition (20-70 mol% $PbTiO_3$) on the dielectric and electromechanical properties of PMN-PT ceramics (Table 2.4).(19) Kelley *et al.* showed that ceramic PMN-PT displays its highest room temperature dielectric constant (K_{RT}=5419), piezoelectric coefficient (d_{33}= 720 pC/N), and electromechanical thickness coupling coefficient (k_t= 0.45) at a $PbTiO_3$ composition of ~34.5 mol% (Fig. 2.7). From the electromechanical and x-ray diffraction data, Kelley *et al.* proposed the coexistence of the two ferroelectric phases between the composition of 28-65 mol% $PbTiO_3$. Below ~26-28 mol% $PbTiO_3$ composition, PMN-PT exhibits exclusively a rhombohedral structure and relaxor ferroelectric behavior.

2.6 PIEZOELECTRIC PROPERTIES OF LEAD-BASED RELAXOR-$PbTiO_3$ SINGLE CRYSTALS

Many lead-based relaxor ferroelectric materials, like $Pb(Mg_{1/3}Nb_{2/3})O_3$ (PMN), display a complex perovskite structure with a general formula of $Pb(B_1B_2)O_3$ (B_1:Mg, Zn, Sc, Ni; B_2: Nb, Ta...). These materials receive their "relaxor" identification, in contrast to a "normal" ferroelectric, from the frequency dependence of the dielectric permittivity below the ferroelectric transformation temperature (T_{max}). Relaxor materials are also characterized by: 1) displaying anomalously high permittivites at T_{max}, 2) showing a broad maximum in permittivities at T_{max}, and 3) not exhibiting Curie-Weiss behavior above the ferroelectric transition.(20,21) The typical lead-based relaxor single crystal shows rhombohedral 3m symmetry below T_{max}, where their polar directions are in the <111>.(22,23) As shown above for the PMN composition, lead-based relaxor ferroelectric materials can be combined with $PbTiO_3$ to form solid solutions with varying dielectric,

Table 2.4: Dielectric and electromechanical properties of (1-x)PMN-xPT.(19)

Composition	Structure (%)		Dielectric constant, K, at room temperature	Piezoelectric charging coefficient, d_{33} (pC/N)	Planar coupling coefficient, k_p (%)[a]	Thickness coupling coefficient, k_t (%)[a]
	Rhombohedral	Tetragonal				
0.80PMN-0.20PT	100	0	2464	230	*	*
0.76PMN-0.24PT	100	0	2562	240	0.20	*
0.74PMN-0.26PT	100	0	2459	240	0.25	*
0.72PMN-0.28PT	69	31	2339	320	0.51	0.38
0.70PMN-0.30PT	63	37	2950	450	0.55	0.41
0.69PMN-0.31PT	60	40	3661	570	0.57	0.44
0.68PMN-0.32PT	57	43	3738	590	0.62	0.43
0.67PMN-0.33PT	55	45	3717	640	0.61	0.43
0.66PMN-0.34PT	49	51	4360	670	0.62	0.42
0.655PMN-0.345PT	49	51	5419	720	0.62	0.45
0.65PMN-0.35PT	48	52	5229	700	0.61	0.44
0.645PMN-0.355PT	46	54	5128	650	0.60	0.42
0.64PMN-0.36PT	40	60	4684	585	0.59	0.38
0.62PMN-0.38PT	35	65	3525	465	0.32	0.15
0.60PMN-0.40PT	28	72	2692	370	0.22	0.10
0.55PMN-0.45PT	6	94	1556	240	0.15	<0.10
0.50PMN-0.50PT	7	93	1085	160	<0.10	<0.10
0.45PMN-0.55PT	5	95	846	80	<0.10	*
0.40PMN-0.60PT	2	98	681	50	*	*
0.35PMN-0.65PT	0	100	584	<50	*	*
0.30PMN-0.70PT	0	100	529	<50	*	*

[a] Asterisk signifies that the quantity was not measurable.

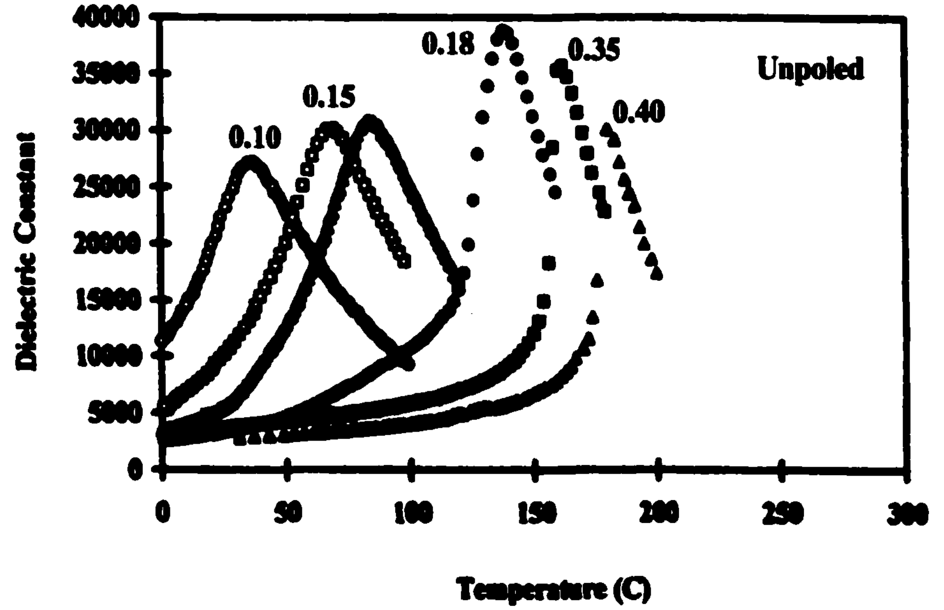

Figure 2.7: Dielectric behavior of (1-x)PMN-xPT ceramics as a function of temperature measured at 1 kHz (Kelly *et al*).(19)

ferroelectric, and piezoelectric properties. Unlike the lead-based relaxor ferroelectric materials, $PbTiO_3$ shows a typical ferroelectric/paraelectric transition at the 490°C transition temperature (T_c). Below T_c, $PbTiO_3$ single crystals show tetragonal 4mm symmetry where the polar vector is in the [001].

Solid solutions of lead-based relaxors and $PbTiO_3$ (general formula $Pb(B_1B_2)O_3$ - $PbTiO_3$) have shown superior piezoelectric properties in single crystal form at compositions on the rhombohedral side of the MPB. Park and Shrout(24,25) showed that single crystal $Pb(Zn_{1/3}Nb_{2/3})O_3$-$PbTiO_3$ (PZN-PT) and PMN-PT oriented and poled in the <001> can produce large E-field strain values, as high as 1.7%, with minimal ferroelastic hysteresis below the field-induced rhombohedral-tetragonal phase transformation. The <001>-oriented crystals showed piezoelectric coefficients (d_{33}) as high as ~2500 pC/N and electromechanical coupling coefficients (k_{33}) of >0.9.

PZN-PT and PMN-PT on the rhombohedral side of the MPB composition show a pseudo-cubic or rhombohedral crystal structure with a 3m symmetry. By poling a rhombohedral PZN-PT or PMN-PT single crystal in the <001>, the crystal will possess four allowable and equivalent domain states with the polar vectors directed along four adjacent <111> directions (Fig. 2.8). Since these polar dipoles have equal components along the <001>, there is no driving force to move the domain walls for an <001>-oriented applied E-field. Thus, the observed strain is a result of intrinsic piezoelectric contributions. This type of crystal manipulation to access a specific domain configuration has been termed "domain engineering".(25) The stable domain engineered configuration has been reported to show three distinct features: 1) hysteresis-free strain vs. E-field behavior due to the restricted domain wall motion, 2) a change of macroscopic

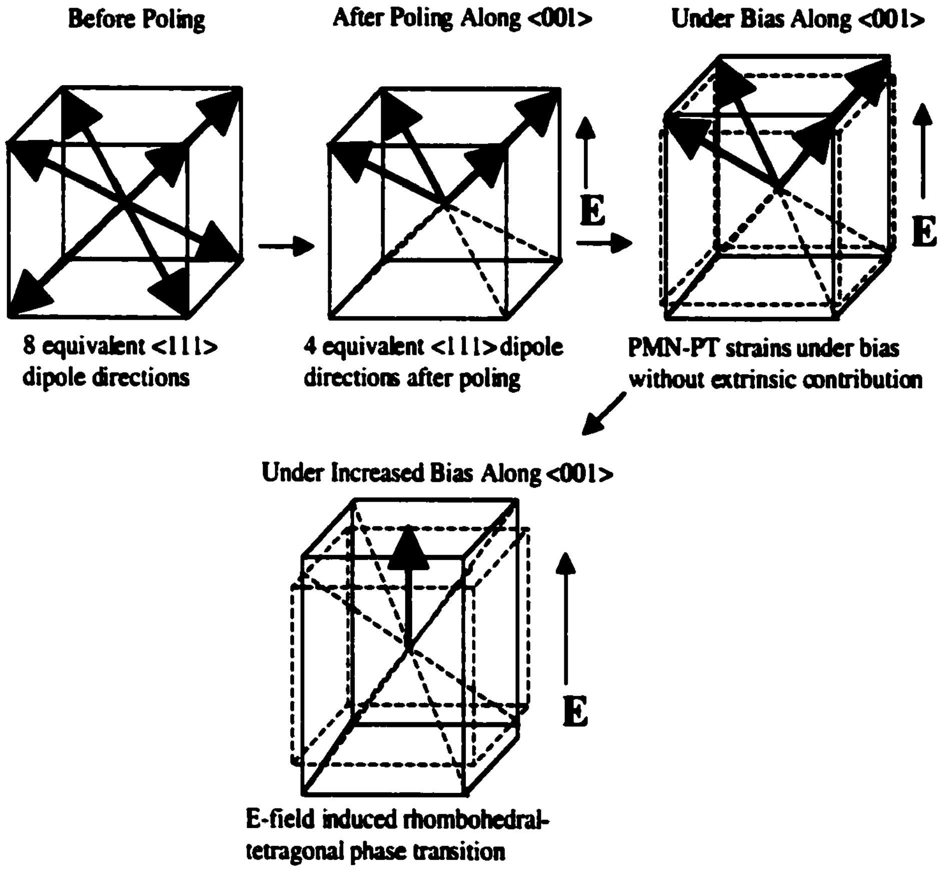

Figure 2.8: Schematic diagram of a unit cell showing the domain configuration for rhombohedral <001>-oriented PMN-PT under an electric bias.(25)

symmetry due to the formation of the four equivalent domain states after poling, and 3) higher piezoelectric constants.(25-28) The macroscopic symmetry has been suggested to transform to the tetragonal 4mm symmetry after poling in the <001>, but this matter is still under some debate.(29)

The higher field induced strains for these domain engineered, rhombohedral lead-based relaxor-$PbTiO_3$ crystals have been attributed to the rotation of the <111>-oriented dipoles towards the <001> due to a field-induced rhombohedral to tetragonal phase transition.(24,25) For these crystals at a $PbTiO_3$ composition just short of the MPB, there remains only a small stress which must be supplied to drive the phase transformation. Depending upon the compositional distance from the MPB, the required energy can be supplied by either an increase in temperature, a mechanical force, or an applied electric field. The application of an electric field will induce a substantial strain as the structure is driven from the rhombohedral to the tetragonal state. <001>-oriented $0.92Pb(Zn_{1/3}Nb_{2/3})O_3$-$0.08PbTiO_3$ (PZN-8PT) single crystals display a large strain and a large piezoelectric coefficient at fields <20 kV/cm due to the softening of the structure just before the phase transition. The strain then further increases at a DC field of ~20-30 kV/cm where the material undergoes the phase transition (Fig. 2.9).(24,25) This phase transition can be identified by the change in the slope of the strain/field plot.

2.7 SOURCES OF PMN AND PMN-PT

The following subsections present an overview of the various processing methods for producing PMN and PMN-PT single crystals, thin films, ceramics, and powders.

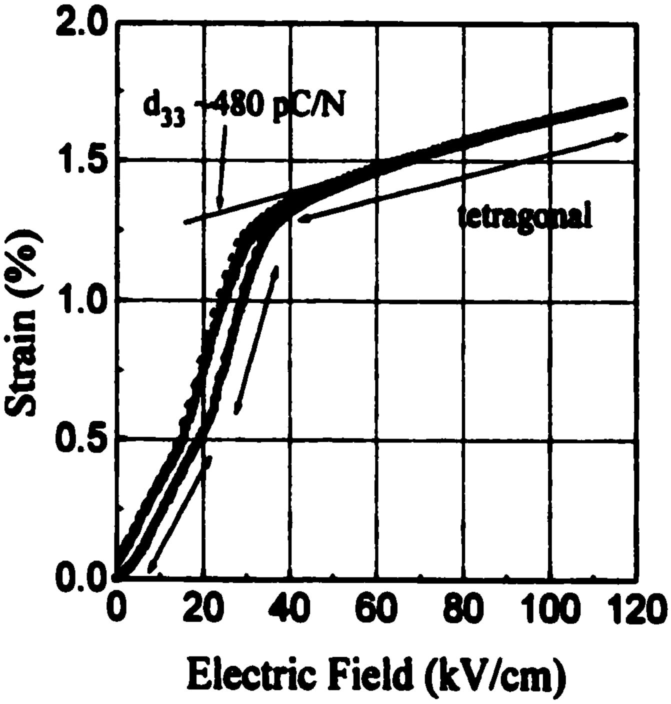

Figure 2.9: % strain versus electric field behavior for <001>-oriented PZN-8PT (Park *et al.*).(25)

2.7.1 PMN-PT Single Crystals

Single crystal PMN was first grown by high-temperature solution growth in PbO and/or PbO-B_2O_3 fluxes encapsulated within Pt crucible.(22,23,30-32) Similar procedures were applied to the growth of various single crystal PMN-PT compositions at temperatures between 980°C to 1300°C in PbO-based solvents and with cooling rates <10°C/hr.(24,25,33,34) The high-temperature solution process is limited by difficulty in: 1) achieving chemical homogeneity throughout the produced batch, 2) controlling nucleation frequency, which affects the size distribution of the crystal batch, and 3) removing the usable crystals from the solidified flux. In addition, the high-temperature solution process requires extremely long soak and growth times which can exceed a few days.

Recently, a great deal of attention has been focused on the Bridgman (or Bridgman-Stockbarger) process to produce PMN-PT and other Pb-based ferroelectric single crystals. The Bridgman process consists of loading a charge, consisting of the solute and solvent material, within a crucible. The crucible may be sealed to control the evaporation of the solvent material. The loaded crucible is pulled into a heated zone or zones to a temperature allowing for full or partial melting of the charge. The crucible is pulled out of the heated furnace zone at a specified rate in order to manipulate the solubility of the melt. The temperature gradient and the rate of cooling determines the nucleation frequency and growth of the nuclei within the melt. Therefore, the primary process variables are the temperature gradient and the cooling rate, which are controlled by the temperature change within the heated zone or zones and the rate of pulling of the loaded crucible, respectively.(35) The gradient-freeze growth technique is analagous to the horizontal Bridgman method, but instead, the temperature gradient is moved over the charge. These directional solidification processes have been applied to the growth of single crystal GaAs, GaP, InAs, InP, other III-V compounds, superconductor compositions, and also to volatile compounds like PbTe, PbSe, PbS, and the fluorides of Ca, La, Cr, Mn, Co, Ni, and Zn.(35,36) The Bridgman technique proved to be invaluable for some of these material systems, since single crystals may be difficult to produce by other means due to the solvent and solute volatility, as in the case of PMN-PT.

Both PZN-PT and PMN-PT single crystals have been produced by the Bridgman method.(37-39) The typical process consists of first producing a highly dense charge. A powder mixture of the solute (PMN-PT or PZN-PT) and PbO (~50/50 mixture) is pressed into pellets and sintered at temperatures >1000°C. This is done to insure that there is a uniform dispersion of the solvent and to increase the fill density of the crucible. The pellets are loaded into a Pt crucible, and the crucible is sealed with a Pt lid to control the volatility of the PbO. As described above, the crucible is loaded into the furnace and slowly pulled out of the hot zone to initiate the nucleation and growth of the crystal/s. Growth rates have been reported between 0.2-0.5 mm/hr.(37-39) The first growth experiments employed a "self-seeded" technique, which means that multiple nucleation sites were allowed during the growth process. During growth, it was found that one or a few crystals dominated and grew at the expense of the surrounding crystals. Lee *et al.*(38) determined by Laue that the larger single crystals displayed a threefold symmetry parallel to the growth direction indicating that the <111> is the fastest growing direction. To control the nucleation frequency and orientation of the growing boule, small crystals were added to the charge end to act as both a seed and a template. The addition of the small crystals controlled the degree of nucleation and aided in determining the direction of crystal growth. Luo *et al.*(39) showed that single crystals with a boule size of >40 mm (diameter) x 80 mm (length) could be achieved, but the crystals still showed various structural and chemical defects. Chemical examination of the grown crystal showed that the $PbTiO_3$ content increased throughout the crystal growth indicating chemical inhomogeneity throughout the crystal. Therefore, the use of the Bridgman growth technique to produce PMN-PT and PZN-PT crystals is currently still limited by chemical inhomogeneity, crystal size, and crystal quality.

Li *et al.*(40) investigated an alternative method to produce millimeter size PMN-PT single crystals which they termed "seeded polycrystal conversion (SPC)". They inserted a singular millimeter size crystal into polycrystalline PMN-35PT powder. After hot-pressing, the sample was annealed at temperatures between 900-1200°C. The boundary of the single crystal migrated into the surrounding polycrystalline material due to the difference in surface free energy between the crystal and the polycrystalline matrix. The process produced a millimeter-sized crystal composed of a porous crystal layer completely surrounding a dense PMN-35PT crystal core. Khan *et al.*(41) showed that the fastest growing direction (~0.14 mm/hr) of the crystal was the <111>, which is similar to the findings for PMN-PT growth by high-temperature solution and Bridgman growth. Li *et al.*(42) modified the process by substituting {111}-$SrTiO_3$ crystal for the PMN-35PT seed crystal. The use of the SPC technique to produce high-quality PMN-PT single crystals is limited by template availability, template size, density of polycrystalline matrix, control of PbO volatility, and a change in crystal growth rate over time due to the grain growth in the matrix. Also, the final grown crystal must be cut or chemically etched from the remnant polycrystalline material.

2.7.2 Thin Film PMN and PMN-PT

The enhanced piezoelectric properties displayed by <001>-oriented PMN-PT at compositions near the MPB would be very beneficial for thin film applications in the MEMS field. PZT has been studied for these same applications. The piezoelectric response of PZT films is limited due to the restricted non-180° wall motion, especially in films under 1 μm thickness.(12,13,43,44) The intrinsic electromechanical response of <001>-oriented rhombohedral PMN-PT single crystals appears not to be related to domain wall motion due to the domain engineering concept. Therefore, a relatively larger fraction of the single crystal piezoelectric response should be available to PMN-PT thin films.

PMN and PMN-PT thin films have been synthesized by a variety of techniques which include sol-gel, metalorganic chemical vapor deposition (MOCVD), rf sputtering, and pulsed laser deposition (PLD).(43,45-56) All of these thin film techniques have been shown to produce oriented films containing from 0-1% pyrochlore phase, especially at higher $PbTiO_3$ content compositions. The sol-gel spin-coating technique has produced [111]-textured (on Pt-coated Si substrates) and [001]-textured (on $LaNiO_3$ substrate and {001}-PT buffered layered Pt-coated Si substrates) PMN-PT at annealing temperatures near 800-850°C.(48-50) <001>-textured thin films of PMN were produced by MOCVD on {001}-$SrTiO_3$ and $SrRuO_3/SrTiO_3$ at substrate temperatures between 700-780°C at a reactor pressure of ~6 Torr.(51) Recently, a great deal of research has been focussed on the deposition of <001>-oriented PMN-PT by PLD. PLD has been shown to produce epitaxial PMN-PT thin films at a substrate temperature ranging between 500-700°C and an oxygen pressure ranging between 200-700 mTorr. Recently published experiments describe growth on {001}-single crystal MgO, $SrTiO_3$, and $LaAlO_3$ and on bottom oxide electrode materials like $LaNiO_3$, $SrRuO_3$, $YBa_2Cu_3O_{7-\delta}$ (YBCO), and $La_{0.5}Sr_{0.5}CoO_3$ (LSCO).(43,52-56) These techniques collectively have produced <001>-textured PMN-PT thin films of a thickness between 0.15-1 μm. The dielectric and piezoelectric properties of these thin films are smaller than single crystals. The room temperature dielectric permittivity ranged between 800-2000 and the piezoelectric coefficients, $d_{33(eff)}$ and $d_{31(eff)}$, were between 20 and 185 pC/N and –28 to -69 pC/N, respectively. The low properties indicate that the films are affected by in-plane stresses developed along the substrate. In addition, mechanical clamping by the passive substrate restricts the free piezoelectric response and the domain wall contributions. PMN-PT thin films are still plagued by inhomogenous distribution of the free charge carriers, high defect concentrations, and thermal and mechanical stresses at the film-substrate interface.(12,13,44)

2.7.3 PMN and PMN-PT Powder and Ceramics

As previously described, the piezoelectric and dielectric properties of PMN-PT ceramics at a composition near the MPB are comparable or better than "soft" PZT ceramics when the use temperature remains below the T_{max} of the PMN-PT composition. PMN-PT ceramics are processed and sintered in a similar manner as PZT ceramics. The difference in processing between the two compositions lies with the higher degree of compositional control that is required during powder synthesis, consolidation, and sintering of the PMN and PMN-PT ceramics. Phase instability plagues the fabrication of PMN-PT ceramics, due to the formation of a Pb-based pyrochlore phase during powder synthesis and ceramic densification. The dielectric and piezoelectric properties of PMN-PT can be dominated by the presence of a small fraction of the pyrochlore phase due to its low dielectric constant (~130).(57)

The typical transformation path to PMN includes the initial formation of various pyrochlore phases which later react with the slow diffusing MgO to form final stoichiometric, perovskite PMN. The crystallization path for the formation of PMN was first proposed by Inada.(58) He concluded by differential thermal analysis (DTA) and x-ray diffraction (XRD) studies that the reaction follows as:

$$3PbO + 2Nb_2O_5 \rightarrow Pb_3Nb_4O_{13} \text{ (}P_3N_4\text{-cubic pyrochlore)}$$

(530°C to 600°C)

$$Pb_3Nb_4O_{13} + PbO \rightarrow 2Pb_2Nb_2O_7 \text{ (}P_2N_2\text{-rhombohedral pyrochlore)}$$

(600°C to 700°C)

$$Pb_2Nb_2O_7 + 1/3MgO \rightarrow Pb(Mg_{1/3}Nb_{2/3})O_3 + 1/3Pb_3Nb_4O_{13}$$

(700°C to 900°C)

Other researchers have since reported another reaction sequence for the formation of PMN. Their findings indicate the formation of only a cubic-pyrochlore ($Pb_3(Mg_xNb_2)O_{8+x}$) between the temperatures of 200-700°C which in turn reacts with PbO and MgO at temperatures >700°C to form pure perovskite PMN.(57,59-63) Therefore, when the MgO is not dispersed homogeneously throughout the precursor or if the reaction is incomplete, MgO was found to reside as residual inclusions within the transformed PMN grains.(64) The isolation of the MgO as small inclusions within the PMN leaves the intermediate pyrochlore phase stranded in the grain boundaries. Furthermore, if there is PbO loss at high temperatures (>1000°C), the PMN-perovskite will revert back to an A-site deficient pyrochlore phase with a formulation of $Pb_{3-x}(Mg\ Nb_2)O_{9-x}$.(57,59,60)

The basic rule for perovskite instability, based on geometrical considerations, was first proposed by Goldschmidt(65) through the concept of the "tolerance factor" (TF), which is expressed as:

$$TF = \frac{(r_A + r_O)}{\sqrt{2}(r_B + r_O)} \qquad \text{Eq. 2.4}$$

where r_A, r_B, and r_O are the ionic radii of the A, B, and oxygen (O) ions, respectively. An ideal perovskite would have a tolerance factor equal to 1, and the perovskite structure is stable for materials with tolerance factors ranging between 0.88-1.09. Halliyal and Shrout(66,67) reported that the stability of perovskites actually depends on two requirements, 1) the material must possess the proper tolerance factor and 2) there must be strong cation-anion ionic bonding within the material. Therefore, to identify the perovskite stability of specific compositions, Halliyal and Shrout plotted the average electronegativity difference between cations and anions versus the tolerance factor of the composition (Fig. 2.10). Without kinetic restrictions, compositions which display a high average electronegativity difference and a tolerance factor close to 1 have the tendency to form a stable perovskite. Since the tolerance factor and average electronegativity difference of PMN are both low, like most lead-based relaxors, these compositions are less stable than perovskites. The structures of these compositions are prone to collapse

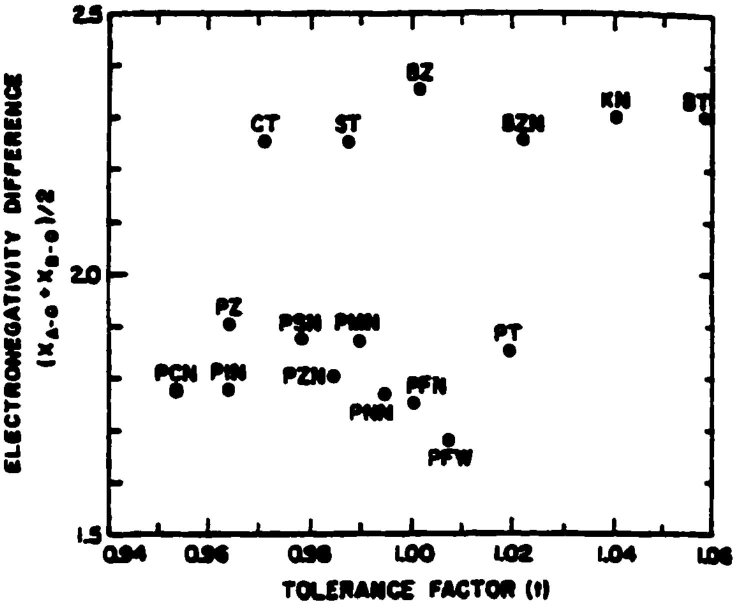

Figure 2.10: Electronegativity difference versus the Goldschmidt tolerance factor for various perovskite materials (Shrout and Halliyal).(66,67)

into the pyrochlore structure, especially with the introduction of any vacancies which would further disrupt the structure.

Swartz *et al.*(61) reported a method to make pyrochlore-free ceramic powder by circumventing the above reaction sequence, therefore, eliminating the formation of the pyrochlore phase. This process includes the prereaction of MgO and Nb_2O_5 to form the columbite $MgNb_2O_6$ phase before the reaction with PbO. The full process reaction is shown as:

$$MgO+Nb_2O_5 \rightarrow MgNb_2O_6$$

$$(\sim 1000°C)$$

$$MgNb_2O_6 + 3PbO \rightarrow 3Pb(Mg_{1/3}Nb_{2/3})O_3$$

$$(\sim 700°C)$$

This process has been termed the columbite percursor method. Through this method, pyrochlore-free PMN ceramics can be formed, exceeding the quality of phase purity of the ceramics where the powder was formed by conventional mixed oxide, co-precipitation, and sol-gel methods.(45,68-74)

2.7.4 PMN Ceramic Powders Synthesized by Coprecipitation, Sol-gel, and Seeded Precursors

PMN and PMN-PT ceramic powders have been synthesized by the coprecipitation method in which water soluble nitrates, chlorides, acetates, or oxalates of Pb, Mg, Nb, and Ti are dissolved in water, mixed, and finally driven to coprecipitate as hydroxides through alteration of the pH.(68-71) The typical precursors used for these processes are: $Pb(NO_3)_2$ or $Pb(CH_3COO)_2 \cdot 3H_2O$, $Mg(NO_3)_2$, $NbCl_2$, and $TiCl_4$. The precipitated precursor is transformed to PMN or PMN-PT after calcination at temperatures ranging between 650-850°C. The final calcined powder for all reported work still included small traces of the pyrochlore phase regardless of the precision of measurement and quality of mixing.

Organic solution methods, like citrate or sol-gel method, have been applied to prepare a multitude of ceramic powders at low temperatures with high purity and nanometer size.(45,72-74) The organic methods have been employed to produce PMN powders at temperatures <800°C, but again, the residual pyrochlore phase is present in the final powder product. Therefore, the concept of seeding the phase transformation was adopted to provide low-energy heteroepitaxial interfaces which selectively increases the crystallization rate and controls the nucleation frequency.(60,75-81) Isostructural perovskite seeds were added to lower the activation barrier for the perovskite PMN phase to a level lower than the activation barrier for the pyrochlore nucleation. The addition of pre-existing nucleation sites to the amorphous precursors affects the solid state transformation by: 1) effectively lowering the transformation temperature, 2) increasing the rate of transformation, and 3) forming particles of a specified phase, size, and orientation.

Ravindranathan *et al.* (75) seeded an amorphous diphasic xerogel of PMN with fine PMN seed particles. The use of 1wt% PMN perovskite seeds led to a pure perovskite phase with a significant lowering of the phase transformation temperature (775°C) of the gel by at least 75°C. Utilizing the knowledge of these doping and seeding experiments on PZN and PMN, Carvalho *et al.* (76) seeded an amorphous PMN precursor prepared from organic citrate solutions with 1 wt% $BaTiO_3$. As a result of the seeding, the fraction of perovskite phase increased from 88% for a pure sample to >95% in the seeded samples calcined at 800°C for 1hr. Similarly, Narendar *et al.*(77,78) seeded EDTA-PMN precursor with approximately 5 wt% fine $BaTiO_3$ particles. This amount accounts for a seeding density of about 1.2×10^{14} $BaTiO_3$ particles/cm^3 of material. At this concentration the formation temperature for the perovskite crystallization decreased from 700°C to approximately 600°C, due to the heteroepitaxial nucleation of the PMN on the seeded BT nucleation sites. Mazon *et al.*(79) seeded PZN-0.05PT with both $BaTiO_3$ and $PbTiO_3$ in order to control the pyrochlore content, particle size, and uniformity of the final ceramic microstructure.

The seeding additions of $BaTiO_3$ and $PbTiO_3$ provided low energy heteroepitaxial nucleation sites to aid in the PMN perovskite phase transformation. These additions also decreased the probability of pyrochlore formation, possibly by stabilizing the final perovskite structure after chemical homogenization. As predicted by Halliyal and Shrout(66,67), $BaTiO_3$, $PbTiO_3$, and $SrTiO_3$ display stable perovskite structures (Fig. 2.10). Small amounts of $BaTiO_3$ and $SrTiO_3$, and larger amounts of $PbTiO_3$, added to PMN increase the stability of the PMN perovskite structure when completely dissolved as a solid solution. These additions raise both the tolerance factor and average electronegativity difference of the PMN solid solution composition.

2.8 GRAIN-ORIENTED FERROELECTRIC CERAMICS

Randomly-oriented ceramics show a macroscopic symmetry of $\infty\infty m$ (spherical symmetry)(Fig. 2.3).(2) This symmetry forces the ceramic to display an average of its crystallographically dependent physical properties. The symmetry of ferroelectric materials may be beneficially altered by poling the sample with an applied electric field, forcing dipole alignment. The increased alignment of the dipoles induces a new macroscopic symmetry which may be described as ∞m (conical symmetry).(2) This lower symmetry allows for the piezoelectric effect to appear for ferroelectric ceramics.

The piezoelectric effect for the ceramic can be further increased by lowering the overall macroscopic symmetry closer to the symmetry shown by its single crystal counterpart. The broadness of the conical symmetry can be reduced by initially orienting the grain structure (texture) before poling, so that the ceramic displays microstructural fiber-texture. An unpoled fiber-textured ceramic would show a macroscopic symmetry of ∞/mm (cylindrical symmetry).(2) A high degree of fiber-texture in the polar direction enables a higher degree of dipole alignment (poling efficiency).

By producing a ferroelectric ceramic which shows a high degree of microstructural texture, the dielectric, pyroelectric, and piezoelectric properties become more directionally dependent like a single crystal. This has been demonstrated for fiber-textured $(Sr,Ba)Nb_2O_6$,(82) $PbNb_2O_6$,(83) and $Bi_4Ti_3O_{12}$(84,85) and sheet-textured $(Sr,La)_2Nb_2O_7$.(86) When the fiber-texture of the grains is in the direction of the polar axis, the piezoelectric and pyroelectric properties were shown to improve drastically due to the increased poling effectiveness. After poling, fiber-textured $(Sr,Ba)Nb_2O_6$, and $PbNb_2O_6$ show pronounced increases in their dielectric, piezoelectric, and/or pyroelectric properties (close to their single crystal values in the polar direction). Duran *et al.*(82) showed that there was a direct correlation between the degree of fiber-texture in the polar direction with the percentage of single crystal-like properties for $(Sr_{0.53},Ba_{0.47})Nb_2O_6$ ceramics. As the fiber-texture increased in the [001], the piezoelectric coefficient increased to a high fraction of the single crystal values. Therefore, by texturing ferroelectric ceramics by conventional ceramic processing routes, it is possible to obtain an inexpensive substitute for single crystals which display similar dielectric, pyroelectric, and piezoelectric properties.

Grain-oriented ceramics (textured ceramics) have been produced by various processing means primarily for materials with low symmetry crystal structures. The development of the texture is usually the result of the orientation and grain growth of aligned anisometric grains. Grain-oriented ceramics have also been formed by directional solidification or melt-texturing.(87,88) The melt-texturing process requires the fastest growing crystallographic direction from the melt, which will dominate the oriented growth, to be either parallel or perpendicular to the desired texture direction. This is most common for materials which have low symmetry crystal structures. The different crystallographic planes have different growth kinetics based on the variance in surface energy leading to the textured microstructures composed of faceted grains.

The critical initial step in forming textured ceramics by most conventional ceramic processing methods is the alignment of the anisometric particles within the starting powder. This is usually done by an applied anisotropic stress during powder consolidation. The particles may be aligned by various green processing methods like tapecasting, extrusion, centrifugal casting, slip casting, sinter forging, and hot-pressing.(82-86,89-96) The efficiency of these processing methods is limited by the interaction of the anisometric particles which controls the degree of initial alignment and green density. The alignment of these grains is retained through the various thermal processing steps (burnout, sintering, annealing...) leading to the development of a textured ceramic. The volume fraction of texture may increase during the thermal processing step due to subsequent densification and grain growth of the aligned particles. In most systems where the grain population is primarily composed of anisometric grains, the increase in texture due to grain growth may be limited by the early impingement of the grains.

In order to avoid particle interaction during green processing, a small fraction of anisometric seeds (or templates) may be aligned in a fine-grained matrix, allowing the templates to be isolated within the matrix during the consolidation process (Fig. 2.11). During thermal processing, the dispersed, aligned templates then grow at the expense of the matrix (Fig. 2.12). This process is typical of exaggerated grain growth where the process is driven by the difference in surface free energy between the matrix and the larger template grains. This process has been termed templated grain growth (TGG).(89) Therefore, TGG allows for improved texturing of ceramics due to a decrease in particle interaction during green processing and minimal grain impingement before texture conversion during thermal processing. The TGG process has been applied to texturing structural ceramics like Al_2O_3 (Figs. 2.13(a,b)),(89) SiC,(90) Si_3N_4,(91) and mullite(92) and ferroelectric ceramics like $Sr_2Nb_2O_7$,(86,96) (Sr,Ba)Nb_2O_6,(82) and $Bi_4Ti_3O_{12}$.(84,85) TGG can also be applied to the growth of an oriented single crystal by aligning only a single

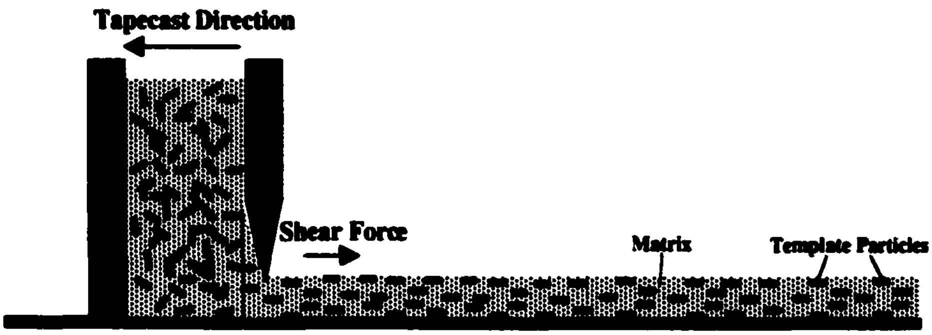

Figure 2.11: Schematic of the process in which the template particles are aligned by the applied shear force under the doctor blade during tape casting.

Figure 2.12: Schematic of the TGG process in which the texture fraction increases with further growth of the template particles within the matrix material during thermal processing.

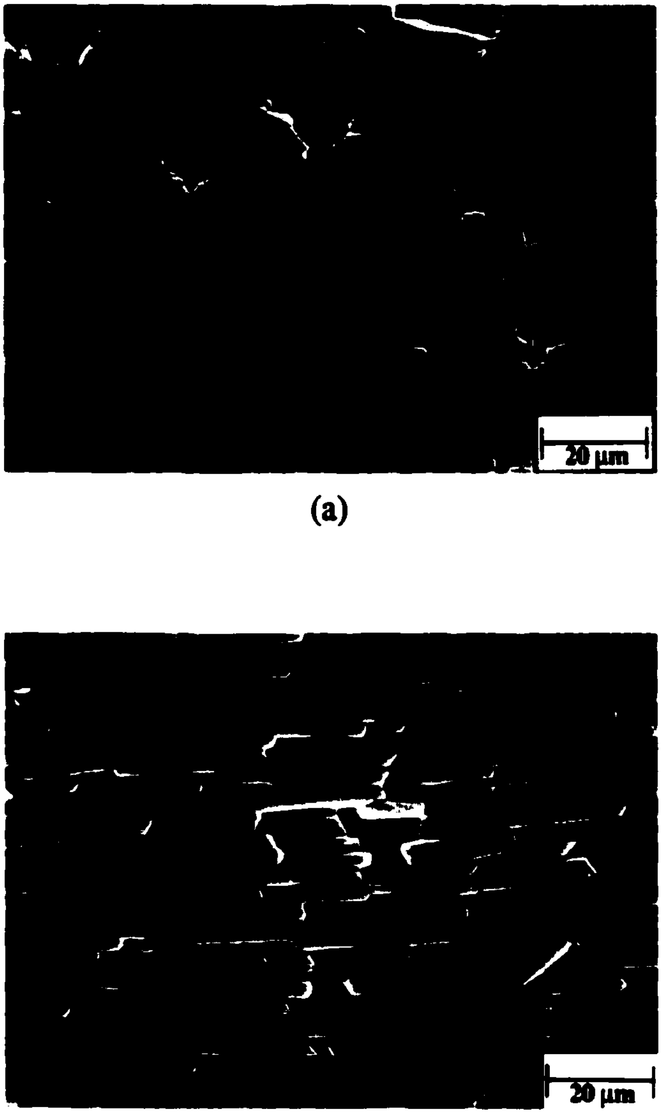

(a)

(b)

Figure 2.13: SEM micrographs of (a) random and (b) TGG textured Al_2O_3 with 5 wt% $CaO+SiO_2$ liquid phase sintered at 1600 °C for 2 h.(89)

template crystal within the matrix. TGG has also been used to produce single crystal Al_2O_3,(97) $BaTiO_3$,(98-100) ferrites,(101) and PMN-PT.(40,42)

2.9 REFERENCES

1) J.F. Nye, *Physical Properties of Crystals.* Oxford Science Publications, Oxford, England (1985).

2) R.E. Newnham, "Composite Electroceramics," *Ferroelectrics,* 68 1-32 (1986).

3) T. Ikeda, *Fundamentals of Piezoelectricity.* Oxford University Press, Oxford, England (1990).

4) B. Jaffe, W.R. Cook, and H. Jaffe, *Piezoelectric Ceramics.* Academic Press, New York (1971).

5) A.J. Moulson and J.M. Herbert, *Electroceramics: Materials, Properties, Applications.* Chapman and Hall, Boundary Row, London (1990).

6) S. Li, W. Cao, and L.E. Cross, "The Extrinsic Nature of Nonlinear Behavior Observed in Lead Zirconate Titanate Ferroelectric Ceramic," *J. Appl. Phys.*, **69** [10] 7219-24 (1991).

7) D. Damjanovic, "Stress and Frequency Dependence of the Direct Piezoelectric Effect in Ferroelectric Ceramics," *J. Appl. Phys.*, **82** [4] 1788-1797 (1997).

8) Q.M. Zhang, H. Wang, N. Kim, and L.E. Cross, "Direct Evaluation of Domain-Wall and Intrinsic Contributions to the Dielectric and Piezoelectric Response and Their Temperature Dependence on Lead Zirconate-Titanate Ceramics," *J. Appl. Phys.*, **75** [1] 454-459 (1994).

9) V. Mueller, E. Fuchs, and H. Beige, "Characterization of Nonlinear Properties of Soft PZT-Piezoceramics," *Ferroelectrics,* **240** 67-74 (2000).

10) S. Hwang and G. Arlt, "Switching in Ferroelectric Polycrystals," *J. Appl. Phys.*, **87** [2] 869-875 (2000).

11) D. Bolten, U. Bottger, T. Schneller, M. Grossmann, O. Lohse, and R. Waser, "Reversible and Irreversible Processes in Donor-Doped $Pb(Zr,Ti)O_3$," *Appl. Phys. Lett.*, **77** [23] 3830-3832 (2000).

12) F. Xu, S. Trolier-McKinstry, W. Ren, B. Xu, Z-L. Xie, and J. Hemker, "Domain Wall Motion and its Contribution to the Dielectric and Piezoelectric Properties of Lead Zirconate Titanate Films," *J. Appl. Phys.*, **89** [2] 1336-1348 (2001).

13) A. Kholkin, "Non-Linear Piezoelectric Response in Lead Zirconate-Titanate (PZT) Films," *Ferroelectrics,* **238** 235-243 (2000).

14) G.H. Haertling, "Ferroelectric Ceramics: History and Technology," *J. Am. Ceram. Soc.*, **82** [4] 797-818 (1999)

15) R.C. Evans, *An Introduction to Crystal Chemistry.* Cambridge University Press, Cambridge, England (1964).

16) J.R. Oliver and R.R. Neurgaonkar, "Ferroelectric Properties of Tungsten Bronze Morphotropic Phase Boundary Systems," *J. Am. Ceram. Soc.*, **72** [2] 202-11 (1989).

17) S.W. Choi, T.R. Shrout, S.J. Jang, and A.S. Bhalla, "Morphotropic Phase Boundary in $Pb(Mg_{1/3}Nb_{2/3})O_3$-$PbTiO_3$ System," *Mater. Lett.*, **8** [6,7] 253-55 (1989).

18) J. Zhao, Q.M. Zhang, N. Kim, and T. Shrout, "Electromechanical Properties of Relaxor Ferroelectric Lead Magnesium Niobate- Lead Titanate Ceramics," *Jpn. J. Appl. Phys., Part I*, **34** [10] 5658-63 (1995).

19) J. Kelly, M. Leonard, C. Tantigate, and A. Safari, "Effect of Composition on the Electromechanical Properties of $(1-x)Pb(Mg_{1/3}Nb_{2/3})O_3$-$xPbTiO_3$ Ceramics," *J. Am. Ceram. Soc.*, **80** [4] 957-64 (1997).

20) L.E. Cross, "Relaxor Ferroelectrics," *Ferroelectrics*, **76** 241-67 (1987).

21) L.E. Cross, "Relaxor Ferroelectrics: An Overview," *Ferroelectrics*, **151** 305-20 (1994).

22) J. Kuwata, K. Uchino, and S. Nomura, "Phase Transitions in the $Pb(Zn_{1/3}Nb_{2/3})O_3$-$PbTiO_3$ System," *Ferroelectrics*, **37** 579-82 (1981).

23) J. Kuwata, K. Uchino, and S. Nomura, "Dielectric and Piezoelectric Properties of $0.91Pb(Zn_{1/3}Nb_{2/3})O_3$-$0.09PbTiO_3$ Single Crystals," *Jpn. J. Appl. Phys.*, **21** 1298-302 (1982).

24) S.-E. Park and T.R. Shrout, "Characteristics of Relaxor-Based Piezoelectric Single Crystals for Ultrasonic Transducers," *IEEE Trans. on Ultrasonics, Ferroelectrics, and Frequency Control*, **44** [5] (1997).

25) S-E. Park and T.R. Shrout, "Ultrahigh Strain and Piezoelectric Behavior in Relaxor Based Ferroelectric Single Crystals," *J. Appl. Phys.*, **82** [4] 1804-11 (1997).

26) S-E Park, S. Wada, L.E. Cross, and T.R. Shrout, "Crystallographically Engineered $BaTiO_3$ Single Crystals for High-Performance Piezoelectrics," *J. Appl. Phys.*, **86** [5] 2746-50 (1999).

27) S. Wada, S.-E. Park, L.E. Cross, and T.R. Shrout, "Engineered Domain Configuration in Rhombohedral PZN-PT Single Crystals and Their Ferroelectric Related Properties," *Ferroelectrics*, **221**, 147-55 (1999).

28) S-F. Liu, S-E. Park, T.R. Shrout, and L.E. Cross, "Electric Field Dependence of Piezoelectric Properties for Rhombohedral 0.955Pb(Zn$_{1/3}$Nb$_{2/3}$)O$_3$-0.045PbTiO$_3$ Single Crystals," *J. Appl. Phys.*, **85** [5] 2810-14 (1999).

29) J. Yin and W. Cao, "Domain Configuration in Domain Engineered 0.955Pb(Zn$_{1/3}$Nb$_{2/3}$)O$_3$-0.045PbTiO$_3$ Single Crystals," *J. Appl. Phys.*, **87** [10] 7438-41 (2000).

30) I.E. Myl'nikova and V.A. Bokov, *Growth of Crystals*. Vol. 3, Consultants Bureau, New York, pg. 309 (1959).

31) V.A. Bokov and I.E. Myl'nikova, "Electrical and Optical Properties of Single Crystals of Ferroelectrics with a Diffuse Phase Transition," *Sov. Phys.-Solid State (Engl. Transl.)*, **3** [3] 613-23 (1961).

32) V.A. Bokov and I.E. Myl'nikova, "Ferroelectric Properties of Monocrystals of New Perovskite Compounds," *Sov. Phys.-Solid State (Engl. Transl.)*, **2** [11] 2428-32 (1961).

33) Z-G Ye, P. Tissot, and H. Schmid, "Pseudo-Binary Pb(Mg$_{1/3}$Nb$_{2/3}$)O$_3$-PbO Phase Diagram and Crystal Growth of Pb(Mg$_{1/3}$Nb$_{2/3}$)O$_3$ (PMN)," *Mat. Res. Bull.*, **25** 739-48 (1990).

34) T.R. Shrout, Z.P. Chang, N. Kim, and S. Markgraf, "Dielectric Behavior of Single Crystals Near the (1-x)Pb(Mg$_{1/3}$Nb$_{2/3}$)O$_3$-(x)PbTiO$_3$ Morphotropic Phase Boundary," *Ferro. Lett.*, **12** 63-69 (1990).

35) B.N. Roy, *Crystal Growth from Melts: Applications to Growth of Groups 1 and 2 Crystals*. John Wiley and Sons, Inc., New York (1992).

36) T. Izumi and Y. Shiohara, "Growth Mechanism of YBa$_2$Cu$_3$O$_y$ Superconductors Prepared by the Horizontal Bridgman Method," *J. Mater. Res.*, **7** [1] 16-23 (1992).

37) K. Harada, S. Shimanuki, T. Kobayashi, S. Saitoh, and Y. Yamashita, "Crystal Growth and Electrical Properties of Pb((Zn$_{1/3}$Nb$_{2/3}$)$_{0.91}$Ti$_{0.9}$)O$_3$ Single Crystals Produced by Solution Bridgman Method," *J. Am Ceram. Soc.*, **81** [11] 2785-2788 (1998).

38) S-G. Lee, R.G. Monteiro, R.S. Feigelson, H.S. Lee, M. Lee, and S-E. Park, "Growth and Electrostrictive Properties of Pb(Mg$_{1/3}$Nb$_{2/3}$)O$_3$ Crystals," *Appl. Phys. Lett.*, **74** [7] 1030-32 (1999).

39) H. Luo, G. Xu, P. Wang, and Z. Yin, "Compositional Homogeneity and Electrical Properties of Lead Magnesium Niobate Titanate Single Crystals Grown by a Modified Bridgman Technique," *Jpn. J. Appl. Phys.*, Part 1 **39** [9B] 5581-85 (2000).

40) T. Li, A.M. Scotch, H.M. Chan, M.P. Harmer, S.-E. Park, T.R. Shrout, and J.R. Michael, "Single Crystals of $Pb(Mg_{1/3}Nb_{2/3})O_3$-35mol% $PbTiO_3$ from Polycrystalline Precursors," *J. Am. Ceram. Soc.*, **81** [1] 244-48 (1998).

41) A. Khan, F.A. Meschke, T. Li, A.M. Scotch, H.M. Chan, and M.P. Harmer, "Growth of $Pb(Mg_{1/3}Nb_{2/3})O_3$-35mol% $PbTiO_3$ Single Crystals from (111) Substrates by Seeded Polycrystalline Conversion," *J. Am. Ceram. Soc.*, **82** [11] 2958-62 (1999).

42) T. Li, S. Wu, A. Khan, A.M. Scotch, H.M. Chan, and M.P. Harmer, "Heteroepitaxial Growth of Bulk Single-Crystal $Pb(Mg_{1/3}Nb_{2/3})O_3$-32 mol% $PbTiO_3$ from (111) $SrTiO_3$," *J. Mater. Res.*, **14** [8] 3189-91 (1999).

43) J-P. Maria, W. Hackenberger, and S. Trolier-McKinstry, "Phase Development and Electrical Property Analysis of Pulsed Laser Deposited $Pb(Mg_{1/3}Nb_{2/3})O_3$-$PbTiO_3$ (70/30) Epitaxial Thin Films," *J. Appl. Phys.*, **84** [9] 5147-54 (1998).

44) K.R. Udayakumar, P.J. Schuele, J. Chen, S.B. Krupanidhi, and L.E. Cross, "Thickness-Dependent Electrical Characteristics of Lead Zirconate Titanate Thin Films," *J. Appl. Phys.*, **77** [8] 3981-86 (1995).

45) L.F. Francis, Y-J. Oh, and D.A. Payne, "Sol-gel Processing and Properties of Lead Magnesium Niobate Powders and Thin Layers," *J. Mater. Sci.*, **25** 5007-12 (1990).

46) K.R. Udayakumar, J. Chen, P.J. Schuele, L.C. Cross, V. Kumar, and S.B. Krupanidhi, "Polarization Reversal and High Dielectric Permittivity in Lead Magnesium Niobate Titanate Thin Films," *Appl. Phys. Lett.*, **60** [10] 1187-89 (1992).

47) K. Kighelman, D. Damjanovic, A. Seifert, L. Sagalowicz, and N. Setter, "Relaxor Behavior and Electricomechanical Properties of $Pb(Mg_{1/3}Nb_{2/3})O_3$ Thin Films," *Appl. Phys. Lett.*, **73** [16] 2281-83 (1998).

48) M. Shyu, T. Hong, and T. Wu, "Properties of Highly (100)-Oriented Thin Films of Sol-gel Derived $Pb[(Mg_{1/3}Nb_{2/3})_{0.675}Ti_{0.325}]O_3$ Prepared on (100)-Oriented $LaNiO_3$ Electrode," *Mater. Lett.*, **23** 221-26 (1995).

49) J.H. Park, F. Xu, and S. Trolier-McKinstry, "Dielectric and Piezoelectric Properties of Sol-gel Derived Lead Magnesium Niobium Titanate Films with Different Textures," *J. Appl. Phys.*, **89** [1] 568-74 (2001)

50) Z. Keigelman, D. Damjanovic, and N. Setter, "Electromechanical Properties and Self-Polarization in Relaxor Pb($Mg_{1/3}Nb_{2/3}$)O_3 Thin Films," *J. Appl. Phys.*, **89** [2] 1393-401 (2001).

51) G.R. Bai, S.K. Streiffer, P.K. Baumann, O. Auciello, and K. Ghosh, S. Stemmer, A. Munkhom, C. Thompson, R.A. Rao, and C.B. Eom, "Epitaxial Pb($Mg_{1/3}Nb_{2/3}$)O_3 Thin Films Synthesized by Metal-Organic Chemical Vapor Deposition," *Appl. Phys. Lett.*, **76** [21] 3106-108 (2000).

52) C. Tantigate, J. Lee, and A. Safari, "Processing and Properties of Pb($Mg_{1/3}Nb_{2/3}$)O_3-$PbTiO_3$ Thin Films by Pulsed Laser Deposition," *Appl. Phys. Lett.*, **66** [13] 1611-13 (1995).

53) G. Catalan, M.H. Corbett, R.M. Bowman, and J.M. Gregg, "Influence of Oxygen Content on Dielectric and Electromechanical Properties of Pb($Mg_{1/3}Nb_{2/3}$)O_3 Thin Films," *Appl. Phys. Lett.*, **74** [20] 3035-37 (1999).

54) V. Nagarajan, C.S. Ganpule, B. Nagaraj, S. Aggarwal, S.P. Alpay, A.L. Roytburd, E.D. Williams, and R. Ramesh, "Effect of Mechanical Constraint on the Dielectric and Piezoelectric Behavior of Epitaxial Pb($Mg_{1/3}Nb_{2/3}$)O_3(90%)-$PbTiO_3$(10%) Relaxor Thin Films," *Appl. Phys. Lett.*, **75** [26] 4183-85 (1999).

55) A. Kholkin, C. Tantigate, and A. Safari, "Electromechanical Properties of PMN-PT Thin Films Prepared by Pulsed Laser Deposition Technique," *Integ. Ferro.*, **22** [1-4] 1035-43 (1998).

56) M. Tyunina, J. Levoska, A. Sternberg, and S. Leppavuori, "Dielectric Properties of Pulsed Laser Deposited Films of Pb($Mg_{1/3}Nb_{2/3}$)-$PbTiO_3$ and Pb($Sc_{1/2}Nb_{1/2}$)O_3-$PbTiO_3$ Relaxor Ferroelectrics," *J. Appl. Phys.*, **86** [9] 5179-84 (1999).

57) T.R. Shrout and S.L. Swartz, "Dielectric Properties of Pyrochlore Lead Magnesium Niobate," *Mater. Res. Bull.*, **18** 663-67 (1983).

58) M. Inada, "Analysis of the Formation Process of the Piezoelectric PCM Ceramics," *Jpn. Natl. Tech. Rept.*,**27** [1] 95-102 (1977).

59) Y. Narendar and G.L. Messing, "Seeding of Perovskite Lead Magnesium Niobate Crystallization from Pb-Mg-Nb-EDTA Gels," *J. Am. Ceram. Soc.*, **82** [7] 1659-64 (1999).

60) F. Chaput, J-P. Boilet, M. Lejeune, R. Papiernik, L.G. Hubert-Pfalzgraf, "Low-Temperature Route to Lead Magnesium Niobate," *J. Am. Ceram. Soc.*, **72** [8] 1335-57 (1989).

61) S.L. Swartz and T.R. Shrout, "Fabrication of Perovskite Lead Magnesium Niobate," *Mater. Res. Bull.*, **18** 663-67 (1982).

62) J.P. Guha, "Reaction Chemistry and Subsolidus Phase Equilibria in Lead-Based Relaxor Systems: Part 1, Formation and Stability of the Perovskite and Pyrochlore Compounds in the System PbO-MgO-Nb_2O_5," *J. Mater. Sci.*, **34** 4985-94 (1999).

63) P. Lucas and W.T. Petuskey, "Phase Equilibria in the Lead-Magnesium-Niobium-Oxygen System at 1000°C," accepted by the *J. Amer. Ceram. Soc.*, (2001).

64) E. Goo, T. Yamamoto, and K. Okazaki, "Microstructure of Lead-Magnesium Niobate Ceramics," *J. Am. Ceram. Soc.*, **69** [8] C-188-C-190 (1986).

65) V.M. Goldschmidt, *Shrifter Norske Videnskaps-Akad.* Oslo 1: Matemot. Naturuid. Klasse, No. 2, 1926.

66) A. Halliyal, U. Kumar, R.E. Newnham, and L.E. Cross, "Stabilization of the Perovskite Phase and Dielectric Properties of Ceramics in the $Pb(Zn_{1/3}Nb_{2/3})O_3$-$BaTiO_3$ System," *Am. Ceram. Soc. Bull.*, **66** [4] 671-76 (1987).

67) T.R. Shrout and A. Halliyal, "Preparation of Lead-Based Ferroelectric Relaxors for Capacitors," *J. Am. Ceram. Soc.*, **66** [4] 704-11 (1987).

68) M.M.A. Sekar, A. Halliyal, and K.C. Patil, "Synthesis, Characterization, and Properties of Lead-based Relaxor Ferroelectrics," *J. Mater. Res.*, **11** [5] 1210-18 (1996).

69) D. Mohan, "Hydroxide Route for the Synthesis of Lead Magnesium Niobate Powder," J. *Mater. Sci. Lett.*, **12** 564-66 (1993).

70) A. Watanabe, H. Haneda, Y. Moriyoshi, S. Shirasaki, S. Kuramoto, and H. Yamamura, "Preparation of Lead Magnesium Niobate by a Coprecipitation Method," *J. Mater. Sci.*, **27** 1245-49 (1992).

71) T. Ando, R. Suyama, and K. Tanemoto, "Preparation of $Pb(Mg_{1/3}Nb_{2/3})O_3$-$PbTiO_3$ Powder by a Wet Chemical Process," *Jap. J. Appl. Phys.*, **30** [4] 775-9 (1991).

72) Y. Narendar and G.L. Messing, "Kinetic Analysis of Combustion Synthesis of Lead Magnesium Niobate from Metal Carboxylate Gels," *J. Am. Ceram. Soc.*, **80** [4] 915-24 (1997).

73) H.K. Guo, X.G. Tang, J.X. Zhang, S.W. Shan, M.M. Wu, and Y.J. Luo, "Preparation and Dielectric Properties of PMN-PT Ceramics," *J. Mat. Sci. Lett.*, **17** [18] 1567-68 (1998).

74) L.F. Francis and D.A. Payne, "Thin-layer Dielectrics in the $Pb(Mg_{1/3}Nb_{2/3})_{1-x}Ti_xO_3$," *J. Am. Ceram. Soc.*, **74** [12] 2996-9 (1991).

75) P. Ravindranathan, S. Komarneni, and R. Roy, "Solid-State Epitaxial Effects in Structurally Diphasic Xerogel of $Pb(Mg_{1/3}Nb_{2/3})O_3$," *J. Am. Ceram. Soc.*, **73** [4] 1024-25 (1990).

76) J. Carvalho, C. Paiva-Santos, M. Zaghete, C.Oliveira, J. Varela, and E. Longo, "Phase Analysis of Seeded and Doped $PbMg_{1/3}Nb_{2/3}O_3$ Prepared by Organic Solution of Citrates," *J. Mater. Res.*, **11** [7] 1795-99 (1996).

77) Y. Narendar, *Regulating Oxide Crystallization from Pb, Mg, Nb- Carboxylate Gels.* Ph.D. Thesis at the Pennsylvania State University, 237-71 (1996).

78) Y. Narender and G.L. Messing, "Seeding of Perovskite Lead Magnesium Niobate Crystallization from Pb-Mg-Nb-EDTA Gels," *J. Amer. Ceram. Soc.*, **82** [7] 1659-64 (1999).

79) T. Mazon, M.A. Zaghete, J.A. Varela, C.O. Paiva-Santos, and E. Longo, "Influence of Seed Particle Frequency on the Phase Formation and on the Microstructure of 0.88PZN-0.07BT-0.05PT Ceramic," *Ceram. Int.*, **26** [7] 727-31 (2000).

80) D. Suvorov, D. Devoino, D. Kolar, and M. Trontelj, "Pyrochlore to Perovskite Transformation of $Pb(Zn_{1/3}Nb_{2/3})O_3$ with $BaTiO_3$ Addition," *Science of Ceramics*, **14** 927-31 (198).

81) D. Kang, K. Yoon, "Stabilization of the Perovskite Phase and Dielectric Properties in the $Pb(Mg_{1/3}Nb_{2/3})O_3$-$BaTiO_3$ System," *J. Mater. Sci.*, **26** 56-60 (1991).

82) C. Duran, S. Trolier-McKinstry, and G.L. Messing, "Fabrication and Electrical Properties of Textured $Sr_{0.53}Ba_{0.47}Nb_2O_6$ Ceramics by Templated Grain Growth," *J. Am. Ceram. Soc.*, **83** [9] 2203-13 (2000).

83) K. Nagata and K. Okazaki, "One-Dimensional Grain-Oriented Lead Metaniobate Ceramics," *Jap. J. Appl. Phys.*, **24** [7] 812-14 (1985).

84) J.A. Horn, S.C. Zhang, U. Selvaraj, G.L. Messing, and S. Trolier-McKinstry, "Templated Grain Growth of Textured Bismuth Titanate," *J. Am. Ceram. Soc.*, **82** [4] 921-26 (1999).

85) S.-H. Hong, S. Trolier-McKinstry, and G.L. Messing, "Dielectric and Electromechanical Properties of Textured Niobium-Doped Bismuth Titanate Ceramics," *J. Am. Ceram. Soc.*, **83** [1] 113-118 (2000).

86) B. Brahmaroutu, *Templated Grain Growth of Textured Strontium Niobate Ceramics.* Ph.D. Thesis, Pennsylvania State University, University Park, PA (1999).

87) S.P. Athur, V. Selvamanickam, U. Balachandran, and K. Salama, "Study of Growth Kinetics in Melt-Textured $YBa_2Cu_3O_{7-x}$," *J. Mater. Res.*, **11** [12] 2976-89 (1996).

88) J.A. Alarco, E. Olsson, S.J. Golden, A. Bhargava, T. Yamashita, J. Barry, and I.D.R. Mackinnon, "Microstructural Characterization of Quenched Melt-Textured $YBa_2Cu_3O_{7-\delta}$ Materials," *J. Mater. Res.*, **12** [3] 624-35 (1997).

89) M.M. Seabaugh, I.H. Kerscht, and G.L. Messing, "Texture Development by Templated Grain Growth in Liquid-Phase-Sintered α-Alumina," *J. Am. Ceram. Soc.*, **80** [5] 1181-88 (1997).

90) M.D. Sacks, G.W. Scheiffele, and G.A. Staab, "Fabrication of Textured Silicon Carbide via Seeded Anisotropic Grain Growth," *J. Am.Ceram. Soc.*, **79** [6] 1611-16 (1996).

91) K. Hirao, T. Nagaoka, M.E. Brito, and S. Kanzaki, "Microstructure Control of Silicon Nitride by Seeding with Rodlike β-Si_3N_4 Particles," *J. Am. Ceram. Soc.*, **77** [7] 1857-62 (1994).

92) S.-H. Hong, W. Cermignani, and G.L. Messing, "Anisotropic Grain Growth in Seeded and B_2O_3-Doped Diphasic Mullite Gels," *J. Euro. Ceram. Soc.*, **16** 133-41 (1996).

93) W.O. Williamson, "Particle Orientation in Clays and Whitewares and Its Relation to Forming Processes,"; pp. 89-98 in *Ceramic Fabrication Processes.* Edited by W.D. Kingery. The Technology Press, MIT, Cambridge, MA, 1958.

94) Y. Ma, K.L. Kruger, and K.J. Bowman, "Texture in Hot Pressed or Forged Alumina," *J. Am. Ceram. Soc.*, **74** [11] 2941-44 (1991).

95) E. Kragness, M.F. Amateau, and G.L. Messing, "Processing and Characterization of Laminated SiC Whisker Reinforced Al_2O_3," *J. Compos. Mater.*, **25**, 417-32 (1991).

96) B. Brahmaroutu, G.L. Messing, S. Trolier-McKinstry, and U. Selvaraj, "Templated Grain Growth of Textured $Sr_2Nb_2O_7$"; pp. 883-86, Vol. 2, *Proceedings of the Tenth International Symposium on the Applications of Ferroelectrics.* Edited by B. Kuwicki, A. Amin, and A. Safari. IEEE, East Brunswick, NJ, 1996.

97) C. Scott, J. Strok, and L. Levinson, "Solid State Thermal Conversion of Polycrystalline Alumina to Sapphire Using a Seed Crystal," U.S. Pat. No. 5 549 746, 1996.

98) T. Yamamoto and T. Sakuma, "Fabrication of Barium Titanate Single Crystals by Solid-State Grain Growth," *J. Am. Ceram. Soc.*, **77** [4] 1107-109 (1994).

99) P.W. Rehrig, S.E. Park, S. Trolier-McKinstry, G.L. Messing, B. Jones, and T.R. Shrout, "Piezoelectric Properties of Zirconium-Doped Barium Titanate Single Crystals Grown by Templated Grain Growth," *J. Appl. Phys.*, **86** [3] 1657-61 (1999).

100) P.W. Rehrig, G.L. Messing, and S. Trolier-McKinstry, "Templated Grain Growth of Barium Titanate Single Crystals," *J. Am. Ceram. Soc.*, **83** [11] 2654-60 (2000).

101) K. Kugimiya, K. Hirota, and K. Matsuyama, "Process for Producing Single Crystal Ceramics," U.S. Pat. 4 900 393, 1990.

Chapter 3

TEMPLATE SELECTION FOR TGG OF PMN-PT

3.1 INTRODUCTION

Texturing materials by the Templated Grain Growth (TGG) process is primarily dependent upon the initial alignment of the template particles within the ceramic body during green processing and the epitaxial nucleation and growth of the desired phase on these oriented templates during high temperature treatment. Therefore, an essential physical component in TGG is the template particle which acts as a substrate for epitaxy and as a seed for the exaggerated grain growth. The epitaxy dictates the crystallographic alignment of a small population of grains, which could be thought of as a population of oriented "exaggerated" grains. Thus, with further exaggerated grain growth, the volume fraction of textured material increases.

For template particles to serve both purposes, there are a few requirements which must be satisfied. The template particle must possess a crystal structure and lattice parameter which is similar to the desired phase to be templated. The templating phase must be able to nucleate and grow from the oriented template particle at elevated temperature. The template particle must have a suitably high aspect ratio morphology (like a whisker, blade or platelet), so that it can be mechanically oriented under an applied shear force during green forming. In instances where the purpose of texturing is to access physical properties which are directly related to crystallographic orientation (like thermal conductivity, dielectricity, piezoelectricity, electrical conductivity...), the template axis must match the desired crystallographic orientation. And, the template particle must be thermodynamically stable within the environment at which it is to function, meaning that the template must not react or dissolve within the matrix material before nucleation and growth of stable oriented nuclei. Since most TGG systems contain a liquid phase to enhance growth kinetics, the template must show sufficient stability in the presence of the liquid phase at the growth temperature. The template must not react with the liquid to form a rogue phase on the surface which would act as a barrier to the nucleation of the desired phase.

In TGG systems where the template and matrix materials are of the same composition, the solubility (S) of the material in the liquid is governed by the Gibbs-Thomson equation:

$$S = S_o \exp(\frac{2\gamma\Omega}{kTr}) \qquad \text{Eq. 3.1}$$

$$S_o = S_{To} = S_{Mo} \qquad \text{Eq. 3.2}$$

where S_{To} and S_{Mo} are the respective equilibrium solubilities of the template and matrix, γ is the solid-liquid surface energy, Ω is the molar volume, k is Boltzmann's constant, T is temperature, and r is the radius of the particle (template or matrix). The larger template particles have a lower solubility than the matrix particles due to the solubility dependence on r ($r_T >> r_M$) which incidentally drives the Ostwald ripening process.$^{(1)}$ In the case where the template and matrix are of different composition, then:

$$S_o \neq S_{To} \neq S_{Mo} \qquad \text{Eq. 3.3}$$

and therefore, for TGG to occur:

$$S_{T_0}\exp(\frac{2\gamma_T\Omega}{kTr_T}) >> S_{M_0}\exp(\frac{2\gamma_M\Omega}{kTr_M}) \qquad \text{Eq. 3.4}$$

This indicates that the TGG process is dependent on the difference in particle size between the template and matrix ($\Delta r = r_T - r_M$), the respective surface energy of the template and matrix (γ_T and γ_M), and the equilibrium solubilities of the two compositions. If the overall solubility of the template is close or below the critical solubility (S^*) of the system, then the stability of the template will be in question.

Single crystals and thin film-coated substrates of many compositions have been used to template the growth of textured Pb-based ferroelectric thin films. Epitaxial thin films of $Pb(Mg_{1/3}Nb_{2/3})O_3$ (PMN), $Pb(Mg_{1/3}Nb_{2/3})O_3$-$PbTiO_3$ (PMN-PT), $Pb(Zr,Ti)O_3$ (PZT) and $PbTiO_3$ (PT) can be grown on MgO, $SrTiO_3$, $MgAl_2O_4$, $LaAlO_3$, $LaNiO_3$, $YBa_2Cu_3O_7$, $(La,Sr)CoO_3$, $SrRuO_3$, and Pt at temperatures usually less than 800°C.(2,3) Many of these compositions should be avoided as candidate templates for the TGG of PMN-PT to eliminate problems with template stability and adverse effects on the dielectric and piezoelectric properties.

The most desirable templates would be whisker or platelet PMN and/or PMN-PT in the size range of 10-50 μm, so that after growth the average grain size will remain <100 μm. Molten flux and hydrothermal crystal growth processes can be controlled to produce large quantities of PMN and PMN-PT crystallites, but currently well-faceted particles with whisker or platelet morphologies have not been produced by these processes.(4-10) Both processes are also plagued by the formation of various pyrochlore phases similar to those observed for PMN-PT powder synthesis by the co-precipitation and mixed-oxide routes.

The best alternative template candidates would be other perovskite ferroelectric materials which display a similar lattice parameter (~4 Å) and can be synthesized into well-faceted, high aspect ratio crystallites. The formation of PZT crystallites by molten flux and hydrothermal methods produces spherical and cuboidal morphologies, similar to those of PMN and PMN-PT.(11-16) Unlike PZT, $PbTiO_3$ crystallites can be produced in both fiber and tabular morphologies primarily by hydrothermal synthesis. Moon *et al.*(17,18) synthesized phase-pure, tabular-like {001}-$PbTiO_3$ particles which are <10 μm in size (aspect ratio <3) and show significant faceted overgrowth. Cheng *et al.*(19,20) and Ohara *et al.*(21) showed that various morphologies (spherical, platelet, and fibers) could be fabricated by altering the pH, Pb/Ti ratio, and temperature. Both Cheng and Ohara's work produced well-faceted, high aspect ratio particles, but the particles consisted of a metastable lead titanate structure.

Lead-free compositions which have the perovskite structure, like $BaTiO_3$ and $SrTiO_3$, could also be used as template materials. Similar to $PbTiO_3$, $BaTiO_3$ and $SrTiO_3$ show very low lattice mismatch to PMN and PMN-PT even at high temperature (Fig. 3.1(a,b)).(22,23) Hydrothermally prepared $BaTiO_3$ results in the formation of nanometer size spherical and cuboidal particles.(24-26) Molten salt synthesis of $BaTiO_3$ crystals has been intensively investigated since the early 1950's. The most common morphologies are {001}-platelet and -"butterfly" twinned platelets of the hexagonal and cubic phase, respectively, which can be grown in KF, $BaCl_2$, K_2CO_3, and Na_2CO_3.(27,28) Utilizing an

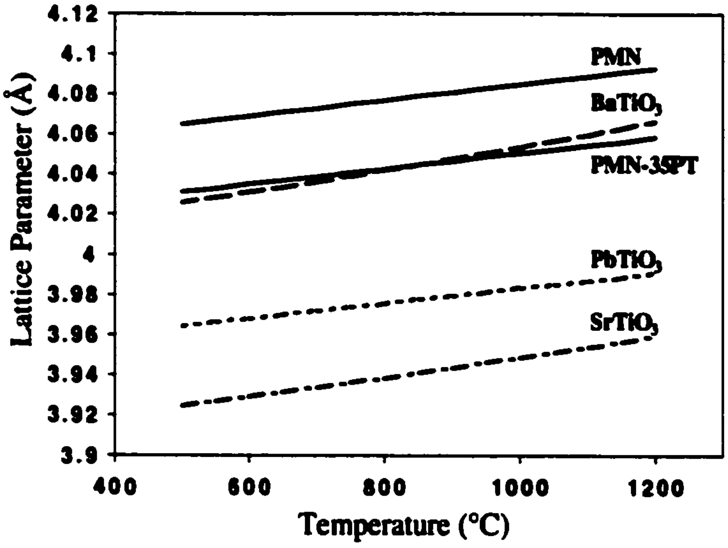

Figure 3.1(a): Lattice parameter of various perovskite ferroelectric materials between 500-1200°C.(22,23)

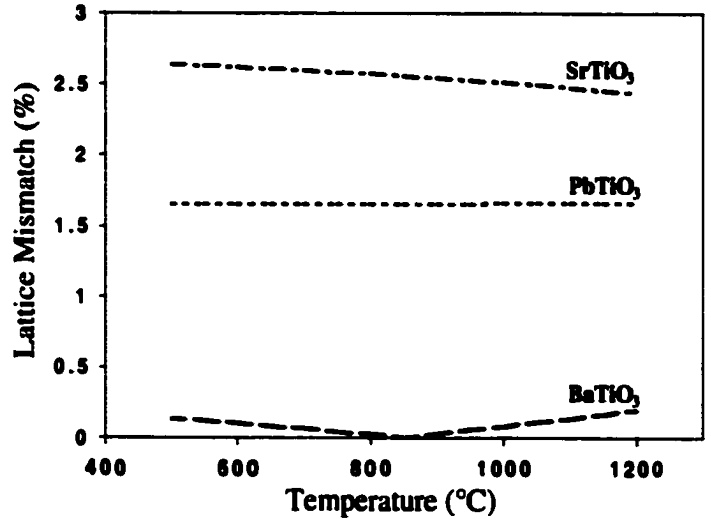

Figure 3.1(b): % lattice mismatch between various perovskite ferroelectric materials and PMN-35PT.(22,23)

ion-exchange reaction within the molten salt and hydrothermal processes, partially crystallized (001)-fiber $BaTiO_3$ has been formed by reacting potassium titanate fibers with a Ba source (i.e. $BaCO_3$ or $Ba(OH)_2$).(29,30) Tabular $SrTiO_3$ has been synthesized by a hydrothermal reaction. Takeuchi *et al.*(31) first demonstrated that epitaxial layers of $SrTiO_3$ could be grown on the surface of $Sr_3Ti_2O_7$ tabular particles. Watari *et al.*(32) utilized this knowledge to react $Sr_3Ti_2O_7$ and excess TiO_2 in molten KCl-NaCl to form tabular stoichiometric {001}-$SrTiO_3$ particles which are 10-20 μm in diameter and ~5 in thickness.

As confirmed by both Takeuchi *et al.* and Watari *et al.*, the $SrTiO_3$ cubic perovskite phase nucleated and grew from a layered-perovskite structure ($Sr_3Ti_2O_7$) at high temperatures (> 800°C). $Sr_3Ti_2O_7$ has a Ruddlesden-Popper-type structure where the *c*-plane is composed of perovskite blocks separated along the *c*-axis by SrO layers.(31,32) The (001)-face has a lattice parameter of $a = 3.9$ Å which is similar to the lattice parameter of most perovskite materials (~ 4 Å). Takeuchi *et al.*(33) also showed that epitaxial single crystal layers of {001}-$PbTiO_3$ could grow on {001}-$Bi_4Ti_3O_{12}$ platelets, another layered perovskite type phase. $Bi_4Ti_3O_{12}$ possesses the Aurivillius structure which consists of three perovskite-like units ($BiTiO_x$) separated by two $(Bi_2O_2)^{2+}$ layers along the *c*-axis.(34) Ramesh *et al.*(35,36) and Ghonge *et al.*(37) used a thin film of $Bi_4Ti_3O_{12}$ to template the epitaxial growth of various heterostructures of PZT in the [001] by pulsed laser deposition. These reports reinforce the idea that compositions which possess layered perovskite structures can be utilized to template cubic perovskite materials, especially Pb-based ferroelectric perovskite compositions like PMN-PT. This would be very beneficial for the TGG of PMN-PT, since anisotropic, (001)-faceted particles of layered perovskite materials are relatively easy to form by molten salt and hydrothermal processes.

Chen *et al.*(38,39) was the first to investigate the reaction between ceramic PZT and $Bi_4Ti_3O_{12}$ powders which were randomly mixed. It was reported that the reaction formed a mixture of isotropic and elongated grains, and the XRD pattern indicated that the final composition of the ceramic was a mixture of PZT and a secondary $Bi_4Ti_3O_{12}$ phase. This work suggested that $Bi_4Ti_3O_{12}$ was stable within the PZT and Pb-rich environment, but it did not directly indicate templated growth of PZT from the $Bi_4Ti_3O_{12}$ particles.

The objective of this work was to identify possible template candidates for texturing PMN-PT ceramics by TGG in the <001> by comparing various cubic perovskite and layered-perovskite materials using the criteria previously stated. This work primarily focused on the use of non-lead based compositions in which the texturing is dependent on heteroepitaxial nucleation and growth. This heteroepitaxial TGG process is different from the usual systems, which are textured by a homoepitaxial TGG process, since the stability of the template within the matrix becomes of great importance to the whole process.

3.2 EXPERIMENTAL PROCEDURES

Eight compositionally different template particle systems were synthesized to investigate their applicability to the TGG of PMN-PT. $Bi_4Ti_3O_{12}$, $Sr_3Ti_2O_7$, $KSr_2Nb_5O_{15}$, and $Sr_2Nb_2O_7$ compositions are not perovskites, and were all made by molten salt processes. The crystal structures of $Bi_4Ti_3O_{12}$ and $Sr_3Ti_2O_7$ were given above. $Sr_2Nb_2O_7$ possesses the high temperature prototype $Sr_2Ta_2O_7$ structure, which belongs to the orthorhombic space group Cmcm.(40) The $Sr_2Nb_2O_7$ crystal structure can be envisioned as a layered perovskite structure, where the unit cell is composed of stacked perovskite-type layers along the *c*-axis containing corner-shared NbO_6 octahedra and twelve-coordinated Sr cations. $KSr_2Nb_5O_{15}$ has a tetragonal tungsten bronze structure (space group P4bm) which is similarly characterized by layers of corner sharing 6-fold coordinated cation sites (perovskite-like units) which are stacked along the *c*-axis.(41) $BaTiO_3$, $SrTiO_3$, and $PbTiO_3$ all have the cubic perovskite structure at elevated temperatures. $BaTiO_3$ and $SrTiO_3$ were both synthesized by a molten salt process, and the $PbTiO_3$ templates were made by a hydrothermal process. The following subsections will describe the procedures used to synthesize the desired template particles. The stability and epitaxial growth of single crystal PMN-PT layers were observed by x-ray diffraction (XRD) and scanning electron microscopy (SEM).

3.2.1 Synthesis of $Bi_4Ti_3O_{12}$ Templates

39.75 wt% Bi_2O_3 (99.99%, Alfa-Aesar, Ward Hill, MA), 10.25wt% fumed TiO_2 (Degussa-Hüls, Frankfurt, Germany), 22wt% NaCl (99.0%, Alfa Aesar, Ward Hill, MA), and 28 wt% KCl (>99.0%, Alfa Aesar) were ball milled in 60 ml high density polyethylene (HDPE) bottle by 3 mm ZrO_2 media for 10 hours in isopropanol. The slurry was dried in air and loaded into a 100 ml alumina crucible. The powder mixture was heated at 1000°C for 6 h. After the isothermal hold, the crucible was cooled at 10°C/min to room temperature. The $Bi_4Ti_3O_{12}$ powder was removed from the cake by washing in hot de-ionized water. The resultant powder was phase pure $Bi_4Ti_3O_{12}$ by XRD. Figure

3.2(a) shows the platelet morphology of the template particles with an average diameter between 5-20 μm and a thickness of ~0.5 μm.

3.2.2 Synthesis of $KSr_2Nb_5O_{15}$ Templates

$KSr_2Nb_5O_{15}$ template particles were synthesized by the method described by Duran *et al.*(42) $SrNb_2O_6$ was first prepared by ball-milling $SrCO_3$ (99%, Alfa Aesar) and Nb_2O_5 (H.C. Starck, Newton, MA) for 24 h in ethanol using 3 mm ZrO_2 media in a HDPE bottle. The powder was dried and calcined at 1050°C for 5 h in an alumina crucible. The KSN templates were then formed by reacting KCl salt (>99.0%, Alfa Aesar) with the $SrNb_2O_6$ at a weight ratio of 1:1. The powder mixture was sealed in an alumina crucible and fired at a heating rate of 5°C/min to 1100°C and held for 6 h. The crucible was then cooled to room temperature at 2°C/min. The salt was removed from the powder through multiple washings in de-ionized water. These procedures produced phase pure $KSr_2Nb_5O_{15}$ acicular template particles (Fig. 3.2(b)) with an average length of 5-20 μm and diameters of ~1 μm.

3.2.3 Synthesis of $Sr_2Nb_2O_7$ Templates

The process to form $Sr_2Nb_2O_7$ templates was based on the results of the Ph.D. thesis of B. Brahmaroutu.(43,44) $SrNb_2O_6$ particles were first formed by mixing Nb_2O_5 (H.C. Starck) and $SrCl_2$ (99%, Aldrich Chemical Company, Inc., Milwaukee, WI) at a 1:1 molar ratio in isopropanol. The mixture was ball-milled using 3 mm ZrO_2 media in an HDPE bottle. The mixture was dried and heated in a sealed alumina crucible at 900°C

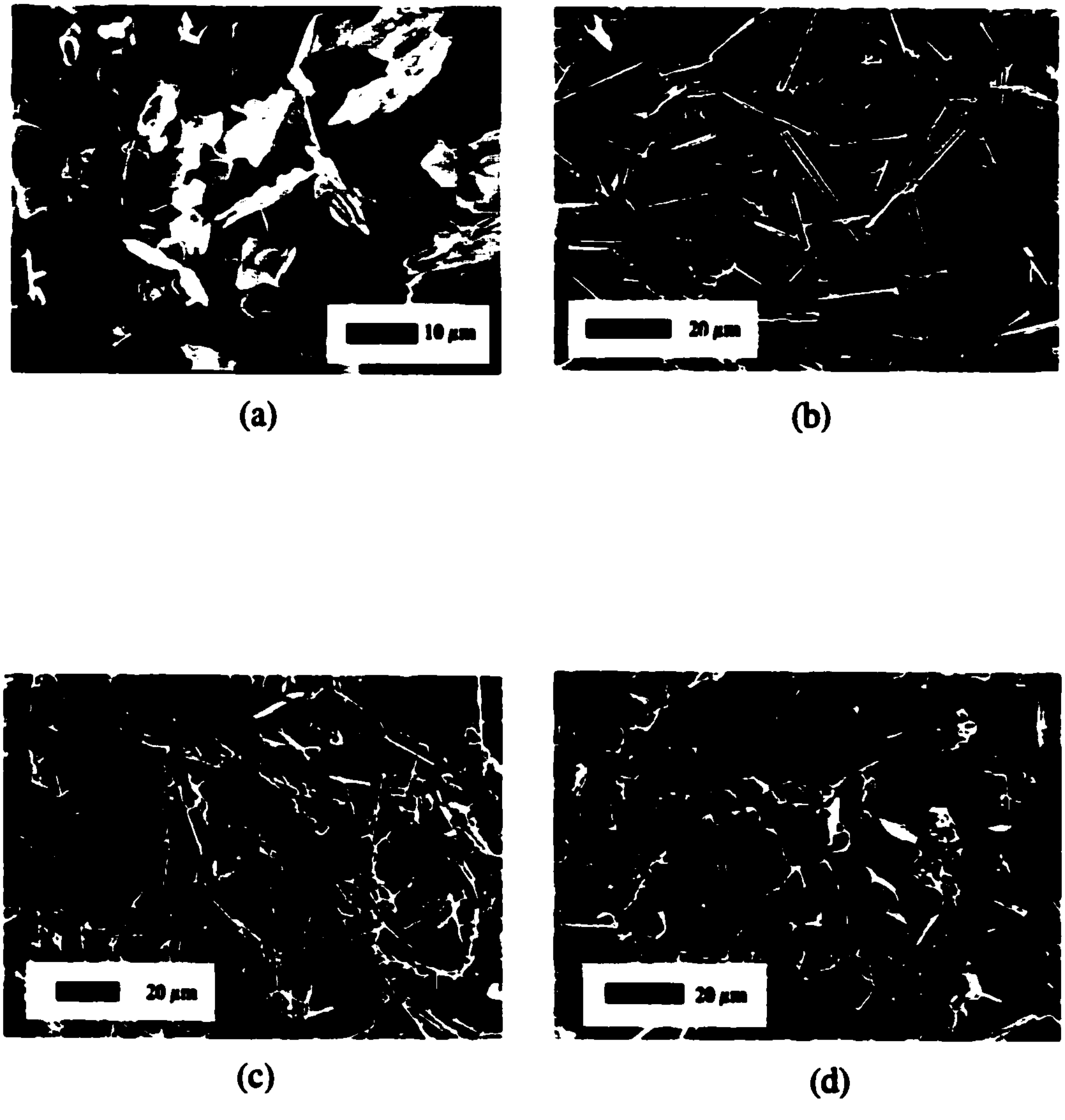

(a) (b)

(c) (d)

Figure 3.2: SEM micrographs of (a) $Bi_4Ti_3O_{12}$, (b) $KSr_2Nb_5O_{15}$, (c) $Sr_2Nb_2O_7$, and (d) $Sr_3Ti_2O_7$ template particles after molten salt synthesis.

for 4 h and then cooled at 3°C/min to room temperature. The excess salt was removed from the powder by multiple washings in de-ionized water. The $SrNb_2O_6$ particles were then mixed with $SrCO_3$ (99%, Alfa Aesar) at a 1:1 molar ratio by the same mixing procedures described above for the synthesis of $SrNb_2O_6$. The mixture was dried and hand mixed with 67wt% KCl (>99.0%, Alfa Aesar). This mixture was then reacted in an alumina crucible at 1100°C for 4 h to form the $Sr_2Nb_2O_7$ particles. The final product was washed multiple times in de-ionized water to eliminate any residual salts. The final $Sr_2Nb_2O_7$ particles displayed a blade-like morphology with average lengths of approximately 5-15 µm (Fig. 3.2(c)).

3.2.4 Synthesis of $Sr_3Ti_2O_7$ and $SrTiO_3$ Templates

The $Sr_3Ti_2O_7$ and $SrTiO_3$ template particles were fabricated by the procedures described by Watari *et al.*(32) $SrCO_3$ (99%, Alfa Aesar) and fumed TiO_2 (Degussa-Hüls) were ball-milled in ethanol by 3 mm ZrO_2 media in an HDPE bottle. The $SrCO_3$ and TiO_2 were mixed at a 3.1:2.0 molar ratio for 10 h KCl (>99.0%, Alfa Aesar) was then added to the slurry, so that the total powder weight consisted of 50% KCl. The slurry was dried and the mixture was sealed in an alumina crucible and reacted at 1300°C for 6 h. The crucible was cooled to room temperature at a rate of 3°C/min. The contents were washed in hot de-ionized water. The resultant powder consisted of only the $Sr_3Ti_2O_7$ composition. These particles were distinctly rectangular platelets with an average length of 10-20 µm and an average thickness of approximately 5 µm (Fig. 3.2(d)).

The $Sr_3Ti_2O_7$ platelets were used as the precursor material for the formation of the platelet $SrTiO_3$ particles. $Sr_3Ti_2O_7$ platelets and fumed-TiO_2 (5.4:1 weight ratio) were mixed in isopropanol in a Pyrex™ beaker with a magnetic stir bar. KCl was added to the suspension after mixing for 24 h, so that the total weight of the powder consisted of 50% KCl. The powder was then allowed to mix for approximately 12 h before drying. The powder was sealed in alumina crucibles and heated at 1200°C for 4 h. The sample was cooled at approximately 10°C/min to room temperature. The powder was washed in hot de-ionized water to remove the KCl. While washing, the suspension was sonicated for 15 min. and then allowed to sit untouched for 4 min. The upper part of the suspension was decanted to remove the fine particles and the unreacted TiO_2. The resultant powder consisted primarily of rectangular platelet particles approximately 10-20 μm in length and >5 μm in thickness which indicates that the aspect ratio slightly decreased from the original $Sr_3Ti_2O_7$ dimensions (Fig 3.3(a)).

3.2.5 Synthesis of $BaTiO_3$ Templates

Both platelet and whisker morphologies of $BaTiO_3$ were investigated in this work. The platelet $BaTiO_3$ was formed by the Remeika method.(27,28) 32.5wt% $BaTiO_3$ (BT-8, Cabot Performance Materials, Boyertown, PA) powder was combined with 67.5wt% KF (Acros, Fisher Scientific, Pittsburgh, PA) in a Pt crucible and sealed with a Pt lid. The crucible was heated at 5°C/min. to 1100°C and isothermally held for 6 h. The crucible was then cooled at 0.35°C/min to 850°C and quenched in air to room temperature. The excess KF was removed by hot de-ionized water. Crystals displaying a thickness <100

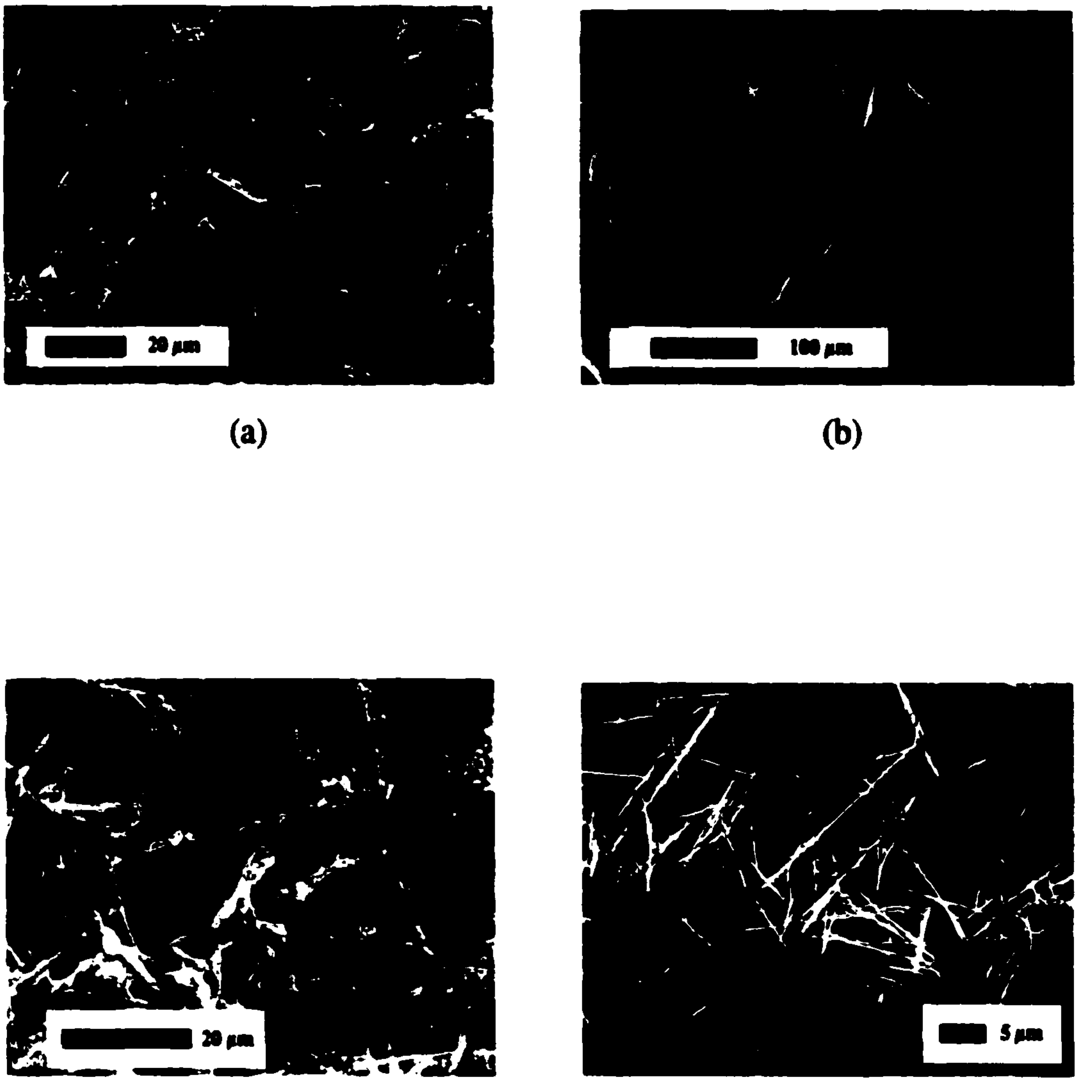

(a) (b)

(c) (d)

Figure 3.3: SEM micrographs of (a) $SrTiO_3$, (b) platelet $BaTiO_3$, (c) fiber $BaTiO_3$, and (d) $PbTiO_3$ template particles after molten salt or hydrothermal synthesis.

μm were selected. These crystals were crushed and then sieved to 75-150 μm (100-200 mesh) which produced templates with an aspect ratio ranging from 2-5 (Fig. 3.3(b)).

The $BaTiO_3$ whisker templates were obtained directly from Sekisui Plastics Co. Ltd., Tenri-city, Japan. The $BaTiO_3$ whiskers were produced by Sekisui Plastics Co. and reproduced in this work by the procedures reported by Ohara *et al.*(29) The initial step was to first form the hydrous potassium titanate ($2K_2O$-$11TiO_2$-$3H_2O$) phase by mixing K_2CO_3 and anatase TiO_2 at a K_2O:TiO_2 molar ratio of 1:3 in H_2O.(45,46) The paste was dried in an alumina crucible at 80°C and then fired in the alumina crucible to 1000°C for 48 h. The product is washed in hot de-ionized water. The resultant $2K_2O{\cdot}11TiO_2{\cdot}3H_2O$ was then mixed with a 1 M aqueous solution of $Ba(OH)_2$-$8H_2O$ at a weight ratio of 20:61.8 in a pressure autoclave (60 vol% fill). The reaction was completed at 500°C for 20 h. The $BaTiO_3$ product was washed again in hot de-ionized water. The $BaTiO_3$ whiskers formed by these procedures have a diameter <1 μm and a length ranging from 20-100 μm (Fig. 3.3(c)). The XRD of the $BaTiO_3$ whiskers show that there is no splitting of the peaks as would be seen for fully crystallized tetragonal $BaTiO_3$. Therefore, the $BaTiO_3$ whiskers may contain residual K^+ and OH^- ions and vacancies within the structure to produce the metastable cubic $BaTiO_3$ phase.

3.2.6 Synthesis of $PbTiO_3$ Templates

Fibrous $PbTiO_3$ was fabricated by the procedures described by Ohara *et al.*(21) and Cheng *et al.*(19,20) Before undertaking the hydrothermal reaction process, three precursor stock solutions were formed. An aqueous 0.5 M stock Pb-acetate ($Pb(CH_3COO)_2$)

(Aldrich Chemical Co.) solution was made in de-ionized water. A stock 0.5 M Ti-isopropoxide ($Ti(OPr^i)_4$) (Aldrich Chemical Co.) solution in ethanol was prepared and stored in an argon filled glove-box. KOH was then added to de-ionized water to form a 2 M stock KOH solution. 0.1 wt% polyvinyl alcohol (PVA) was added to the KOH stock solution.

The Ti-isopropoxide solution was added to the Pb-acetate solution in a 21 ml Teflon-lined Parr hydrothermal autoclave (Parr Instrument Company, Moline, IL) at a Pb/Ti ratio=1.4. The 2 M KOH solution was added to the Parr autoclave until the pH was 13.8. The addition of the KOH produced a thick yellowish-white gel in the Parr autoclave. The gel filled 50 vol% of the Teflon autoclave cell. The Parr autoclave was sealed and heated to 165°C for 5 h. The resultant powdered cake was filter-washed with de-ionized water. The pH of the wash water was altered to ~10 by NH_4OH to decrease Pb leaching from the $PbTiO_3$ particles during washing. The $PbTiO_3$ fibers are <1 μm in diameter and between 10-20 μm in length (Fig. 3.3(d)). Cheng *et al.* (19,20) reported that the resultant particles show a $(PbTiO_3)_n$ pattern. The $(PbTiO_3)_n$ phase was determined to have a tetragonal, body-centered structure (I4 symmetry). Cheng *et al.* and Suzuki *et al.*(47) reported that the acicular particles crystal structure changed to the tetragonal $PbTiO_3$ structure above 650°C without altering the morphology of the particles.

3.2.7 Stability of Templates within a PMN-35PT Matrix

As previously stated, the three primary requirements which dictate the utility of templates for the TGG process are: 1) the template must display a sufficient aspect ratio in order to mechanically orient by a shear force during green processing, 2) the template must provide the proper atomic structure and lattice parameter for heteroepitaxial nucleation of the desired phase and orientation, and 3) the template must be thermodynamically stable within its environment at the nucleation and/or growth temperatures. The templates described above were chosen since they fulfill the first requirement. The stability of the templates and their ability to act as nucleation sites for the growth of oriented PMN-PT were then investigated. The stability of the templates was investigated in a $0.65Pb(Mg_{1/3}Nb_{2/3})O_3$-$0.35PbTiO_3$ (PMN-35PT) matrix powder containing 0 and 1 wt% excess PbO. PMN-PT powder containing excess PbO has been shown to increase densification and grain growth, and decrease the formation of the pyrochlore phase due to PbO vaporization.

PMN-35PT was synthesized by the columbite method by milling $MgNb_2O_6$ (TRS Inc., State College, PA), $(PbCO_3)_2Pb(OH)_2$ (Aldrich Chemical Co.), and fumed TiO_2 (Degussa-Hüls) at the proper stoichiometry in de-ionized H_2O (pH=10.5). The composition was ball-milled for 12 h with high purity ZrO_2 media (3 mm diameter). The slurry was dried and the powder was reacted in an alumina crucible at 850°C for 6 h. The excess PbO was added by ball-milling the proper concentration of $(PbCO_3)_2Pb(OH)_2$ with fully calcined PMN-35PT in toluene for 10 h. The powder was dried at ~100°C and calcined at 550°C for 4 hours. The average particle size of the PMN-35PT powders after milling, measured by centrifugal sedimentation (Horiba CAPA-700), was approximately 0.8 μm.

The two PMN-35PT matrix compositions were mixed with 10 vol% of each template composition in isopropanol The slurries were mixed in Pyrex beakers by magnetic stir bars for 24 h, and then dried while stirring. 0.3 grams of each composition was uniaxially pressed in a 6 mm diameter die. The compact was uniaxially pressed at 7 MPa, and then cold isostatically pressed at 210 MPa. Each sample was encapsulated in an ~7 mm diameter, two piece Pt crucible. The Pt encapsulated samples were packed in a double crucible setup using PMN-35PT as the packing powder to control PbO volatilization.

Two separate heating profiles were used to sinter the samples in this experiment. The first heating profile (hereafter named *Profile 1*) consisted of a 10°C/min ramp to 800°C with a 5 h isothermal hold followed by a second ramp at 10°C/min to the sintering temperature of 1150°C with another 5 h hold. The intention of this heating profile was to investigate the possibility of a necessary nucleation step below the melting temperature of the Pb-based liquid phase in the system (~830-885°C).(48-50) The second profile (hereafter named *Profile 2*) consisted of heating the samples at 10°C/min directly to the sintering temperature of 1150°C where the samples were isothermally held for 5 h. The samples were weighed after thermal processing to monitor the degree of PbO volatilization. Samples which lost greater than 0.5 wt% were disregarded to obtain samples with a relatively constant PbO concentration over the processing conditions.

X-ray diffraction (XRD), scanning electron microscopy (SEM), and energy dispersive spectroscopy (EDS) were utilized to characterize the stability and the ability to nucleate and grow the PMN-PT composition from the templates.

3.3 RESULTS AND DISCUSSION

3.3.1 Template Compositions with a Non-Perovskite Crystal Structure

The XRD pattern of the sintered PMN-35PT ceramic samples containing $Bi_4Ti_3O_{12}$, $Sr_3Ti_2O_7$, $KSr_2Nb_5O_{15}$, and $Sr_2Nb_2O_7$ templates and no excess PbO is displayed in Fig. 3.4(a). These samples were first isothermally held at 800°C for 5 h before being heated to the sintering temperature of 1150°C. The purpose for *Profile 1* was to allow for a possible nucleation process to occur below the melting temperature of any Pb-rich liquid formation (<830°C).(48-50) This temperature also reflects the upper thermal conditions (~800°C) used by Ramesh *et al.*(35,36) to nucleate epitaxial heterostructure PZT films on $Bi_4Ti_3O_{12}$ thin films. The XRD pattern for *Profile 1* and *Profile 2* were found to produce the same diffraction patterns, therefore, only the results of *Profile 1* will be described.

The $Bi_4Ti_3O_{12}$ templated sample shows the diffraction pattern (Fig. 3.4(a)) of randomly oriented PMN (JCPDS Powder Diffraction File Card No. 27-1199) and the presence of a second phase with the highest intensity peaks at 2θ values of 29.3°, 58.0°, 48.86°, and 33.94° (order in descending relative intensity). The secondary set of diffraction peaks do not correspond to the diffraction pattern of $Bi_4Ti_3O_{12}$ (JCPDS Powder Diffraction File Card No. 35-0795). This indicates that the $Bi_4Ti_3O_{12}$ templates were not thermodynamically stable in pure PMN-35PT during the thermal processing. These additional diffraction peaks match well with the cubic-pyrochlore structure of $Pb_{1.83}Mg_{0.29}Nb_{1.71}O_{6.39}$ (JCPDS Powder Diffraction File Card No. 33-0769). This result indicates that the high temperature reaction of $Bi_4Ti_3O_{12}$ and PMN-PT powder gives rise

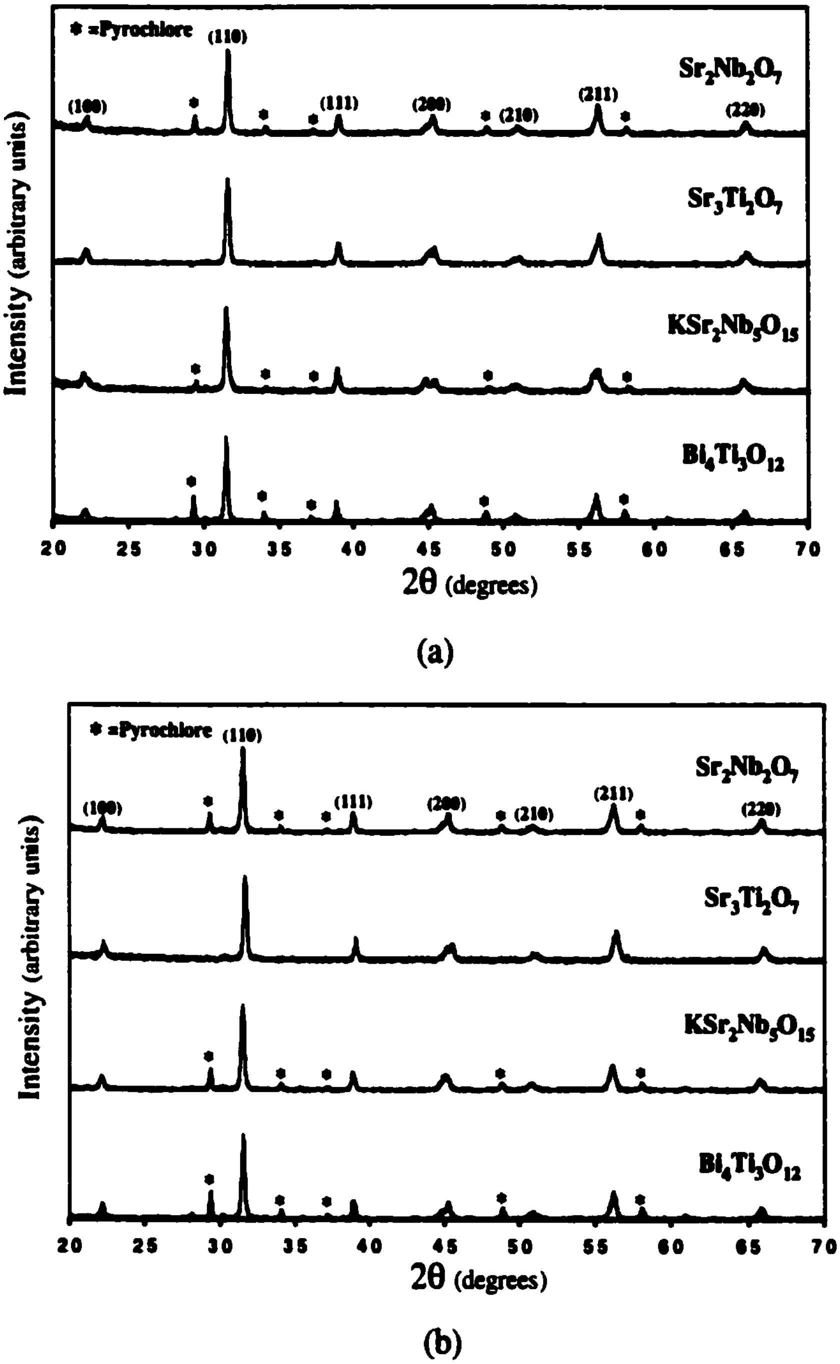

Figure 3.4: X-ray diffraction patterns of PMN-35PT ceramics containing 10 vol% $Sr_2Nb_2O_7$, $Sr_3Ti_2O_7$, $KSr_2Nb_5O_{15}$, and $Bi_4Ti_3O_{12}$ templates with (a) 0 wt% and (b) 1wt% excess PbO (sintered by heating *Profile 1*).

to the pyrochlore phase. Since Bi^{3+} ions and Pb^{2+} ions are of similar sizes and their oxides form a low temperature eutectic (602°C), it is understandable that there would be interdiffusion between the two phases. The $Bi_4Ti_3O_{12}$ composition closely resembles the composition of a cubic-pyrochlore, therefore, the reaction and interdiffusion between the two phases would probably result in the degradation of the perovskite and the formation of the pyrochlore structure. This result contradicts the observations reported by Chen *et al.*(38,39) Chen *et al.* indicated that a mixture of perovskite PZT and $Bi_4Ti_3O_{12}$ resulted in the formation of the $Bi_4Pb_4Ti_4O_{15}$ phase (JCPDS Powder Diffraction File Card No. 43-0972) and residual $Bi_4Ti_3O_{12}$ when sintered at temperatures between 1000-1200°C in air. The three highest intensity peaks observed by Chen *et al.* were located at 2θ values of ~28.75°, ~32.5°, and ~69.69° which differ from the three highest intensity peaks of $PbBi_4Ti_4O_{15}$ (30.22°, 23.2°, and 32.93°). Instead, the secondary phase should have a composition closer to the pyrochlore $Pb_2Ti_2O_6$ (JCPDS Powder Diffraction File Card No. 26-0142), with Bi^{3+} substituted in the A-site with accompanying vacancy formation. The results obtained by Chen *et al.* correlate better with the findings of this work stating that there is a high temperature (>800°C) reaction between $Bi_4Ti_3O_{12}$ and Pb-based perovskite ferroelectric materials (like PMN-PT and PZT) to form the pyrochlore phase. Additions of $Bi_4Ti_3O_{12}$ either destabilizes the PMN-PT perovskite by an ion-exchange process or acts as a seed for the phase formation of isolated pyrochlore throughout the material. In either case, this work shows that $Bi_4Ti_3O_{12}$ is an unacceptable template candidate for TGG at this sintering and growth condition.

The diffraction patterns for PMN-35PT containing both $Bi_4Ti_3O_{12}$ templates and 1wt% excess PbO sintered using *Profile 1* are displayed in Fig. 3.4(b). Again, *Profile 1* and *Profile 2* resulted in the same diffraction pattern. The diffraction pattern shows the same peaks and peak intensities as the diffraction pattern for the 0 wt% excess PbO composition. The presence of the excess PbO did not alter the reaction between the $Bi_4Ti_3O_{12}$ and PMN-35PT. The intentionally added excess PbO should form a Pb-rich liquid phase at temperatures between 830-886°C which would wet the grain boundaries.$^{(48-50)}$ The liquid would enhance the kinetics of sintering and grain growth by allowing for higher mobility of the species through the grain boundaries by a dissolution/precipitation process. The presence of the liquid phase, and thus, the enhanced ion mobility, did not alter the degree of pyrochlore formation. Therefore, it may be assumed that either the pyrochlore formation is not drastically dependent upon the dissolution of the $Bi_4Ti_3O_{12}$ templates or the reaction occurs rapidly without a need for enhanced kinetics or transport.

Figure 3.4(a) and Fig. 3.4(b) show similar results for the PMN-35PT samples containing $KSr_2Nb_5O_{15}$ and $Sr_2Nb_2O_7$ templates as for the samples containing the $Bi_4Ti_3O_{12}$ templates. The $KSr_2Nb_5O_{15}$ and $Sr_2Nb_2O_7$ templates both reacted in the PMN-35PT matrix composition containing 0 wt% excess PbO (Fig. 3.4(a)) or 1 wt% excess PbO (Fig. 3.4(b)). Like the $Bi_4Ti_3O_{12}$ containing samples, these samples formed the same pyrochlore phase represented in the diffraction patterns with peaks at 2θ values of approximately 29.3°, 58.0°, 48.9°, and 33.9° (ordered in descending relative intensity). The presence of the excess PbO did not affect the relative extent of the pyrochlore formation. Also, there was no effect of the heating profile (*Profile 1* versus *Profile 2*) on the reaction. Therefore, $Bi_4Ti_3O_{12}$, $KSr_2Nb_5O_{15}$, and $Sr_2Nb_2O_7$ templates all react similarly with PMN-35PT; they form the parasitic pyrochlore phase, making these compositions undesirable TGG templates in the given environment.

The additions of $Sr_3Ti_2O_7$ to PMN-35PT resulted in the formation of the perovskite phase without the formation of the pyrochlore phase as displayed by the diffraction patterns (Fig. 3.4(a,b)). This result was consistent for both sintering profiles and both the matrix compositions (0 wt% and 1wt% excess PbO). The SEM of the microstructure (Fig. 3.5(a)), for the sample sintered using ***Profile 1***, shows a uniform, high density microstructure. The grains can be characterized as possessing a non-faceted morphology with an average grain size of ~10 µm. The absence of a bimodal population of grain sizes indicates that the $Sr_3Ti_2O_7$ did not succeed in templating the PMN-35PT composition. The uniform microstructure verifies normal grain growth of the PMN-35PT composition regardless of the presence of 10 vol% of $Sr_3Ti_2O_7$ particles. Figure 3.5(b) shows the presence of small inclusions within some of the grains. EDS indicates that these inclusions contain a higher concentration of Sr. Thus, the $Sr_3Ti_2O_7$ particles are not stable at high temperatures, since the Pb-rich environment at these temperatures induces the dissolution and incorporation of the templates into the matrix material. This instability suggests that the use of the $Sr_3Ti_2O_7$ particles as templates is not plausible at these TGG conditions.

3.3.2 Template Compositions with a Perovskite Crystal Structure

The XRD patterns of the sintered samples containing 10 vol% $PbTiO_3$, $BaTiO_3$, or $SrTiO_3$ and a matrix PMN-35PT composition containing 0 wt% or 1 wt% excess PbO

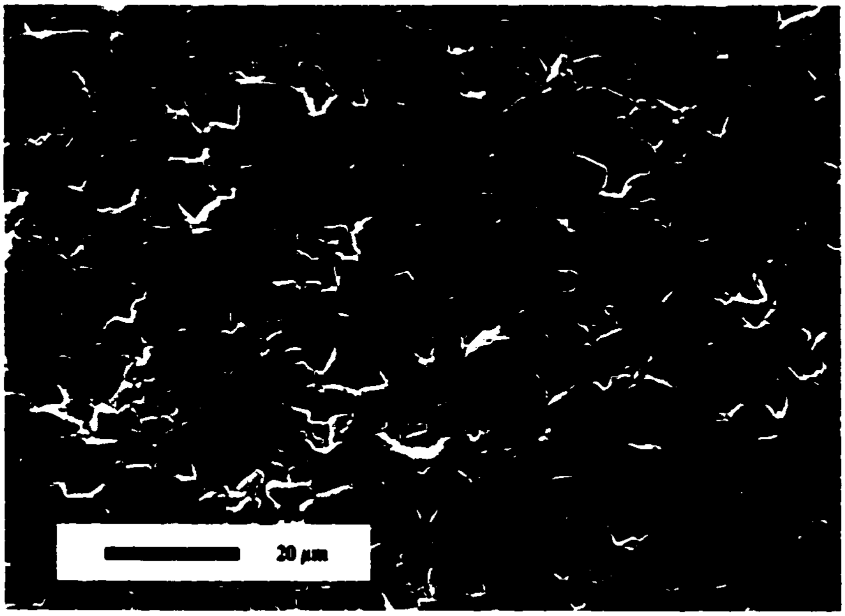

Figure 3.5(a): SEM micrograph of a PMN-35PT ceramic containing 10 vol% $Sr_3Ti_2O_7$ templates with 1 wt% excess PbO (sintered by heating *Profile 1*).

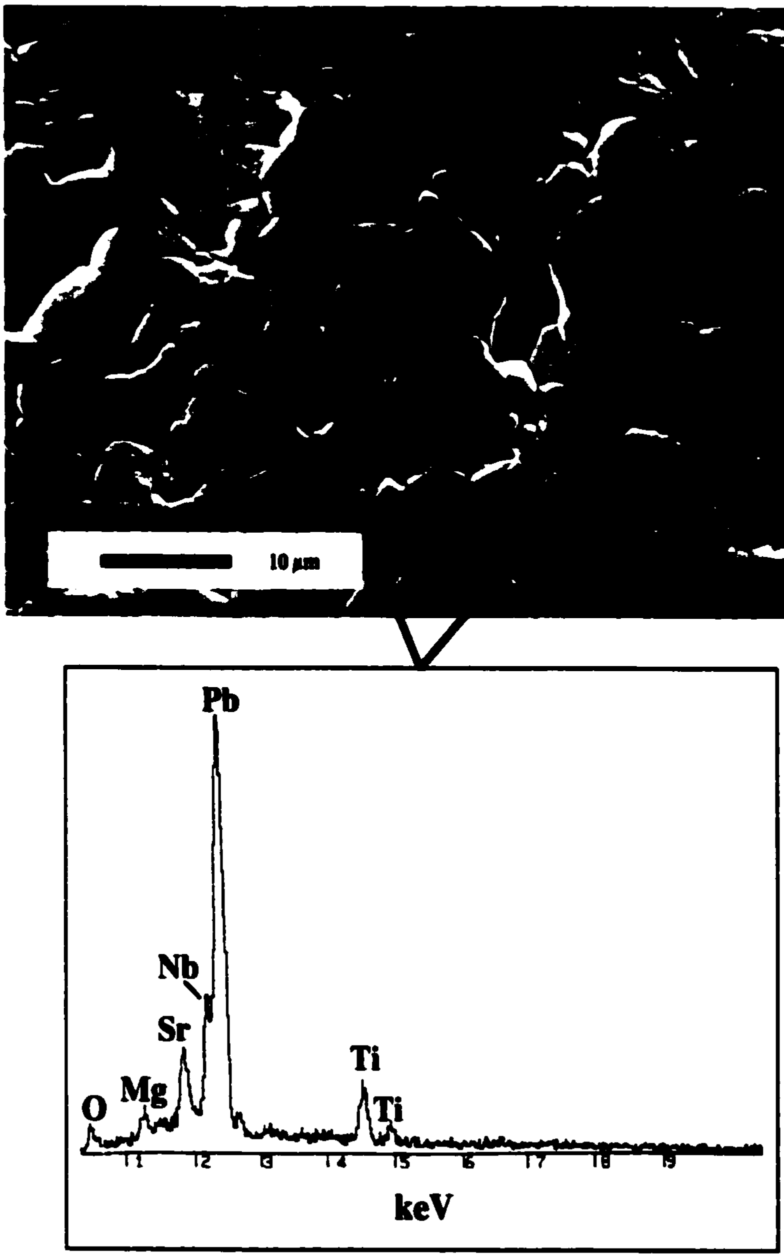

Figure 3.5(b): SEM micrograph with EDS pattern of a PMN-35PT ceramic containing 10 vol% $Sr_3Ti_2O_7$ templates with 1 wt% excess PbO (sintered by heating *Profile 1*).

are displayed in Fig. 3.6(a) and Fig. 3.6(b), respectively. Samples in Figs. 3.6(a) and 3.6(b) were sintered using heating *Profile 1*, but again, *Profile 1* and *Profile 2* resulted in the same diffraction patterns. Therefore in all cases, a low temperature holding step did not seem to alter the final phase assemblage.

The additions of the various perovskite compositions to the PMN-35PT matrix did not initiate the formation of a pyrochlore phase during the high temperature processing. As shown by Fig. 3.6(a) and 3.6(b), additions of the $PbTiO_3$ and $BaTiO_3$ whisker particles caused significant splitting of all of the diffraction peaks except for the (110) and (111). The powder diffraction pattern of PMN-35PT used in this work shows singular broad peaks at all peak positions since the composition lies at the MPB (Fig. 3.7). At the MPB, both the rhombohedral and tetragonal forms of the perovskite phase are at equilibrium, and this state is displayed by broad peaks indicating various lattice distortions throughout the material. The distinct splitting of the peaks (especially noticeable for the {002} position) may indicate that the PMN-35PT composition was pushed into the tetragonal phase state. The preferential formation of the tetragonal PMN-PT phase implies that there was a compositional change initiated by the dissolution of the tetragonal perovskite $PbTiO_3$ and $BaTiO_3$ into the matrix PMN-35PT. The splitting may also indicate that a $(Ba,Pb)TiO_3$ solid solution formed, especially when excess PbO was added to the matrix composition. Figure 3.8 displays the microstructure of the sintered PMN-35PT ceramic containing 10 vol% $PbTiO_3$ template particles. The microstructure is uniform and dense and consists of equiaxed grains with an average grain size of ~17 μm. There is no physical evidence of remnant $PbTiO_3$ templates. The microstructure of the PMN-35PT samples containing the $BaTiO_3$ whisker particles (Fig. 3.9) distinctly shows

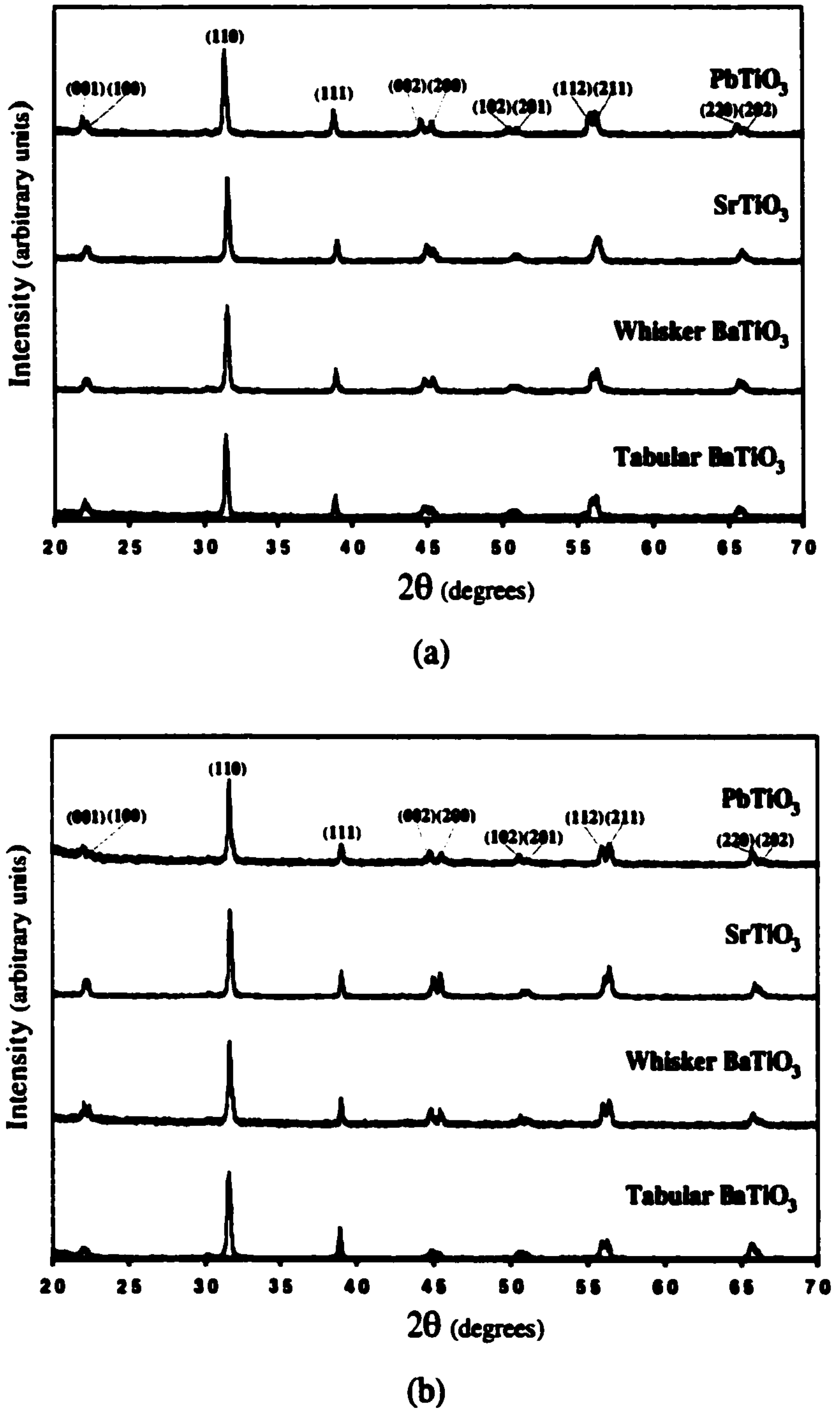

Figure 3.6: X-ray diffraction patterns of PMN-35PT ceramics containing 10 vol% $PbTiO_3$, $SrTiO_3$, and $BaTiO_3$ templates with (a) 0 wt% and (b) 1wt% excess PbO (sintered by heating *Profile 1*).

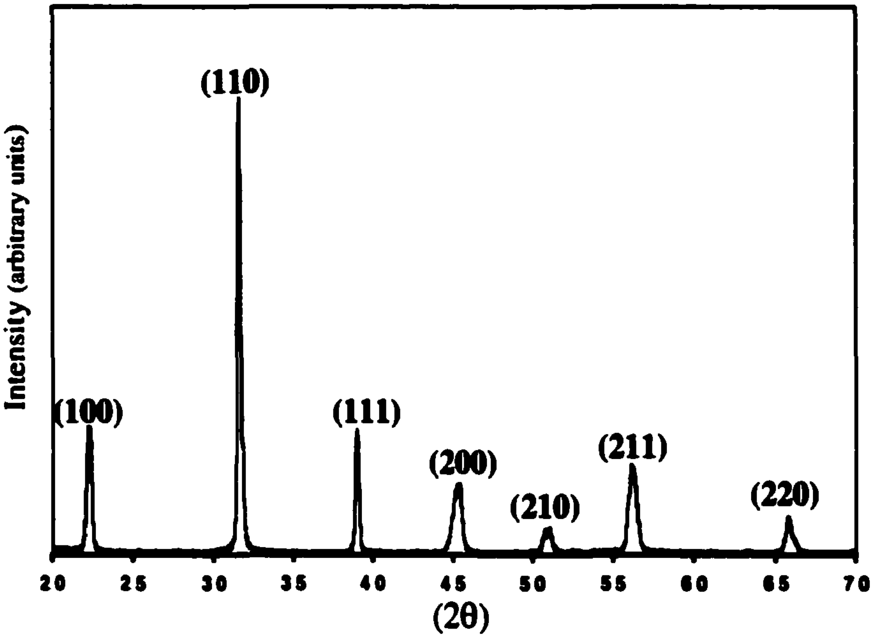

Figure 3.7: X-ray diffraction pattern of a PMN-35PT ceramic containing 0 wt% excess PbO (sintered by heating *Profile 1*).

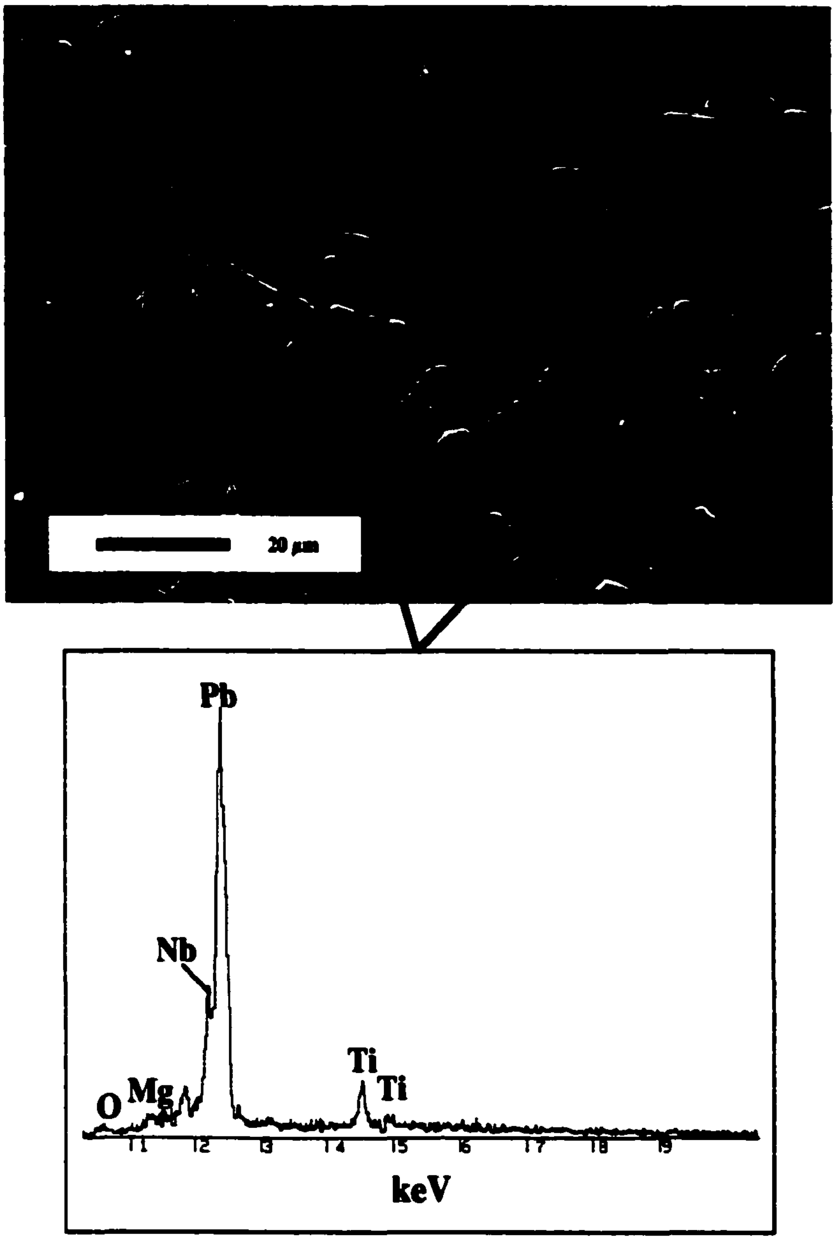

Figure 3.8: SEM micrograph with EDS pattern of a PMN-35PT ceramic containing 10 vol% $PbTiO_3$ whisker templates with 1 wt% excess PbO (sintered by heating *Profile 1*).

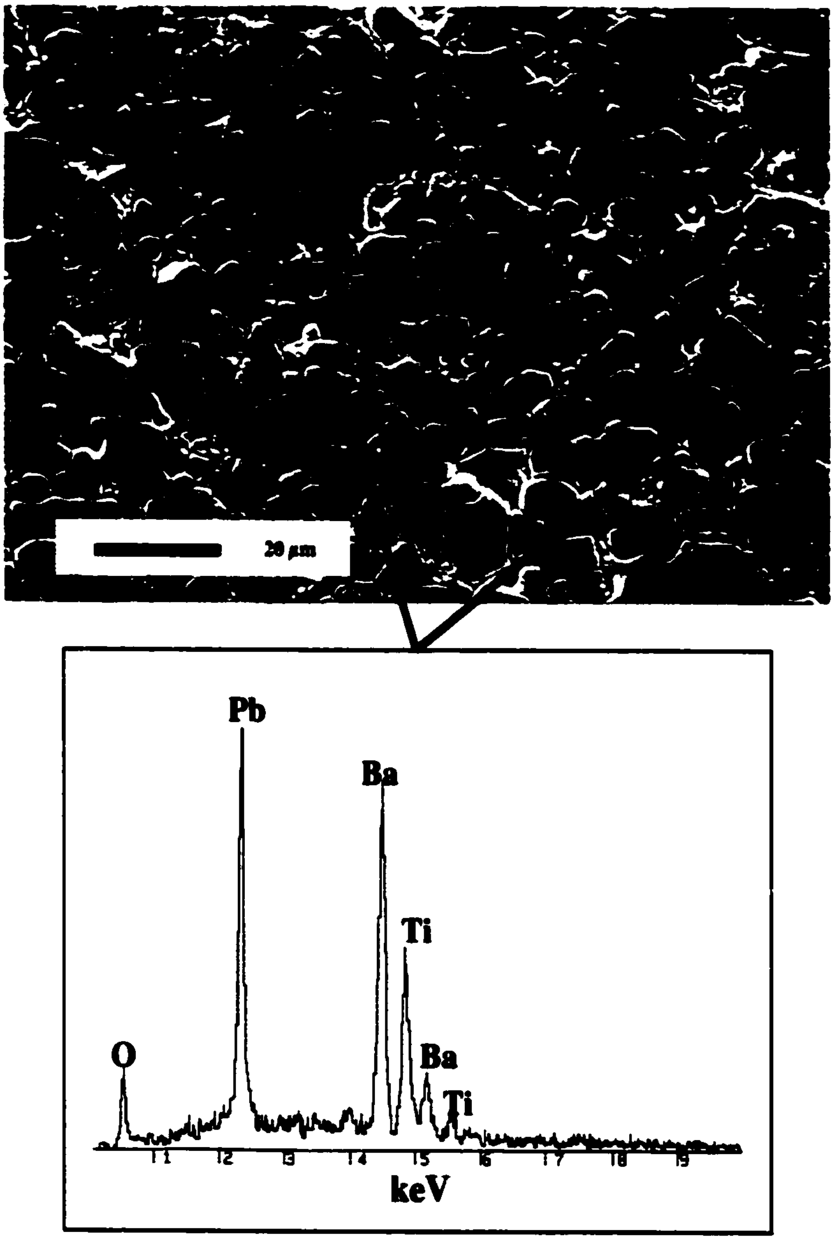

Figure 3.9: SEM micrograph with EDS pattern of a PMN-35PT ceramic containing 10 vol% $BaTiO_3$ whisker templates with 1 wt% excess PbO (sintered by heating *Profile 1*).

the location of grains containing a high concentration Ba incorporation by the contrast difference between the grains. EDS indicates that the dark grains contain a high Ba concentration where as the light grains possess an EDS pattern like that of pure PMN-PT. Again, the microstructure is quite uniform and dense, but the average grain size (~8 μm) is almost half that of the $PbTiO_3$ additions.

The question of the stability of the $PbTiO_3$ and $BaTiO_3$ whiskers can be related back to the degree of crystallinity of these particles after hydrothermal synthesis. The diffraction pattern of the $PbTiO_3$ and $BaTiO_3$ whiskers after synthesis is shown in Figs. 3.10(a) and Fig. 3.10(b), respectively. The $PbTiO_3$ whiskers did not show the macedonite-$PbTiO_3$ phase pattern (JCPDS Powder Diffraction File Card No. 6-0452), instead it showed the diffraction pattern of a metastable phase, which Cheng *et al.*(19,20) described as a body-centered tetragonal (I4); the details of the structure are still is uncertain. The $PbTiO_3$ whiskers were shown to transform to the tetragonal perovskite phase (Fig. 3.10(a)) after firing in air above ~600°C, as stated by Cheng et al. The stability of the perovskite phase, as indicated by the increased magnitude of the peak intensities, became greater with an increase in temperature from 650°C to 1000°C for 1 h isothermal holds. There was a slight development of a secondary pyrochlore phase, but this was probably due to the higher vapor pressure of PbO at these higher temperatures. In this experiment, there was no attempt to suppress PbO evaporation by regulating the PbO vapor pressure. Even though the phase stability of the perovskite structure was preserved at the elevated temperatures, the morphological structure of the template particle was altered, transforming from the desired whisker shape to an isotropic shape (Fig. 3.11). The degradation of the particle morphology is probably a result of the phase

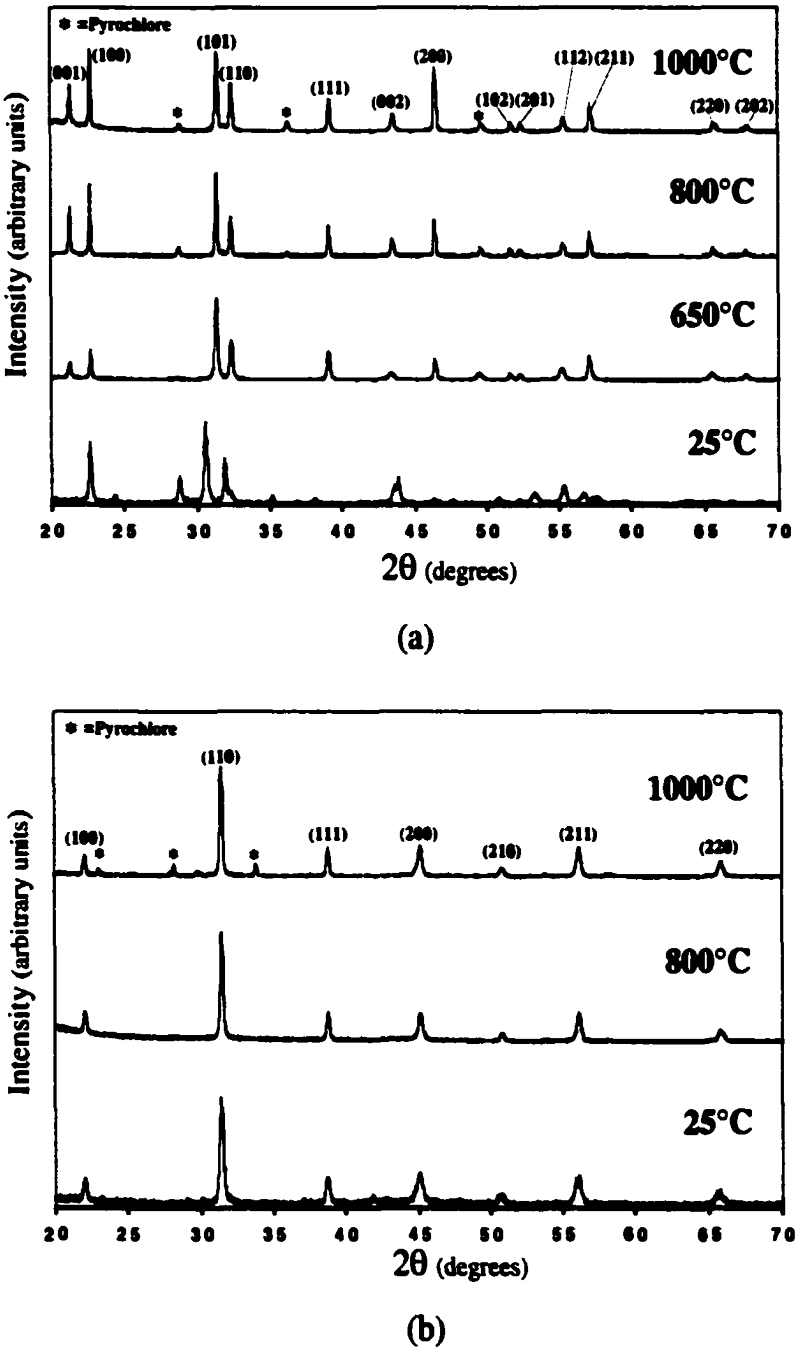

Figure 3.10: X-ray diffraction patterns of whisker (a) $PbTiO_3$ and (b) $BaTiO_3$ particles after 1 h heat treatments in air.

transformation which causes the collapse of the original structure due to the multiple vacancies attributed to Ti deficiency (Cheng *et al.*).(20) The collapse of the structure would cause the formation of multiple grains separated by low angle grain boundaries across the particles. The instability of the particle morphology and phase development of the perovskite structure indicates that these $PbTiO_3$ are unsuitable as templates for TGG of PMN-35PT.

The diffraction pattern of the $BaTiO_3$ whiskers (Fig.3.10(b)) after synthesis shows there is no tetragonal splitting of the diffraction peaks as expected at room temperature (JCPDS Powder Diffraction File Card No. 5-0626). The breadth of the diffraction peaks decreased slightly after annealing at either 800°C or 1000°C for 1 h. After annealing at 1000°C for 1 h, a secondary pyrochlore phase also developed in the $BaTiO_3$ acicular powder. Unlike the $PbTiO_3$ whiskers, the morphology of the $BaTiO_3$ whiskers is preserved throughout the various high temperature treatments (Fig. 3.12). Although the morphology of the whiskers remains, the metastable state of the $BaTiO_3$ implies that the particles include multiple defects and vacancies which might prompt preferential dissolution of the particles into the PMN-35PT matrix and/or residual Pb-rich liquid phase.

The PMN-35PT ceramics which contained $SrTiO_3$ templates also show peak splitting, but not as extensive as the PMN-35PT ceramics which contained the $PbTiO_3$ and $BaTiO_3$ whiskers (Figs. 3.6(a,b)). The secondary diffraction peaks could not be due to residual $SrTiO_3$ which remained in the final ceramic, since the location of all $SrTiO_3$ diffraction peaks (JCPDS Powder Diffraction File Card No. 35-0734) lie at least 1° (2θ) higher than the PMN-35PT diffraction peaks. One would assume that the additions of

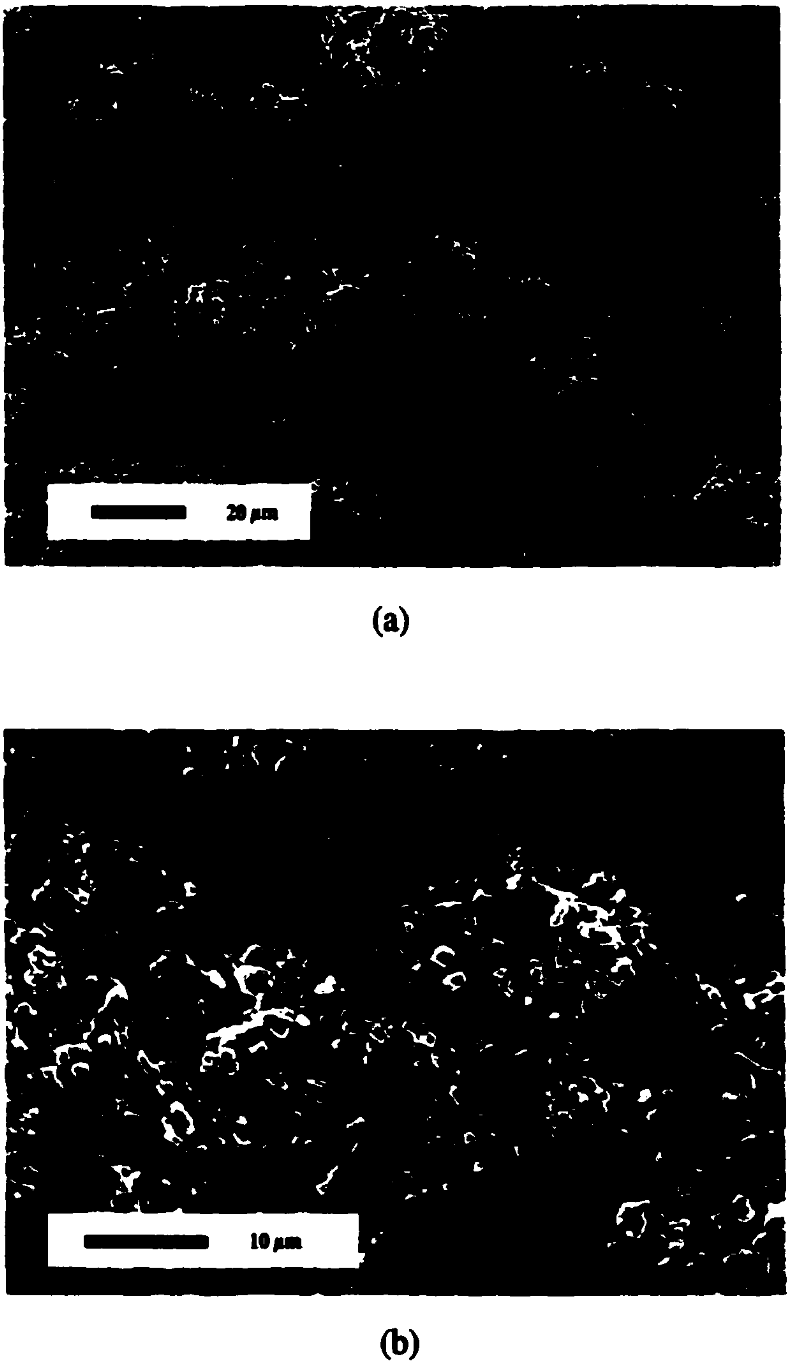

Figure 3.11: SEM micrograph of whisker $PbTiO_3$ templates which were heat treated at 800°C for 1 h (magnification at (a) 750x and (b) 2000x)

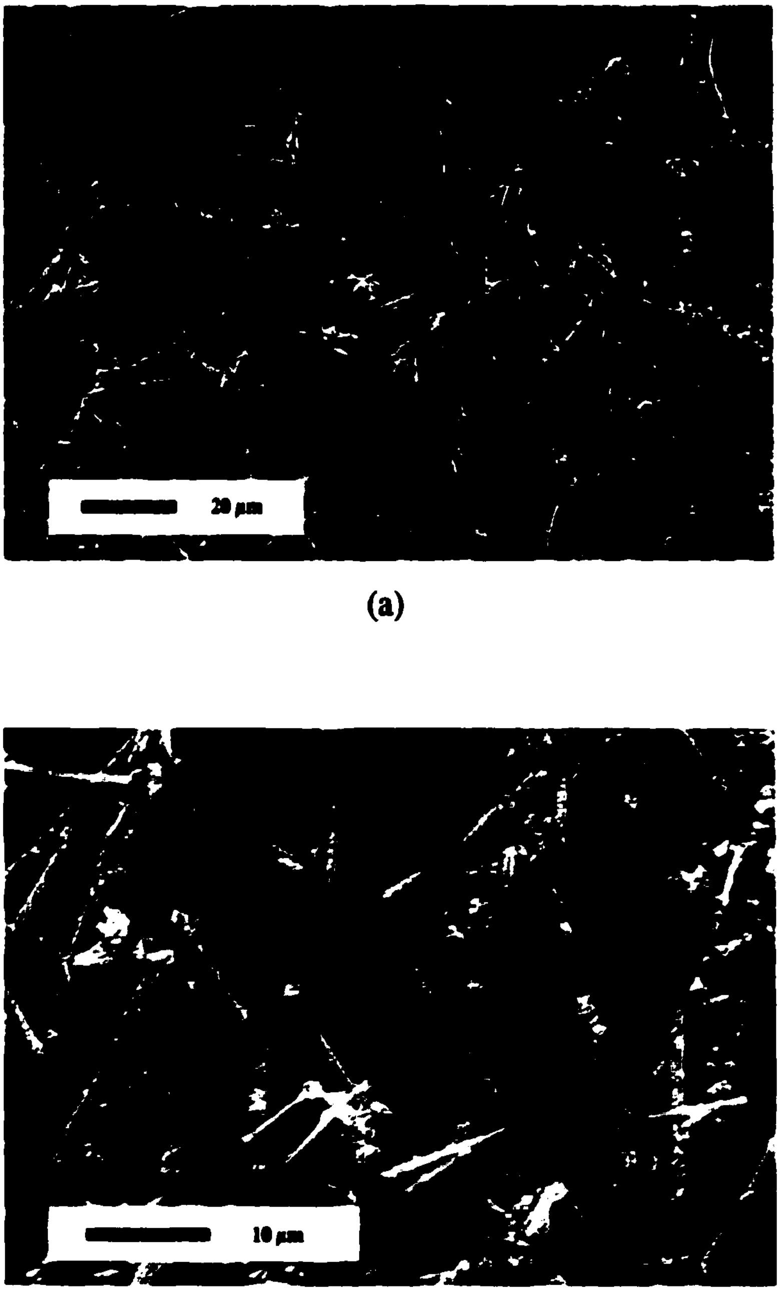

(a)

(b)

Figure 3.12: SEM micrograph of whisker $BaTiO_3$ templates which were heat treated at 800°C for 1 h (magnification at (a) 750× and (b) 2000×)

$SrTiO_3$, when completely dissolved into the PMN-PT structure, would cause PMN-35PT to slightly favor the rhombohedral phase. Isupov(51) proposed that Pb-based relaxor ferroelectrics which possess the perovskite structure have a rhombohedral structure when their Goldschmidt(52) perovskite tolerance factor (TF) is ≤ 0.97, and otherwise, the materials will favor a tetragonal distortion of the perovskite structure (TF ≥ 0.98). However PMN, which displays a rhombohedral distortion, has a TF=0.989. In Isupov's calculations, he used the ionic radii provided by Shannon and Prewitt, but the tolerance factors were calculated with different coordination numbers (CN) than those required for the ions in the perovskite structure ($CN_{A\text{-site}}=12$, $CN_{B\text{-site}}=6$, and $CN_{O\text{-site}}=6$). Using the correct coordination numbers, the rhombohedral perovskite distortion would be stable at an approximate $TF \leq 1.0$ and the tetragonal distortion would be stable at $TF > 1.0$.(53) Since $TF \approx 1.0$ for PMN-35PT, dissolving $SrTiO_3$ ($TF \approx 1.0$) into PMN-35PT would further stabilize the PMN-35PT structure. The problem with this assumption is that $SrTiO_3$ lowers the T_c(54), which may force the solid solution to reside in the tetragonal phase field at room temperature. Therefore, the origin of the tetragonal-like peak splitting is still not evident. Figure 3.13(a) shows the microstructure of the $SrTiO_3$ containing PMN-35PT ceramics. The microstructure shows a diversity of grain sizes and morphologies with clusters of grains <10 µm surrounded by grains >20 µm in size. Figure 3.13(b) is a higher magnification SEM micrograph of one of the larger grains. The EDS of the region of the grain which shows the different etching characteristics, has a high content of Sr. The Sr-rich areas of the larger grains do not present a clear distinction of the fate of the $SrTiO_3$ template. It is unclear if the PMN-35PT matrix is templating from the surface of

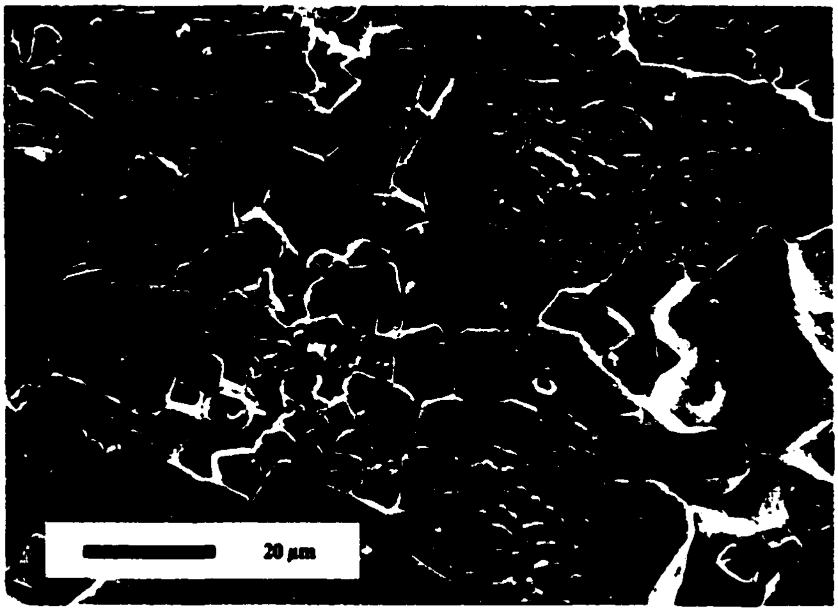

Figure 3.13(a): SEM micrograph of a PMN-35PT ceramic containing 10 vol% $SrTiO_3$ templates with 1 wt% excess PbO (sintered by heating *Profile 1*).

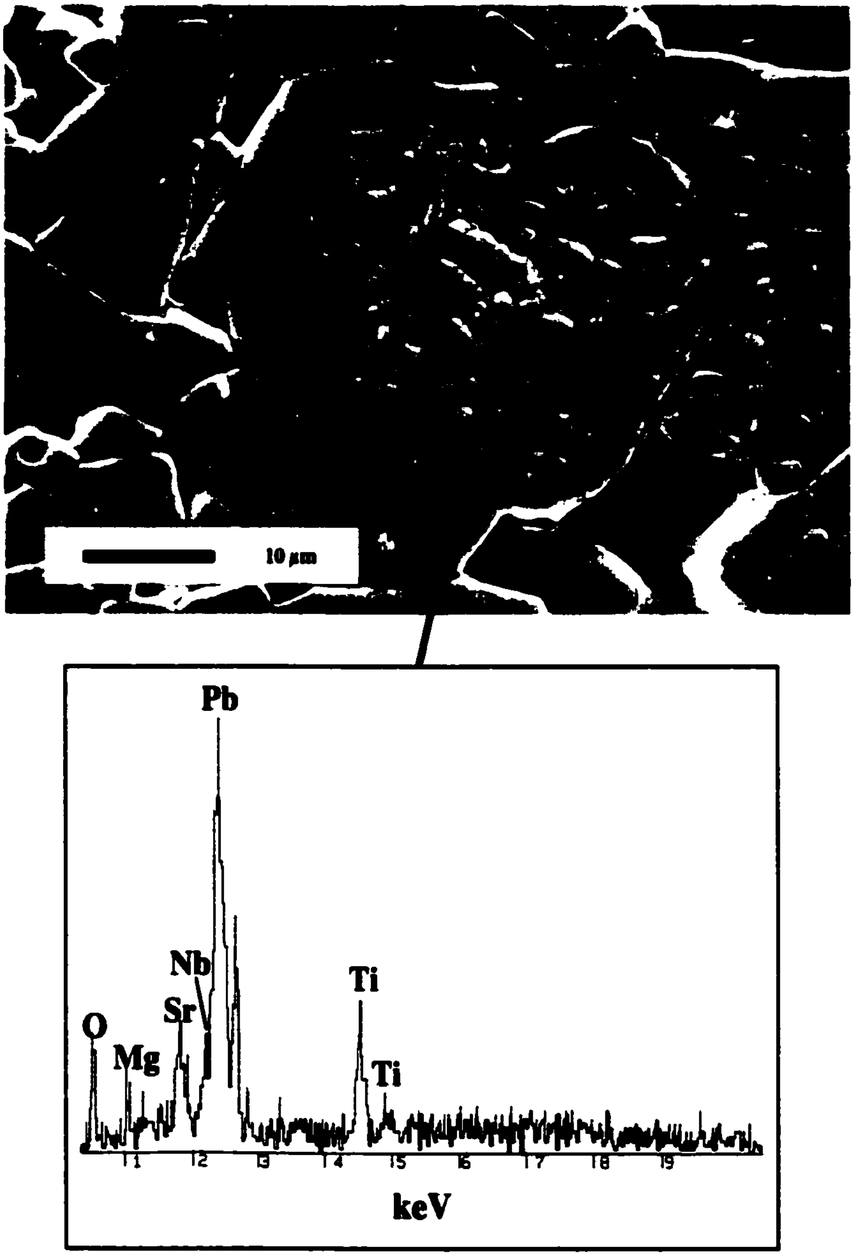

Figure 3.13(b):SEM micrograph with EDS pattern of a PMN-35PT ceramic containing 10 vol% $SrTiO_3$ templates with 1 wt% excess PbO (sintered by heating *Profile 1*).

the $SrTiO_3$ particles or if the Pb-rich environment is dissolving the particles and redistributing the Sr and Ti ions throughout the matrix. If the PMN-35PT is templating from the $SrTiO_3$ templates, then the secondary diffraction peaks may be the result of a population of grains with a mixed PMN-PT-ST composition.

The diffraction pattern of the PMN-35PT ceramic with the additions of platelet $BaTiO_3$ particles shows two distinct diffraction patterns (Figs. 3.6(a,b)). The first is the diffraction pattern of PMN-35PT and the second is of $BaTiO_3$. This indicates the two materials did not undergo complete solid solution during the thermal treatment. The SEM micrograph (Fig. 3.14) supports this result by showing the presence of the two distinct phases. The micrograph displays the original $BaTiO_3$ particles (dark regions) left as inclusions within large PMN-PT grains (lighter regions). The $BaTiO_3$ tabular particles are located at the center of the large grains. Also, it can be seen that the large grains all contain multiple spherical pores radiating from, but never contained within the $BaTiO_3$ particle. These two results insinuate that the growth of the large grains was initiated on the surface of the $BaTiO_3$ particles and that the growth rate of these grains was very high. Therefore, it can be concluded that the $BaTiO_3$ particles successfully acts as a template for the growth of PMN-PT.

3.3.3 Characterization of Heteroepitaxial TGG from $BaTiO_3$ Template Crystals

In order to isolate the growth process, so that it may be investigated more closely, a single millimeter size {001}-$BaTiO_3$ single crystal (1.0 mm^2 × 0.4 mm) was embedded into the PMN-35PT matrix. The PMN-35PT matrix composition contained 3 wt% excess PbO in order to enhance the growth kinetics of the single crystal layer. The cross-section

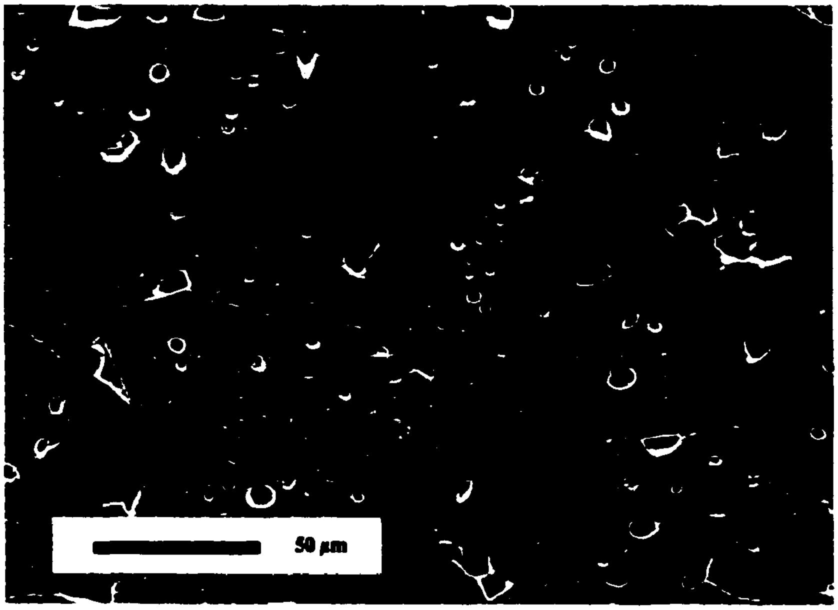

Figure 3.14: SEM micrograph of a PMN-35PT ceramic containing 10 vol% tabular $BaTiO_3$ templates with 1 wt% excess PbO (sintered by heating *Profile 1*).

of the TGG sample sintered at 1150°C for 15 min. is displayed in Fig. 3.15. The figure shows >60 μm growth of a crystal layer from the original {001}-$BaTiO_3$ interface. Within the grown crystal layer, there are entrapped spherical pores that increase in size further from the original $BaTiO_3$ interface. The size of the pores in the crystal ranged from <1 μm at the initial interface of the $BaTiO_3$ to ~5 μm at the matrix interface. The gradient in the size of the pores in the grown crystal is a result of the coarsening of the porosity in the matrix.

An electron diffraction pattern performed on the sample by transmission electron microscopy (TEM) confirms that the grown layer is a single crystal with an epitaxial match to the $BaTiO_3$ template crystal (Fig. 3.16). The TEM image and diffraction pattern were completed on a sample containing a {001}-$BaTiO_3$ Remeika crystal embedded in a PMN-35PT matrix composition containing 3wt% excess PbO heated at 10°C/min. to 950°C and then quenched to room temperature.

EDS (Prism EDS system, Princeton Gamma Tech) was preformed across the $BaTiO_3$/templated crystal interface. The minimum mass sensitivity, concentration resolution, spatial resolution, and spectral resolution of the EDS system are 1×10^{-13}g, 1000 ppm, 1.0 μm, and 130 eV, respectively. The EDS scan showed that there was diffusion across the $BaTiO_3$/templated crystal interface of the sample containing 3 wt% excess PbO sintered at 1150°C for 1 h. As seen in Fig. 3.17, a trace of Pb is detected within 2 μm of the interface in the $BaTiO_3$ crystal, but there was no Ba in the grown crystal. Trace amounts of Pb located in the $BaTiO_3$ crystal may reside within a formed (Ba,Pb)TiO_3 precipitate(55,56) or as a defect of polishing and thermal etching. The

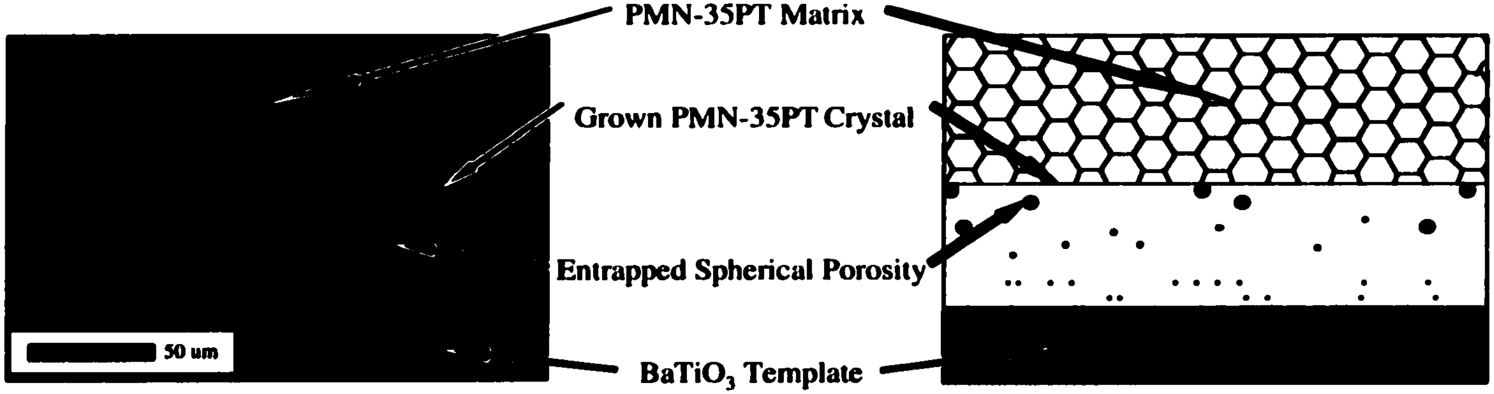

Figure 3.15: TGG of a PMN-35PT single crystal layer on a {001}-BaTiO3 template crystal in a PMN-35PT matrix containing 3wt% excess PbO sintered at 1150°C, 15 min.

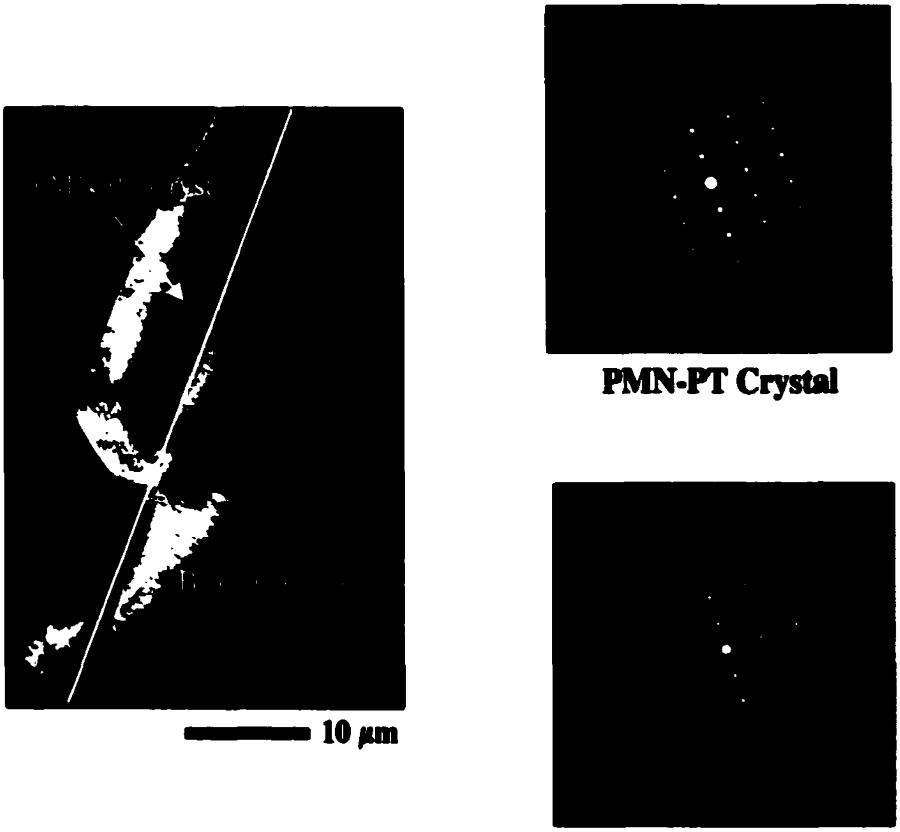

PMN-PT Crystal

$BaTiO_3$ Template

Figure 3.16: TEM micrograph and electron diffraction patterns showing heteroepitaxy of PMN-35PT single crystal grown on a {001}-$BaTiO_3$ template from a PMN-35PT matrix containing 3wt% excess PbO, heated to 950°C and then quenched in air to room temperature. (TEM work courtesy of I.M. Reaney)

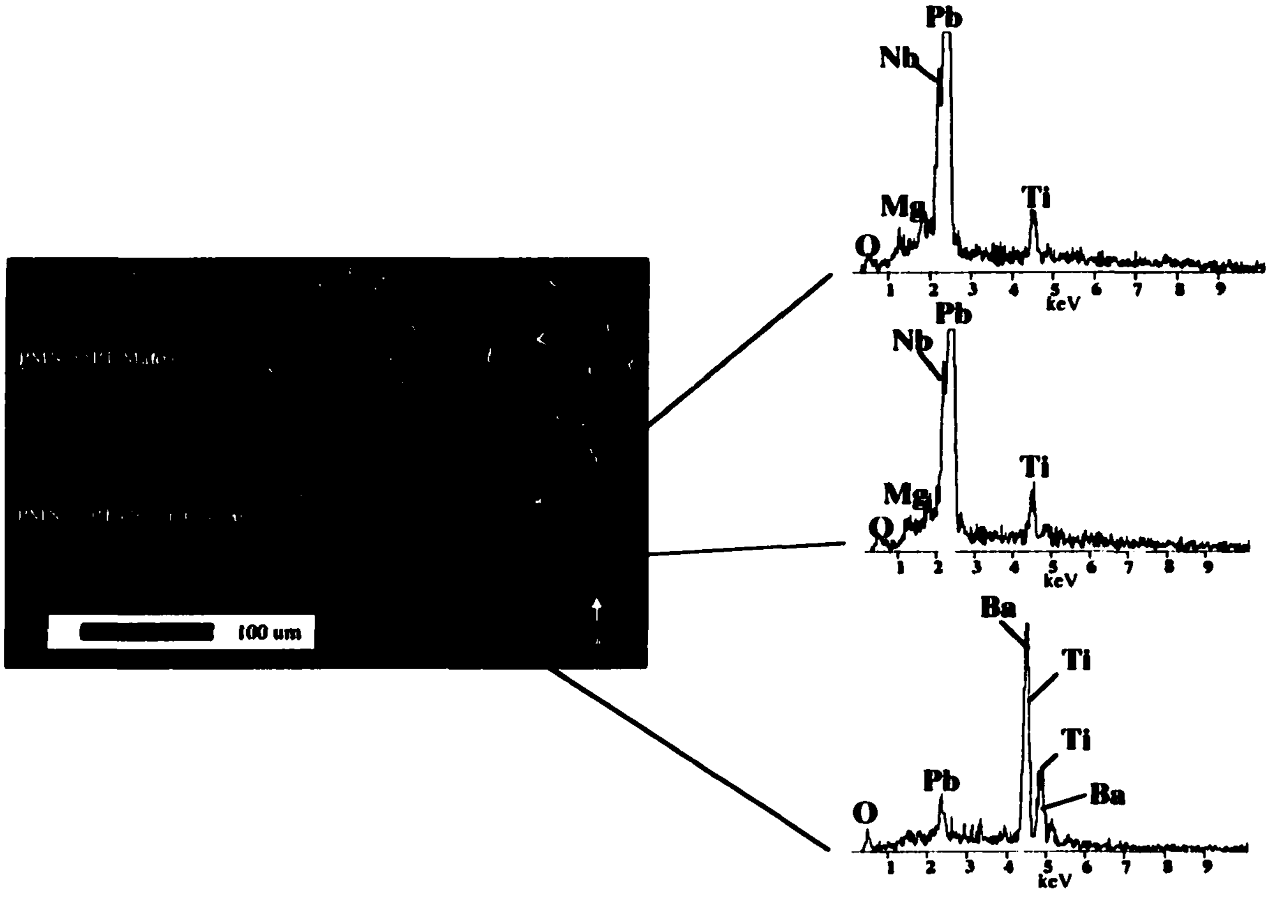

Figure 3.17: SEM micrograph with the EDS of a grown PMN-35PT crystal layer and matrix containing 3 wt% excess PbO sintered at 1150°C for 1 h.

intensity of the EDS peaks for Pb, Mg, Nb, and Ti were constant across the grown crystal beginning from 2 μm into the newly formed crystal layer, which indicates that the PMN-35PT composition was constant over the grown region.

Single crystal {110}- and {111}-$BaTiO_3$ cuts (Lockheed-Sanders, Nashua, NH) were embedded in the same manner described for the {001}-$BaTiO_3$ Remeika crystals. The matrix composition consisted of PMN-35PT with 3 wt% excess PbO. When these samples were sintered at 1150°C for 5 h, the single crystal PMN-PT grew completely through the sample thickness (1.5 mm) with the crystal originating from the $BaTiO_3$ template crystal (~0.25 mm in thickness) in the center of the polycrystalline pellet. As seen in Fig. 3.18, the crystals grown from the {110} and {111} templates took on the respective 2-fold and 3-fold symmetry of the given orientation, as dictated by the perovskite prototype m3m symmetry. This result suggests that other $BaTiO_3$ plane orientations besides the {001} are stable within the high temperature, Pb-rich environment and that the growth kinetics of some of these orientations may be very high.

The stability of the $BaTiO_3$ crystals within the high temperature, Pb-rich environment was further observed by a simple experiment in which 0.01 g of PbO was distributed on the surface of {001}- and {111}-$BaTiO_3$ crystals. After firing these samples to 1150°C for 1 h in an ambient air atmosphere, the samples displayed well-faceted $(Pb,Ba)TiO_3$ nuclei on the surface of the crystals (Fig. 3.19(a,b)).(55,56) The {001}-crystal showed approximately square nuclei while the {111}-crystal presented triangular nuclei. Again, the features on the crystal surface reflected the symmetry of the template crystal orientation. When the same experiment was carried out on a {001}-$SrTiO_3$, the crystal surface did not show any faceted features. The crystal surface showed

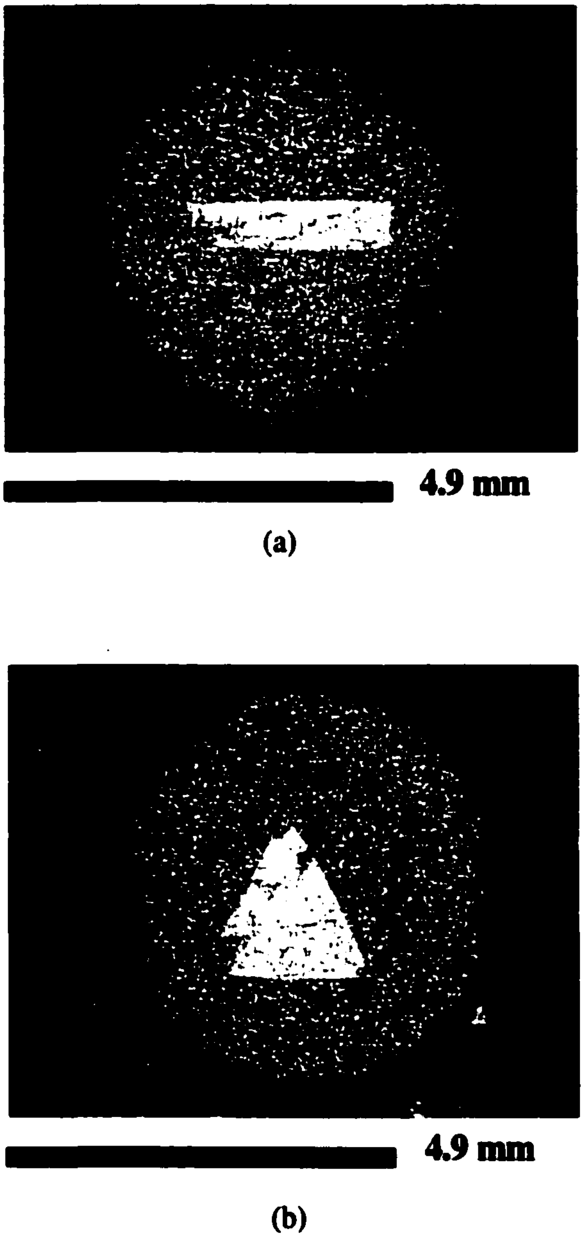

Figure 3.18: Optical micrograph of PMN-35PT single crystals grown by Templated Grain Growth from (a) $\{110\}$- and (b) $\{111\}$-$BaTiO_3$ template crystals embedded in a PMN-35PT ceramic containing 3wt% excess PbO (1150°C, 5 h).

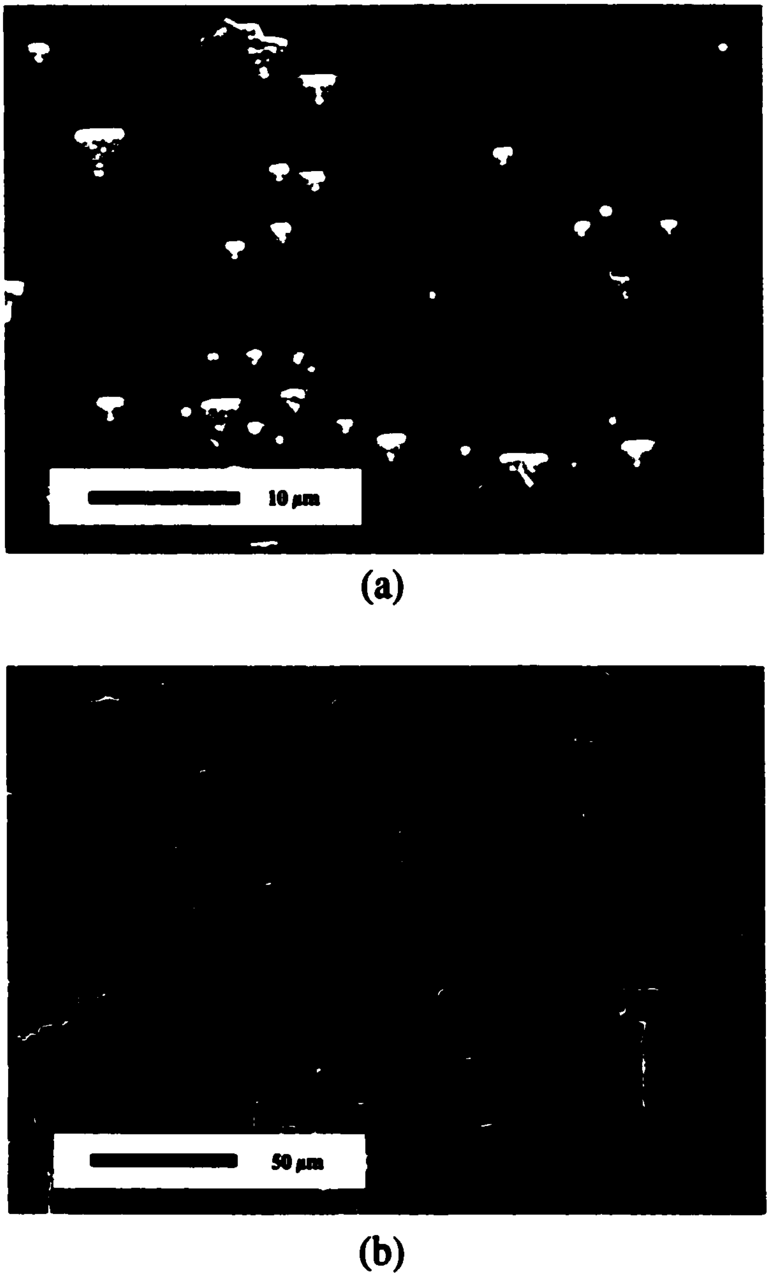

Figure 3.19: SEM micrograph of the surface of (a) {111}-$BaTiO_3$ and (b) {001}-$BaTiO_3$ single crystals after their reaction with 0.01 g. of PbO at 1150°C for 1 h.

a very rough appearance, indicating that the molten PbO attacked the {001}-$SrTiO_3$ surface at this temperature (Fig. 3.20). This result supports the notion that the {001}-$SrTiO_3$ is not as stable in Pb-rich environments and that any Pb-based liquid phase available in the PMN-PT matrix would readily dissolve $SrTiO_3$ template surface, and thus, render it useless to act as a template for TGG. On the other hand, the results of this experiment further emphasize the stability of $BaTiO_3$ and its ability to act as a template for texturing PMN-PT by TGG.

3.4 CONCLUSIONS

This work emphasized the importance of the thermodynamic stability of the template within the matrix composition in the given sintering environment. Particles which show the proper template size, shape, and epitaxial relation may not be qualified to act as the template due to their instability. The instability can be exhibited by the degradation of the structure (morphologic or crystallographic), the dissolution, or the chemical reaction of the template particle. Many of these various possible template/matrix interactions were identified and presented in this work.

The template compositions which possess a layered perovskite or tungsten bronze crystal structure ($Bi_4Ti_3O_{12}$, $Sr_3Ti_2O_7$, $KSr_2Nb_5O_{15}$, and $Sr_2Nb_2O_7$) were shown to be thermodynamically unstable in the PMN-35PT matrix regardless of the excess PbO content. The $Bi_4Ti_3O_{12}$, $KSr_2Nb_5O_{15}$, and $Sr_2Nb_2O_7$ templates all reacted with the matrix material and formed a cubic-pyrochlore phase. The $Sr_3Ti_2O_7$ templates did not similarly form the pyrochlore phase when added to the PMN-35PT matrix, but the $Sr_3Ti_2O_7$ templates showed signs of dissolution into the PMN-35PT matrix. Also, the

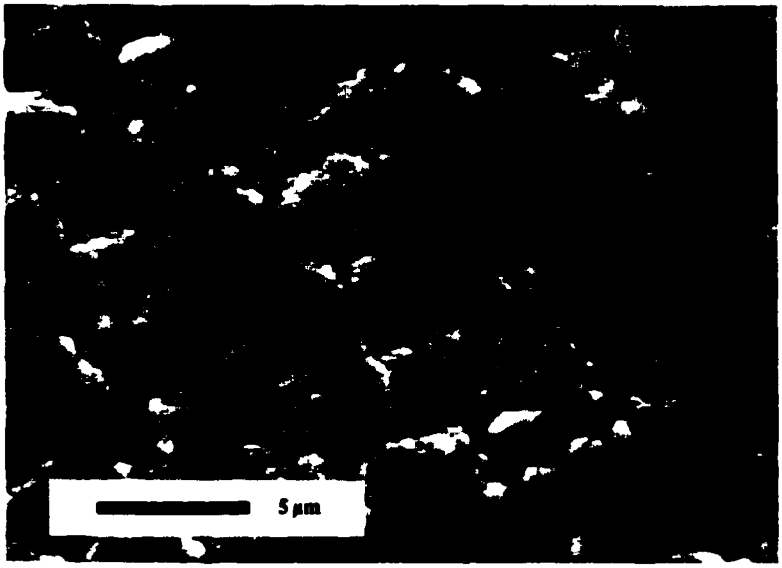

Figure 3.20: SEM micrograph of the surface of a {001}- $SrTiO_3$ single crystal after its reaction with 0.01 g of PbO at 1150°C for 1 h.

microstructure of the ceramic containing the $Sr_3Ti_2O_7$ particles did not display the presence of any templated grains.

The particles with a perovskite composition and structure did not result in the formation of the pyrochlore phase when reacted with the PMN-35PT matrix. The $PbTiO_3$ and $BaTiO_3$ whisker templates showed significant dissolution into the PMN-35PT matrix due to the chemical instability of the as-synthesized particles. The reaction between both the $SrTiO_3$ and $BaTiO_3$ platelet particles and the PMN-35PT matrix resulted in the formation of a population of exaggerated grains. The degradation of the {001}-$SrTiO_3$ template crystal in the presence of excess PbO and the slight presence of Sr in the surrounding PMN-35PT matrix implied that the {001}-$SrTiO_3$ template crystals may not be the proper templates to use in a PbO-rich environment. The {001}-$BaTiO_3$ platelet particles showed no significant dissolution into the PMN-35PT matrix and excess PbO. Templated growth of single crystal PMN-PT layers was observed from the surface of the $BaTiO_3$ crystals in various sintering conditions. Therefore, this work identified $BaTiO_3$ as a suitable composition to act as a template material for the TGG of PMN-PT.

3.5 REFERENCES

1) M.N. Rahaman, *Ceramic Processing and Sintering*. Marcel Dekker, Inc., New York (1995).

2) A. Seifert, F.F. Lange, and J.S. Speck, "Epitaxial Growth of $PbTiO_3$ Thin Films on (001) $SrTiO_3$ from Solution Precursors," *J. Mater. Res.*, **10** [3] 680-91 (1995).

3) J. Moon, J.A. Kerchner, J. LeBleu, A.A. Morrone, and J.H. Adair, "Oriented Lead Titanate Film Growth at Lower Temperatures by the Sol-Gel Method on Particle-Seeded Substrates," *J. Am. Ceram. Soc.*, **80** [10] 2612-23 (1997).

4) K. Yanagisawa, "Formation of Perovskite-type $Pb(Mg_{1/3}Nb_{2/3})O_3$ Under Hydrothermal Conditions," *J. Mat. Sci.*, **12** [23] 1842-43 (1993).

5) K. Yanagisawa, "Stability of Lead Magnesium Niobate Under Hydrothermal Conditions," *J. Mat. Sci.*, **30** [5] 1361-66 (1995).

6) K. Yanagisawa, J.C. Rendon-Angeles, H. Kanai, and Y. Yamashita, "Stability and Single Crystal Growth of Dielectric Materials Containing Lead Under Hydrothermal Conditions," *J. Euro. Ceram. Soc.*, **19** 1033-36 (1999).

7) K.H. Yoon, Y.-S. Cho, D.-H. Lee, and D.-H. Kang, "Powder Characteristics of $Pb(Mg_{1/3}Nb_{2/3})O_3$ Prepared by Molten Salt Synthesis," *J. Am. Ceram. Soc.*, **76** [5] 1373-76 (1993).

8) K.H. Yoon, Y.S. Cho, and D.-H. Kang, "The Formation and Phase Stability of Lead Magnesium Niobate in the Presence of a Molten Flux," *J. Mat. Sci.*, **30** 4244-48 (1995).

9) Y. Zupei, Q. Shaobo, T. Changsheng, "Effect of Excess PbO or MgO and Purity of MgO on Phase Structure and Dielectric Properties of PMN-PT Ceramics Prepared by Molten Salt Synthesis," *J. Mat. Sci. Lett.*, **19** 1743-46 (2000).

10) C.C. Li, C.C. Chiu, and S.B. Desu, "Formation of Lead Niobates in Molten Salt Systems," *J. Am. Ceram. Soc.*, **74** [1] 42-47 (1991).

11) M. Traianidis, C. Courtois, A. Leriche, and B. Thierry, "Hydrothermal Synthesis of Lead Zirconium Titanate (PZT) Powders and Their Characteristics," *J. Euro. Ceram. Soc.*, **19** 1023-26 (1999).

12) J. Moon, J.A. Kerchner, H. Krarup, and J.H. Adair, "Hydrothermal Synthesis of Ferroelectric Perovskites from Chemically Modified Titanium Isopropoxide and Acetate Salts," *J. Mater. Res.*, **14** [2] 425-35 (1999).

13) J.Y. Choi, C.H. Kim, and D.K. Kim, "Hydrothermal Synthesis of Spherical Perovskite Oxide Powders Using Spherical Gel Powders," *J. Am. Ceram. Soc.*, **81** [5] 1353-56 (1998).

14) H. Cheng, J. Ma, B. Zhu, and Y. Cui, "Reaction Mechanisms in the Formation of Lead Zirconate Titanate Solid Solutions under Hydrothermal Conditions," *J. Am. Ceram. Soc.*, **76** [3] 625-29 (1993).

15) T. Kimura, A. Takenaka, T. Mifune, Y. Hayashi, and T. Yamaguchi, "Preparation of Needle-like $TiZrO_4$ and PZT," *J. Mat. Sci.*, **27** 1479-83 (1992).

16) R.H. Arendt, J.H. Rosolowski, and J.W. Szymaszek, "Lead Zirconate Titanate Ceramics from Molten Salt Solvent Synthesized Powders," *Mat. Res. Bull.*, **14** 703-9 (1979).

17) J. Moon, T. Li, C. Randall, and J.H. Adair, "Low Temperature Synthesis of Lead Titantate by a Hydrothermal Method," *J. Mater. Res.*, **12** [1] 189-97 (1997).

18) J. Moon, M.L. Carasso, H.G. Krarup, J.A. Kerchner, and J.H. Adair, "Particle-shape Control and Formation Mechanisms of Hydrothermally Derived Lead Titanate," *J. Mater. Res.*, **14** [3] 866-75 (1999).

19) H. Cheng, J. Ma, Z. Zhao, and D. Qiang, "Hydrothermal Synthesis of Acicular Lead Titanate Fine Powders," *J. Am. Ceram. Soc.*, **75** [5] 1123-28 (1992).

20) H. Cheng, J. Ma, and Z. Zhao, "Hydrothermal Synthesis of $PbO-TiO_2$ Solid Solution," *Chem. Mater.*, **6** 1033-40 (1994).

21) Y. Ohara, K. Koumoto, T. Shimizu, and H. Yanagida, "Hydrothermal Synthesis of Fibrous Lead Titanate Powders," *J. Mater. Sci.*, **30** 263-66 (1995).

22) D. Taylor, "Thermal Expansion Data VIII., Complex Oxides, ABO_3, the Perovskites," *Brit. Ceram. Trans.*, **84** [6] 181-8 (1985).

23) D.K. Agrawal, R. Roy, and H.A. McKinstry, "Ultra Low Thermal Expansion Phases: Substituted 'PMN' Perovskites," *Mat. Res. Bull.*, **22** 83-8 (1987).

24) J.H. Lee, C.W. Won, T.S. Kim, and H.S. Kim, "Characteristics of $BaTiO_3$ Powders Synthesized by Hydrothermal Process," *J. Mat. Sci.*, **35** [17] 4271-74 (2000).

25) I.J. Clark, T. Takeuchi, N. Ohtori, and D.C. Sinclair, "Hydrothermal Synthesis and Characterisation of $BaTiO_3$ Fine Powders: Precursors, Polymorphism and Properties," *J. Mater. Chem.*, **9** [1] 83-91 (1999).

26) L. Zhao, A.T. Chien, F.F. Lange, and J.S. Speck, "Microstructural Development of $BaTiO_3$ Powders Synthesized by Aqueous Methods," *J. Mater. Res.*, **11** [6] 1325-28 (1996).

27) J.P. Remeika, "A Method for Growing Barium Titanate Single Crystals," *J. Am. Chem. Soc.*, **76** [3] 940-41 (1954).

28) R.C. DeVries, "Observations on Growth of $BaTiO_3$ Crystals from KF Solutions," *J. Am. Ceram. Soc.*, **42** [11] 547-58 (1959).

29) Y. Ohara, K. Koumoto, and H. Yanagida, "Barium Titanate Ceramics with High Piezoelectricity Fabricated from Fibrous Particles," *J. Am. Ceram. Soc.*, **68** [4] C108-C109 (1985).

30) Y. Hayashi, T. Kimura, and T. Yamaguchi, "Preparation of Rod-Shaped $BaTiO_3$ Powder," *J. Mat. Sci.*, **21** 757-62 (1986).

31) T. Takeuchi, T. Tani, and T. Satoh, "Microcomposite Particles $Sr_3Ti_2O_7$-$SrTiO_3$ with an Epitaxial Coreshell Structure," *Solid State Ionics*, **108** [1-4] 67-71 (1998).

32) K. Watari, B. Brahmaroutu, G.L. Messing, S. Trolier-McKinstry, and S.-C. Cheng, "Epitaxial Growth of Anisotropically Shaped, Single-Crystal Particles of Cubic $SrTiO_3$," *J. Mater. Res.*, **15** [4] 846-49 (2000).

33) T. Takeuchi and T. Tani, "Synthesis of $Bi_4Ti_3O_{12}$-$PbTiO_3$ Micro-Composite Particles," *J. Am. Ceram. Soc.*, **106** [10] 947-50 (1998).

34) H. Idink, V. Srikanth, W.B. White, and E.C. Subbarao, "$Bi_4Ti_3O_{12}$," *J. Appl. Phys.*, **76** [3] 1819-23 (1994).

35) R. Ramesh, H. Gilchrist, T. Sands, V. Keramidas, R. Haakenaasen, and D. Fork, "Ferroelectric La-Sr-Co-O/Pb-Zr-Ti-O/La-Sr-Co-O Heterostructures on Silicon via Template Growth," *Appl. Phys. Lett.*, **63** [26] 3592-94 (1993).

36) C.L. Canedy, S. Aggarwal, H. Li, T. Venkatesan, R. Ramesh, F.W. Van Keuls, R.R. Romanofsky, and F.A. Miranda, "Structural and Dielectric Properties of Epitaxial $Ba_{1-x}Sr_xTiO_3$-$Bi_4Ti_3O_{12}$-ZrO_2 Heterostructures Grown on Silicon," *Appl. Phys. Lett.*, **77** [10] 1523-25 (2000).

37) S.G. Ghonge, E. Goo, R. Ramesh, R. Haakenaasen, and D.K. Fork, "Microstructure of Epitaxial Oxide Thin Film Heterostructures on Silicon by Pulsed Laser Deposition," *Appl. Phys. Lett.*, **64** [25] 3407-09 (1994).

38) X.M. Chen and J.S. Yang, "PZT-based Piezoelectric Ceramics with Complex Structures," *Mater. Lett.*, **25** 53-55 (1995).

39) X.M. Chen and J.S. Yang, "Toughening of PZT Piezoelectric Ceramics by In-Situ Complex Structures," *J. Euro. Ceram. Soc.*, **18** 1059-62 (1998).

40) N. Ishizawa, F. marumo, T. Kawamura, and M. Kimura, "The Crystal Structure of $Sr_2Nb_2O_7$, a Compound with Perovskite-Type Slabs," *Acta Cryst.*, **B31** 1912-15 (1975).

41) R.U. Devlikanova, "Crystallochemical Criteria for the Existence of Oxides with the Tetragonal Tungsten Bronze Structure and Ferroelectric Properties," *Inorg. Mater.*, **30** [10] 1217-21 (1994).

42) C. Duran, S. Trolier-McKinstry, and G.L. Messing, "Fabrication and Electrical Properties of Textured $Sr_{0.53}Ba_{0.47}Nb_2O_6$ by Templated Grain Growth," *J. Am. Ceram. Soc.*, **83** [9] 2203-13 (2000).

43) B. Brahmaroutu, *Templated Grain Growth of Textured Strontium Niobate Ceramics.* Ph.D thesis, Penn State University (1999).

44) B. Brahmaroutu, "Molten Salt Synthesis of Anisotropic $Sr_2Nb_2O_7$ Particles," *J. Am. Ceram. Soc.*, **82** [6] 1565-68 (1999).

45) T. Shimizu, H. Yanagida, M. Hori, K. Hashimoto, and Y. Nishikawa, "New Fibrous Phase of Potassium Titanate," *Yogyo-Kyokai-Shi*, **87** [5] 273-75 (1979).

46) T. Shimizu, H. Yanagida, M. Hori, K. Hashimoto, and Y. Nishikawa, "Hydrothermal Reaction Between the Hydrous Potassium Titanate Fibers and Barium Hydroxide," *Yogyo Kyokaishi*, **87** [10] 500-5 (1979).

47) M. Suzuki, S. Uedaira, H. Masuya, and H. Tamura, "Hydrothermal Synthesis of Lead Titanate Fine Powder"; pp. 163-70 in *Ceramic Transactions*, Vol. 1, Ceramic Powder Science II. Edited by G.L. Messing, E.R. Fuller, and H. Hausner. American Ceramic Society, Westerville, OH, 1988.

48) Z.G. Ye, P. Tissot, and H. Schmidt, "Pseudo-Binary $Pb(Mg_{1/3}Nb_{2/3})O_3$-PbO Phase Diagram and Crystal Growth of $Pb(Mg_{1/3}Nb_{2/3})O_3$ [PMN]," *Mat. Res. Bull.*, **25** 739-48 (1990).

49) J.P. Guha, "Reaction Chemistry and Subsolidus Phase Equilibria in Lead-Based Relaxor Systems: Part I: Formation and Stability of the Perovskite and Pyrochlore Compounds in the System PbO-MgO-Nb_2O_5," *J. Mater. Sci.*, **34** 4985-94 (1999).

50) R.S. Roth, "PbO-Nb_2O_5 Phase Diagram," *J. Res. Natl. Bur. Stand.*, **62** [1] 34 (1959).

51) V.A. Isupov, "Physical Phenomena in Ferroelectric Complex Perovskites," *Bull. Acad. Sci. USSR, Physical Series*, **47** [3] 559-65 (1983).

52) V.M. Goldschmidt, *Shrifter Norske Videnskaps-Akad.* Oslo 1: Matemot. Naturuid. Klasse, No. 2, 1926.

53) T.S. Shrout and A. Halliyal, "Preparation of Lead-Based Ferroelectric Relaxors for Capacitors," *Am. Ceram. Soc. Bull.*, **66** [4] 704-11 (1987).

54) F. Jona and G. Shirane, *Ferroelectric Crystals.* Dover Publications, Inc., New York (1993).

55) A. Hirata and T. Yamaguchi, "Interfacial Reaction of $BaTiO_3$ Ceramics with PbO-B_2O_3 Glasses," *J. Am. Ceram. Soc.*, **80** [1] 79-84 (1997).

56) Y. Kuromitsu, S.F. Wang, S. Yoshikawa, and R. Newnham, "Interaction Between Barium Titanate and Binary Glasses," *J. Am. Ceram. Soc.*, **77** [2] 493-98 (1994).

Chapter 4

KINETICS OF TEMPLATED GRAIN GROWTH OF PMN-35PT CRYSTALS FROM $BaTiO_3$ TEMPLATE CRYSTALS

4.1 INTRODUCTION

Lead-based relaxor-$PbTiO_3$ ferroelectric crystals are grown by high-temperature flux processes.(1-5) Relatively large lead-based relaxor single crystals have been grown at mm/h rates by the Bridgman method.(6,7) An alternative, but less efficient method, of growing lead-based relaxor single crystals is solid state conversion. In this method, a single crystal is embedded in a polycrystalline ceramic and heated to induce the growth of the embedded crystal. Li *et al.*(8) produced millimeter size $0.65Pb(Mg_{1/3}Nb_{2/3})O_3$-$0.35PbTiO_3$ (PMN-35PT) single crystals by the solid state conversion method. Contacting the ceramic with an oriented single crystal template produces a single crystal grown with a specific orientation. The term templated grain growth (TGG) is used to distinguish this process from solid state conversion.(9)

The TGG process, similar to that of solid state conversion, is driven by the difference in surface free energies between the advancing crystal plane and the matrix grains during thermal processing. TGG can be applied to the growth of either an oriented single crystal in a fine grained matrix or to the growth of many well oriented template particles in a matrix leading to an increase in the texture fraction of specific orientation. TGG has been used to produce single crystals of many materials as described in Chapter 2. These materials were primarily grown by a homoepitaxial TGG process which means the growing single crystal or textured ceramic has the same composition and crystal structure as the template material. Alternatively, the TGG method can be heteroepitaxial when the template material has a different composition, but the same crystal structure as the matrix material. In Chapter 3, various template materials were investigated to act as heteroepitaxial templates for the oriented growth of the PMN-PT composition. These materials were of different compositions and crystal structures. {001}-$BaTiO_3$ crystals synthesized by the Remeika method were shown to be the most stable in the PMN-PT matrix and also showed signs of templated growth. This work indicated that $BaTiO_3$ crystals could be used as templates for the TGG of PMN-PT single crystals or textured ceramics.

A fundamental understanding of the heteroepitaxial nucleation and growth of the single crystal PMN-PT from the oriented template crystal is useful for understanding the factors affecting TGG of textured ceramics. Rehrig *et al.*(10,11) showed that $BaTiO_3$ and $(Ba,Zr)TiO_3$ crystals of various orientations could be grown using either a $BaTiO_3$ or $SrTiO_3$ template crystal. This process was shown to follow cubic growth kinetics, and thus, was proposed to be controlled by diffusion. Similar information would be useful for the design of solid state processes for the growth of single crystal or textured ceramics of PMN-PT and other relaxor-PT systems.

PMN-PT single crystal and the PMN-PT matrix grains are usually grown in the presence of a PbO-rich liquid phase as a means to facilitate densification, crystal growth, and to compensate for PbO volatilization (Li *et al.*(8,12)). Both the crystal layer and the matrix grow by an Ostwald ripening-type process in which the surface free energy of the system provides the driving force for the process. Growth at the single crystal layer interface is controlled by supersaturation of the liquid (for both interface- and diffusion-controlled mechanisms). Therefore, the behavior of the matrix grains must be well characterized since the degree of supersaturation depends on the scale of the matrix.

The objective of this work was to systematically evaluate the growth of the single crystal PMN-35PT from $BaTiO_3$ template crystals. This investigation focused on the physical and compositional evolution of the growing crystal during various stages of thermal processing. The PMN-35PT matrix grain growth was also monitored to evaluate how the driving force changes during the growth process. To account for the effect of matrix growth, the template growth kinetics were fit to a diffusion-controlled model with a non-constant driving force.(13) The effect of variables like temperature, template orientation, and matrix composition (liquid phase content) on the TGG of the crystal layer was investigated.

4.2 EXPERIMENTAL PROCEDURES

PMN-35PT powder (TRS, Inc., State College, PA) was milled with basic $PbCO_3$ (Aldrich Chemical Company, Inc., Milwaukee, WI, diameter= ~3 μm) in HDPE bottles by 3 mm ZrO_2 media for 10 hours to obtain powder compositions containing 0, 1, 3, and 5 wt% excess PbO. For milling, 25 wt% powder was dispersed in toluene with 0.5 wt% dispersing agent (KD3 Hypermer, ICI Surfactants). The powders were dried and calcined at 550°C for 4 hours. The average particle diameter of the PMN-35PT powder, measured by centrifugal sedimentation (Horiba CAPA-700), was approximately 0.8 μm.

{001}-$BaTiO_3$ crystals approximately 1.0 mm^2 × 0.4 mm in size were synthesized by the Remeika process.(14,15) {110}- and {111}-$BaTiO_3$ crystals of the same dimensions were cut from crystals obtained from Lockheed-Sanders, Inc. (Nashua, NH). The $BaTiO_3$

template crystals were embedded in 0.3 grams of PMN-35PT/PbO powder and uniaxially pressed in a 6 mm diameter die. The compact was uniaxially pressed at 7 MPa, and then cold isostatically pressed at 210 MPa. For sintering and growth experiments, the samples were encapsulated in an ~7 mm diameter, two piece Pt crucible. The Pt encapsulated samples were packed in a double crucible setup using PMN-35PT (with 7 wt% excess PbO) as the packing powder to control PbO volatilization. The double crucible setup first included encasing the samples within 2.5 grams of the packing powder inside a 3.75 x 1.25 x 1.25 cm alumina boat. This alumina boat was then placed in a 2.5 cm x 7.5 cm diameter crucible and sealed with an alumina lid. The samples were heated at 10°C/min between 950°C-1150°C and held for 0 to 5 h. The samples were weighed after thermal processing to monitor the degree of PbO volatilization. Samples which lost greater than 0.5 wt% were eliminated to obtain samples with a relatively constant PbO concentration over all processing conditions.

The samples were cut perpendicular to the pellet face, polished to 0.5 μm, and then thermally etched at 100°C below the sintering temperature for 15 min. From the SEM micrographs, the extent of crystal growth was measured from the original $BaTiO_3$ interface to the matrix interface. Since the growth distance of the PMN-PT crystal layer varied along the original $BaTiO_3$ template crystal, the average distance and standard deviation were calculated from distances measured every 20 μm along the length of the $BaTiO_3$ template crystal. The average grain size and standard deviation were also measured for all the samples in which the crystal growth was measured. The average lineal intercept was measured for approximately 350 grains from SEM micrographs by utilizing stereological analysis software.(16) The average lineal intercept was multiplied by 1.56 to obtain the average grain size.(17)

4.3 RESULTS AND DISCUSSION

4.3.1 Grain Growth Kinetics of the PMN-35PT Matrix

Figures 4.1(a-d) display the average radius and standard deviation of the matrix grains within the TGG samples containing 0, 1, 3, or 5 wt% excess PbO, respectively. For all matrix compositions, the grains began to coarsen at temperatures as low as 950°C, initially starting from a particle size of ~0.8 μm and growing to a diameter of 2.0-4.0 μm. This means that the dissolution/precipitation mechanism of growth began just above the melting temperature of the liquid phase, which ranges between 830-886°C (18-20), depending on the liquid phase composition. With longer sintering times at all temperatures, the average grain size saturated for all matrix compositions. The liquid phase content did not seem to affect the final saturated grain size, which is contrary to the prediction of diffusion-controlled models.(21)

The width of the grain size distribution increased for longer sintering times, as indicated by the larger standard deviations, but abnormally large grains were not observed. Chemical heterogeneity and PbO volatilization are reasons given for exaggerated grain growth in the PMN-PT system.(22) Thus, fine roll milling of the PbO precursor and the control of PbO vaporization (<0.5 wt% loss) probably contributed to a series of samples with a more homogenous distribution of the liquid phase than those demonstrating exaggerated grain growth.

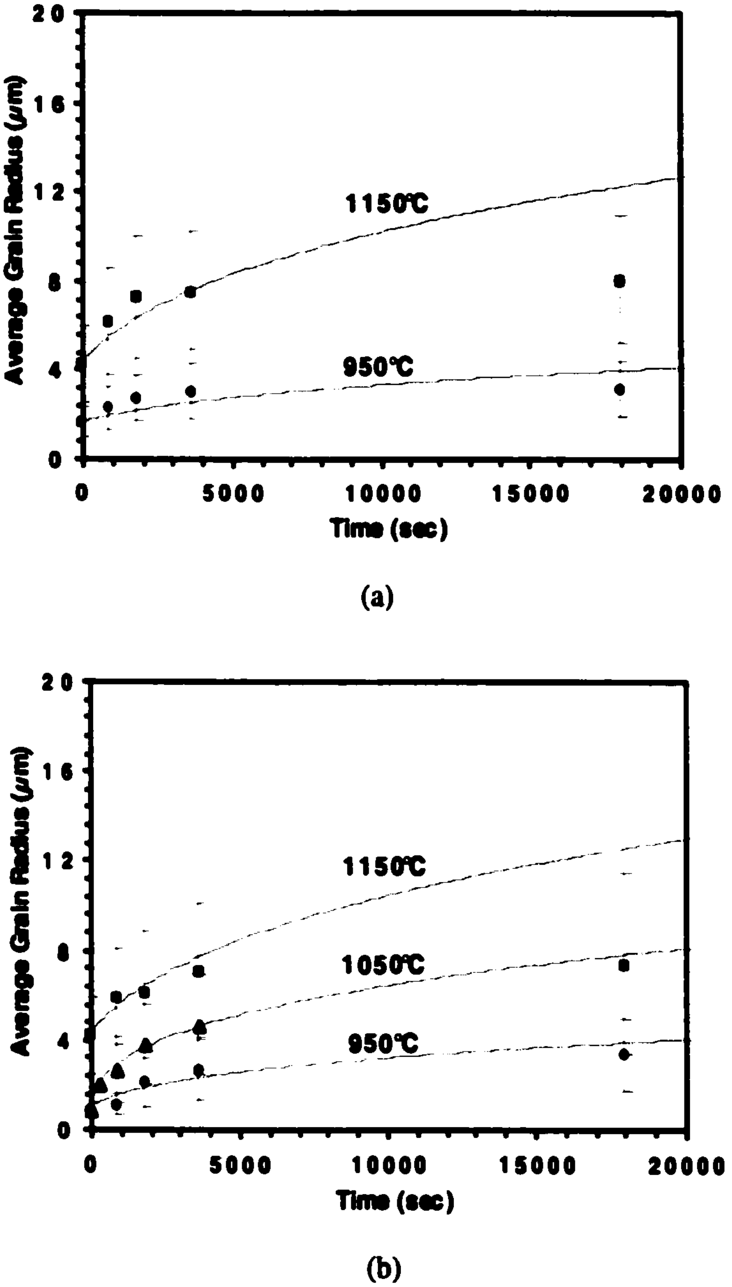

(a)

(b)

Figure 4.1: Matrix grain growth of PMN-35PT with a composition containing (a) 0 wt%, (b) 1 wt%, (c) 3 wt%, and (d) 5 wt% excess PbO. (The solid line is the fitted Lay model.)

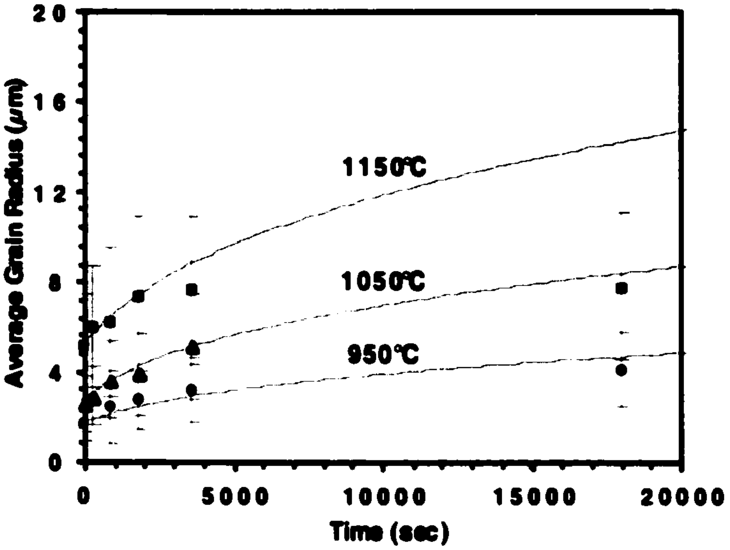
20
16
12
8
4
0
Average Grain Radius (μm)
0
5000
10000
15000
20000
Time (sec)
1150°C
1050°C
950°C

(c)

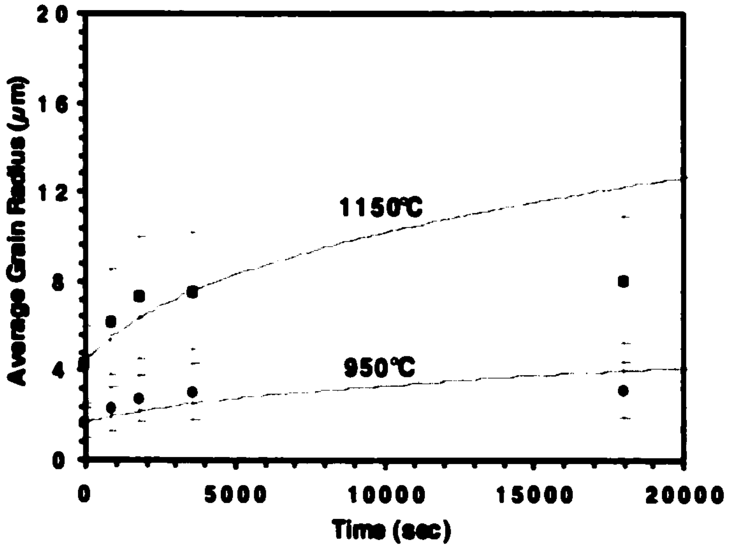
20
16
12
8
4
0
Average Grain Radius (μm)
0
5000
10000
15000
20000
Time (sec)
1150°C
950°C

(d)

The common characteristic of the growth kinetics for all compositions is the decrease in the growth rate resulting in a saturation of the grain size. To explain these observations, we need to consider the factors that affect the grain boundary mobility in ceramics containing a liquid phase. The increase in grain size indicates that the solubility gradient between the growing matrix grains decreases. As long as the size distribution around the critical grain size (average grain size) remains self-consistent, then the driving force for growth should decrease by a degree which would be predicted by the Lay model.(23) Since the distribution of grain sizes in this study remained relatively constant for all samples, the mobility may have decreased because of an increase in the liquid boundary layer thickness with matrix coarsening. The thicker grain boundary would limit the diffusion.

Figure 4.2(a) shows that the samples containing 3 wt% and 5 wt% excess PbO densified quickly after the formation of the liquid phase at temperatures <950°C. The 0 wt% and 1 wt% excess PbO containing samples did not experience the same accelerated densification as the higher liquid content samples. Figure 4.2(b) shows that the density increased by increasing the sintering temperature to 1150°C. During extended isothermal treatment at 1150°C, the density of the samples decreased by 1 to 6%, especially for 3 and 5 wt% excess PbO concentrations for longer sintering times. Therefore, another reason for the decrease in growth rate is a reduction in mobility due to pore drag. The source of the porosity in the PbO saturated PMN-PT ceramics is still uncertain. Kwon *et al.*(24) proposed that undissolved gases, like nitrogen, originally trapped within the liquid and pores during densification migrates and forms pores during grain growth. Samples sintered in oxygen do not undergo these pore coarsening and dedensification processes

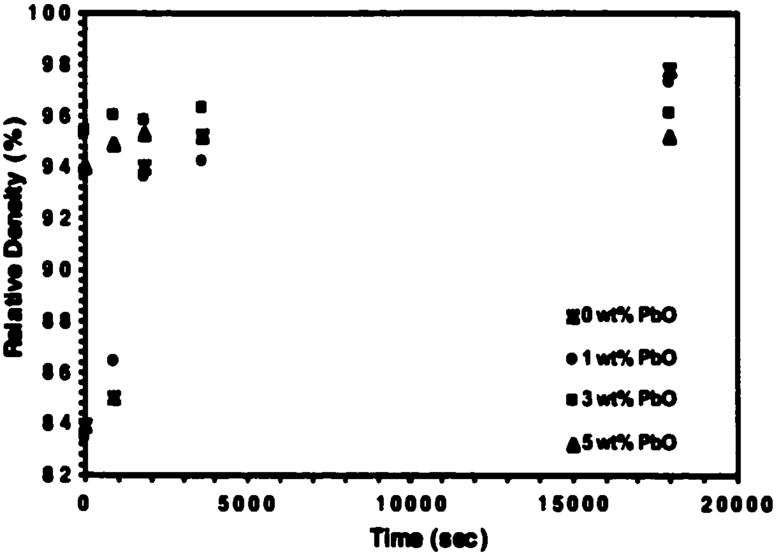

(a)

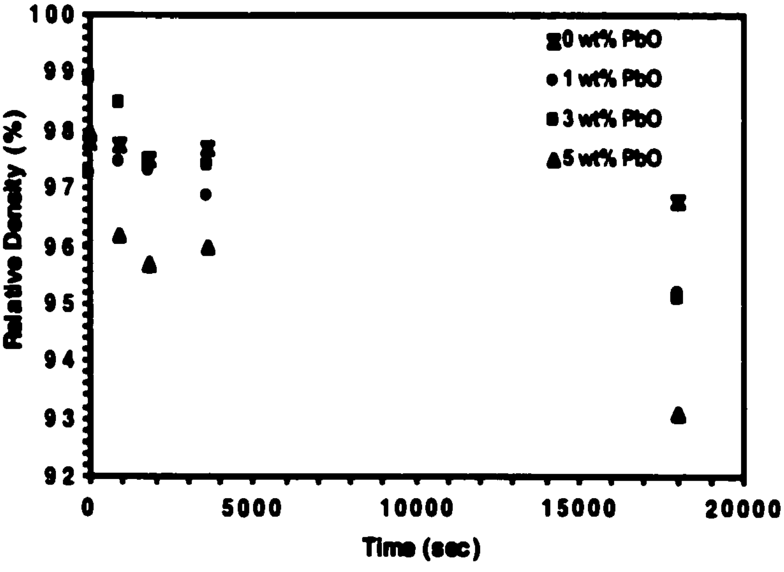

(b)

Figure 4.2: Density measured by stereology of the PMN-35PT samples sintered at (a) 950 °C and (b) 1150°C.

which suggests that nitrogen plays a critical role in pore evolution for air sintered samples.

Alternatively, the change in mobility may have been the result of the faceting of the grains and/or the impingement of these faceted grains. This phenomena is typical of systems which display exaggerated grain growth in the presence of a liquid phase.(25) PMN-PT compositions containing excess PbO have been known to display well faceted, cubic grains. Fig. 4.3(a) shows the SEM micrograph of the grain structure of the matrix composition containing 3 wt% excess PbO after being heated to 950°C without an isothermal hold. The microstructure is very uniform, consisting of grains with a spherical-like morphology. With an increase in temperature to 1150°C, the grain morphology of the 3 wt% excess PbO sample was altered, where many of the grains began to present an angular, block-type morphology (Fig. 4.3(b)). After a 0.5 h isothermal hold at 1150°C for the same composition, the grain morphology of the entire grain population displayed the block-type shape (Fig. 4.3(c)). The other matrix compositions showed the same tendency for the grain morphology to evolve from the spherical to the angular shape (Figs. 4.4(a,b)). The system seems to be driving towards an equilibrium cubic shape which might be expected in a perovskite material like PMN-PT, but the grains never attain a distinctly faceted morphology. Therefore, it is unlikely that the grain growth is governed purely by an interface- or nucleation-controlled mechanism, although, the observed morphology change at the higher temperatures may suggest a mixed growth mechanism.

Lay reported(23) the following equation for diffusion-controlled grain growth in the presence of a liquid phase;

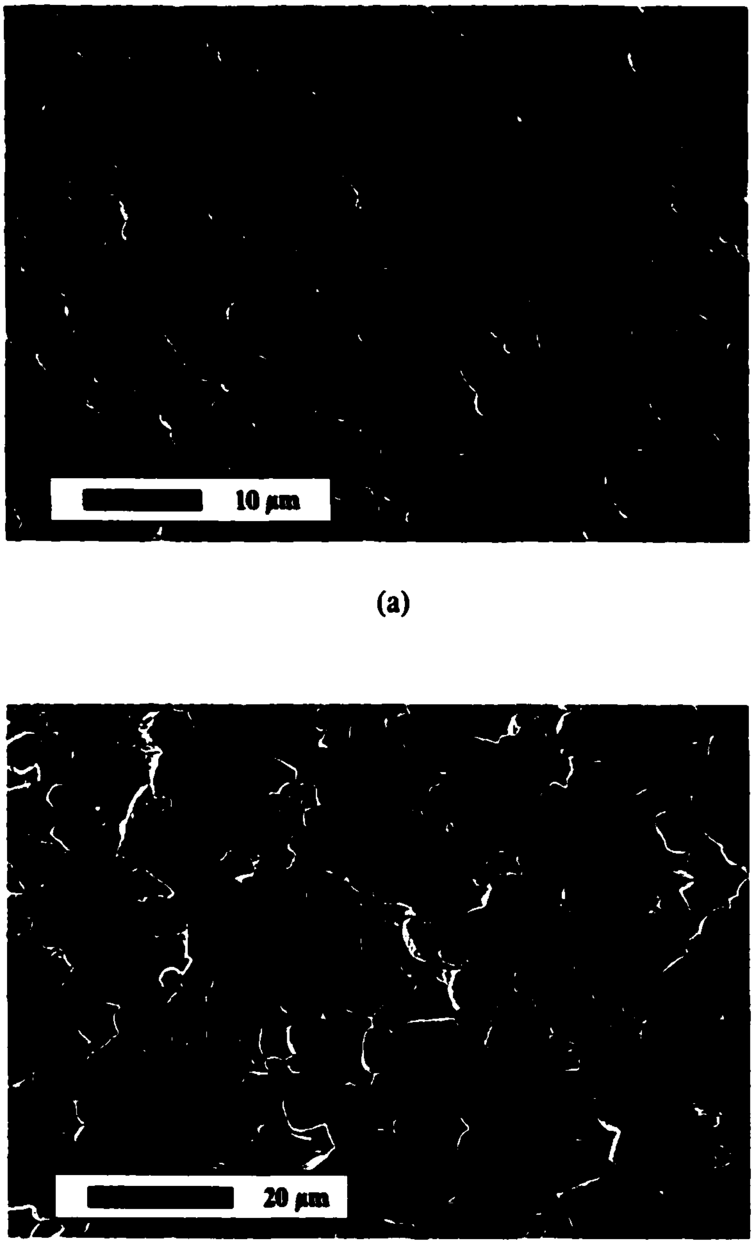

(b)

Figures 4.3: SEM micrograph of the microstructure of polycrystalline PMN-35PT containing 3 wt% excess PbO sintered at (a) 950°C for 0 h. and (b) 1150°C for 0 h, and (c) 1150 for 0.5 h.

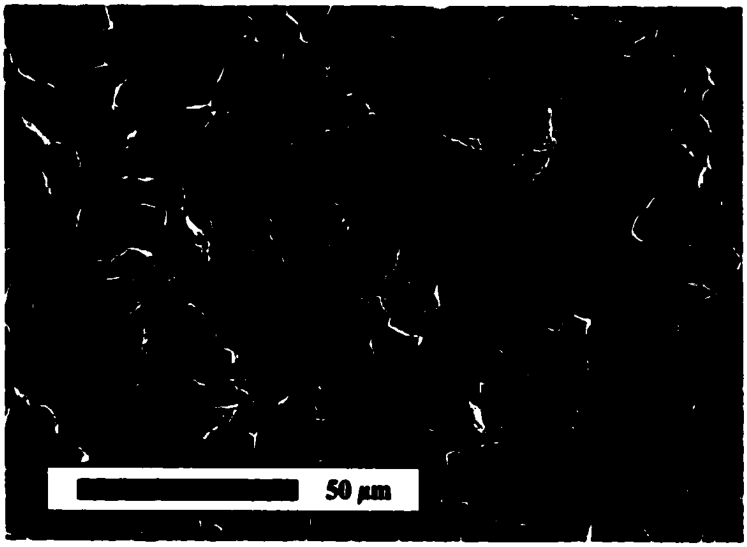

(c)

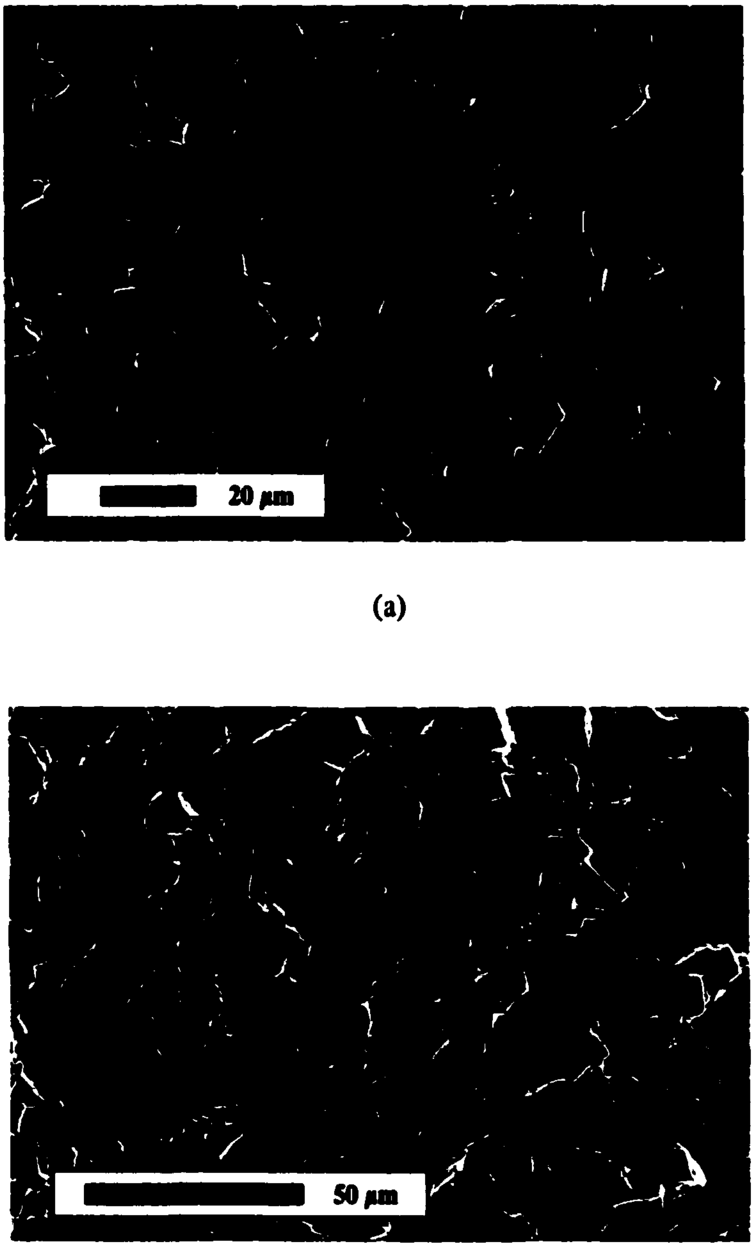

(a)

(b)

Figures 4.4: SEM micrograph of the microstructure of polycrystalline PMN-35PT containing (a) 1 wt% and (b) 5 wt% excess PbO sintered at 1150°C for 0.5 h.

$$r^3 - r_o^3 = 1.05K_m t \qquad \text{Eq. 4.1}$$

where *t* is time and K_m is the kinetic constant which is defined as;

$$K_m = \frac{DS_o M\gamma}{RT\rho c} \qquad \text{Eq. 4.2}$$

In Eq. 4.2, *D* is the diffusion constant, S_o is the equilibrium solubility, *M* is the molar weight, γ is the average surface energy of the matrix grains, *R* is the gas constant, *T* is temperature, ρ is the density of the matrix grains, and *c* is a constant which relates the diffusion layer thickness (δ) to the grain size *r*. The diffusion layer thickness is given by;

$$\delta = cr = \frac{2rV_L}{3V_S} \qquad \text{Eq. 4.3}$$

where *r* is the average radius of matrix grains and V_L and V_S are the liquid and solid volumes, respectively. The matrix grain growth data in Figs. 4.1(a-d) was fit to Lay's model. The kinetic constants (K_m) ranged between 3.0×10^{-21}-1.4×10^{-19} m^3/sec. The model agreed with the data for the times less than one hour for all temperatures and excess PbO concentrations (R^2>0.98). However, the model did not fit the $t^{1/3}$ dependence for the 1150°C data and for all PbO concentrations when a sintering time of five hours was included in the data set.

The variables contained within the constant K_m directly determine the magnitude of the growth rate. By estimating values from published reports for the variables contained within K_m, a theoretical kinetic dependence could be compared to the empirical fit of the Lay model. From published viscosity measurements for molten PbO, diffusion constants between 6.0×10^{-10} m^2/cm and 1.5×10^{-9} m^2/cm were estimated for temperatures between 950°C and 1150°C using the Stokes-Einstein equation.(26) This estimation is valid since it can be assumed that the liquid phase consists primarily of molten PbO. An equilibrium solubility of 3019-5179 kg/m^3 and a c constant of 0.017-0.057 were estimated from the available PMN-PbO phase diagram(18) for excess PbO concentrations of 1, 3, and 5 wt%. The average surface energy was assumed to be $\sim500\times10^{-3}$ J/m^2.(11,27,28) From the estimated values, K_m was calculated to be between 1.0×10^{-17}-1.0×10^{-16} m^3/sec for all temperatures and PbO concentrations. The calculated K_m constants were substituted into Lay's expression and applied to the kinetic data obtained for the matrix growth for 950°C, 1050°C, and 1150°C and excess PbO concentrations of 0, 1, 3, and 5 wt%. The magnitude of the calculated K_m constants from the Lay model exceeded the collected data by at least three orders of magnitude. The deviation of the predicted model is probably due to inaccurate estimates of S_o, c, and/or D which are contained within the kinetic constant. However, it is unlikely that inaccurate estimations of the surface energy, density, molar weight, or even the diffusion coefficient alone would affect the K_m by three orders of magnitude. This issue is further discussed below.

4.3.2 Templated Grain Growth of PMN-35PT from {001}-BaTiO$_3$

The cross-section of a TGG sample heated at 10°C/min to 950°C and then cooled to room temperature without an isothermal hold is shown in Fig. 4.5(a). The sample contained an oriented {001}-$BaTiO_3$ single crystal embedded in a PMN-35PT matrix with 3 wt% excess PbO. The figure shows ~10 μm of growth of a crystal layer on the original {001}-$BaTiO_3$ interface. The crystal layer displays a uniform thickness across the $BaTiO_3$ crystal, indicating that the mobility of the crystal interface is reasonably uniform at these processing conditions and this environment. Fig. 4.5(b) displays a TGG sample of the same composition heated directly to 1150°C and then cooled to room temperature. The crystal layer thickness has extended to ~40 μm. With further annealing time at 1150°C (0.5 h), the crystal layer grew to a thickness of ~75 μm (Fig. 4.5(c)). Within the grown crystal layer for the samples heated to 1150°C, entrapped spherical pores are now present showing that the mobility of crystal interface was greater than the mobility of the coarsening pores in some cases. The variance in etching behavior between the samples processed at various temperatures (Fig. 4.5(a,b)) suggests that there is a compositional difference across the interface indicating that the nucleating composition may not be stoichiometric PMN-35PT. The alteration or absence of this structure for samples treated at higher temperatures implies that the interface becomes more homogenous through the interdiffusion of the chemical species. The difference in etching may also be attributed to the presence or elimination of excess PbO near the sample surface at different processing and etching temperatures. The concentration of excess PbO does affect the etching behavior of PMN-PT. The compositional evolution of the growing single crystal layer will be further discussed in the following sections.

Similar microstructures were observed for all excess PbO concentrations at these temperatures and growth times. The general appearance of the crystal layer grown was

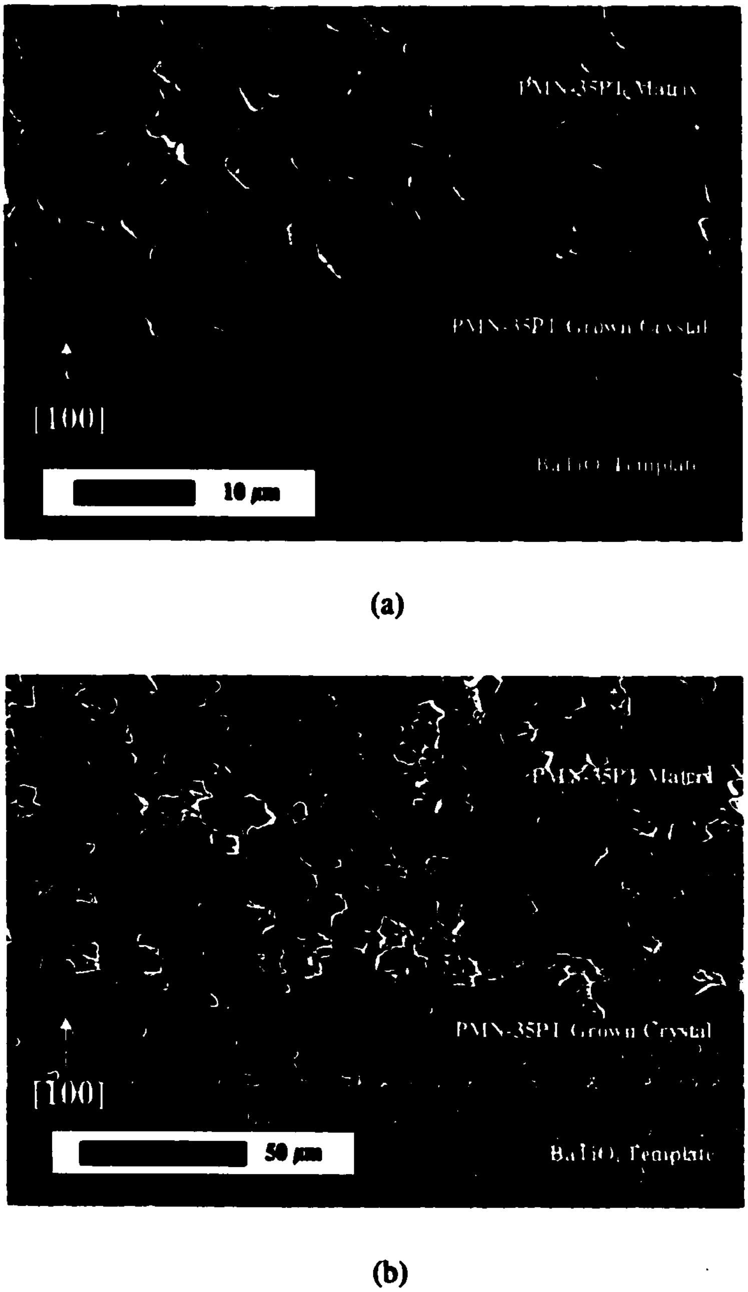

Figure 4.5: SEM micrograph of the Templated Grain Growth of a PMN-35PT single crystal layer on a {001}-$BaTiO_3$ in a PMN-35PT matrix containing 3 wt% excess PbO sintered at (a) 950°C for 0 h., (b) 1150°C for 0 h., and (c) 1150°C for 0.5 h.

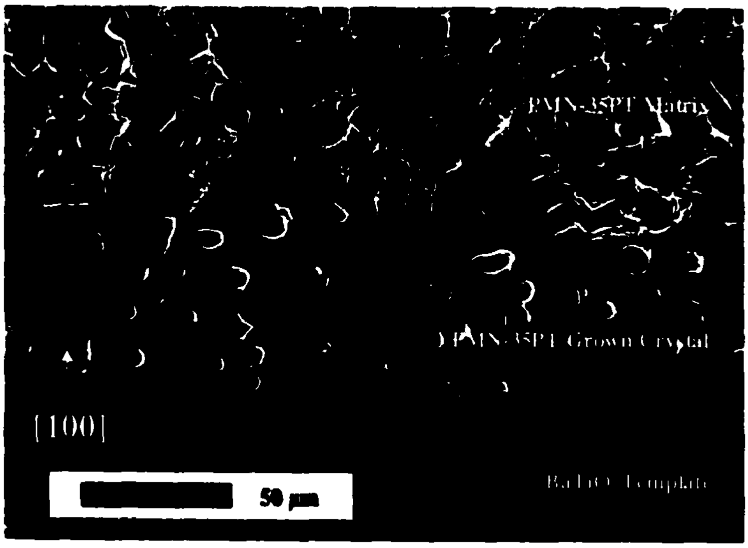
PMN-35PT Matrix
PMN-35PT Grown Crystal
[100]
50 µm
BaTiO3 Template

(c)

similar for all cases. Figs. 4.6(a-c) display the SEM micrographs for TGG samples consisting of a PMN-35PT matrix containing 0, 1, and 5 wt% excess PbO sintered at 1150°C for 0.5 h.

4.3.3 TGG Kinetics from {001}-BaTiO$_3$ Templates

Figure 4.7(a) shows the average growth of the PMN-35PT crystal layer from the original {001}-BaTiO$_3$ interface in 0 wt% excess and 1 wt% excess PbO, for various times and temperatures. The 0 wt% excess PbO sample shows no growth on heating to 950°C, and at this temperature, does not show growth until annealing at 950°C for >1 h. The sample containing 1 wt% excess PbO grows approximately 1 μm during heating to 950°C. The growth saturates quickly to a value of <10 μm with further heating at 950°C. When the 1 wt% excess PbO containing sample is sintered at 1050°C, the templated crystal grows approximately 16 μm during heating and then saturates to approximately 35 μm after 5 h at 1050°C. When the 0 wt% and 1 wt% excess PbO matrix compositions are heated to 1150°C, the crystals grow approximately to 10 μm and 19 μm, respectively, during heating and then continue to grow at a decreasing rate for longer times at 1150°C. This result shows that the addition of just 1 wt% excess PbO to the PMN-35PT increases the growth kinetics ~1.5 times.

Figure 4.7(c) displays the average crystal growth for the samples grown in the presence of 3 wt% excess PbO for the same temperatures and times as the 1 wt% excess PbO samples. The growth distances for the samples containing 3 wt% excess PbO display a similar growth trend as the 1 wt% excess PbO samples, but the magnitude of

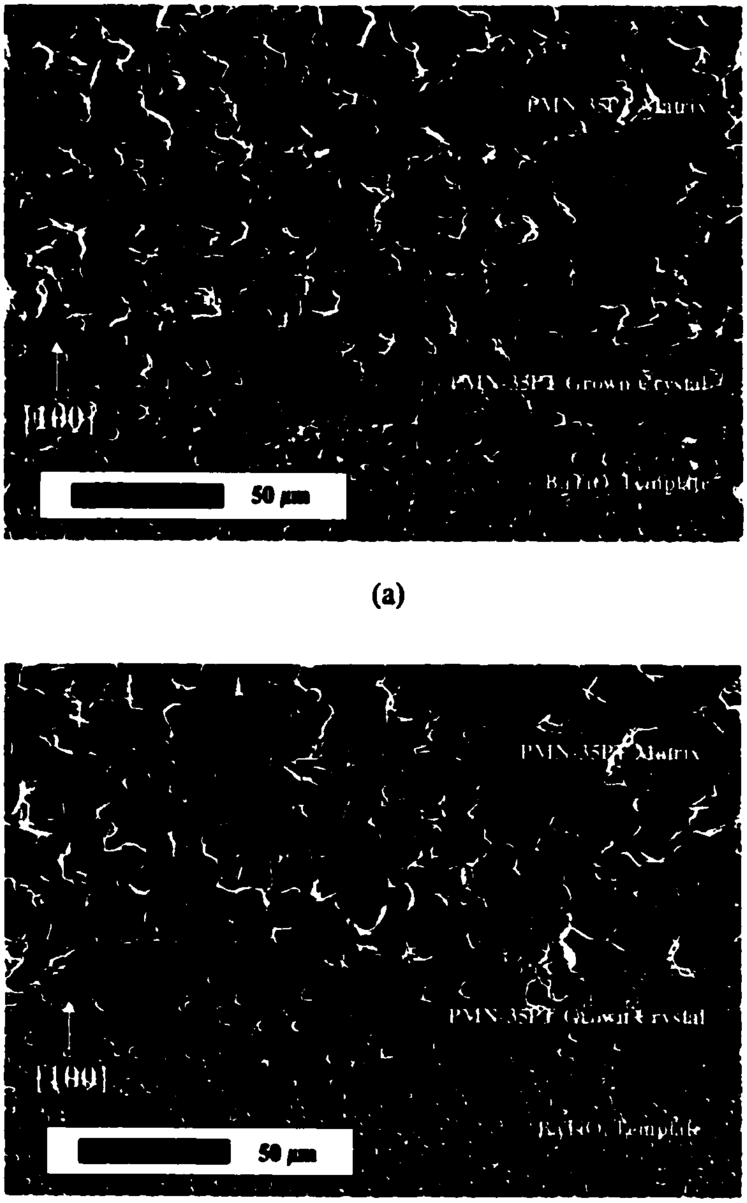

(a)

(b)

Figure 4.6: SEM micrograph of the Templated Grain Growth of a PMN-35PT single crystal layer on a {001}-$BaTiO_3$ in a PMN-35PT matrix containing (a) 0 wt%, (b) 1 wt%, and (c) 5 wt% excess PbO sintered at 1150°C for 0.5 h.

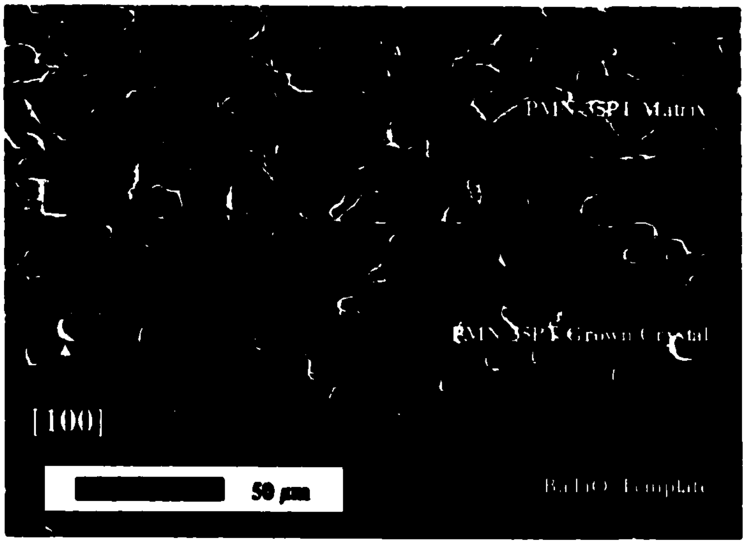
PMN-35PT Matrix
PMN-35PT Grown Crystal
[100]
50 μm
BaTiO3 Template

(c)

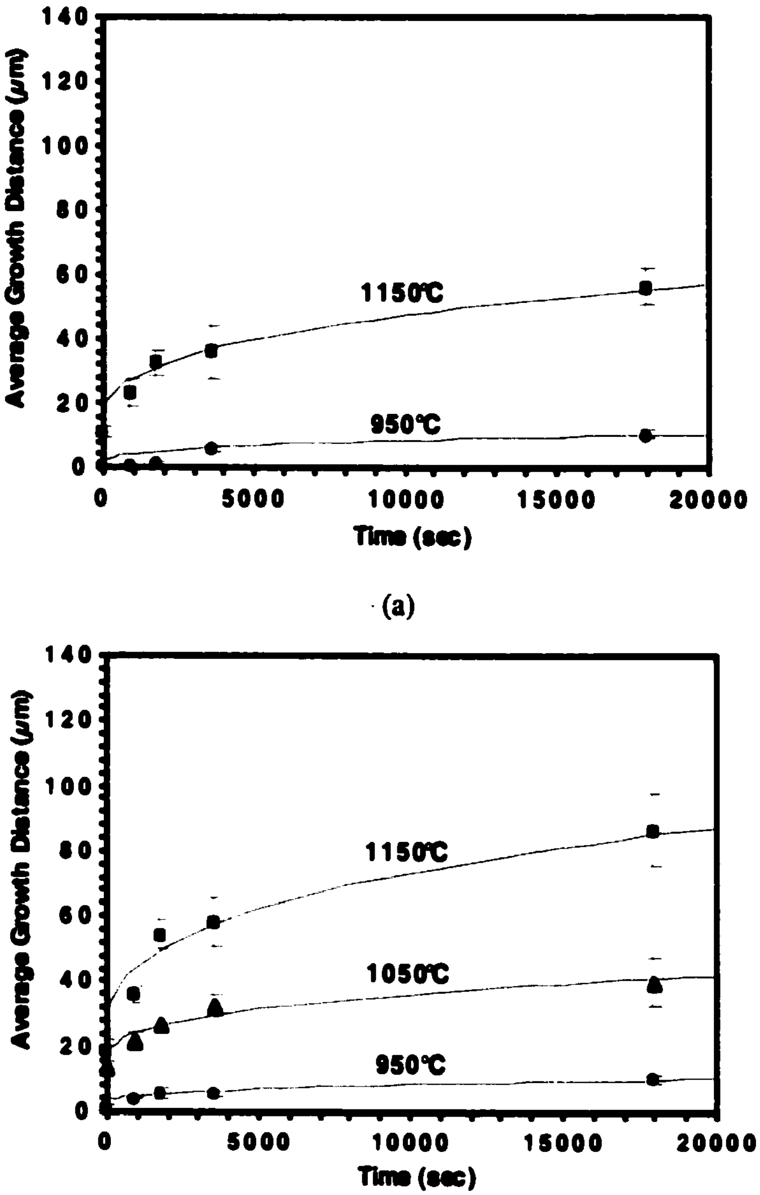

(a)

(b)

Figure 4.7: Templated grain growth of PMN-35PT from {001}-$BaTiO_3$ template crystals with a composition containing (a) 0 wt%, (b) 1 wt%, (c) 3 wt%, and (d) 5 wt% excess PbO. (The solid line is the fitted Seabaugh *et al.* model.)

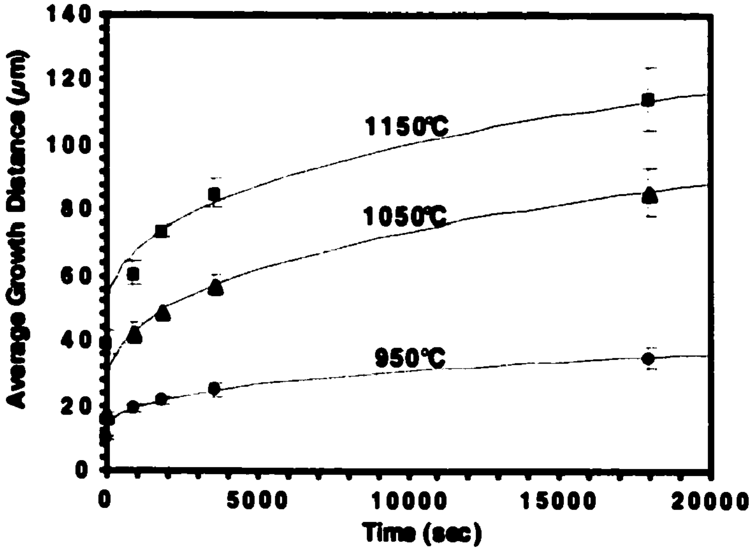
140
120
100
80
60
40
20
0
Average Growth Distance (μm)
0
5000
10000
15000
20000
Time (sec)
1150°C
1050°C
950°C

(c)

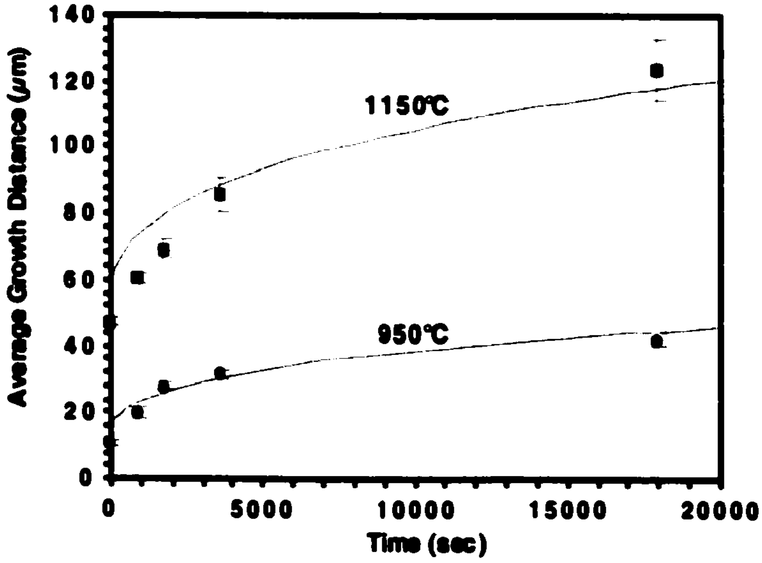
140
120
100
80
60
40
20
0
Average Growth Distance (μm)
0
5000
10000
15000
20000
Time (sec)
1150°C
950°C

(d)

growth is higher for all temperatures. The 3 wt% excess PbO samples show an initial growth of approximately 10 μm during heating to 950°C, which then saturates at 20 μm for longer sintering times. This value is 10 μm greater than that shown by the 1 wt% excess PbO samples fired at 950°C. The growth for the 3 wt% excess PbO samples at temperatures of 1050°C or 1150°C is 20 μm greater than the values displayed for the same temperatures for the 1 wt% excess PbO samples. This result indicates that the increase in the grain boundary thickness due to the increase of liquid phase volume did not significantly inhibit the growth of the crystal.

The magnitude and trend for the growth of PMN-35PT single crystal in the presence of 5 wt% excess PbO was similar to the samples containing 3 wt% excess PbO (Fig. 4.7(d)). Therefore, it may be concluded that the mechanism of growth is altered between liquid phase contents of 1 wt% and 3 wt% excess PbO. At compositions greater than 5 wt% excess PbO, the growth mechanism may remain constant, although the growth rate may vary due to the alteration in grain boundary thickness as a result of the higher volume of liquid phase.

The Hennings *et al.* model(28) considered that growth of exaggerated grains was controlled by the supersaturation of the intergranular liquid phase, which completely separated the matrix grains from each other and from the growing exaggerated grains. The environment described by Hennings is analogous to the PMN-PT system when the grain boundaries are completely saturated with the PbO-rich liquid. In the Hennings *et al.* model, the growth rate of the large grains is driven by a constant gradient composed of the difference in solubility between the exaggerated grain and the matrix (i.e. supersaturation). The Hennings *et al.* equation is;

$$\frac{dL}{dt}=\frac{D\Delta S}{\delta\rho}=\frac{DS_o}{\delta\rho}\left((1-k_{hkl})+\frac{2\gamma M}{\rho RTr}\right) \qquad \text{Eq. 4.4}$$

where ΔS is defined as the difference in solubility between the exaggerated grain and average matrix grains, and k_{hkl} is defined as;

$$k_{hkl}=\frac{S_{hkl}}{S_o} \qquad \text{Eq. 4.5}$$

where S_{hkl} is the solubility of a specific crystal surface orientation and S_o is the equilibrium solubility.

In this study, the growth kinetics of the {001}-single crystal PMN-35PT layer did not display a linear relationship (L=kt) as predicted by Hennings and other authors(29,30) for the growth of single crystal within a polycrystalline matrix. The single crystal growth process also did not display parabolic kinetics ($L=kt^{1/2}$) which is typical of a reaction- or interface-controlled mechanism.(31)

Seabaugh *et al.*(13) concluded that the Hennings *et al.* model could be applied to the growth of a single crystal within a ceramic matrix containing an intergranular liquid phase. However, they believed it was necessary to account for the non-constant driving force throughout the growth process due to the coarsening of the matrix grains and subsequent change in supersaturation within the liquid phase system. Seabaugh *et al.* combined Lay's expression (Eq. 4.1) and the Hennings' expression (Eq. 4.4). to give the following expression for single crystal growth in a coarsening matrix;

$$L_t - L_o = 5.81 K_m^{1/3} t^{1/3} + 1.48 K_m^{2/3} \left(\frac{\rho RT}{M\gamma} (1 - k_{hkl}) \right) t^{2/3} \qquad \text{Eq. 4.6}$$

where L_t is the crystal growth thickness and L_o is the original crystal growth thickness at time "zero". K_m is the same kinetic constant that is contained within the Lay expression.

Because the Lay model fit the matrix grain growth kinetics for times <1 h at 1150°C for all excess PbO concentrations (R^2>0.98), it is reasonable to apply the Seabaugh *et al.* expression (Eq. (4.6)) to the TGG of the PMN-35PT single crystal layer for growth times <1 h. In Figs. 4.7(a-d), the Seabaugh *et al.* model was best fit to the collected TGG data (R^2>0.98). The kinetics for the samples containing 0 wt% excess PbO sintered at 1150°C were better fit to the Seabaugh *et al.* expression (R^2~0.986) than to a $t^{1/2}$ dependence (R^2~0.968). The solubility constant, k_{hkl}, was assumed to have a value of 1, since the equilibrium solubility (S_o) should be similar to the solubility of the {001}, which is the lowest energy plane for the perovskite structure of PMN-35PT. By applying this assumption, the resulting equation displays a $t^{1/3}$ relation between the growth distance (L_t) and time (t). This $t^{1/3}$ dependence is characteristic of a diffusion-controlled mechanism for grain growth in the presence of a liquid phase. The correlation between the kinetics of the 0 wt% excess PbO sample (where little liquid-phase is present) with the $t^{1/3}$ relation is not well understood. A liquid phase may always be present in the PMN-PT system due to the metastable formation of a fine liquid layer within the grain boundaries due to incorporation of a small amount PbO from the environment. In these experiments, L_o was assumed to be the crystal thickness at time "zero" of the isothermal hold. This normalizes the initial growth during heating for all growth trends. The kinetic constants, K_m, calculated from the fitted equations, are comparable to those calculated for matrix grain growth. The calculated K_m values are displayed in Table 4.1. The K_m values decrease from 1.15×10^{-19} m^3/sec to 1.55×10^{-22} m^3/sec with decreasing temperature and decreasing amounts of excess PbO.

The morphology of the growing crystal further supports the proposed diffusion-controlled growth mechanism. SEM micrographs showing the interface between the matrix grains and growing crystal layer of samples containing 1 wt% and 3 wt% excess PbO are shown in Figs. 4.8(a,b) and Figs. 4.9(a,b), respectively. The micrographs for the 1 wt% and 3 wt% excess PbO samples sintered at 950 °C for 15 min. display some curvature at the crystal interface with the matrix ((Fig. 4.8(a), Fig. 4.9(a)). The matrix grains, for both matrix compositions, display a spherical type morphology after limited grain growth from the starting grain size (~0.8 μm). The presence of curvature at the crystal/matrix boundary is physical evidence of diffusion-controlled grain growth at these growth conditions.

When the same sample compositions are sintered at 1150 °C for 15 min., the curvature of crystal/matrix interface decreased, but the PMN-PT crystal still did not show a distinct facet (Fig. 4.8(b), Fig. 4.9(b)). The shape alteration of the crystal/matrix boundary appears to be the result of a change in the morphology and size of the matrix grains that are in contact with the crystal. The matrix developed an angular shape during heating above 950 °C, substantially reducing the matrix grain curvature. In the presence of the intergranular PbO-based liquid phase, the matrix grains appear to be proceeding towards the stable {001}-faceted cubic shape for the perovskite structure, but either due to grain impingement or inhomogeneous solid/liquid interaction, the cubic shape was not

Table 4.1: Kinetic constants (K_m) calculated from the Seabaugh *et al.* model fit to the collected TGG data.

Excess PbO Concentration

Temperature (°C)	0 wt%	1 wt%	3 wt%	5 wt%
1150	2.50×10^{-20}	8.19×10^{-20}	1.15×10^{-19}	1.00×10^{-19}
1050		5.73×10^{-21}	9.21×10^{-20}	
950	2.50×10^{-22}	1.55×10^{-22}	4.46×10^{-21}	1.12×10^{-20}

units= m^3/sec

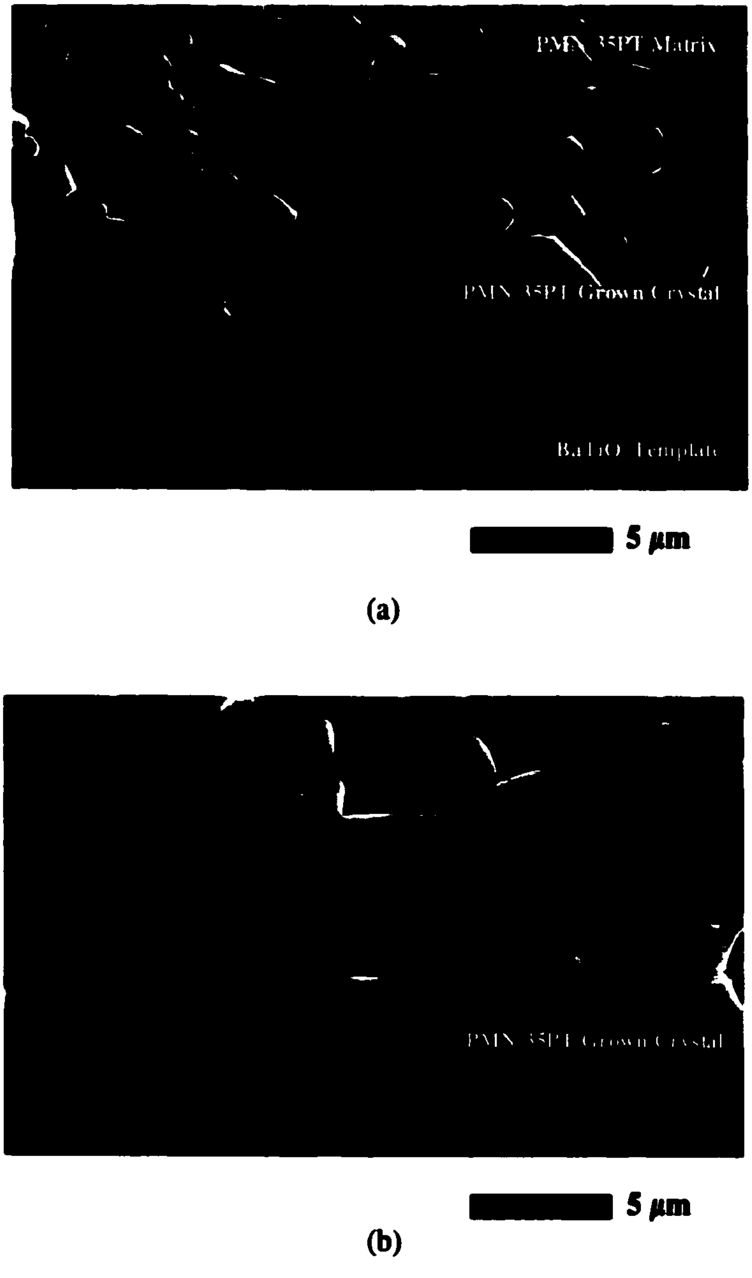

Figure 4.8: SEM micrograph of the Templated Grain Growth of a PMN-35PT single crystal layer on a {001}-BaTiO$_3$ in a PMN-35PT matrix containing 1 wt% excess PbO sintered at (a) 950°C for 15 min. and (b) 1150°C for 15 min.

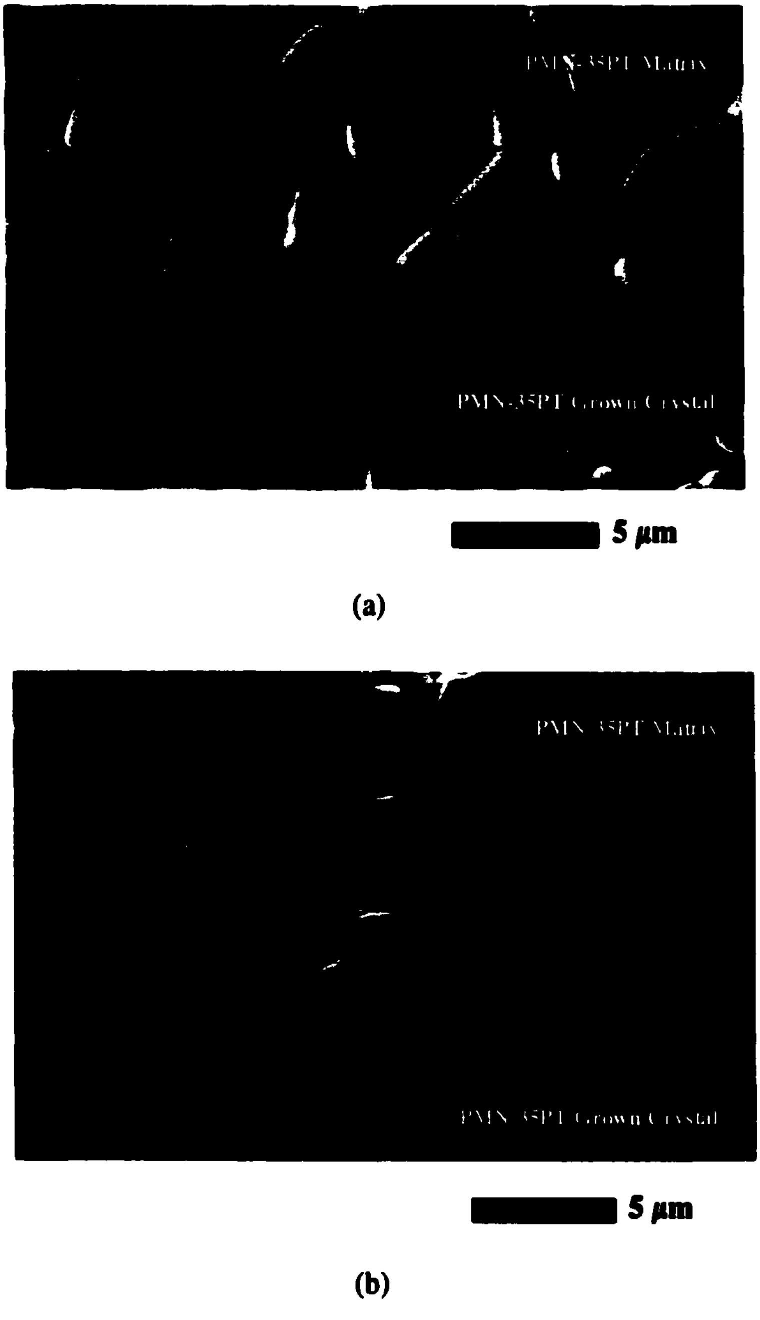

Figure 4.9: SEM micrograph of the Templated Grain Growth of a PMN-35PT single crystal layer on a {001}-$BaTiO_3$ in a PMN-35PT matrix containing 3 wt% excess PbO sintered at (a) 950°C for 15 min. and (b) 1150°C for 15 min.

attained. It is reasonable that the solid/liquid phase reaction (dissolution/precipitation process) would not be homogeneous across a stable faceted plane in the PMN-PT system. As a consequence of the chemical variance of the off-valent Mg and Nb ions residing in the *B*-sites of the PMN-PT perovskite structure, there would be uncompensated charge distributed across the planes which may induce preferential nucleation in isolated locations.(32,33) Therefore, stable planes like the {001} may show a distribution in localized surface energy values allowing for multiple nucleation sites across the plane.(26,34,35)

The change in the matrix grain morphology displayed in Fig. 4.8 and Fig. 4.9 would decrease the average surface energy of a grain, since many of the high energy planes were eliminated during the grain growth. The matrix supersaturation or solubility (S_m) at a given temperature is dependent primarily on the grain size and the average surface energy of the grain as dictated by the Gibbs-Thomson equation. Therefore, the decrease in surface energy would effectively decrease the matrix solubility, causing the matrix kinetics to deviate from Lay's grain growth equation due to the non-steady state kinetics constant. This scenario may be an additional cause for the departure of the PMN-PT matrix kinetics from that predicted by Lay's expression, since the growth kinetics was fitted with a singular kinetic constant. A change in matrix solubility due to a change in surface energy would have a greater effect on the matrix growth kinetics than on the crystal growth kinetics since the relative difference between the average grain size of the matrix and the individual matrix grains is small compared to that of the template crystal.

4.3.4 TGG Kinetics from {110}- and {111}-$BaTiO_3$ Templates

The same TGG experiments performed with {001}-$BaTiO_3$ template crystals were completed using {110}- and {111}-$BaTiO_3$ crystals obtained from crystals donated by Lockheed-Sanders. The crystals were cut to the same dimension as the {001}-$BaTiO_3$ crystals used in the previous TGG experiments. The crystals were embedded and sintered in the same manner. These crystals were embedded only in a PMN-35PT matrix containing 3 wt% excess PbO and sintered for times ≤ 1 h at 950°C and 1150°C.

Figure 4.10(a) is an SEM micrograph showing the cross-section of a TGG sample containing an embedded {110}-$BaTiO_3$ crystal heated to 950°C and then cooled to room temperature. The initial growth of the crystal layer is not planar like that seen for the {001}-$BaTiO_3$ crystal. The cross-sectional cut of the crystal interface is composed of non-parallel crystal faces which form multiple triangles of various sizes connected along the length of the {110}-$BaTiO_3$ template crystal. The angle of the triangles are not consistent. The appearance of these multiple triangular sites suggest that nucleation of the crystal layer occurred in various locations across the template crystal at various times, and with further growth, these nuclei coalesced and formed a single covering layer across the template crystal. Fig. 4.10(b) and Fig. 4.10(c) further supports this by showing the elimination of the number of non-parallel faces with further growth at 1150°C.

The growth of the single crystal layer from the {111}-$BaTiO_3$ template crystal was similar to that of the {110}-crystal (Figs. 4.11(a-c)). At temperatures <950°C, the crystal layer initially nucleated in separate locations across the template. In the cross-sectional view of the TGG sample heated to 950°C (Fig. 4.11(a)), the various crystal

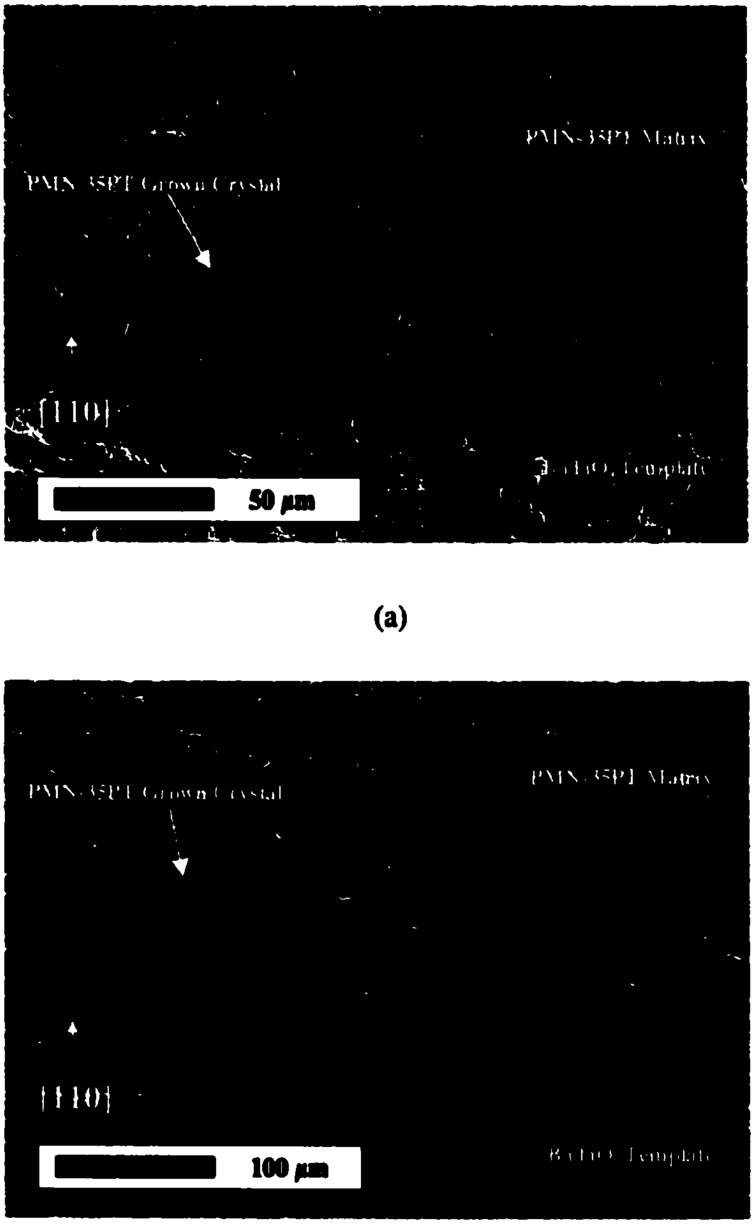

(a)

(b)

Figure 4.10: SEM micrograph of the Templated Grain Growth of a PMN-35PT single crystal layer on a {110}-$BaTiO_3$ in a PMN-35PT matrix containing 3 wt% excess PbO sintered at (a) 950°C for 0 h., (b) 1150°C for 0 h., and (c) 1150°C for 0.5 h.

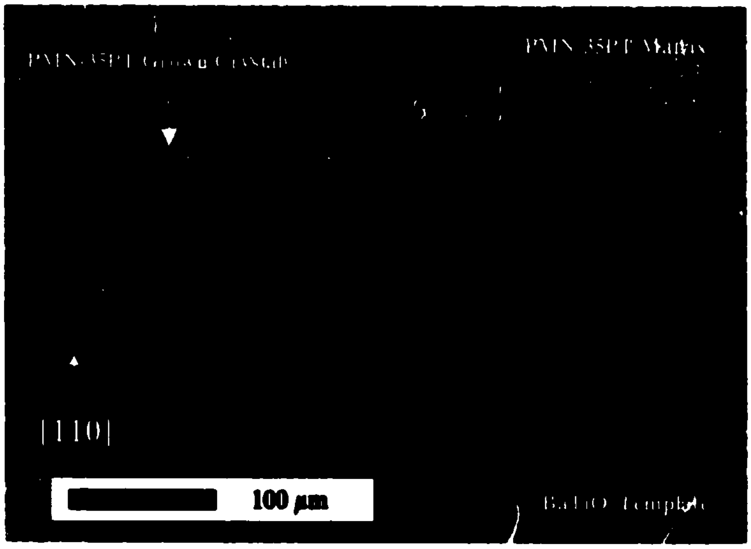
PMN-35PT Grown Crystal
PMN-35PT Matrix
[110]
100 µm
BaTiO3 Template

(c)

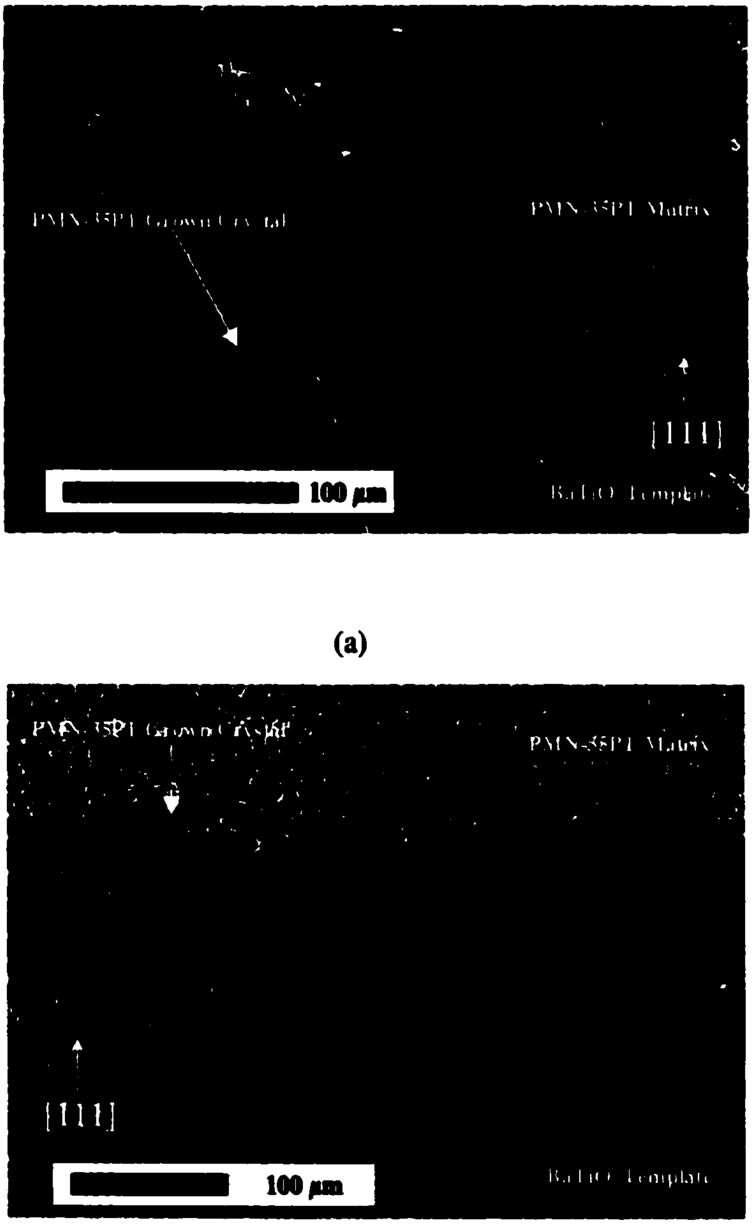

(a)

(b)

Figure 4.11: SEM micrograph of the Templated Grain Growth of a PMN-35PT single crystal layer on a {111}-$BaTiO_3$ in a PMN-35PT matrix containing 3 wt% excess PbO sintered at (a) 950°C for 0 h., (b) 1150°C for 0 h., and (c) 1150°C for 0.5 h.

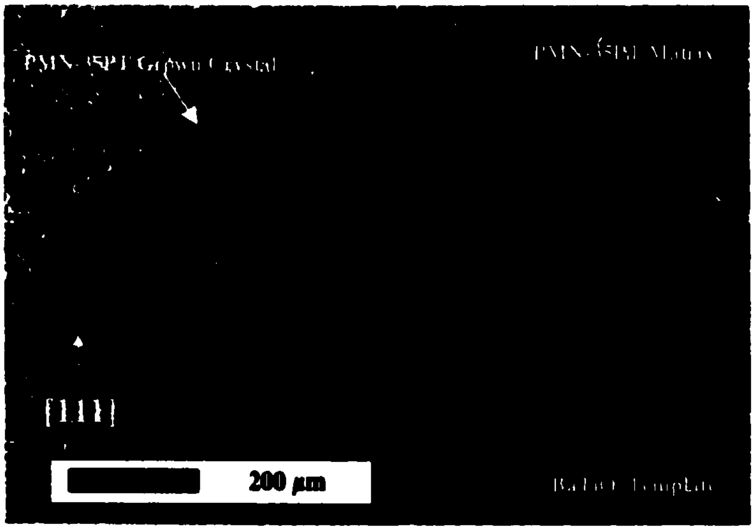
PMN-35PT Grown Crystal
PMN-35PT Matrix
[111]
200 µm
BaTiO3 Template

(c)

growth sites are represented as triangular features along the {111}-template. The size and peak angle are different for each of the crystal features. With further heating at higher temperatures (1150°C), the separate growth sites coalesce into a continuous crystal layer across the template crystal (Figs. 4.11(b,c)). The structure of the crystal interface changes with further growth, where the number of the triangular sites decreases and the size of the remaining sites increases.

By the micrographs of the cross-sectioned TGG samples, it appears that the {110}- and {111}-crystals show similar nuclei and growth shape. The ability to observe the topographical morphology of the growing {110}- and {111}-crystal face is difficult in the TGG samples, since the template and growing crystal are embedded within the dense PMN-PT matrix. The removal of the intergranular PbO-based liquid phase and matrix material by various etches resulted in the alteration and degradation of the PMN-PT crystal interface. The optical micrographs, which were presented in Chapter 3, show that the {110} and {111} template crystals display a rectangular and triangular shape, respectively, when the crystals are grown on the surface of the sample (Figs. 3.18(a,b)). This suggests that the crystal(s) growing from the {110}-template have a triangular prism shape (Fig. 4.12(a)) which would maintain the two-fold symmetry imposed by the crystal symmetry for prototype perovskite structure (m3m). The triangular shape at the surface of the sample would indicate that the crystal(s) are growing in a triangular pyramid shape (Fig. 4.12(b)) from the {111}-crystal template, thus, the crystal(s) are assuming the 3-fold symmetry dictated by the m3m symmetry.

Figures 4.13(a,b) compares the crystal growth kinetics of TGG samples containing {001}-, {110}-, and {111}-$BaTiO_3$ crystals embedded in a PMN-35PT matrix

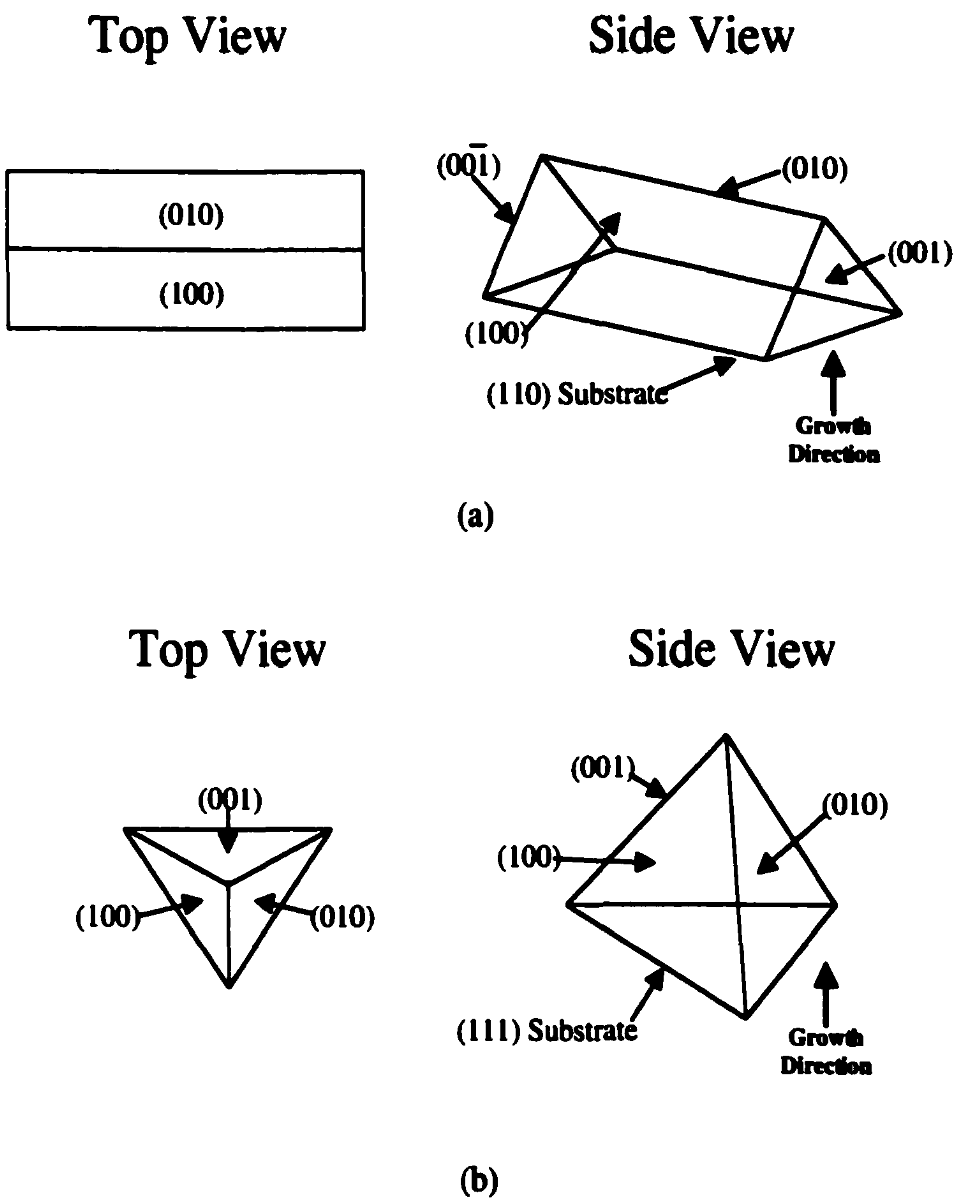

Figure 4.12: Schematic of the habit formation of a PMN-PT crystal growing from an a) {110}- and b) {111}-$BaTiO_3$ template.

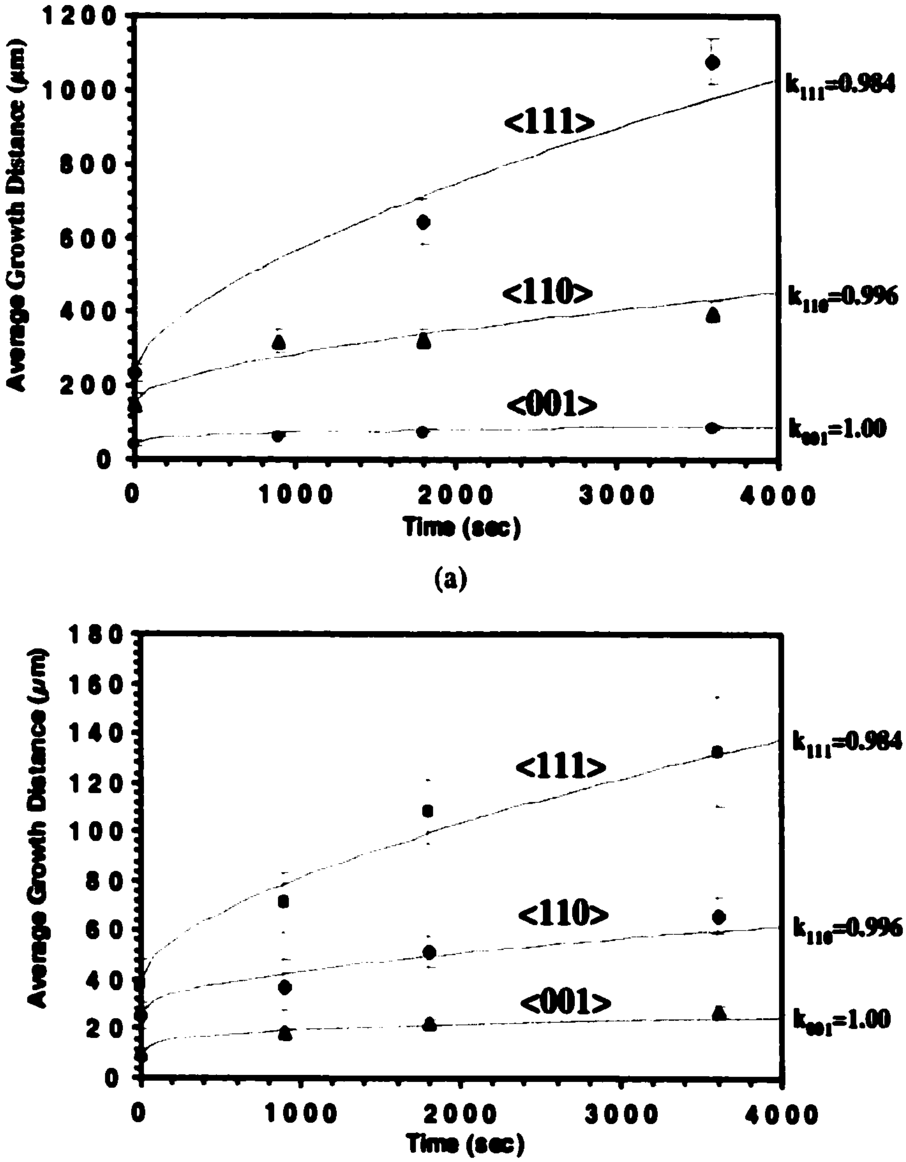

(a)

(b)

Figure 4.13: Templated grain growth of PMN-35PT from {001}-, {110}-, and {111}-$BaTiO_3$ template crystals with a composition of 3 wt% excess PbO sintered at (a) 950 °C and (b) 1150 °C. (The solid line is the fitted Seabaugh *et al.* model.)

with 3 wt% excess PbO sintered for ≤1 h at 950°C and 1150°C, respectively. The average growth distance of the PMN-PT crystal layer was measured every 20 μm along the length of the $BaTiO_3$ template crystal. Since the crystal layer grown from both the {110}- and {111}-crystals did not show a planar topology, the sample had to be sectioned at the point of maximum crystal growth. This was especially important for the {111}-crystal due to the triangular-pyramid growth facet of this orientation. The maximum growth distance from the {110}-crystal was easier to observe since any cross-section of a triangular-prism perpendicular to the prism base would reveal the same distance. The location of the template crystal center was marked on each sample and cross-sectioned at this location after the growth. The growth distance was observed for each sample cross-section after multiple successive polishings in order to view the maximum extent of growth.

At a growth temperature of 950°C, the PMN-PT crystal layer grew at a higher average rate in the <110> than in the <001> (~3.5 times faster). The <111> grew at an average rate that was at least 9.6 times greater than the <001> (Fig. 4.13(a)). The growth rate from both the {001} and the {110} began to quickly saturate after reaching 950°C, but the crystal layer continued to grow without saturating in the [111]. When the same samples where heated to 1150°C, the crystal layer grew an average of 8.7 and 24.1 times faster than the <001> in the <110> and <111>, respectively (Fig. 4.13(b)). Again, the crystal layer growth rate began to saturate for the {001} and {110} planar orientations after reaching the sintering temperature, but the crystal layer continued to grow from the {111}-crystal without a significant decrease in rate.

The Seabaugh *et al.* model was best fit for the growth kinetics of the PMN-PT crystal layer from the {110}- and {111}-$BaTiO_3$ template crystals in a PMN-35PT matrix containing 3 wt% excess PbO. The kinetic constants for the matrix growth (K_m) at 950°C and 1150°C, reported in Table 4.1 for the growth from the {001} template crystal, were substituted into Eq. 4.6. The kinetics equation was then fit to crystal growth trends from the {110} and {111} planar orientations by altering the solubility constant (k_{hkl}). The solubility constant accounts for the differences in localized solubility along various crystal planes relative to the equilibrium solubility (Eq. 4.5).(13) The solubility of a crystal plane reflects the ionic bonding and packing character of the plane, which would be different for the various orientations. The solubility constant was previously assumed to equal 1.0 for the {001} planar orientation at all temperatures and excess PbO concentrations. At 950°C, the solubility constants were found to equal 0.996 and 0.984 for the {110} and {111}, respectively (R^2>0.98). The same solubility constants were found to best fit the Seabaugh *et al.* model to the collected data for crystal growth at 1150°C. The fit confidence for the growth from the {110} remained the same, but the fit for the {111} decreased to an R^2≈0.95. The change in fit for the {111} at higher temperature is probably due to the difficulty in obtaining a representative micrograph of the full growth distance due the macroscopic crystal faceting into the triangular-pyramid shape after extensive growth and coalescence (Fig. 4.11(b,c)).

The lower solubility constants indicate that the {110} and the {111} plane have a lower solubility than the {001} plane in the available PbO-based liquid phase. Since the proposed growth mechanism is driven by the solubility gradient between the average matrix grains (S_m) and the crystal (S_{hkl}), then the greater difference in solubilities ($\Delta S = S_m - S_{hkl}$) would provide a greater driving force for transport and growth. Therefore, the lower solubility of the {111} plane would produce a greater solubility gradient than the other orientations, resulting in higher growth kinetics. As expected, the magnitude of the solubilities directly reflects the bonding character of these crystal planes in the perovskite crystal structure. The plane which shows the highest planar density and the strongest planar bonding would display the lowest solubility.(26) Assuming the prototypical perovskite structure with an average lattice parameter of 4.0 Å, the {111} has the highest planar packing density (0.144 ions/ $Å^2$) followed by the {110} (0.133 ions/ $Å^2$) and the {001} (0.125 ions/ $Å^2$). Therefore, the projected solubilites correlate well with the structure of the corresponding planes.

Crystal habit formation can be attributed to either the equilibrium surface energy of the crystal or the kinetics of the growth process.(36) The Seabaugh *et al.* model does not fully describe the effect of planar surface energy on the {001}-habit formation of PMN-PT, since the model focuses on the kinetics issues related to ionic transport in the liquid medium. The difference in surface energy between the crystallographic planes is only accounted in the difference in solubilities as defined by the Gibbs-Thomson equation. The surface energy plays a larger role in the thermodynamic issues relating to the formation of a stable nuclei and the final crystal habit.(37) Therefore, the effect of ionic attachment and thermodynamic stability of the planes are missing in the description of the TGG of PMN-PT. It is difficult to attribute the final formation of the {001}-habit to thermodynamic or kinetic contributions.

The magnitude of surface energies is commonly correlated to the planar density of uncompensated bonds (broken bonds) per area along the crystallographic plane.(26,34) When all cationic bonds are assumed to be equal in strength, the {111}-, {110}-, and {001}-planes have a broken bond density of 0.325 bonds/Å^2, 0.354 bonds/ Å^2, and 0.313 bonds/ Å^2, respectively. These bond densities are calculated for a unit cell with a= 4.0 Å. The high uncompensated bond density of the {110} makes this plane the most thermodynamically unstable, while the {001} would be the most stable. If the growth of the crystal is entirely controlled by ionic attachment, the {001} plane would be the slowest growing plane due to the low broken bond density. Many materials with the perovskite structure are commonly associated to crystals which exhibit a cubic morphology displaying {001} habits, especially in cases when the ionic adsorption and attachment to the crystal surface limits the growth.(26,38) Other crystal morphologies are displayed for perovskite compositions when the growth is controlled by defects like penetrating or lamellar twins along the [110] and/or [111].(26,38)

Comparing the broken bond density is not sufficient to explain the macroscopic habit formation of the {001} in PMN-PT/PbO system. It is more important to look at the type and number of bonds which are broken per area for each atomic plane in the perovskite structure.(26,35,38) The (111) has 0.108 B-O bonds/Å^2 (B-oxygen ion bonds/area) and 0.217 A-O bonds/Å^2 (A-oxygen ion bonds/area) broken. The (110) has 0.088 B-O bonds/Å^2 and 0.265 A-O bonds/Å^2 and the (001) has 0.063 B-O and 0.25 A-O bonds/Å^2 broken. This simple prediction assumes that the crystal terminates with the plane indicated and not other integer planes which may present a different ionic arrangement. The (200) and (222) planes have the same total and type of broken bonds as the (100) and (111) planes, respectively, therefore these orientations do not present alternative bonding arrangements. The (220) has 0.177 *B-O* bonds/Å^2 and 0.088 *A-O* bonds/Å^2, which is different than the (110) plane and greater than that shown by the (111). In the case where the {110} cut terminated with the (220) plane, then the growth kinetics may be greater than that displayed by the (111).

Since the *B*-site in the perovskite structure is coordinated by 6 ions (CN=6) and has a +4 charge, its electrostatic bond strength (charge/CN) is ~1.33. The *A*-site has an electrostatic bond strength of ~0.33 (CN=12, +2 charge). Therefore, the (111) would be lacking a greater number of higher energy, stronger bonds/area which would increase the ability for the diffusing ions to adsorb and attach. In descending order, the (110) and (001) have the next greatest number of absent *B-O* bonds/area. The difference in the number of missing *B-O* bonds/area may account for the {001}-habit formation of the PMN-PT crystals and grains, since the adsorption, surface diffusion, and final attachment of the ions would be affected by the total potential bond strength of the plane. As discussed in the last subsection, this issue is even more complex for the PMN-PT system since the *B*-sites contain a high concentration of off-valent ions which have a mixed valence of +2 and +5 charge, resulting in variable distribution of electrostatic bond strengths across the crystal planes. The solvation character (adsorption and attachment) of the *B*-site ions will be dependent upon these localized electrostatic attractions which are affected by both short- and long-range neighbor interactions.(26,35,38)

4.3.5 Compositional Evolution of the Crystal Layer During TGG

The variance in etching behavior of TGG samples processed at different temperatures suggests that there is a difference between the composition of the initial nucleating crystal and the final crystal grown at high temperature. Fig. 4.14 shows the SEM micrograph and EDS patterns of the templated crystal growth from a {001}-$BaTiO_3$ crystal in matrix composition of 3 wt% excess PbO which was heated to 950°C at 10°C/min. and then quenched in air. The sample was sectioned, polished, and cleaned, but never etched in order to preserve the sample surface. The resolution and sensitivity limits of the EDS system are stated in Chapter 3. The EDS pattern shows that at a distance of ~1 μm within the $BaTiO_3$ crystal, the composition appeared to be qualitatively $BaTiO_3$. At a distance of ~1 μm outside the $BaTiO_3$ crystal, the composition was similar to the composition displayed at a distance of ~4 μm from the interface. The EDS pattern observed at 1 μm and 4 μm are identical to that obtained from the PMN-32.5PT matrix. Fig. 4.15 shows an EDS elemental map of the same sample near the crystal interface taken over a two minute scan. The patterns show the chemical stability of the two phases at this temperature. These results indicate that the growing crystal has a PMN-PT based composition and there seems to be little interdiffusion between the template and the crystal layer when thermally processed to 950°C. The precision of the chemical measurements was limited by the resolution of EDS.

The TGG sample thermally treated to 950°C represents the beginning stage of the growth process. Fig. 4.16 shows a cross-sectional SEM micrograph and EDS patterns of a TGG sample annealed at 1150°C for 1 h. The TGG sample thermally treated at this

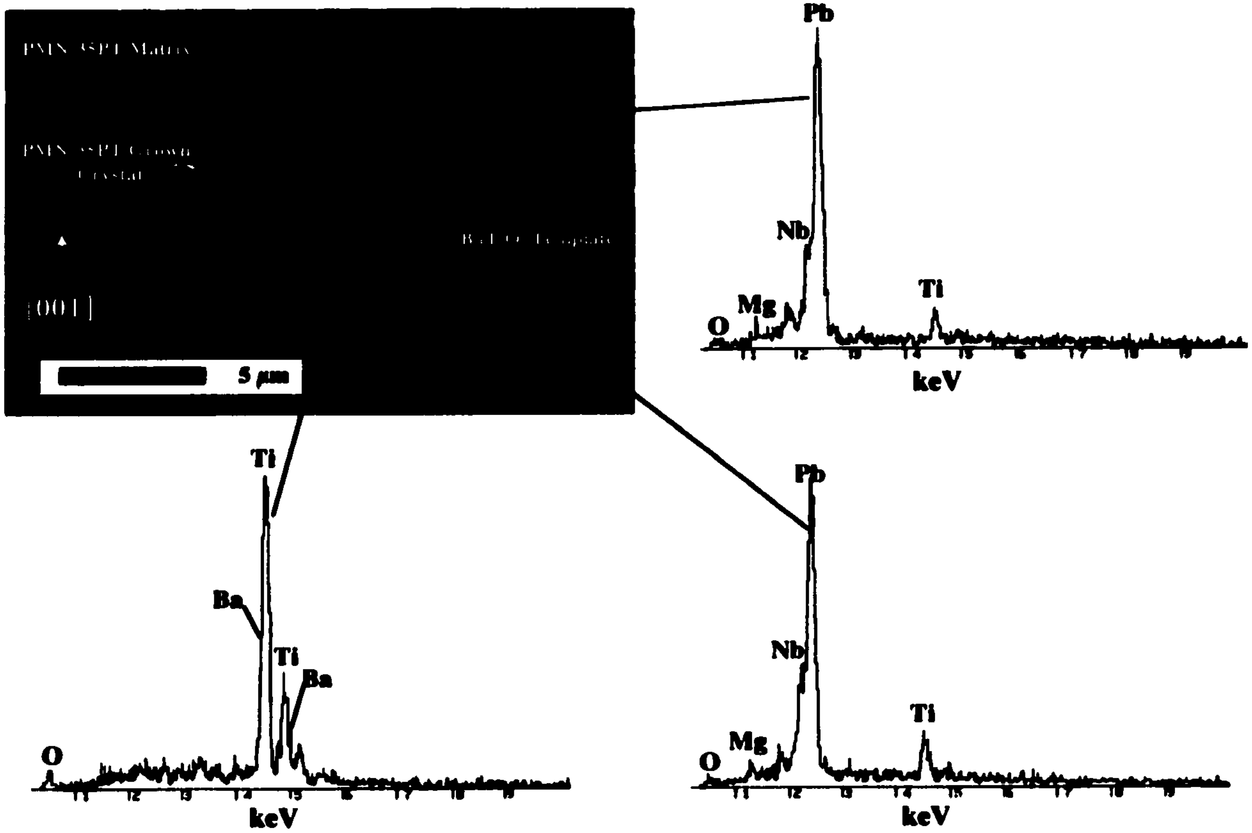

Figure 4.14: SEM micrograph and EDS patterns at the template/grown crystal interface of a PMN-35PT TGG sample containing a {001}-$BaTiO_3$ template and 3 wt% excess PbO heated to 950°C and quenched in air.

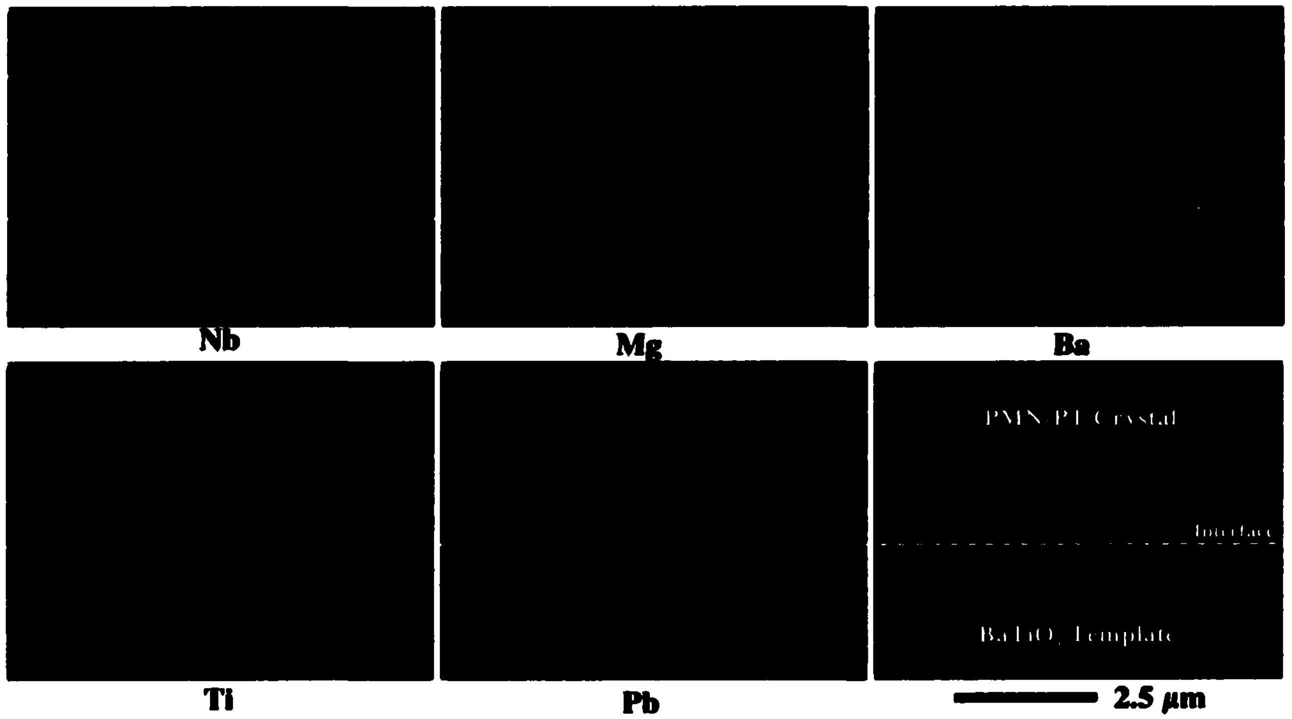

Figure 4.15: EDS elemental map of the template/grown crystal interface of a PMN-35PT TGG sample containing a {001}-$BaTiO_3$ template and 3 wt% excess PbO heated to 950°C and quenched in air.

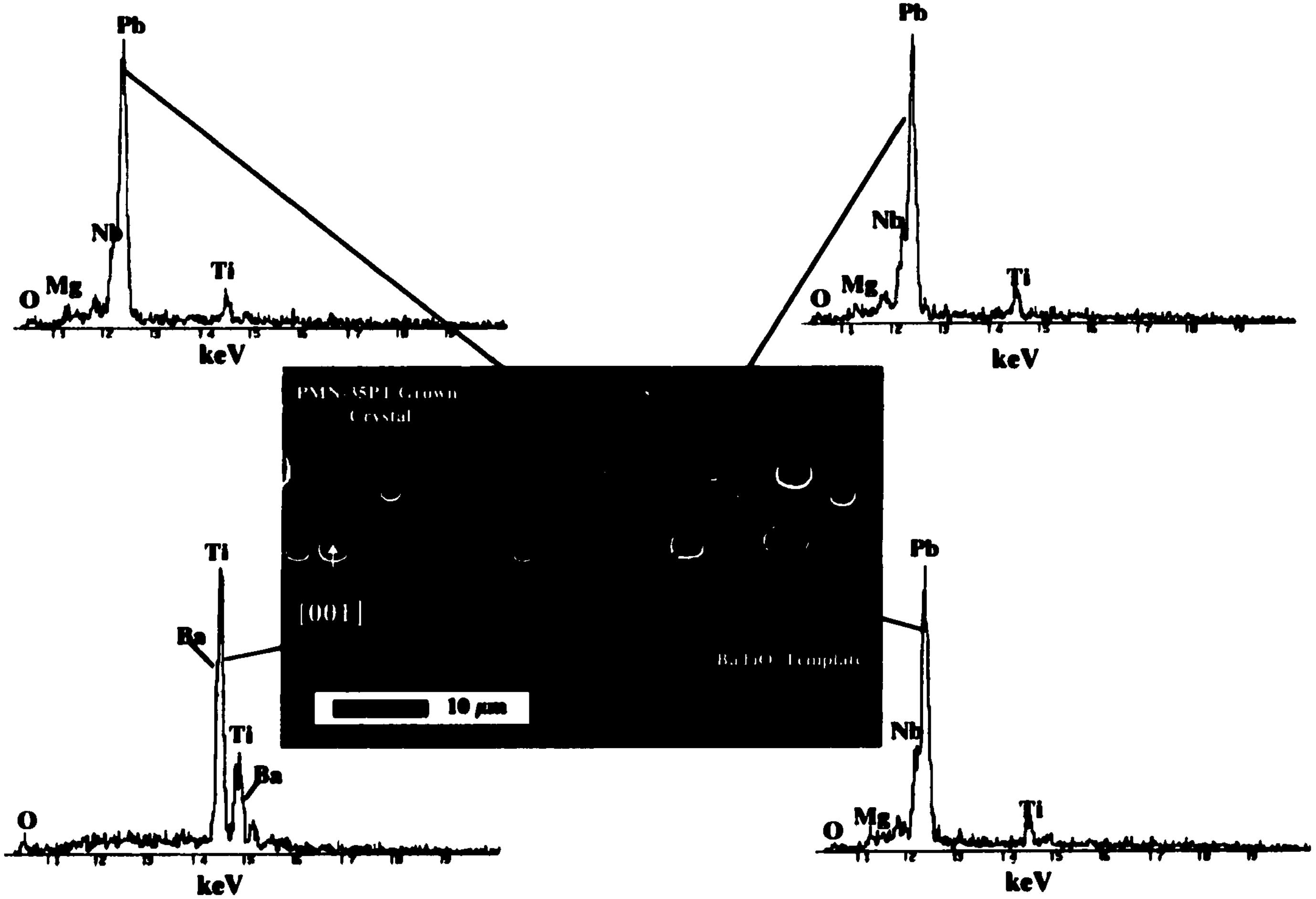

Figure 4.16: SEM micrograph and EDS patterns at the template/grown crystal interface of a PMN-35PT TGG sample containing a {001}-$BaTiO_3$ template and 3 wt% excess PbO heated to 1150°C for 1 h and then quenched in air.

condition depicts the crystal growth process near its kinetic saturation point. Again, the sample was not etched in order to preserve the sample surface. The EDS spectra showed the same results as the sample processed merely to 950°C. The EDS pattern collected ~1 μm within the $BaTiO_3$ template displayed a $BaTiO_3$ spectra without Pb or any other residual ions. The patterns at a distance of ~1, 5, and 10 μm from the interface displayed a PMN-PT spectra which was identical to that obtained from the matrix. The EDS elemental map (Fig. 4.17) near the crystal interface showed a similar distribution of ions as the sample processed to 950°C (Fig. 4.15). The EDS analysis identified little chemical redistribution even after the extended annealing at 1150°C. These results emphasize that the composition of the growing crystal seems to be consistent over time and distance and both the template and crystal are chemically stable at temperatures between 950-1150°C.

4.4 CONCLUSIONS

PMN-35PT single crystal layers were grown heteroepitaxially on {001}-, {110}-, and {111}-$BaTiO_3$ template crystals. Excess PbO was found to be the primary factor controlling the growth rate of the single crystal layer and the matrix grains. A minimum excess PbO concentration between 1 and 3 wt% was shown to accelerate the growth of the crystal layer. Crystal growth kinetics were also found to differ for various crystallographic orientations with the <111>-direction being the fastest and the <001>-direction the slowest.

The initial matrix grain growth was fit to the Lay model which indicated that diffusion controls the matrix grain growth for <1 h. The crystal growth fit the Seabaugh

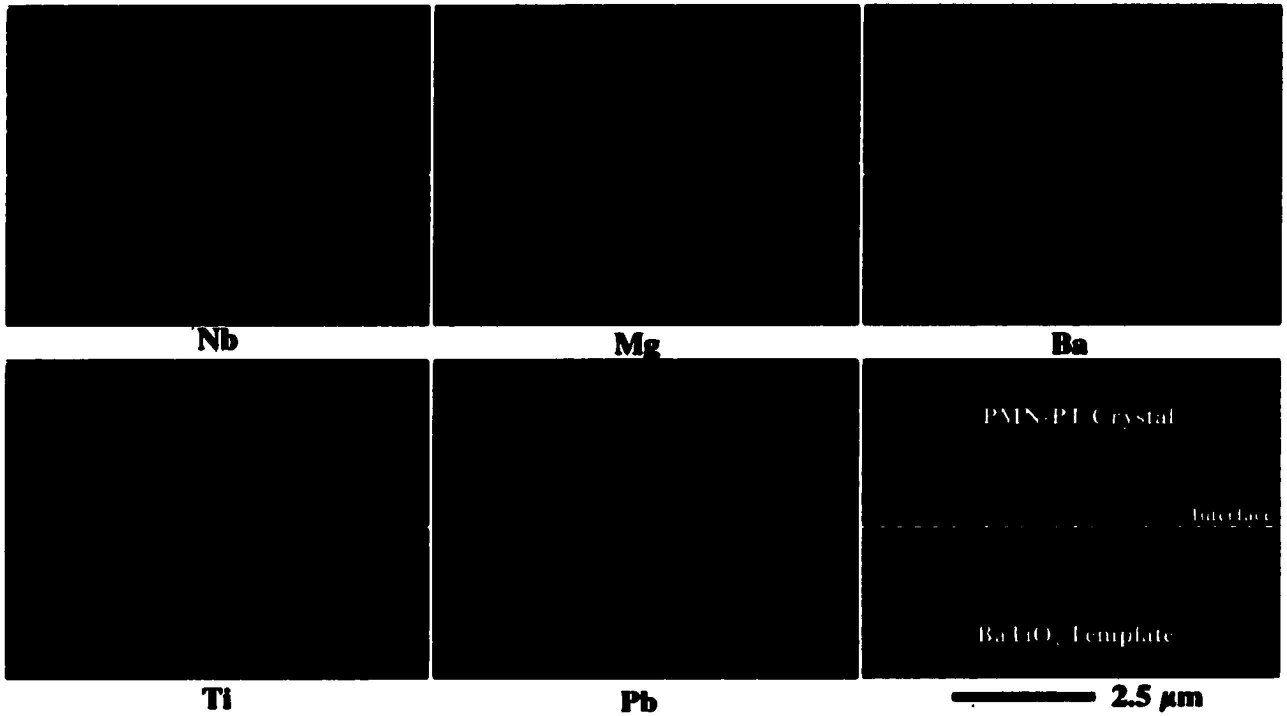

Figure 4.17: EDS elemental map of the template/grown crystal interface of a PMN-35PT TGG sample containing a {001}-$BaTiO_3$ template and 3 wt% excess PbO heated to 1150°C for 1 h and quenched in air.

et al. expression rather well. Therefore, the PMN-35PT single crystal layer must also be controlled by diffusion and the extent of growth was limited by the decrease in the driving force due to the coarsening and shape change of the matrix grains.

4.5 REFERENCES

1) J. Kuwata, K. Uchino, and S. Nomura, "Dielectric and Piezoelectric Properties of $0.91Pb(Zn_{1/3}Nb_{2/3})O_3$-$0.09PbTiO_3$ Single Crystals," *Jpn. J. Appl. Phys.*, **21**, 1298-302 (1982).

2) S.W. Choi, T.R. Shrout, S.J. Jang, and A.S. Bhalla, "Dielectric and Pyroelectric Properties in the $Pb(Mg_{1/3}Nb_{2/3})O_3$-$PbTiO_3$ System," *Ferroelectrics*, **100** 29-38 (1989).

3) S.-E. Park and T.R. Shrout, "Characteristics of Relaxor-Based Piezoelectric Single Crystals for Ultrasonic Transducers," *IEEE Trans. Ultrasonics, Ferroelectrics, and Frequency Control*, **44** [5] (1997).

4) S.-F. Liu, S.-E. Park, T.R. Shrout, and L.E. Cross, "Electric Field Dependence of Piezoelectric Properties for Rhombohedral $0.955Pb(Zn_{1/3}Nb_{2/3})O_3$-$0.045PbTiO_3$ Single Crystals," *J. Appl. Phys.*, **85** [5] 2810-14 (1999).

5) S.-E. Park and T.R. Shrout, "Ultrahigh Strain and Piezoelectric Behavior in Relaxor Based Ferroelectric Single Crystals," *J. Appl. Phys.*, **82** [4] 1804-11 (1997).

6) K. Harada, S. Shimanuki, T. Kobayashi, S. Saitoh, and Y. Yamashita, "Crystal Growth and Electrical Properties of $Pb((Zn_{1/3}Nb_{2/3})_{0.91}Ti_{0.09})O_3$ Single Crystals Produced by Solution Bridgman Method," *J. Am. Ceram. Soc.*, **81** [11] 2785-88 (1998).

7) S.G. Lee, R.G. Monteiro, R.S. Feigelson, H.S. Lee, M. Lee, and S.E. Park, "Growth and Electrostrictive Properties of $Pb(Mg_{1/3}Nb_{2/3})O_3$ Crystals," *Appl. Phys. Lett.*, **74** [7] (1999).

8) T. Li, A.M. Scotch, H.M. Chan, M.P. Harmer, S.-E. Park, T.R. Shrout, and J.R. Michael, "Single Crystals of $Pb(Mg_{1/3}Nb_{2/3})O_3$-35mol% $PbTiO_3$ from Polycrystalline Precursors," *J. Am.. Ceram. Soc.*, **81** [1] 244-48 (1998).

9) M.M. Seabaugh, I.H. Kerscht, and G.L. Messing, "Texture Development by Templated Grain Growth in Liquid-Phase-Sintered α-Alumina," *J. Am. Ceram. Soc.*, **80** [5] 1181-88 (1997).

10) P.W. Rehrig, S.E. Park, S. Trolier-McKinstry, G.L. Messing, B. Jones, and T.R. Shrout, "Piezoelectric Properties of Zirconium-Doped Barium Titanate Single Crystals Grown by Templated Grain Growth," *J. Appl. Phys.*, **86** [3] 1657-61 (1999).

11) P.W. Rehrig, G.L. Messing, and S. Trolier-McKinstry, "Templated Grain Growth of Barium Titanate Single Crystals," *J. Am. Ceram. Soc.*, **83** [11] 2654-60 (1999).

12) T. Li, S. Wu, A. Khan, A.M. Scotch, H.M. Chan, and M.P. Harmer, "Heteroepitaxial Growth of Bulk Single-Crystal $Pb(Mg_{1/3}Nb_{2/3})O_3$-32 mol% $PbTiO_3$ from (111) $SrTiO_3$," *J. Mater. Res.*, **14** [8] 3189-91 (1999).

13) M.M. Seabaugh, E. Suvaci, B. Brahmaroutu, and G.L. Messing, "Modeling Anisotropic Single Crystal Growth Kinetics in Liquid Phase Sintered α-Al_2O_3," *Interface Science*, **8** [2-3] 257-267 (2000).

14) J.P. Remeika, "Method of Growing Barium Titanate Single Crystals," *J. Am. Chem. Soc.*, **76** [3] 940-41 (1954).

15) R.C. DeVries, "Observations on Growth of $BaTiO_3$ Crystals from KF Solutions," *J. Am. Ceram. Soc*, **42** [11] 547-58 (1959).

16) NIH Image, V.1.56, by W. Rasband, National Institute of Health, USA.

17) R.L. Fullman, "Measurement of Particle Sizes in Opaque Bodies," *J. Metals*, **3** 447-52 (1953).

18) Z.G. Ye, P. Tissot, and H. Schmid, "Pseudo-Binary $Pb(Mg_{1/3}Nb_{2/3})O_3$-PbO Phase Diagram and Crystal Growth of $Pb(Mg_{1/3}Nb_{2/3})O_3$ [PMN]," *Mat. Res. Bull.*, **25** 739-48 (1990).

19) J.P. Guha, "Reaction Chemistry and Subsolidus Phase Equilibria in Lead-Based Relaxor Systems: Part I: Formation and Stability of the Perovskite and Pyrochlore Compounds in the System PbO-MgO-Nb_2O_5," *J. Mater. Sci.*, **34** 4985-94 (1999).

20) R.S. Roth, "PbO-Nb_2O_5 Phase Diagram," *J. Research Natl. Bur. Standards*, **62** [1] 34 (1959).

21) J.D. Powers and A.M. Glaeser, "Grain Boundary Migration in Ceramics," *Interface Science*, **6** 23-39 (1998).

22) A. Khan, F.A. Meschke, T. Li, A.M. Scotch, H.M. Chan, and M.P. Harmer, "Growth of $Pb(Mg_{1/3}Nb_{2/3})O_3$-35 mol% $PbTiO_3$ Single Crystals from (111) Substrates by Seeded Polycrystal Conversion," *J. Am. Ceram. Soc.*, **82** [11] 2958-62 (1999).

23) K.W. Lay, "Grain Growth in UO_2-Al_2O_3 in the Presence of a Liquid Phase," *J. Am.. Ceram. Soc.*, **51** [7] 373-76 (1968).

24) S. Kwon, E.M. Sabolsky, and G.L. Messing, "Low Temperature Reactive Sintering of 0.65PMN-0.35PT," *J. Am. Ceram. Soc.*, **84** [3] 648-50 (2000).

25) S.-K Kwon, S.-H. Hong, D.-Y. Kim, and N.M. Hwang, "Coarsening Behavior of Tricalcium Silicate (C_3S) and Dicalcium Silicate (C_2S) Grains Dispersed in a Clinker Melt," *J. Am. Ceram. Soc.*, **83** [5] 1247-52 (2000).

26) D. Elwell and H.J. Scheel, *Crystal Growth from High-Temperature Solutions*. Academic Press, New York, New York (1975).

27) G.W. Greenwood, "The Growth of Dispersed Precipitates in Solutions," *Acta Metall.*, **4** [5] 243-48 (1956).

28) D.F.K. Hennings, R. Janssen, and P.J.L. Reynen, "Control of Liquid-Phase-Enhanced Discontinuous Grain Growth in Barium Titanate," *J. Am. Ceram. Soc.*, **70** [1] 23-27 (1987).

29) R.D. Monahan and J.W. Halloran, "Single-Crystal Boundary Migration in Hot-Pressed Aluminum Oxide," *J. Am. Ceram. Soc.*, **62** [11-12] 564-67 (1979).

30) Y. Finkelstein, S.M. Wiederhorn, B.J. Hockey, C.A. Handwerker, and J.E. Blendell, "Migration of Sapphire Interfaces into Vitreous Bonded Aluminum Oxide"; pp. 258-79 in Ceramic Transactions, Vol. 7, *Sintering of Advanced Ceramics*. Edited by C.A. Handwerker, J. Blendell, and W.A. Kaysser. American Ceramic Society, Westerville, OH, 1990.

31) C. Wagner, "Theorie der Alterung von Niedershlägen durch Umlösen (Ostwald-Reifung)," Z. *Electrochemie*, **65** 581-91 (1961).

32) J. Chen, H.M. Chan, and M.P. Harmer, "Ordering Structure and Dielectric Properties of Undoped and La/Na-Doped $Pb(Mg_{1/3}Nb_{2/3})O_3$," *J. Am. Ceram. Soc.*, **72** [4] 593-98 (1998).

33) A.D. Hilton, D.J. Barber, C.A. Randall, and T.R. Shrout, "On Short Range Ordering in the Perovskite Lead Magnesium Niobate," *J. Mater. Sci.*, **25** 3461-66 (1990).

34) B. Lewis, "Nucleation and Growth Theory,"; pp. 23-63, *Crystal Growth, Vol.16*. Edited B. Pamplin. Pergamon Press, Oxford, England, 1980.

35) W.R. Wilcox, "Fundamentals of Solution Growth,"; pp. 119-41, *Crystal Growth in Science and Technology*. Edited by H. Arend and J. Hulliger. Plenum Press, New York, 1989.

36) K.A. Jackson, "A Review of the Fundamental Aspects of Crystal Growth,"; pp. 17-24, *Crystal Growth: Proceedings of an International Conference on Crystal Growth*. Edited by H. Peiser. Pergamon Press, Oxford, England, 1966.

37) B. Mutaftschiev, "Nucleation Theory,"; pp. 187-247, *Handbook of Crystal Growth: Fundamentals of Thermodynamics and Kinetics*. Edited by D.T.J. Hurle. North-Holland, Amsterdam, Netherlands, 1993.

38) F.W. Perry, "Single-Seed Growth of (Ba,Pb)TiO_3 from Borate Melts,"; pp. 483-87, *Crystal Growth: Proceedings of an International Conference on Crystal Growth*. Edited by H. Peiser. Pergamon Press, Oxford, England, 1966.

Chapter 5

FIBER-TEXTURED PMN-32.5PT CERAMICS

5.1 INTRODUCTION

As stated in Chapter 2, traditional ceramic consolidation processes usually result in the formation of a material, which possesses a randomly-oriented grain structure. A ceramic with this grain structure generally displays an average of the directionally dependent physical properties due to the isotropic nature of the bulk ceramic.(1) Electrical, optical, magnetic, mechanical, thermal, electromechanical, and other physical properties of random ceramics are governed by the macroscopic $\infty\infty m$ symmetry. This macroscopic symmetry can be altered by orienting the grain structure of the ceramic, making the physical properties anisotropic in nature similar to the single crystal form. Various processing routes which have been used to form grain-oriented materials are also discussed in Chapter 2.

The objective of this work was to grain-orient (texture) the $0.675Pb(Mg_{1/3}Nb_{2/3})O_3$-$0.325PbTiO_3$ (PMN-32.5PT) composition in the <001> in order to access the enhanced electromechanical properties identified for the single crystal of this orientation. The Templated Grain Growth (TGG) was chosen as a viable processing route to form the textured PMN-PT ceramic. The TGG process involves the orientation of anisotropically-shaped template particles in a dense, fine-grained matrix by a shear-forming technique.(2) The template particles must be relatively large and anisometric in shape, so that they can be effectively oriented during forming and grow preferentially during heating. The driving force for the TGG process is supplied by the difference in surface free energy between the templates and the matrix grains. This energy difference is supplied by the relative difference in the size between the templates and the matrix during growth. The final degree of texture is strongly dependent on the template growth rate, the initial template alignment and distribution, and the template concentration.

The effective use of the TGG process has been shown to produce highly textured samples with single crystal-like anisotropy and properties.(2-10) The majority of compositions previously textured by the TGG process possessed low symmetry crystal structures, therefore, anisometric template particles of these compositions were accessible. In most reported cases, the resultant texture due to the alignment and growth of these anisometric template particles produced a ceramic which displayed a cylindrical symmetry (∞/mm symmetry). A textured ceramic which displays this cylindrical symmetry is considered to show fiber-texture (1-D texture).(11-12) Fiber-texturing of a bulk ceramic composition which displays a high symmetry crystal structure has proven to be difficult.(13-14) The ability to texture a high symmetry system by TGG or any other processing method is limited by comparatively isotropic growth character of these systems. Either due to thermodynamic or kinetic limitations, the grain and particle structures of these isotropic systems usually grow to a spherical, octahedral, or well-faceted cubic shape.(15-17) Thus, the ability to synthesize anisotropic template particles of these compositions is restricted. Since PMN-PT displays a high symmetry prototype structure, these same problems limit the ability to fiber-texture PMN-PT ceramics.

In Chapters 3 and 4, it was shown that $BaTiO_3$ was well suited to act as the template for the TGG of a PMN-PT ceramic. The other template compositions in Chapter 3 were shown to be unstable in an PbO and/or PMN-PT environment, where they either dissolved into the matrix or formed the pyrochlore phase. The Remeika process was shown to consistently produce {001}-oriented $BaTiO_3$ crystals which displayed an anisometric geometry.(18,19) These crystals proved to be quite stable in the Pb-rich environment, and they acted as suitable substrates to nucleate the desired growth of the PMN-PT crystal layer. It was also found that the TGG kinetics from the $BaTiO_3$ templates were highly dependent on the excess PbO content within the PMN-PT matrix. By increasing the excess PbO content in the matrix, the growth kinetics were increasingly accelerated. These observations can be utilized to produce highly textured PMN-32.5PT ceramics.

This study focused on the effect of the TGG processing conditions on the degree of texturing and the quality of the final textured ceramic. Factors like the template concentration, growth temperature and time, and initial density were investigated. The degree of orientation and density of the final textured PMN-PT ceramic are important since these factors directly control the degree of property anisotropy and enhancement.

5.2 EXPERIMENTAL PROCEDURES

The $0.675Pb(Mg_{1/3}Nb_{2/3})O_3$-$0.325PbTiO_3$ (PMN-32.5PT) matrix powder was prepared by the columbite process by milling the appropriate amount of $(PbCO_3)_2Pb(OH)_2$ (Aldrich Chemical Company, Inc., Milwaukee, WI), $MgNb_2O_6$ (TRS Ceramics, Inc., State College, PA), and fumed TiO_2 (Degussa-Hüls, Frankfurt, Germany). The precursor powder was ball milled in HDPE bottles by high density ZrO_2 media (3 mm) for 10 h in deionized water. The slurry was dried on a hot plate while stirring with a magnetic stir bar and calcined at 850°C for 5 h. In this work, excess PbO was added to the matrix composition by milling with the appropriate amount of $(PbCO_3)_2Pb(OH)_2$ in toluene with 0.5 wt% dispersing agent (KD3 Hypermer, ICI Surfactants). The matrix powder was dried and calcined at 550°C for 5 hours to remove the dispersant and to transform the lead carbonate to lead oxide.

{001}-$BaTiO_3$ template crystals were synthesized by the Remeika process as described in Chapter 3 and 4. Only crystals displaying a thickness <75 μm were selected from the crystal batch. These crystals were roll milled and sieved to 75-150 μm (100-200 mesh). This procedure produced template crystals which had an average thickness of ~50 μm and a diameter of ~100 μm with an aspect ratio ranging from 2-5.

The {001}-$BaTiO_3$ template crystals were aligned within the PMN-32.5PT matrix by tape casting. A slurry containing 69 wt% PMN-32.5PT matrix and 31 wt% polyvinyl alcohol binder solution (15.6 wt% Air Products 523 polyvinyl alcohol (PVA), 12.8 wt% glycerol, 71.6 wt% deionized water) was mixed with 5-10 vol% $BaTiO_3$ templates (calculated for the final ceramic volume) by a magnetic stir bar in a Pyrex™ beaker for 12 h. Water was removed from the slurry to thicken the slurry to a viscosity of ~1000 mPa·s. The slurry was tape cast using a blade height of 400 μm at a shear rate of ~200 s^{-1} (~7 cm/sec casting speed). The tape was dried, cut, and laminated to a thickness of ~1 mm. The laminated tape was burned-out in air and then loaded into a 1.25 cm diameter graphite die. The samples were hot-pressed in argon at 900°C for 30 min at a pressure of 70 MPa. The hot-pressed samples were then encapsulated in two piece Pt crucibles and packed in PMN-PT (3 wt% excess PbO) packing powder to control the PbO volatilization. The samples were heated at 10°C/min to 1150°C and annealed in an O_2

atmosphere for ≤10 h in order to drive the TGG process. The sample surface and cross-section were polished, thermally etched (same as Chapter 4), and characterized by both scanning electron microscopy (SEM) and x-ray diffraction (XRD). The degree of <001>-texture was estimated from the collected XRD patterns by applying the Lotgering method.(20) The Lotgering factor (*f*) is defined as the area fraction of textured material in the [hkl] of interest. The degree of <001>-texture for the PMN-32.5PT ceramics was calculated by using the Lotgering relation:

$$f_{(00l)} = \frac{P_{(00l)} - P_0}{1 - P_0} \qquad \text{Eq. 5.1}$$

where

$$P_{(00l)} = \frac{\sum I_{(00l)}}{I_{(hkl)}} \qquad \text{Eq. 5.2}$$

$$P_0 = \frac{\sum I_{o(00l)}}{I_{o(hkl)}} \qquad \text{Eq. 5.3}$$

$\Sigma I_{(00l)}$ is the summation of the XRD peak intensities of all the (00l) peaks (i.e. 001, 002...) in the textured sample pattern. $\Sigma I_{(hkl)}$ is the summation of the peak intensities of all (hkl) peaks which appear in the XRD pattern. $\Sigma I_{o(00l)}$ and $\Sigma I_{o(hkl)}$ are summations of the XRD peak intensities for a randomly, oriented sample. The *f* factors were calculated for a 2θ scan between 20-70°. For XRD patterns containing broader peak widths, the Lotgering factor was calculated using peak area instead of peak intensity. The calculated

f describes the degree of texture defined by the surface area which was characterized by XRD. The f factor is considered to be an estimation of the volume fraction of textured material.

The texture fractions which were measured in this work should be considered to be approximate values, since the XRD patterns varied across the thickness of the samples due to the size and inhomogeneous mixing of the oversized template particles. From multiple XRD patterns taken of the same sample at different thickness levels, the texture fraction was found to vary between ±0.047. Therefore, the reported texture fraction for each sample in this work were calculated and averaged over ≥3 XRD patterns taken at various depths through the sample thickness. The surfaces of both sides of the samples were x-rayed and then >50μm of each surface was removed by polishing. The listed texture fractions contain approximately ±5% error, therefore, the samples displaying texture fractions which were similar within ±5% were grouped.

5.3 RESULTS AND DISCUSSION

5.3.1 Prediction of Texturing Kinetics for an Ideally Templated Model

An ideally templated ceramic would contain a volume fraction of templates (f_T) which display a square platelet morphology and are perfectly distributed and aligned in three dimensions. Let us assume that the square platelet templates have dimensions L (length) and h (height). In order for the ceramic to be completely texture, the templated grains must completely consume the total sample volume (V_s) in all three dimensions by growing a distance Δx, which is restricted by the volume conservation relation:

$$(L+\Delta x)^2\cdot(h+\Delta x)=\frac{V_S-V_T N_T}{N_T} \qquad \text{Eq. 5.4}$$

where V_T is the volume of a single template and N_T is the number of templates. Eq. 5.4 can be further simplified to:

$$(L+\Delta x)^2\cdot(h+\Delta x)=(L^2\cdot h)\cdot(\frac{1}{f_T}-1) \qquad \text{Eq. 5.5}$$

Figure 5.1 shows a schematic of the ideally templated ceramic in which the texture was constrained by the above relation. This calculation assumes that full-texture is achieved when all the faces of the perfectly packed grains touch and growth is not stopped by impingement. Also, this simple model assumes that the template growth distance (Δx) is equal in all three dimensions and the growth is limited by the kinetics in the template <001>. If the template particles have an average length of 100 µm and an aspect ratio (AR) ranging between 3-5, then all the dimensions of the templates must increase by 80-120 µm in order to achieve full-texture under these ideal assumptions (Fig. 5.2). Fig. 5.2 shows that by decreasing the template size and increasing the aspect ratio for a 5 vol% template concentration, the templates would have to grow a smaller distance in order to fully texture the ceramic. Since the $BaTiO_3$ template particles used in this study are relatively large (~75-150 µm diameter) with low aspect ratios (<5), then the templates must grow over rather large distances (>75 µm) to produce a fully textured PMN-PT ceramic.

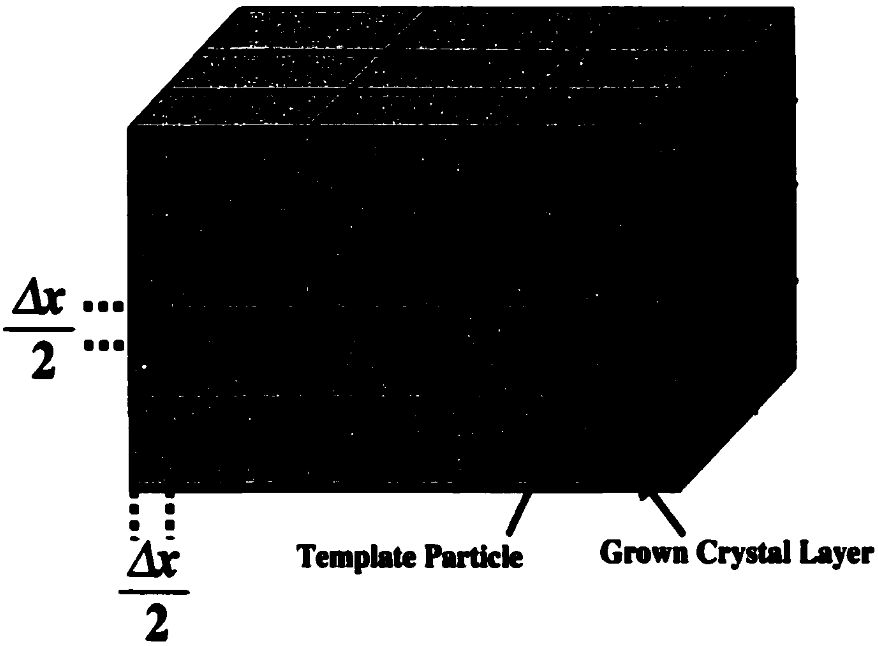

L= Template length
h= Template height
f_T= Volume Fraction of Templates
Δx = Growth Distance to Full-Texture

Figure 5.1: Schematic of an ideally templated and fully textured (f=1) sample.

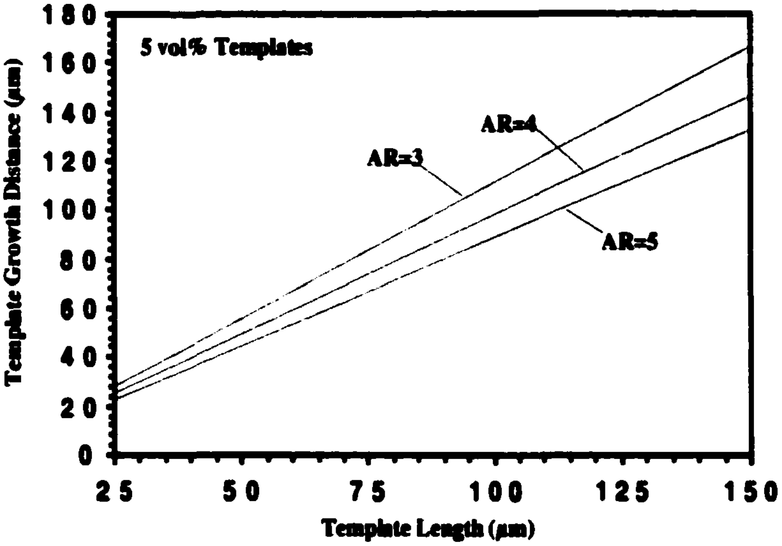

Figure 5.2: Required growth distance(Δx) of the templates of various lengths in order to produce a fully textured ceramic (*f*=*1.0*) when the templates are ideally aligned and dispersed.

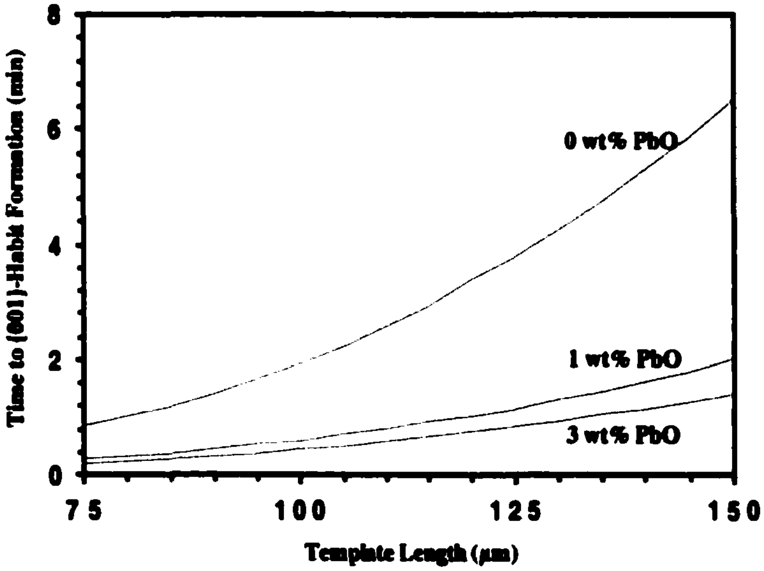

Figure 5.3: Time to {001}-habit formation of a circular platelet of various lengths solved from the Seabaugh *et al.* relations for matrix compositions containing 0-3 wt% excess PbO.

By applying the growth kinetics observed and fitted to the Seabaugh *et al.* model$^{(21)}$ in Chapter 4, the total growth time for ideal 100%-texturing (f=1) conditions can be estimated for the PMN-PT matrix compositions containing various concentrations of excess PbO. This means that the minimum required annealing time to fully texture the PMN-PT ceramic can be found by solving the Seabaugh *et al.* relation as a function of Δx. Δx was previously defined as the total template growth distance in the <001>. Therefore, it must be assumed that the growth in the <001> dominates the TGG kinetics. This is physically suggested in the PMN-PT system by the observation of the {001}-habit formation of the matrix grains and templated crystals, as discussed in Chapter 4. This assumption can be further supported by comparing the time required to form a {001}-habit for a spherical platelet due to anisotropic growth in the planar <hk0> at 1150°C. Assuming the <110> is the fastest growing direction in the plane, a spherical platelet would display a square platelet morphology when the growth distance in the <110> and <001> geometrically satisfies the condition:

$$(\frac{L}{2}+x)=\sqrt{2}(\frac{L}{2}+Ax) \qquad \text{Eq. 5.6}$$

where A is the growth rate ratio ($v_{<110>}/v_{<001>}$), x is the growth distance in the <001>, and L is the template length (diameter). The appropriate Seabaugh *et al.* relations from Chapter 4 were substituted into Eq. 5.6, and the solutions for the growth time to {001}-habit formation for various matrix compositions were calculated for templates ranging in size L=75-150 μm (Fig. 5.3). This simple calculation suggests that the habit formation is very rapid (<6 min) for these template sizes regardless of the matrix composition, and the growth of the templated grains at 1150°C is solely limited by the growth of the {001} planes. This will be further discussed in the following sections.

Figure 5.4 displays the time to full-texture as a function of template length for a matrix containing a 5 vol% template concentration and 0 wt% excess PbO annealed at 1150°C. The idealized texturing model indicates that a sample would require an annealing time of 2-20 h for templates ranging in size from 100-150 μm with aspect ratios between 3-5. Since the PMN-32.5PT templated sample possesses a distribution of template sizes and aspect ratios, the model indicates that the required growth time to full-texture can range anywhere over this time (2-20 h). Due to the large growth distances required to texture the PMN-PT ceramic and the slower growth kinetics, it is expected that the time required to highly texture the 0 wt% excess PbO containing ceramic would take >10 h.

It was calculated that when 1 wt% excess PbO is added to the matrix composition, the required growth time to attain the ideal full-texture at 1150°C significantly decreases below 5 h for all template sizes <150 μm (Fig. 5.5). If templates display an average length of 100 μm, then the required growth time would be <1 h for a matrix containing 1 wt% excess PbO. Therefore, the idealized model predicts that the PMN-PT ceramic containing 5 vol% $BaTiO_3$ templates could be fully-textured in a time <5 h if 1 wt% excess PbO was added to the matrix composition.

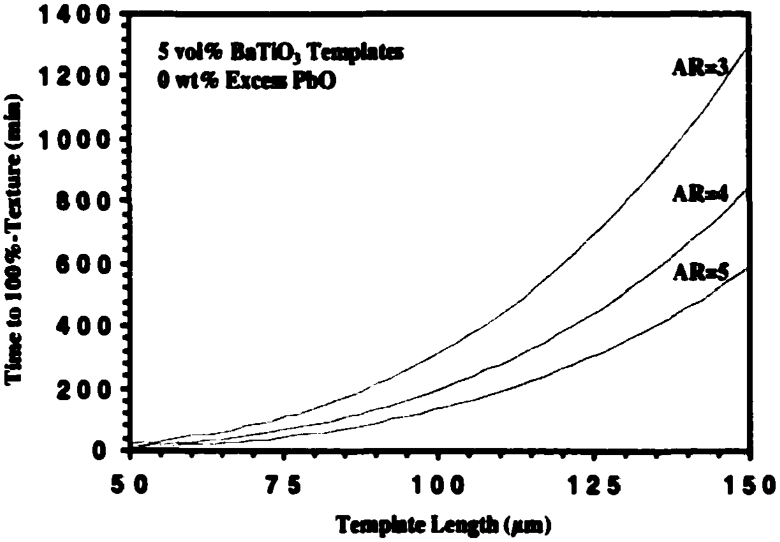

Figure 5.4: Required growth time at 1150°C calculated from an idealized texturing model to produce a fully textured PMN-32.5PT (0 wt% excess PbO) ceramic containing 5 vol% $BaTiO_3$ templates of various lengths.

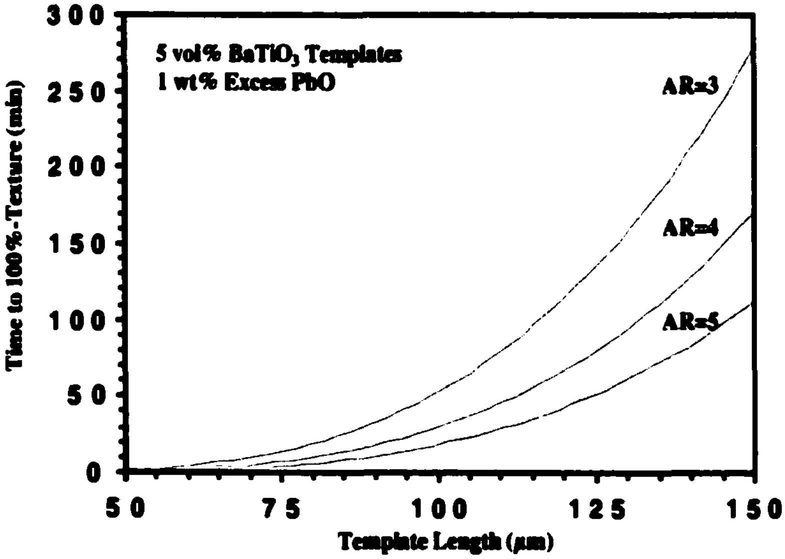

Figure 5.5: Required growth time at 1150°C calculated from an idealized texturing model to produce a fully textured PMN-32.5PT (1 wt% excess PbO) ceramic containing 5 vol% $BaTiO_3$ templates of various lengths.

5.3.2 Texturing PMN-32.5PT Ceramics Containing 0 wt% Excess PbO and 5 vol% $BaTiO_3$ Templates

Figure 5.6 compares the XRD patterns of the annealed samples with those of randomly-oriented (hot-pressed, but unannealed) samples containing 5 vol% $BaTiO_3$ template concentration with no excess PbO in the matrix. The unannealed samples did not show a change in the relative peak intensities compared to that of the random pattern as a result of the presence of the aligned template particles. Annealing the templated samples at 1150°C increased the intensity of the <001> peaks and decreased all other (hkl) peak intensities. This intensity change represents an increase in the <001>-texture volume fraction. The samples annealed at 1150°C for 5 h showed a Lotgering factor of ~0.4. With a 5 h increase in annealing time (10 h total annealing), the texture fraction increased to ~0.45. The texturing rate was shown to saturate by 5 h due to the decrease in TGG kinetics for reasons described in Chapter 4. Fig. 5.7 shows an SEM micrograph of a singular templated grain grown after a 5 h anneal at 1150°C. The $BaTiO_3$ template appears as a dark black region within a rectangular gray region (the templated PMN-PT crystal). The two parallel sides of the $BaTiO_3$ template are the {001}-crystal faces and the irregular-shaped ends are some <hkl> direction. The micrograph shows that the PMN-PT crystal layer grew <25 μm in <001> and 30-45 μm in the <hk0>. These growth distances resulted in doubling the size (length and thickness) of the templated grain. The templated crystal is completely surrounded by the polycrystalline PMN-32.5PT matrix which remained randomly-oriented after annealing, since the matrix was not consumed by the growing crystal at these growth conditions. Therefore, a matrix composition containing 0 wt% excess PbO was shown to possess insufficient growth

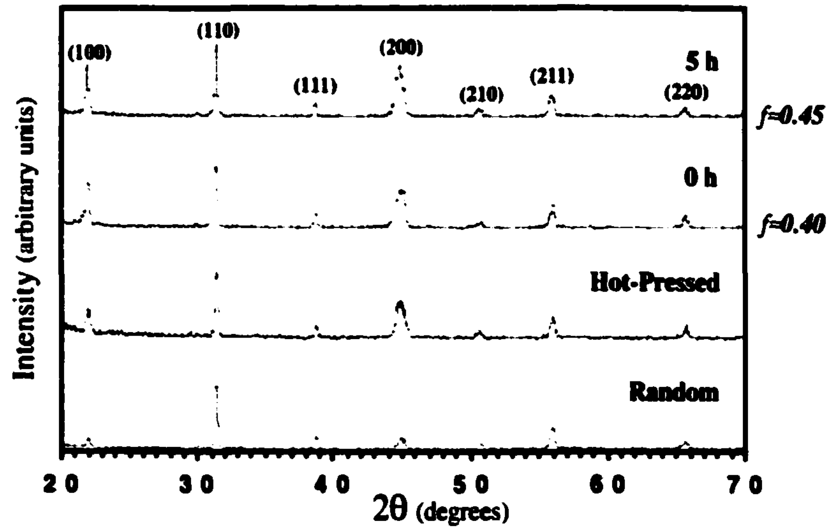

Figure 5.6: XRD patterns of a PMN-32.5PT (0 wt% excess PbO) ceramics containing 5 vol% oriented {001}-BaTiO$_3$ templates annealed at 1150°C for 0-5 h.

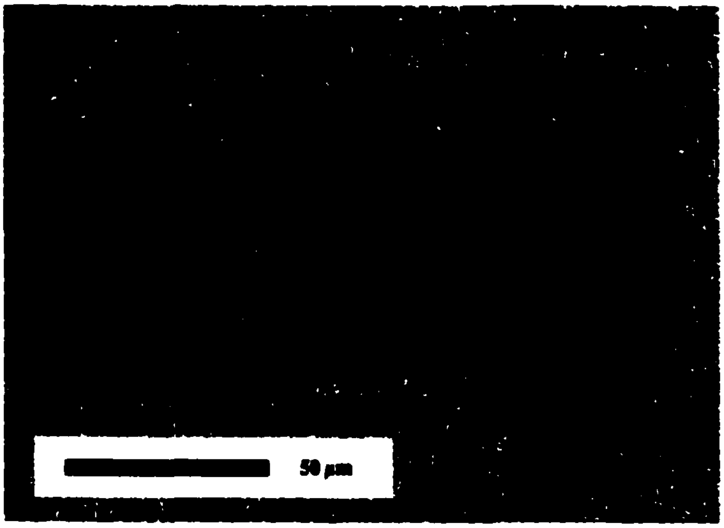

Figure 5.7: SEM micrograph showing the cross-sectional view of a singular templated grain in a PMN-32.5PT (0 wt% excess PbO) ceramic sample containing 5 vol% oriented{001}-BaTiO$_3$ templates annealed at 1150°C for 5 h.

kinetics over a reasonable annealing time (<10 h) to highly texture the PMN-32.5PT ceramic with a template concentration of 5 vol%. This is in qualitative agreement with the idealized texturing model.

5.3.3 Texturing PMN-32.5PT Ceramics Containing 1 wt% Excess PbO and 5 vol% $BaTiO_3$ Templates

As discussed in Chapter 4 and suggested by the ideal texturing model, the presence of a Pb-based intergranular liquid phase during growth can increase the TGG growth rate >1.5 times. Figure 5.8 shows the evolution of the XRD patterns for templated samples with 5 vol% $BaTiO_3$ templates and a matrix composition containing 1 wt% excess PbO annealed at 1150°C for 0-5 h. The samples were initially densified by hot-pressing as described in the experimental procedures. Included in Fig. 5.8 are the XRD patterns of a random and unannealed sample of the same composition. Fig. 5.8 shows no alteration in the XRD pattern of the templated sample after hot-pressing compared to that for the random sample. The additional oriented template particles did not appear to affect the relative intensities due to the increased volume fraction of oriented material within the ceramic. When the templated samples were heated at a rate of 10°C/min to 1150°C and then quenched to room temperature, the peak intensity of the {001} increased and all other peaks decreased in intensity. A Lotgering factor of ~0.8 was calculated for these samples. This indicates that a significant amount of template growth occurred just on heating to 1150°C, which was similar to observations reported in Chapter 4 for the TGG of the PMN-35PT single crystal layers. With annealing at 1150°C for 1 and 5 h, the texture fraction was increased to ~0.85 and 0.90, respectively (Fig. 5.8).

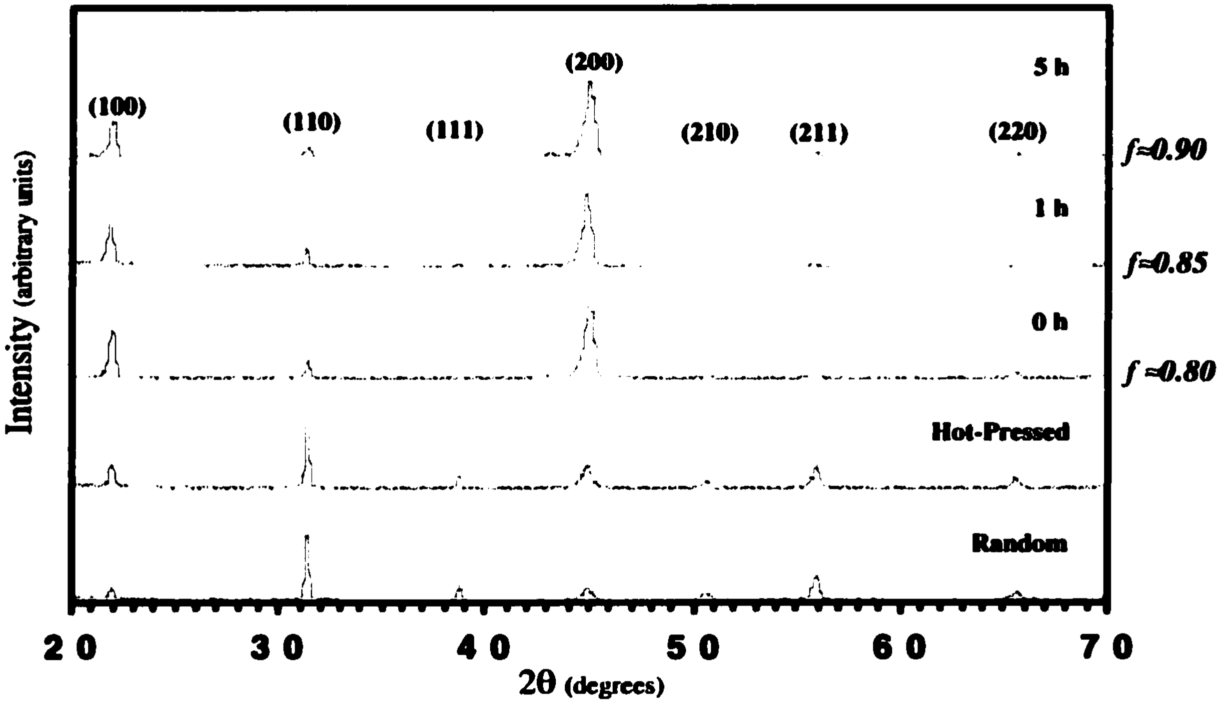

Figure 5.8: XRD patterns of a PMN-32.5PT (1 wt% excess PbO) ceramics containing 5 vol% oriented {001}-BaTiO$_3$ templates annealed at 1150°C for 0-5 h.

The texture rate seemed to begin saturating before the sample reached the 1150°C annealing temperature. The saturation of the texturing rate can be attributed in part to the decrease in the growth rate of the single crystal layer due to the coarsening and shape change of the matrix grains, as described in Chapter 4. A second factor slowing the rate of texturing is the impingement of the templated grains, since the template particles are not ideally situated in the ceramic. But as predicted by the simple texturing model, the addition of 1 wt% excess PbO to the matrix composition did accelerate the template growth process resulting in the highly textured PMN-PT ceramic in <5 h.

Grain impingement is a process when faceted grains come into contact restricting the mobility of the stable planes.(2,7,22) The impinged grains can only continue to grow by presenting planes of lower stability, resulting in an increase in the overall energy of the grain. Fig. 5.9(a) is an SEM micrograph of the cross-section of a templated sample (1 wt% excess PbO, 5 vol% $BaTiO_3$ templates) heated to 1150°C and then quenched to room temperature (0 h annealing time). The micrograph shows the impingement of the templated grains and the area of non-textured matrix grains. As predicted above, the templated grains had already achieved the {001}-habit before reaching the 1150°C annealing temperature. Fig. 5.9(b) is an SEM micrograph of the top surface of the templated sample, parallel to the fiber-textured direction. This figure shows the random in-plane orientation of the templated grains supporting the cylindrical (∞/mm) symmetry of fiber-textured ceramics. Fig. 5.9(b) also displays the grain capacity to remain {001}-faceted even after impingement. The growth distance in the template <001> ranged between ~25-40 μm. The growth on just heating was greater than that displayed by the

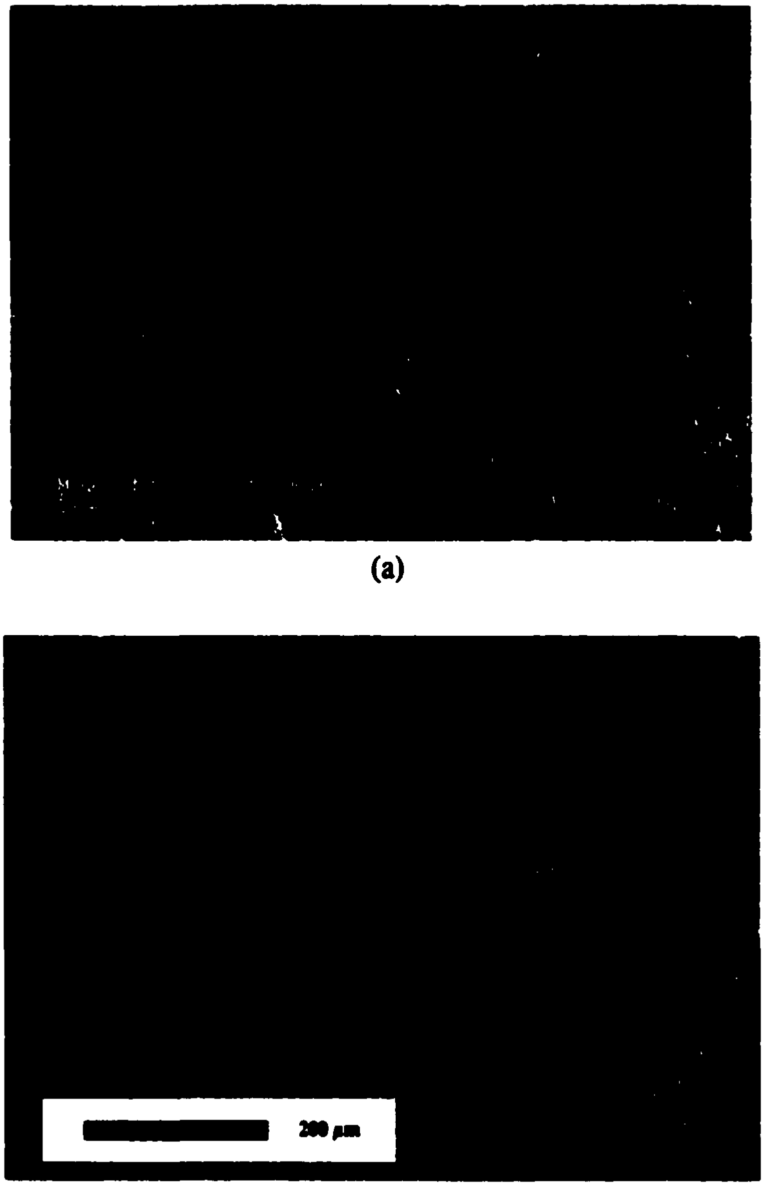

(a)

(b)

Figure 5.9: SEM micrographs showing the (a) cross-sectional and (b) top view of a PMN-32.5PT (1 wt% excess PbO) ceramic sample containing 5 vol% {001}-$BaTiO_3$ templates, heated to 1150°C (annealed for 0 h).

templated samples containing 0 wt% excess PbO after 5-10 h of annealing (Fig. 5.2 and 5.3). The SEM micrographs of the sample annealed at 1150°C for 5 h shows that the matrix is further consumed by the growing oriented grains. However, some of the matrix still remains due to the inability of the impinged grains to effectively grow as a result of the limited interface mobility at the point of templated-grain/templated-grain contact (Fig. 5.10(a,b)). Figure 5.10(b) shows that some templated grains are still growing after impingement, even growing into other templated grains. This means that grain impingement does not completely stop the growth. As texturing increases, the volume of matrix decreases, and the total surface area/volume of templated-grain/matrix interfaces would also decrease. The decreased concentration of these types of higher curvature boundaries would cause a steady decrease in the overall growth and texturing rate.

The XRD patterns for the textured samples in Fig. 5.8 show broad {001} peaks, sometimes displaying multiple overlapping peaks in close proximity of the 2θ angle position. The peak splitting is only observed for the {001} peaks. Therefore, the origin of the splitting is related to the templated grains since the increased intensity of these peaks is based primarily on the diffraction from the oriented grains. Fig. 5.11 shows a XRD step scan around the (200) diffraction peak of the 90%-textured PMN-32.5PT (1 wt% excess PbO) ceramic containing 5 vol% $BaTiO_3$ templates. The $BaTiO_3$ peak positions are shown for reference. It is clear that the splitting of the {200} peaks do not overlap with the rhombohedral PMN-PT peaks and the (200)/(002) peaks of tetragonally distorted $BaTiO_3$. The multiple peaks could be the result of lattice distortions in the templated grains due to interdiffusion between the template and the growing crystal layer. This probably is not the case, since in Chapter 4 it was shown that there was <5 μm of

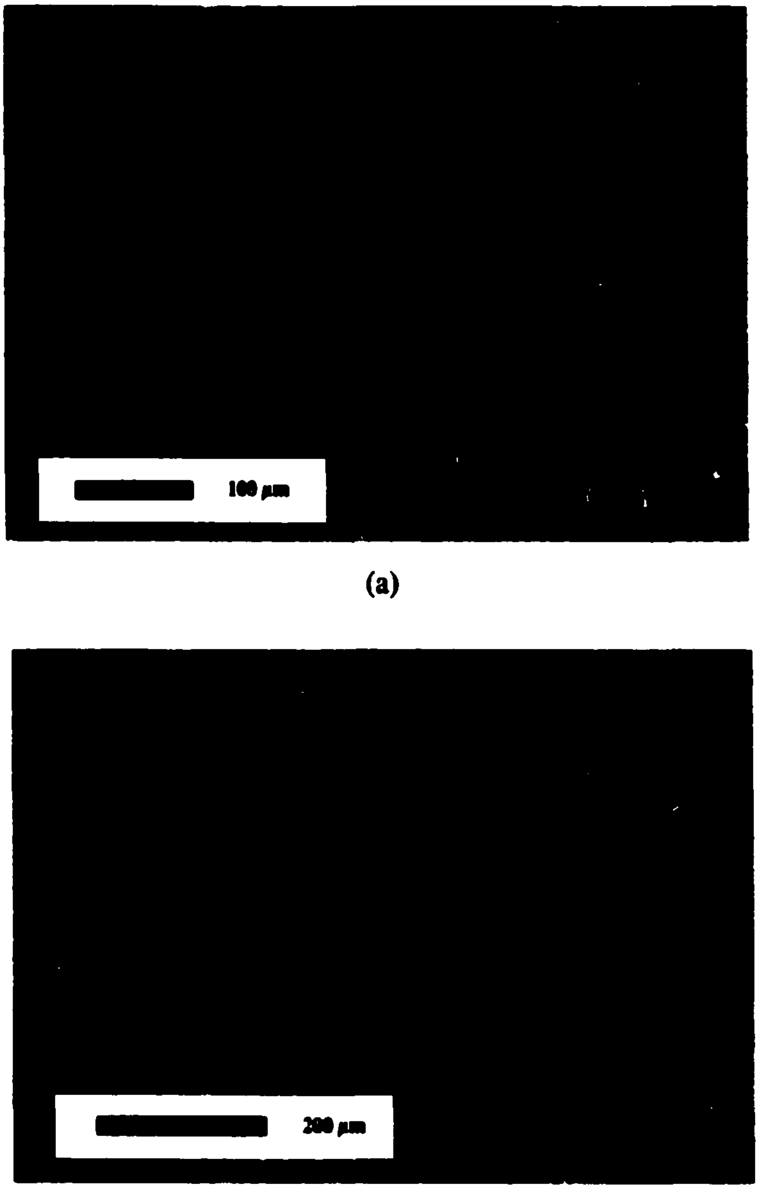

Figure 5.10: SEM micrographs showing the (a) cross-sectional and (b) top view of a PMN-32.5PT (1 wt% excess PbO) ceramic sample containing 5 vol% oriented {001}-$BaTiO_3$ templates annealed at 1150°C for 5 h.

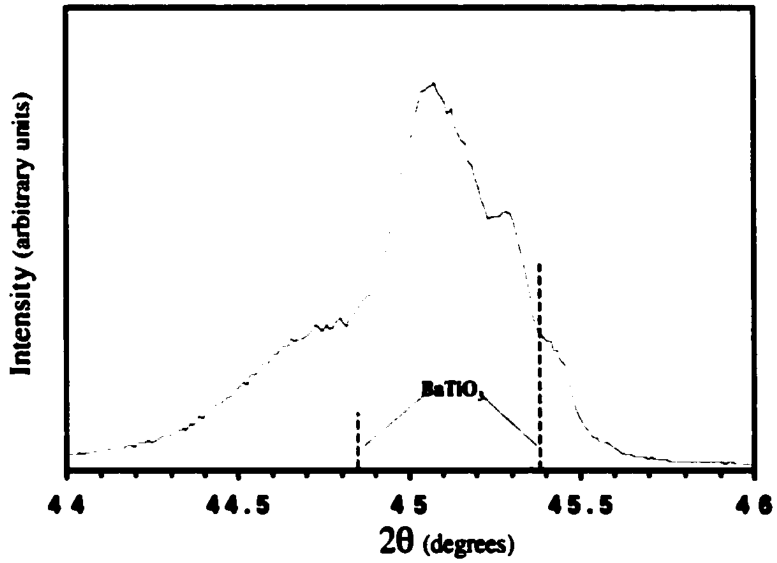

Figure 5.11: XRD pattern of the (200) peak of a ~90%-textured PMN-32.5PT (1 wt% excess PbO) ceramic containing 5 vol% oriented{001}-$BaTiO_3$ templates annealed at 1150°C for 5 h.

interdiffusion across the crystal interface, and this volume would be insufficient to produce these intense peaks. The templated PMN-32.5PT grains may also be mechanically constrained by the $BaTiO_3$ template which may locally lock the grown PMN-PT crystal into the tetragonal phase. Durbin *et al.*(23) recently showed the coexistence of rhombohedral and tetragonal domains in poled PZN-8PT single crystals (a rhombohedral composition) by XRD of the {002} peak. The appearance of Fig. 5.11 (at $2\theta > 44.8°$) is similar to that shown by Durbin *et al.* The PMN-32.5PT composition is an analogous composition to the PZN-8PT composition in relation to the MPB. Therefore, the splitting in the diffraction pattern may indicate that the $BaTiO_3$ templates are stabilizing the tetragonal domain structure in the templated grains by clamping.

All of the textured samples discussed thus far were hot-pressed at 900°C in argon at a pressure of 70 MPa before being annealed at 1150°C in O_2 to drive the TGG process. For both the 0 wt% and 1 wt% excess PbO sets of samples (5 vol% template concentration), the samples showed high densities (~8.1 g/cc) after hot-pressing and the densities remained above 7.92 g/cc even after annealing at 1150°C (Table 5.1). Although the hot-pressing step was shown to be very effective, the process still remains as an inefficient technique which should be avoided if possible. Therefore, the 5 vol% templated PMN-32.5PT samples containing 1 wt% excess PbO were fired to 1150°C without hot-pressing in order to both densify and texture the samples. Fig. 5.12 shows the XRD patterns of the randomly-oriented and textured samples sintered at 1150°C without the initial hot-pressing step. The patterns show a similar increase in peak intensity of the {001} and a decrease in intensity of all other peaks with prolonged

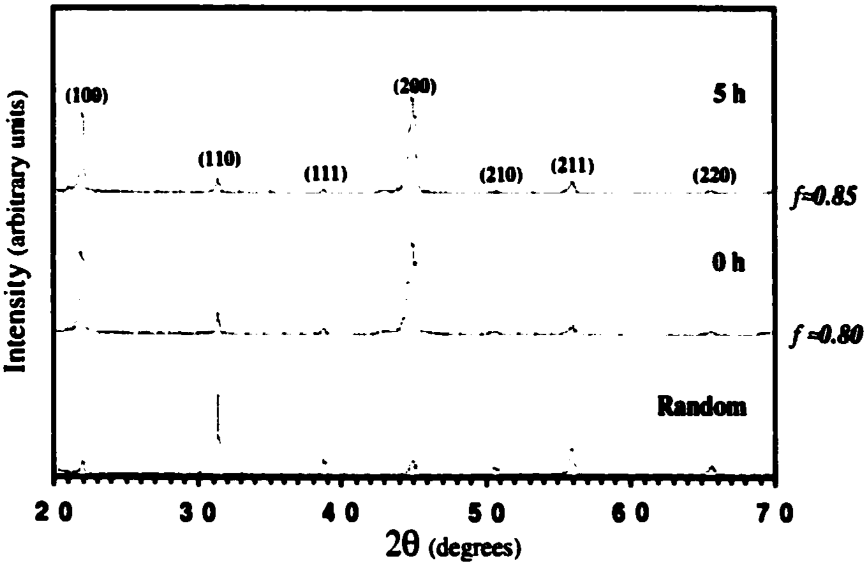

Figure 5.12: XRD patterns of a PMN-32.5PT (1 wt% excess PbO) ceramics containing 5 vol% oriented {001}-$BaTiO_3$ templates which were not hot-pressed, but directly sintered at 1150°C for 0-5 h.

thermal treatment. On heating to temperature, the texture fraction increased to ~0.80-0.83, and with further heating at 1150°C for 5 h, the texture fraction slightly increased to ~0.85. The samples did not texture to the same degree as the samples which were hot-pressed. Fig. 5.13 shows the SEM micrographs of the cross-sectional (Fig. 5.13(a)) and top view (Fig. 5.13(b)) of the templated sample sintered for 5 h at 1150°C. The figures display similar grain structures as those presented for the hot-pressed samples of the same annealing temperature and time, but the percentage of unconsumed matrix grains is higher, visually supporting the texture fraction measured by XRD. The figures show the presence of delamination and porosity around the templated grains which have impinged during growth. Table 5.1 shows that the density of these samples is much lower than the samples which were hot-pressed with the samples showing anywhere between 4-10% porosity. The development of pores and cracks can be attributed to constrained sintering which would develop around the rather large, dense template particles. The shrinkage of the matrix around these relatively large particles causes tensile stresses to develop at the surface of the templates.(24,25) Such stresses would result in void and crack formation which apparently can only be partially relaxed by the presence of the PbO liquid phase. Hot-pressing at 900°C for 30 min. allowed for full densification of the ceramics and the healing of any delamination or cracks without initiating a large degree of grain growth.

5.3.4 Texturing PMN-32.5PT Ceramics Containing 1 wt% Excess PbO and 10 vol% $BaTiO_3$ Templates

By increasing the template concentration above 5 vol%, the PMN-32.5PT ceramic should texture at a higher rate due to the smaller inter-template distance in which the

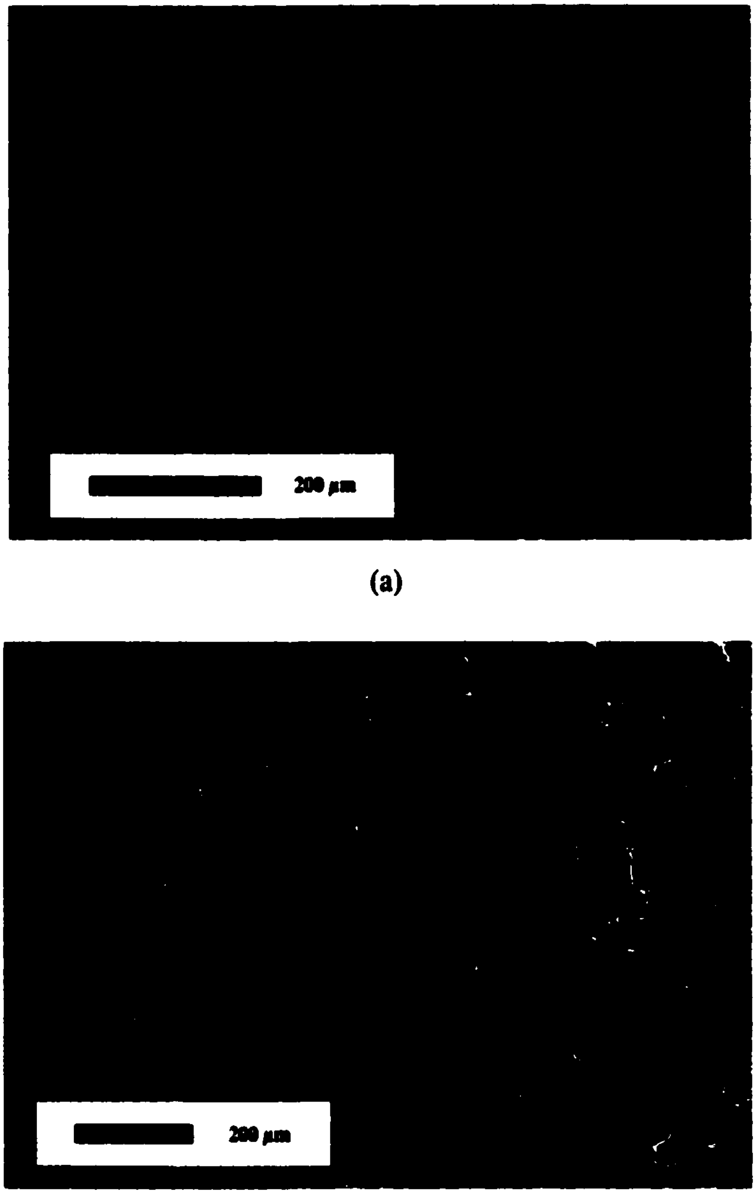

(a)

(b)

Figure 5.13: SEM micrographs showing the (a) cross-sectional and (b) top view of a PMN-32.5PT (1 wt% excess PbO) ceramic sample containing 5 vol% oriented {001}-$BaTiO_3$ templates which was not hot-pressed, but directly sintered at 1150°C for 5 h.

Table 5.1: **Effect of processing on the density of templated PMN-32.5PT ceramics (measured by Archimedes method).**

Processing Condition	5 vol% BT 0 wt% PbO *Hot-Pressed*	5 vol% BT 1 wt% PbO *Hot-Pressed*	5 vol% BT 1 wt% PbO *Not Hot-Pressed*	10 vol% BT 1 wt% PbO *Hot-Pressed*
Post Hot-Pressing	8.09±0.08	8.11±0.02	—	8.11±0.12
1150°C *0 h*	8.09±0.09	7.93±0.04	7.84±0.14	7.90±0.04
1150°C *5 h*	8.10±0.08	7.92±0.02	7.25±0.13	7.70±0.04
1150°C *10 h*	8.10±0.09	—	—	—

Density units=g/cc

$\rho_{(PMN-32PT)} \approx 8.13$ g/cc

$\rho_{(PMN-32PT-5BT)} \approx 8.03$ g/cc

$\rho_{(PMN-32PT-10BT)} \approx 7.92$ g/cc oriented crystals must grow. Also, the initial orientation of the larger volume of templates would automatically increase the total textured volume even before growth. Of course, these assumptions neglect the possible interaction or percolation of the template particles during alignment which may cause the initial misalignment of the templates, and thus, a decrease in the volume fraction of textured material during growth. Fig. 5.14 displays the time of full-texture solution for the idealized texturing model when the volume percent of template particles, which are perfectly dispersed and aligned in the PMN-32.5PT matrix (1 wt% excess PbO), is increased to 10 vol%. The solution shows that the PMN-32.5PT ceramic would fully texture in <45 min for templates sizes <150 µm (AR≈3-5) at 1150°C. It has been previously shown that there is significant PMN-PT crystal growth just on heating to 1150°C, therefore, the model suggests that the PMN-32.5PT ceramic at this PbO and template concentration would instantly texture. The degree of texturing would only be limited by grain impingement.

Figure 5.15 shows the XRD patterns of textured PMN-32.5PT ceramic samples containing 10 vol% aligned templates annealed for 0-5 h at 1150°C. The samples were hot-pressed and annealed in the same manner as the other samples in this work. The diffraction pattern after hot-pressing showed a slight increase in {001} peak intensity compared to that of the random sample, but the initially aligned templates did not significantly increase the volume fraction of textured material (f<0.2). On heating to 1150°C, the samples were shown to quickly texture to a fraction of ~0.85-0.90. With further annealing at 1150°C for 5 h, the texture fraction of the samples was shown to increase to as high as ~0.95 (Fig. 5.15). The texture fraction did not increase beyond

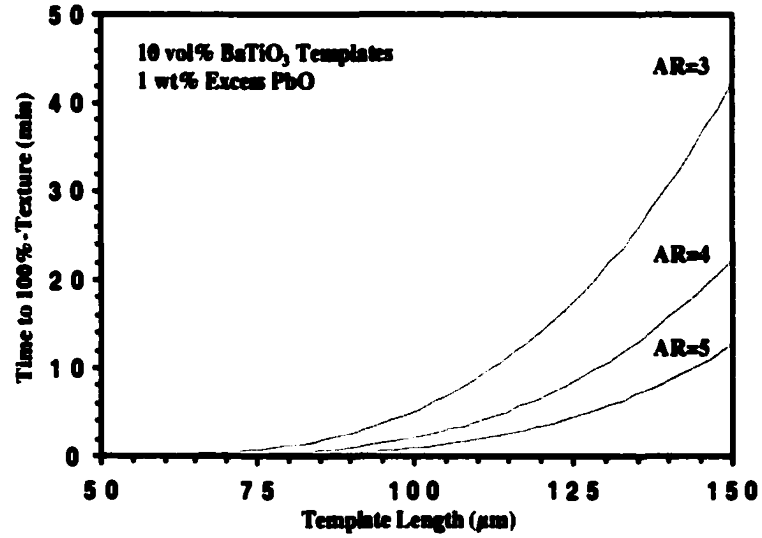

Figure 5.14: Required growth time at 1150°C calculated from an idealized texturing model to produce a fully textured PMN-32.5PT (1 wt% excess PbO) ceramic containing 10 vol% $BaTiO_3$ templates of various lengths.

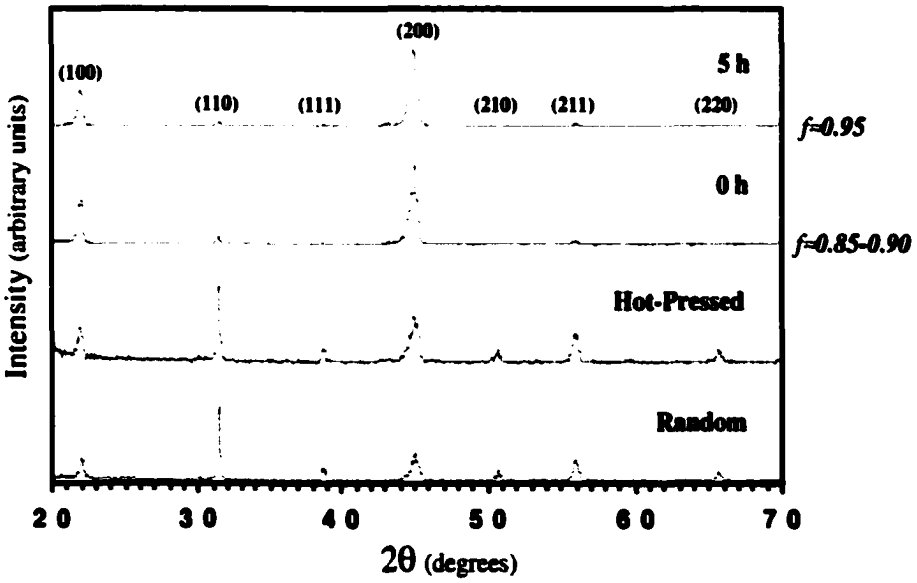

Figure 5.15: XRD patterns of a PMN-32.5PT (1 wt% excess PbO) ceramics containing 10 vol% oriented {001}-$BaTiO_3$ templates annealed at 1150°C for 0-5 h.

0.95 with further annealing. The obtained results strayed from the kinetics predicted by the idealized texturing model due to the early impingement, but the model did qualitatively characterize and contrast the texturing kinetics between samples of different PbO and template concentrations.

The cross-sectional and surface SEM micrographs (Fig. 5.16(a) and Fig. 5.16(b), respectively) of the 10 vol% templated samples heated to 1150°C (0 h anneal) shows the misalignment of the templates due to particle interaction during the forming process. Templates which were not homogenously distributed impinged early during growth due to the shorter inter-template distances. This restricted the continued growth of these grains, leaving areas of untextured matrix grains. The further 5 h annealing period drove the additional growth of the templated grains, but the extent of growth was limited by the impingement of the faceted grains. This is supported by the development of the XRD patterns during the growth duration. The growth, and therefore the degree of texturing, was also limited by the development of intergranular porosity and voids. Figs. 5.17(a,b) show the presence of these defects around and between the templated grains. The particle interaction and grain impingement brought about the formation of these defects which lowered the density of the samples (Table 5.1). The cause of the porosity is still uncertain. Other authors proposed that the porosity develops due to grain rearrangement forced by fast growing grains in the presence of a liquid phase.(26,27) The growing grains and the displaced liquid phase associated with these grains may push the matrix grains resulting in the development of porosity and liquid pools. The additional template concentration increased the degree of texturing and the texturing kinetics, but promoted a

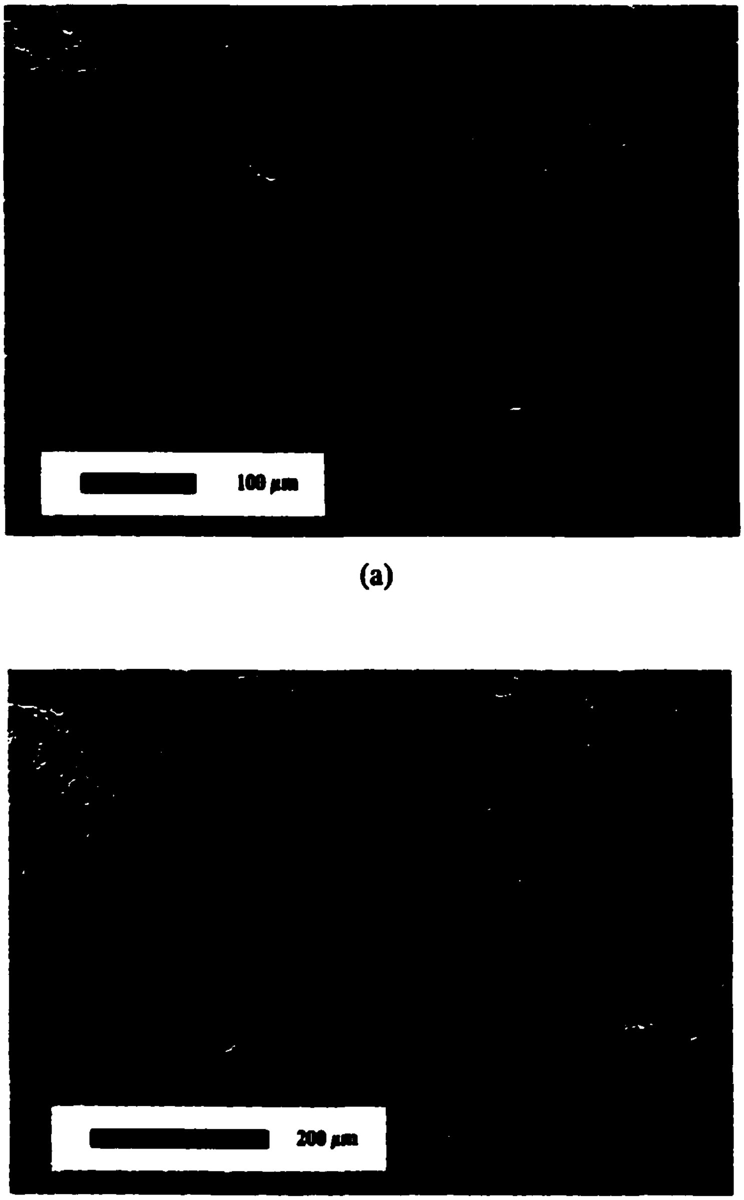

(a)

(b)

Figure 5.16: SEM micrographs showing the (a) cross-sectional and (b) top view of a PMN-32.5PT (1 wt% excess PbO) ceramic sample containing 10 vol% oriented {001}-$BaTiO_3$ templates, heated to 1150°C (annealed for 0 h).

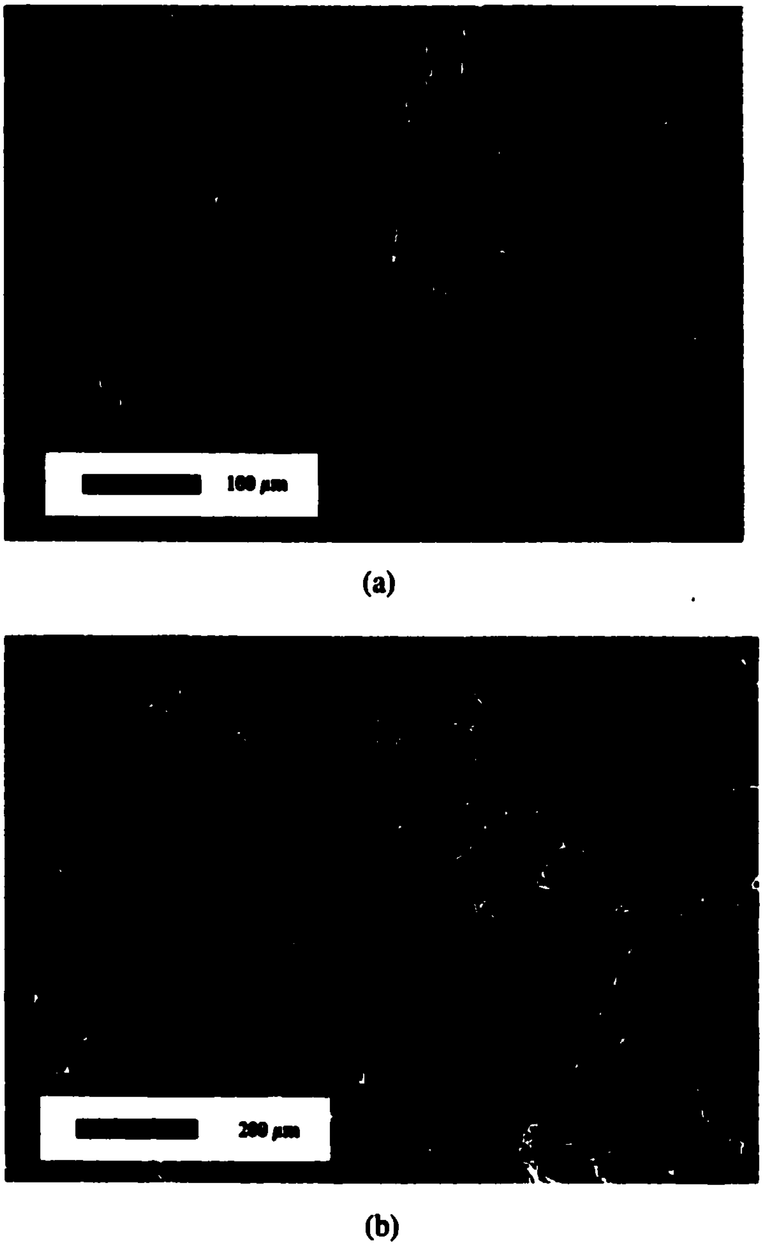

Figure 5.17: SEM micrographs showing the (a) cross-sectional and (b) top view of a PMN-32.5PT (1 wt% excess PbO) ceramic sample containing 10 vol% oriented {001}-$BaTiO_3$ templates annealed at 1150°C for 5 h.

decrease in the final density of the samples which affects both the electrical and mechanical properties of the material.

5.4 CONCLUSIONS

PMN-32.5PT ceramics were fiber-textured in the <001> through the use of the TGG process. {001}-$BaTiO_3$ Remeika crystals of ~75-150 μm in diameter were used as the templates for the process. Samples which contained a 5 vol% template concentration without excess PbO were textured to $f\approx0.45$ in 10 h at 1150°C. The growth kinetics were increased with the addition of 1 wt% excess PbO such that ~90%-textured PMN-PT ($f\approx0.90$) was obtained at 1150°C for 5 h with a template concentration of 5 vol%. The saturation in the rate of template growth, and therefore the texturing, was found to result from a decrease in the driving force for growth due to the coarsening matrix. Also, the increase in grain impingement and the decrease in template/matrix interfaces restricted further template growth. The rate of texturing was further accelerated by increasing the template concentration to 10 vol% where the ceramic would texture to $f\approx0.90$ on heating to 1150°C. Again, a further increase in texture fraction was limited by the contact of the templated grains. Template growth was also found to be restricted by the increase in porosity and intergranular void formation due to the grain impingement with further texturing.

5.5 REFERENCES

1) R.E. Newnham, "Composite Electroceramics," *Ferroelectrics*, **68** 1-32 (1986).

2) M.M. Seabaugh, I.H. Kerscht, and G.L. Messing, "Texture Development by Templated Grain Growth in Liquid-Phase-Sintered α-Alumina," *J. Am. Ceram. Soc.*, **80** [5] 1181-88 (1997).

3) C. Duran, S. Trolier-McKinstry, and G.L. Messing, "Fabrication and Electrical Properties of Textured $Sr_{0.53}Ba_{0.47}Nb_2O_6$ Ceramics by Templated Grain Growth," *J. Am. Ceram. Soc.*, **83** [9] 2203-13 (2000).

5) J.A. Horn, S.C. Zhang, U. Selvaraj, G.L. Messing, and S. Trolier-McKinstry, "Templated Grain Growth of Textured Bismuth Titanate," *J. Am. Ceram. Soc.*, **82** [4] 921-26 (1999).

6) S.-H. Hong, S. Trolier-McKinstry, and G.L. Messing, "Dielectric and Electromechanical Properties of Textured Niobium-Doped Bismuth Titanate Ceramics," *J. Am. Ceram. Soc.*, **83** [1] 113-118 (2000).

7) M.D. Sacks, G.W. Scheiffele, and G.A. Staab, "Fabrication of Textured Silicon Carbide via Seeded Anisotropic Grain Growth," *J. Am.Ceram. Soc.*, **79** [6] 1611-16 (1996).

8) K. Hirao, T. Nagaoka, M.E. Brito, and S. Kanzaki, "Microstructure Control of Silicon Nitride by Seeding with Rodlike β-Si_3N_4 Particles," *J. Am. Ceram. Soc.*, **77** [7] 1857-62 (1994).

9) S.-H. Hong, W. Cermignani, and G.L. Messing, "Anisotropic Grain Growth in Seeded and B_2O_3-Doped Diphasic Mullite Gels," *J. Euro. Ceram. Soc.*, **16** 133-41 (1996).

10) B. Brahmaroutu, G.L. Messing, S. Trolier-McKinstry, and U. Selvaraj, "Templated Grain Growth of Textured $Sr_2Nb_2O_7$"; pp. 883-86, Vol. 2, *Proceedings of the Tenth International Symposium on the Applications of Ferroelectrics*. Edited by B. Kuwicki, A. Amin, and A. Safari. IEEE, East Brunswick, NJ, 1996.

11) H.J. Bunge, "Textures in Non-Metallic Materials," *Textures and Microstructures*, **14-18** 283-326 (1991).

12) B.D. Cullity, *Elements of X-ray Diffraction, 2nd Ed.*, Addison-Wesley Publishing Company, Inc., Reading, MA (1978).

13) Y. Ohara, K. Koumoto, and H. Yanagida, "Barium Titanate Ceramics with High Piezoelectricity Fabricated from Fibrous Particles," *J. Am. Ceram. Soc.*, **68** [4] C108-C109 (1985).

14) T. Tani, "Crystalline-oriented Piezoelectric Bulk Ceramics with a Perovskite-type Structure," *J. Kor. Phys. Soc.*, **32** S1217-S1220 (1998).

15) D. Elwell and H.J. Scheel, *Crystal Growth from High-Temperature Solutions*. Academic Press, New York, New York (1975).

16) B.N. Roy, *Crystal Growth from Melts: Applications to Growth of Groups 1 and 2 Crystals*. John Wiley and Sons, Inc., New York (1992).

17) S.-K Kwon, S.-H. Hong, D.-Y. Kim, and N.M. Hwang, "Coarsening Behavior of Tricalcium Silicate (C_3S) and Dicalcium Silicate (C_2S) Grains Dispersed in a Clinker Melt," *J. Am. Ceram. Soc.*, **83** [5] 1247-52 (2000).

18) J.P. Remeika, "Method of Growing Barium Titanate Single Crystals," *J. Am. Chem. Soc.*, **76** [3] 940-41 (1954).

19) R.C. DeVries, "Observations on Growth of $BaTiO_3$ Crystals from KF Solutions," *J. Am. Ceram. Soc*, **42** [11] 547-58 (1959).

20) F.K. Lotgering, "Topotactical Reactions with Ferrimagnetic Oxides Having Hexagonal Crystal Structures-I," *J. Inorg. Nucl. Chem.*, **9** 113-23 (1959).

21) M.M. Seabaugh, E. Suvaci, B. Brahmaroutu, and G.L. Messing, "Modeling Anisotropic Single Crystal Growth Kinetics in Liquid Phase Sintered α-Al_2O_3," *Interface Science*, **8** [2-3] 257-267 (2000).

22) J.D. Powers and A.M. Glaeser, "Grain Boundary Migration in Ceramics," *Interface Science*, **6** 23-39 (1998).

23) M.K. Durbin, J.C. Hicks, S.-E. Park, and T.R. Shrout, "X-ray Diffraction and Phenomenological Studies of the Engineered Monoclinic Crystal Domains in Single Crystal Relaxor Ferroelectrics," *J. Appl. Phys.*, **87** [11] 8159-64 (2000).

24) O. Sudre and F.F. Lange, "Effect of Inclusions on Densification: I, Microstructural Development in an Al_2O_3 Matrix Containing a High Volume Fraction of ZrO_2 Inclusions," *J. Am. Ceram. Soc.*, **75** [3] 519-24 (1992).

25) O. Sudre, G. Bao, B. Fan, F.F. Lange, and A.G. Evans, "Effect of Inclusions on Densification: II, Numerical Model," *J. Am. Ceram. Soc.*, **75** [3] 525-31 (1992).

26) H. Sato, N. Otsuka, G.L. Liedl, and S. Mansour, "Formation of Elongated Particles in β-SiC Compacts," *Mater. Lett.*, **4** [3] 136-44 (1986).

27) D.R. Clarke, T.H. Shaw, A. Phillipse, and R.G. Horn, "Possible Electrical Double-Layer Contribution to the Equilibrium Thickness of Intergranular Glass Films in Polycrystalline Ceramics," *J. Am. Ceram. Soc.*, **76** [9] 1201-204 (1993).

Chapter 6

DIELECTRIC AND PIEZOELECTRIC PROPERTIES OF <001> FIBER-TEXTURED PMN-32.5PT CERAMICS

6.1 INTRODUCTION

Rhombohedral single crystal PZN-PT and PMN-PT near the MPB composition show enhanced strain levels combined with large piezoelectric and electromechanical coupling coefficients.(1,2) The large increase in these properties has been attributed to the domain engineering concept. Domain engineering of PZN-PT and PMN-PT requires single crystals to be poled in the <001>, which configures the dipoles along any of the four equivalent <111> directions ~54.7° from the poling direction. The four equivalent domains have the same energy state when the field is applied along the <001>, which results in a low driving force for domain wall movement. (1-3) The limited mobility of the domain walls produces the low piezoelectric (strain-field) hysteresis below the field-induced rhombohedral-tetragonal phase transformation. The enhanced strains are a result of the rotation of the dipoles within the stable domains towards the <001> with increasing field. The macroscopic displacement during this phase transformation is pronounced for rhombohedral compositions very near to the MPB composition. The low hysteresis and high strain levels are desired for the next generation of piezoelectric actuators and transducers.

As previously stated, the enhanced electromechanical properties for the domain engineered materials have been primarily identified for PZN-PT and PMN-PT single crystals. Recently, $BaTiO_3$ and Zr-doped $BaTiO_3$ single crystals have shown similar increased properties and decreased piezoelectric hysteresis due to the application of the domain engineering concept for perovskite ferroelectrics which show a rhombohedral-tetragonal phase transition.[4,5] The domain engineering technique seems to be suitable for single crystals, therefore, one would believe that domain engineering would also apply to thin films and ceramics textured in the <001> of the same compositional systems. Regardless of the <001> orientation of PMN-PT thin films, the piezoelectric coefficients always decreased by the substrate clamping.[6,7] The property enhancement due to <001>-texturing in rhombohedral Pb-based relaxor-$PbTiO_3$ ceramics, or in any ferroelectric ceramic showing an rhombohedral-tetragonal MPB composition, has not yet been investigated.

In this work, PMN-32.5PT ceramics were fiber-textured in the <001> by the TGG process using a low concentration ($\leq$10 vol%) of oriented {001}-$BaTiO_3$ crystals. The objective was to observe the effect of <001> fiber-texture on the dielectric and piezoelectric properties of the PMN-32.5PT ceramics. Many issues are addressed in this work relating to the effect of excess PbO, residual $BaTiO_3$, and texture degree on the piezoelectric response of the textured ceramics. The absence of three-dimensional texture and the presence of intragranular $BaTiO_3$ inclusions are two key issues which may have adverse effects on the piezoelectric response of the textured PMN-PT ceramics. Both may cause mechanical clamping of the oriented grains, which would decrease the overall property improvement related to crystallographic and domain engineering. These subjects are all addressed in this work.

6.2 EXPERIMENTAL PROCEDURES

As described in Chapter 5, polycrystalline 0.675Pb(Mg$_{1/3}$Nb$_{2/3}$)O$_3$-0.325PbTiO$_3$ (PMN-32.5PT) was fiber-textured in the <001> by the TGG process. The matrix PMN-32.5PT powder used for the study was synthesized by the columbite method and mixed with $(PbCO_3)_2Pb(OH)_2$ (Aldrich Chemical Company, Inc., Milwaukee, WI) to produce a matrix composition containing 1 wt% excess PbO. All textured samples characterized in this work contained 1 wt% excess PbO in order to drive the TGG process to completion. The matrix was mixed with 5 vol% or 10 vol% {001}-BaTiO$_3$ template crystals which were grown by the Remeika process. The template crystals displayed thicknesses of <75 μm and diameters of approximately 75-150 μm. The matrix composition was tape cast, cut, and laminated. The samples were burned out and then hot-pressed in argon at 900°C for 30 min. at 40 MPa. The samples were cut to a dimension of 4x3x0.350 mm and annealed in O$_2$ at 1150°C for times ≤5 h to allow adequate time for template growth to increase the total texture fraction. The surface of the samples was polished to 1 μm roughness and XRD was performed on the sample surfaces to determine the texture fraction. The texture fraction was determined by the Lotgering method.(8) Gold electrodes were sputtered on the sample surface perpendicular to the textured <001>.

The texture fractions varied across the volume of the samples due to the size and inhomogeneous mixing of the oversized template particles. The texture fractions reported for each sample in this work were calculated and averaged over ≥3 XRD patterns taken at various depths through the sample thickness. The listed texture fractions contain approximately ±5% error, therefore, the samples displaying similar texture fractions which were similar within ±5% were grouped for property versus texture comparisons.

Standard dielectric and piezoelectric data of randomly-oriented PMN-32.5PT ceramics containing 0 wt%, 1 wt%, and 3 wt% excess PbO were measured on the same matrix powder used for the texturing experiments. The cylindrical-shaped random samples were formed by isostatic-pressing at room temperature. The random samples were sintered at 1150°C and then polished to a final dimension of ~6.3 mm. in diameter and 0.350 mm. in thickness. These sample dimensions were chosen in order to have random samples of similar area and thickness as the textured samples. The sample densities were ~98-99% of theoretical density, depending upon the excess PbO content. Samples which lost >0.5 wt% after sintering were discarded from the study.

The low field dielectric constant and loss (at 1 V) were measured as a function of temperature by a multifrequency impedance meter (HP 4284A LCR meter) combined with an oven regulated by an Eurotherm controller (Euro 808). The dielectric constant and loss were measured between the temperatures of 0-300 °C for frequencies between 1 kHz-1 MHz. Poled samples were measured on heating and unpoled samples were measured on cooling. The samples were heated and cooled at a rate of 4°C/min. The untextured and textured PMN-32.5PT samples were typically poled with a DC-bias of 40 kV/cm for 15 min at room temperature in polydimethylsiloxane (Dow Corning 200).

The dielectric polarization versus electric field measurements (P-E hysteresis loops) were completed using a modified Sawyer-Tower circuit. The unipolar strain versus electric field measurements (strain-field curves) were concurrently measured using the Sawyer-Tower circuit in conjunction with a linear variable differential transducer, driven by a lock-in amplifier (Standford Research Systems, Model SR830). The required high fields were generated by a Trek 609C-6 high-voltage amplifier. The strain and polarization of the samples were measured while immersed in Galden HT-200 to prevent arcing. The P-E measurements were traced using a triangular wave form. Unipolar strain-field curves were measured using the same apparatus by applying half of a sinusoidal wave to the poled samples.

The low-field piezoelectric coefficients (d_{33}) for the samples were estimated from the slope of the unipolar strain-field curves. The piezoelectric coefficients were also measured with a Berlincourt d_{33} meter (Institute of Acoustics, Academia Sinica, Model ZJ-2). The longitudinal and lateral electromechanical coupling coefficients (k_{33}, k_{31}) were measured in accordance with the IEEE standards for the resonance technique (ANSI/IEEE Std. 176-1978) using a HP 4194A impedance/gain phase analyzer. From the measured resonance (f_r) and antiresonance (f_a) frequencies, the compliance (s_{33}^E, s_{33}^D, s_{11}^E, s_{11}^D) and piezoelectric coefficients (d_{33}, d_{31}) were also calculated. The f_r and f_a frequencies were determined from the first minimum and maximum impedance peaks in the impedance/frequency scan.

6.3 RESULTS AND DISCUSSION

6.3.1 Dielectric Properties of Random PMN-32.5PT Ceramics

Figure 6.1 shows the dielectric constant and loss as a function of temperature for an unpoled (Fig. 6.1(a)) and poled (Fig. 6.1(b)) PMN-32.5PT randomly-oriented sample containing 0 wt% excess PbO. Both the unpoled and poled PMN-32.5PT samples show

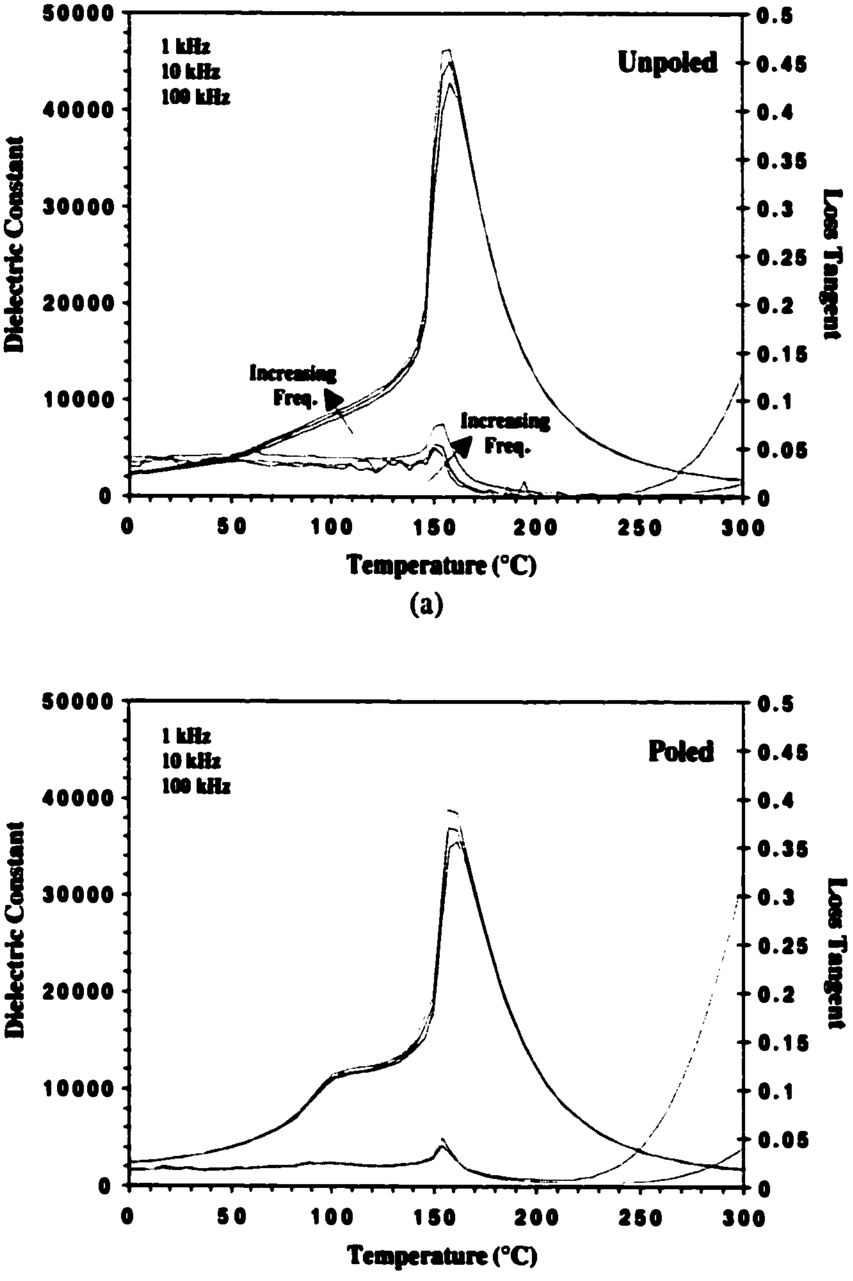

(a)

(b)

Figure 6.1: Dielectric constant and loss as a function of temperature for an a) unpoled and b) poled PMN-32.5PT ceramic containing 0 wt% excess PbO.

little frequency dispersion and have relatively narrow permittivity peaks. The poled sample displays two major anomalies in the dielectric constant as a function of temperature. The anomaly at ~90-100°C ($T_{r\text{-}t}$) indicates the phase transition from the ferroelectric rhombohedral to the tetragonal state.(9-11) The second anomaly describes the phase transition from the ferroelectric tetragonal state to the paraelectric cubic state.(9-14) The unpoled sample shows only one distinct dielectric anomaly marking the paraelectric-ferroelectric phase transition. This temperature will be designated as the maxima temperature (T_{max}), since the PMN-32.5PT composition shows a slightly diffuse phase transition. PMN-PT compositions containing lower $PbTiO_3$ concentrations usually show greater dielectric broadening at the paraelectric-ferroelectric phase transition due to compositional fluctuations.(9,10,12,13) The diffusive phase transition indicates the presence of multiple localized phase transition temperatures, therefore the dielectric anomaly maximum is usually termed the T_{max}. T_{max} did not change with poling state ($T_{max}^{unpoled} \approx 158°C$ and $T_{max}^{poled} \approx 159°C$). The phase diagram reported by Zhao *et al.*(11) shows that a PMN-PT composition with 32.5 mol% $PbTiO_3$ has a $T_{max} \approx$ 162°C and a $T_{r\text{-}t} \approx$ 78°C. This implies that the actual matrix composition may be between 31.5-32 mol% $PbTiO_3$, since the MPB of the PMN-PT system curves towards the PMN composition resulting in a higher T_{max} and a lower $T_{r\text{-}t}$.

The unpoled sample showed a maximum dielectric constant (ε_{max}) of ~46,300 (1 kHz) at T_{max} with a loss tangent of ~0.022 (Fig. 6.1(a)). The room temperature (25°C) dielectric constant (ε_{rt}) was ~3060 (1 kHz) with a loss tangent ~0.03. The maximum and room temperature dielectric constant was found to be smaller for the poled sample with a

ε_{max} ≈36900 (1 kHz) and a ε_{rt} ≈2880 (1 kHz) (Fig.6.1(b)). The ε_{max} observed in these experiments were greater than those reported by Choi *et al.*(9,10) and Kelley *el al.*(13) ($\varepsilon_{max}^{unpoled}$ ≈30,000-40,000, $\varepsilon_{max}^{poled}$≈ 30,000) and the ε_{rt} was lower ($\varepsilon_{rt}^{unpoled}$ ≈3700-4100, ε_{rt}^{poled} ≈5000). The maximum dielectric constant and loss were noticeably affected by poling and heating the sample through the rhombohedral-tetragonal phase transition. This may be due in part to the differences in the domain wall contributions to the dielectric constant and loss.(15,16)

The effect of an intergranular Pb-rich phase on the dielectric properties of PMN-PT has been reported by many authors.(17-25) The thin, intergranular layer of a Pb-rich phase lowers the dielectric constant and increases the loss for various PMN-PT compositions. These effects have been successfully described by brick-wall dielectric mixing laws.(17-25) Similarly in this work, the addition of excess PbO to the PMN-32.5PT composition was found to suppress the dielectric constant of the material. A comparison of the dielectric constants, loss tangents, and transition temperatures for the PMN-32.5PT ceramic samples containing 0 wt%, 1 wt%, and 3 wt% excess PbO is listed in Table 6.1. With the addition of 1 wt% or 3 wt% excess PbO, the poled ε_{max} decreased to ~20,300 and ~17,700 (1 kHz), respectively (Fig. 6.2). The additions of excess PbO also shifted the phase transition temperatures (T_{r-t}, T_{max}) to higher temperatures. Shifts in the T_{max} for PMN and PZT have been attributed to the volume of intergranular low-ε (low polarizable) phases and defects.(23,26) The presence of low-ε phases and vacancies at the grain boundaries affects the space-charge field and surface stresses around the grains. The presence of intergranular imperfections may alter the stress distribution and stabilize

Table 6.1: Dielectric properties of random PMN-32.5PT ceramics.

Unpoled

Excess PbO (wt%)	ε_{rt}	Tanδ_{rt}	ε_{max}	Tanδ_{max}	T_{max} (°C)
0	3060	0.030	46300	0.022	158
1	2430	0.019	21800	0.016	166
3	2290	0.026	20500	0.015	167

Poled

Excess PbO (wt%)	ε_{rt}	Tanδ_{rt}	ε_{max}	Tanδ_{max}	T_{max} (°C)
0	2880	0.018	36900	0.038	159
1	2220	0.025	20300	0.019	166
3	1970	0.026	17700	0.019	167

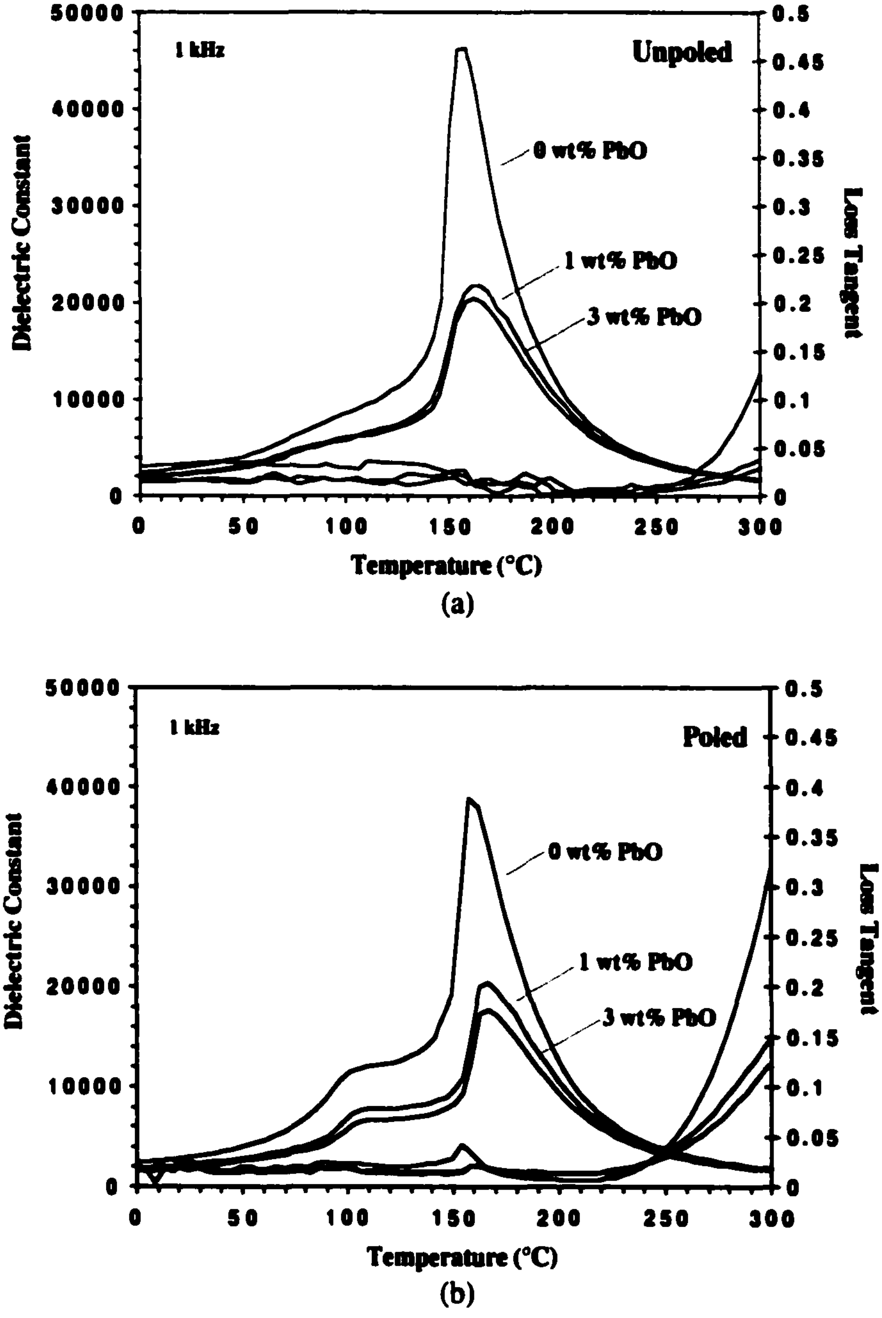

Figure 6.2: Dielectric constant and loss as a function of temperature for a) unpoled and b) poled PMN-32.5PT ceramics containing 0 , 1, and 3 wt% excess PbO.

the space-charge field around the grains which would "lock-in" the ferroelectric polarization, allowing the dipoles to persist to higher than normal temperatures.(23,26,27) The dielectric loss for these samples containing excess PbO were still relatively low (δ<0.05), therefore the influence of the space-charge may not have induced the temperature shift. The shift may be the result of incidental noise from the property measurement.

6.3.2 Ferroelectric Hysteresis of Random PMN-32.5PT Ceramics

Figure 6.3 shows the effect of excess PbO content on the dielectric polarization as a function of applied electric field measured. All of the matrix compositions possess well-saturated P-E hysteresis loops displaying a "soft" ferroelectric nature. The remanent polarization (P_r) and coercive field (E_c) values measured from the P-E hysteresis loops are listed in Table 6.2. The obtained values for both the P_r (~32 $\mu C/cm^2$) and E_c (~5-7 kV/cm) were higher than those reported in literature ($P_r \approx 25$ $\mu C/cm^2$, $E_c \approx 4.5$ kV/cm).(28) With an increase in PbO content, the P_r decreased and the E_c increased. This is expected since the low polarizability of the PbO-phase in the grain boundary would limit the localized applied field on the grains, therefore, the grains would experience a smaller fraction of the total applied field, resulting in an increase in the required field to move the domain walls. Also, as previously discussed, the presence of the low-ε intergranular phase affects the surface space-charge restricting the dipole movement within the grains.(26,27,29-31) This would cause a decrease in the macroscopic polarization and an increase in the field required to move the domain walls.

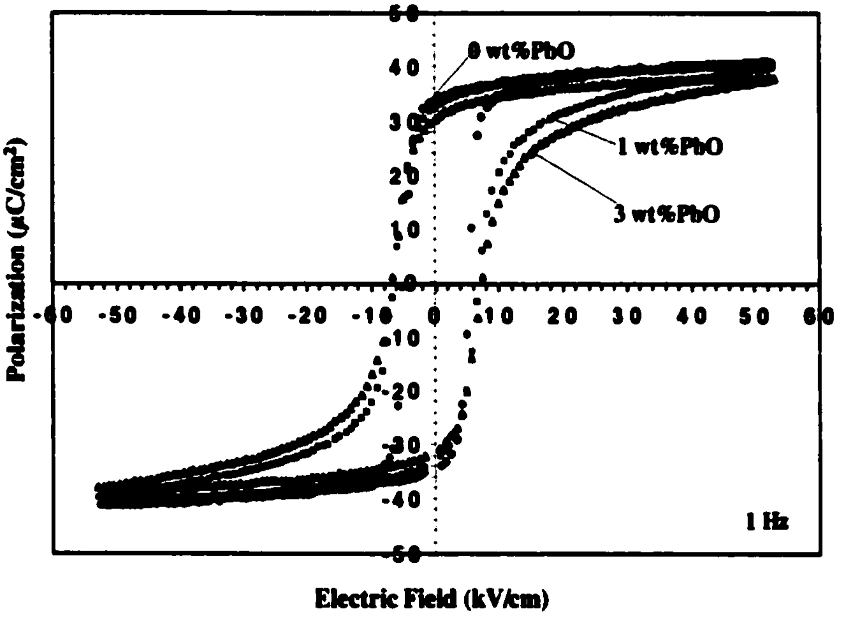

Figure 6.3: Polarization-electric field hysteresis for PMN-32.5PT ceramics containing 0 , 1, and 3 wt% excess PbO.

Table 6.2: E_c and P_r of random PMN-32.5PT ceramics.

Excess PbO (wt%)	E_c (kV/cm)	P_r ($\mu C/cm^2$)
0	5.1	34.6
1	6.7	32.4
3	7.1	30.4

6.3.3 Diffuseness Characteristics of Random PMN-32.5PT Ceramics Containing Excess PbO

For normal ferroelectric materials, the temperature dependence of the dielectric constant for a fixed frequency can be described by the Curie-Weiss relationship. Above the T_c, Curie-Weiss behavior exhibits a linear relationship between the inverse of the dielectric constant and temperature ($T-T_c$). This relationship does not hold for relaxor ferroelectric materials like PMN. Due to the diffuseness of the phase transition, Smolenski(32,33) found that relaxor ferroelectrics follow the empirical relationship:

$$\frac{1}{\varepsilon}=\frac{1}{\varepsilon_{\max}}+\frac{(T-T_{\max})^2}{2\delta^2\varepsilon_{\max}} \qquad \text{Eq. 6.1}$$

where ε is the temperature dependent dielectric constant, ε_{max} is the dielectric constant at T_{max}, and δ is a diffusiveness parameter. This relationship shows that the dependence of the inverse dielectric constant to temperature follows a quadratic law. It has been reported that various pure or substituted PMN-PT and PZN-PT ceramic compositions show intermediate behavior between the Curie-Weiss and quadratic laws. Therefore, these expressions were modified to produce an intermediate empirical power law which is given as:

$$\frac{1}{\varepsilon}=\frac{1}{\varepsilon_{\max}}+\frac{(T-T_{\max})^{\gamma}}{C} \qquad \text{Eq. 6.2}$$

where γ is the diffuseness exponent.(34) The γ can range between 1 and 2, where γ=1 and γ=2 describes the behavior of a purely normal and relaxor ferroelectric, respectively. The ratio of C/ε_{max} (units are in °C^{γ}) is a relative measure of the degree of diffuseness for the material. By fitting Eq. 6.2 to the data presented in Fig. 6.2(a), the γ and C/ε_{max} were calculated (R^2>0.99) for the PMN-32.5PT ceramics samples containing 0 wt%, 1 wt%, and 3 wt% excess PbO. The pure PMN-32.5PT showed a dielectric behavior favoring that displayed by a relaxor ferroelectric (γ=1.65 and a C/ε_{max}=139). The magnitude of γ increased with the addition of excess PbO, where γ equaled 1.68 and 1.78 for the 1 wt% and 3 wt% excess PbO samples, respectively. The C/ε_{max} also increased with the addition of PbO, 328 and 625 for 1 wt% and 3 wt% excess PbO, respectively. The increase in γ and C/ε_{max} indicated that the PMN-PT samples are shifting towards more diffuse phase transitions. The broad dielectric peak could be the result of the intergranular PbO acting as a Curie point depressor.(21)

6.3.4 Piezoelectric Properties of Random PMN-32.5PT Ceramics from Berlincourt and Strain-Field Measurements

The piezoelectric coefficient (d_{33}) was measured using a Berlincourt d_{33} meter for randomly-oriented PMN-32.5PT ceramics containing 0 wt%, 1 wt%, and 3 wt% excess PbO. These samples showed initial d_{33} values of approximately 580±5 pC/N, 425±6 pC/N, and 420±5 pC/N at 100 Hz, respectively. These d_{33} coefficients decreased at a rate of ~4%/decade (sec) due to aging (Fig. 6.4). The final, stable d_{33} values for the 0 wt%, 1 wt%, and 3 wt% excess PbO samples were approximately 550 pC/N, 380 pC/N, and 360

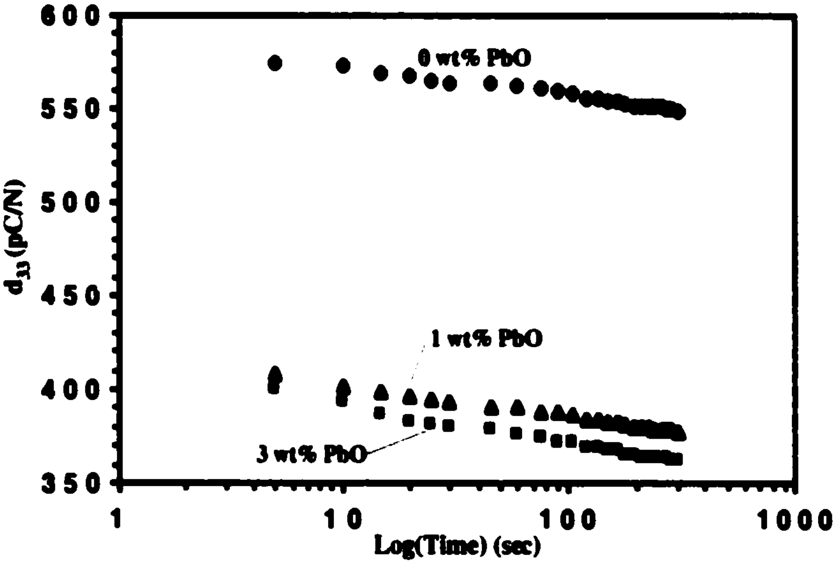

Figure 6.4: Piezoelectric coefficients (d_{33}) as a function of measuring time by a Berlincourt meter for PMN-32.5PT ceramics containing 0, 1, and 3 wt% excess PbO measured.

pC/N, respectively. The initial d_{33} values measured for the 32.5 mol% $PbTiO_3$ composition were comparable with the coefficients reported in literature, but the stable d_{33} values were at least 40-160 pC/N lower.(9,10,13,35,36)

The d_{33} coefficients were also measured by direct observation of the unipolar strain-field curves collected by the low contact variable transducer. Fig. 6.5 shows the typical strain-field response for the PMN-32.5PT samples containing variable excess PbO concentrations. The sample having 0 wt% excess PbO showed a slightly higher strain response than the samples containing excess PbO. The strain (% strain/field) for all compositions decreased with higher fields. The d_{33} coefficients were estimated from the slope of the curves at fields <5 kV/cm and <10 kV/cm. The d_{33} values, maximum strain (at 50 kV/cm), and maximum piezoelectric opening in the strain/field curves (i.e. maximum difference between increasing and decreasing field curves) are reported in Table 6.3. The hysteresis is a result of domain wall motion due to non-stable domain configurations.(2) The d_{33} coefficients, strain levels, and hysteresis were shown to be very similar for all samples regardless of the composition.

6.3.5 Piezoelectric Properties of Random PMN-32.5PT Ceramics from IEEE Resonance Measurements

IEEE resonance measurements were completed in order to investigate the set of low-field properties. The piezoelectric coefficients (d_{33}, d_{31}), mechanical compliances (s_{33}^E, s_{33}^D, s_{11}^E, s_{11}^D), and the electromechanical coupling coefficients (k_{33}, k_{31}) can be calculated from the measured resonant frequency (f_r) and the anti-resonant frequency (f_a) of the sample impedance. In order to calculate the longitudinal coefficients (k_{33}, s_{33}...),

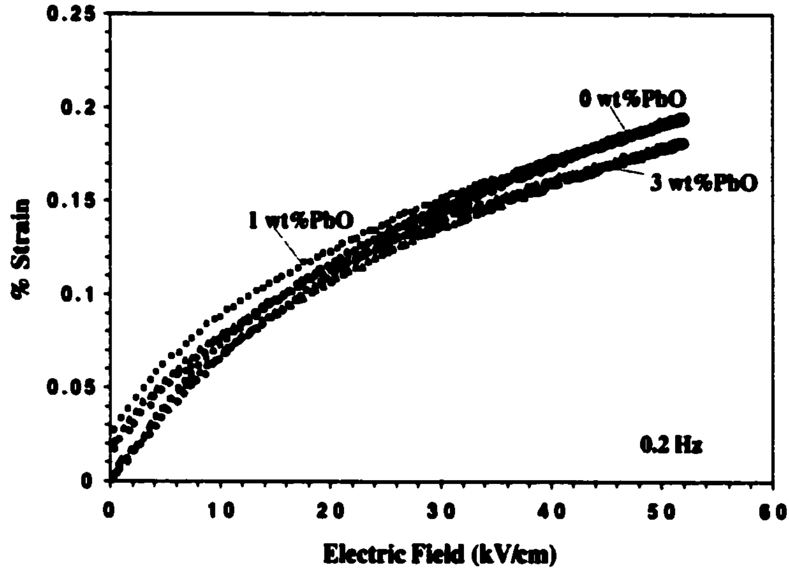

Figure 6.5: Unipolar strain-electric field curves for PMN-32.5PT ceramics containing 0 , 1, and 3 wt% excess PbO.

Table 6.3: Piezoelectric properties of random PMN-32.5PT ceramics measured from the strain-field plots.

Excess PbO (wt%)	d_{33} (pC/N) (<5 kV/cm)	d_{33} (pC/N) (<10 kV/cm)	% Strain (50 kV/cm)	Max. Opening in Curve (%)
0	726	580	0.180	0.0180
1	721	593	0.177	0.0200
3	720	572	0.171	0.0195

the samples were cut to the dimensional ratio of 5:1:1 (5×1×1 mm) and the impedance was measured along the length (poled direction). The transverse coefficients were obtained from samples with the dimensional ratio of 4:1:0.4 (4×1×0.4 mm) with the impedance measured in the thickness direction (poled direction). The various mechanical and electromechanical constants were calculated using the following relationships (ANSI/IEEE Std. 176-1978):

$$k_{33}=\frac{\pi}{2}\cdot\frac{f_r}{f_a}\cdot\tan\left(\frac{\pi}{2}\cdot\frac{\Delta f}{f_a}\right) \qquad \frac{k_{31}^2}{1-k_{31}^2}=\frac{\pi}{2}\cdot\frac{f_a}{f_r}\cdot\tan\left(\frac{\pi}{2}\cdot\frac{\Delta f}{f_r}\right)$$

$$\frac{1}{s_{33}^D}=4\cdot\rho\cdot f_a\cdot l^2 \qquad \frac{1}{s_{11}^E}=4\cdot\rho\cdot f_r\cdot l^2$$

$$s_{33}^E=\frac{s_{33}^D}{(1-k_{33}^2)} \qquad s_{11}^D=(1-k_{31}^2)s_{11}^E$$

$$d_{33}=k_{33}\sqrt{\varepsilon_0\varepsilon_{33}^T s_{33}^E} \qquad d_{31}=-k_{31}\sqrt{\varepsilon_0\varepsilon_{33}^T s_{11}^E}$$

The superscripts *T*, *E*, and *D* indicate that the property was measured at constant stress, electrical field, or dielectric displacement, respectively. Figure 6.6 shows the typical longitudinal resonance impedance spectra obtained for random PMN-32.5PT ceramics containing 0 wt% excess PbO (Fig. 6.6(a)) and 1 wt% excess PbO (Fig. 6.6(b)). The resonance and anti-resonance peaks are well defined with little interference from other

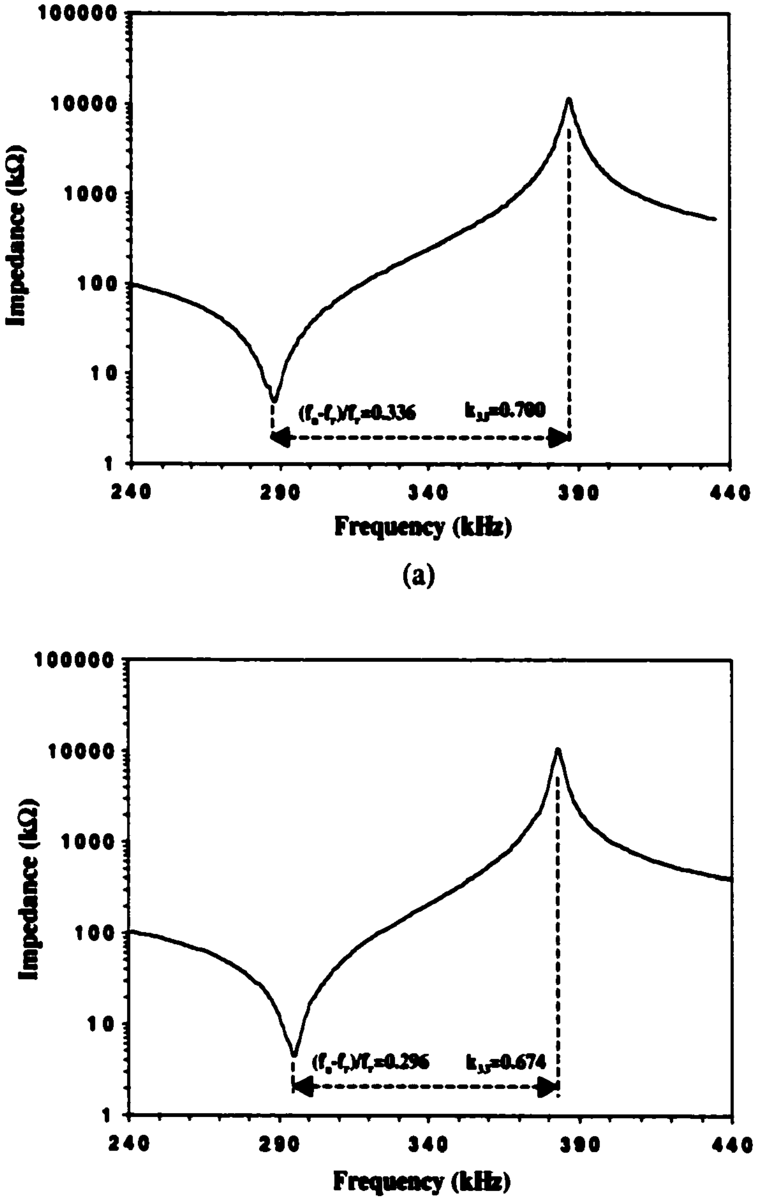

(a)

(b)

Figure 6.6: Impedance as a function of frequency near resonance of PMN-32.5PT ceramics containing (a) 0 wt%, (b) 1 wt%, and (c) 3 wt% excess PbO (longitudinal measurement).

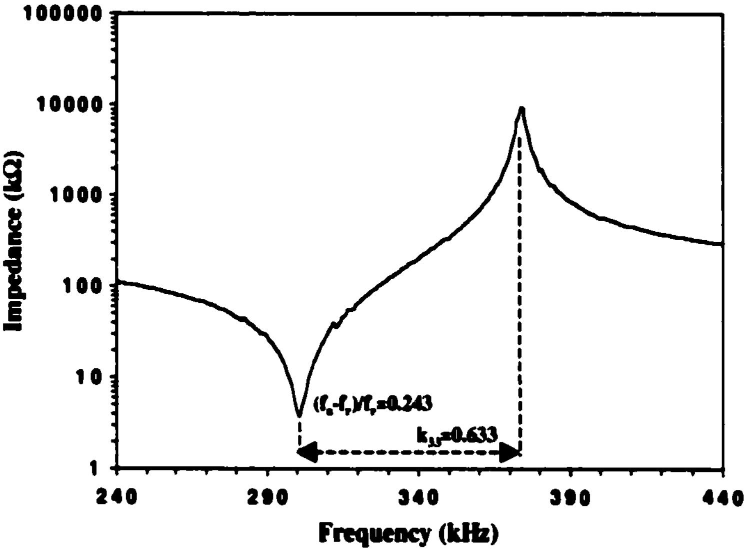
100000
10000
1000
100
10
1
Impedance (kΩ)
240
290
340
390
440
Frequency (kHz)
$(f_a-f_r)/f_r=0.243$
$k_{33}=0.633$

(c)

Table 6.4: Piezoelectric, electromechanical coupling, and compliance coefficients of random PMN-32.5PT ceramics measured by the resonance technique.

Excess PbO (wt%)	d_{33} (pC/N)	d_{31} (pC/N)	k_{33}	k_{31}	s_{33}^E (×10^{-12} m^2/N)	s_{11}^E (×10^{-12} m^2/N)
0	450 ±16	-211 ±10	0.719 ±0.02	0.403 ±0.003	17.7 ±0.41	12.5 ±0.01
1	376 ±6	-195 ±8	0.673 ±0.002	0.402 ±0.001	15.6 ±0.05	11.7 ±0.05
3	346 ±24	-168 ±7	0.635 ±0.028	0.355 ±0.001	15.0 ±0.44	11.9 ±0.01

peaks. The calculated values for the material constants are listed in Table 6.4. The standard deviations were collected for a set of >5 samples. The calculated constants show values similar to a soft PZT. The d_{33}/d_{31} ratio was found to be ~2.05 which is close to that typically found for many perovskite ferroelectric materials (~2.32).(7) All of the calculated constants decreased with an excess PbO concentration. This is in contrast to the strain-field measurements, where there was little change in the piezoelectric response with an increase in PbO content. Also, the low field d_{33} values calculated from the resonance technique were only 48-62% of the values measured from the strain-field curves (<5 kV/cm). This shows that the d_{33} values observed from the stain-field response were inflated due to the extrinsic contribution of the domain wall movement even when the samples exhibited relatively little hysteresis.(15,16,37) Since the resonance measurement is a low field technique (<0.05 kV/cm), domain wall movement contributes less to the piezoelectric response.

6.3.6 Effect of DC Bias on the Resonance Measurements of Random PMN-32.5PT Ceramics

The hysteresis in the strain-field curves indicated the presence of domain states which can be altered by an applied electrical field. In order to stabilize the domain state on the piezoelectric coefficient, a DC bias was applied to the sample during the AC resonance measurements. A DC bias ≤10 kV/cm was applied to a k_{31} resonant sample containing 0 wt% excess PbO during an impedance sweep. The calculated k_{31} values decreased from 0.415 to 0.379 with an increase in DC bias from 0-10 kV/cm (Fig. 6.7). Fig. 6.8 shows the effect of a forward and reverse DC bias on the poled dielectric

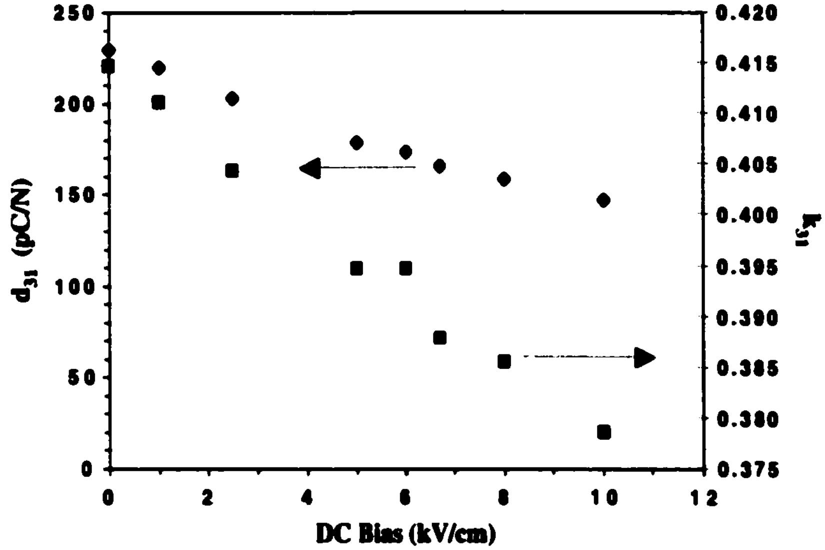

Figure 6.7: d_{31} and k_{31} as a function of DC bias for PMN-32.5PT ceramics containing 0 wt% excess PbO.

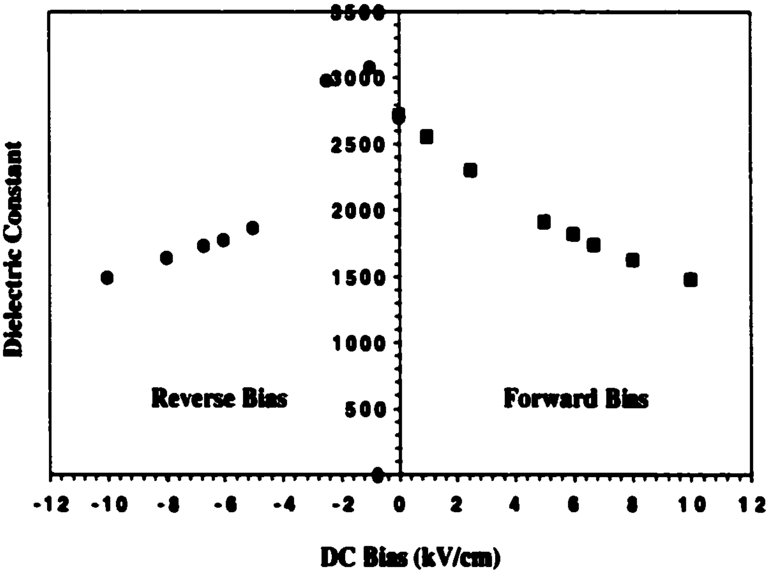

Figure 6.8: Dielectric constant (ε_{33}^{T}) as a function of DC bias for PMN-32.5PT ceramics containing 0 wt% excess PbO.

constant (ε_{33}^T). As expected, the ε_{33}^T decreased with an increase in forward bias due to the decrease in dielectric compliance.(38) On reverse bias, the ε_{33}^T was shown to first increase as the coercive field (~5 kV/cm) was approached then dropped again as the sample repoled. Since, both the k_{31} and ε_{33}^T decreased with an increasing DC bias, the d_{31} also decreased (Fig. 6.7). This indicates that the samples were sufficiently poled, and the DC bias was shown to have a negative effect on the dielectric and mechanical compliance of the material.

6.3.7 Dielectric Properties of <001>-Textured PMN-32.5PT Ceramics

Figures 6.9-6.11 show plots of the dielectric constant as a function of temperature for three PMN-32.5PT ceramic samples containing 5 vol% {001}-$BaTiO_3$ template particles (PMN-32.5PT-5BT). The samples all contained 1 wt% excess PbO in order to increase the TGG kinetics. The samples were densified to ~99% by hot-pressing in argon. Each sample experienced a different high temperature annealing treatment to drive the TGG process. Two sample sets were annealed to 1150°C for 0 h or 5 h, which resulted in samples having a <001>-texture fraction of ~0.80 (Fig. 6.10) and ~0.90 (Fig. 6.11), respectively. The last sample set was only annealed to 800°C for 10 h in order to reoxidize the sample without altering the random ($f \approx 0$) PMN-PT/$BaTiO_3$ microstructure (Fig. 6.9). Table 6.5 lists the maximum and room temperature dielectric constant and loss for the poled and unpoled textured samples. The unpoled (Fig. 6.9(a)) and poled (Fig. 6.9(b)) dielectric responses of the random PMN-32.5PT-5BT sample were similar, with both showing a very broad peak at a $T_{max} \approx 167°C$. This random PMN-32.5PT-5BT

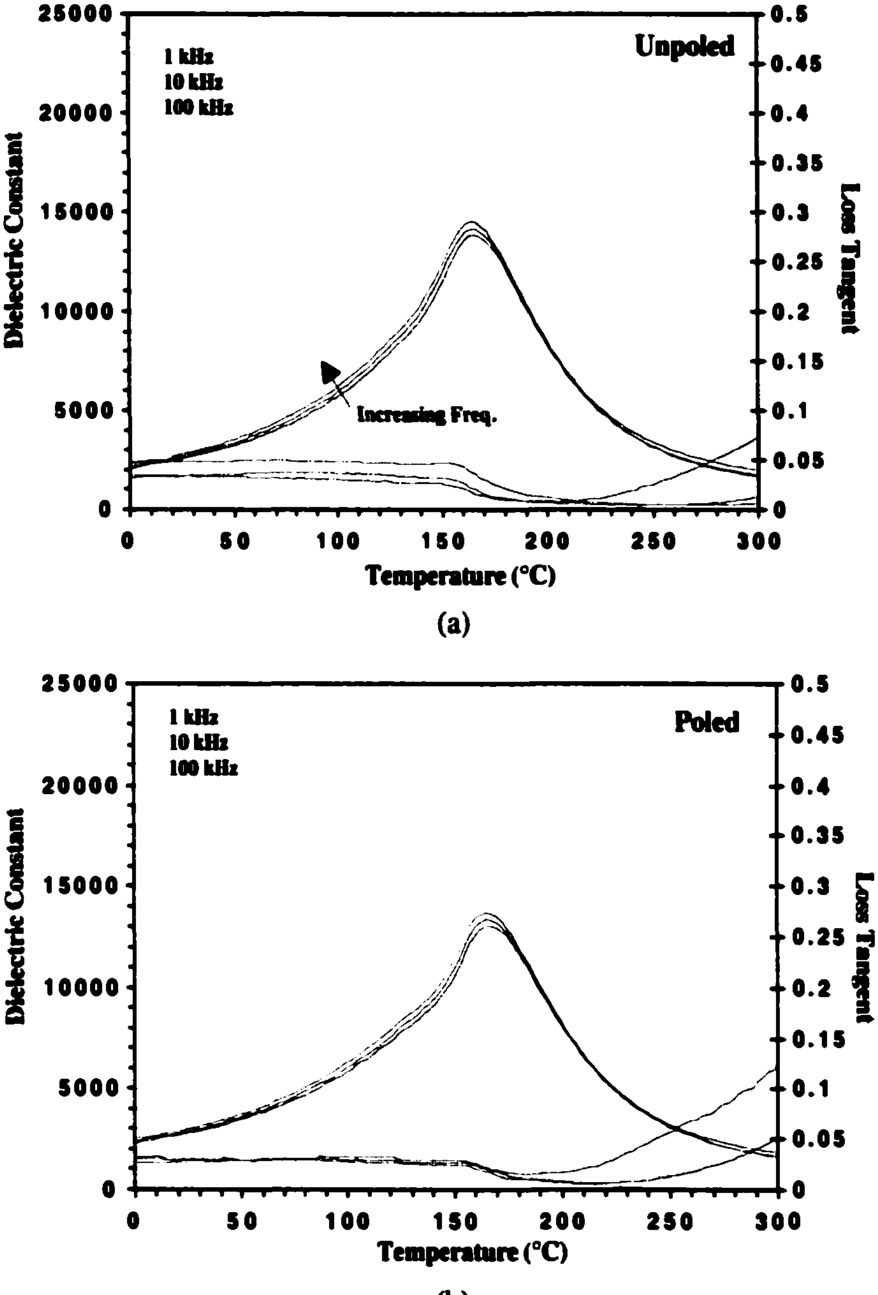

(a)

(b)

Figure 6.9: Dielectric constant and loss as a function of temperature for an a) unpoled and b) poled PMN-32.5PT ceramic containing 5 vol% $BaTiO_3$ templates (PMN-32.5PT-5BT) annealed at 800°C for 10 h.

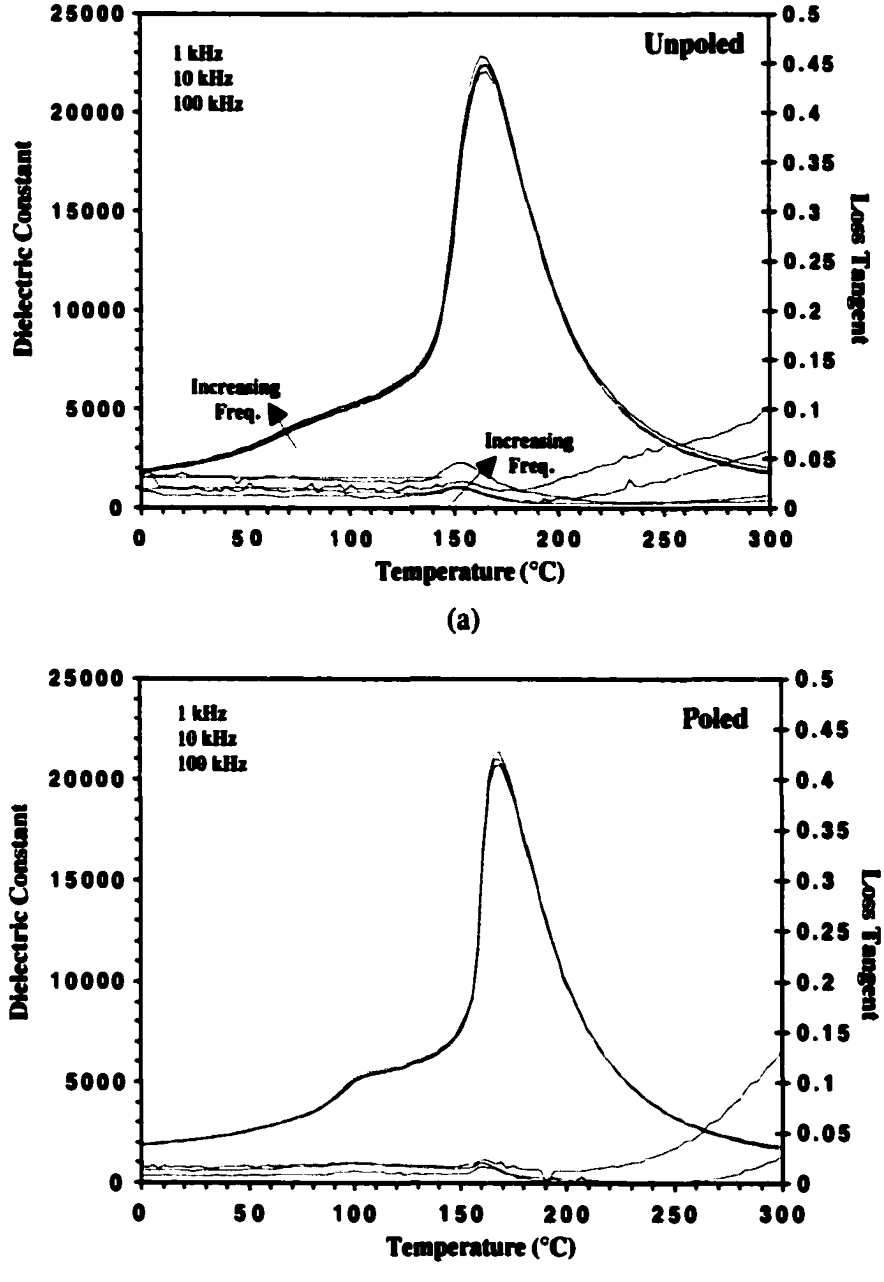

(a)

(b)

Figure 6.10: Dielectric constant and loss as a function of temperature for an a) unpoled and b) poled PMN-32.5PT ceramic containing 5 vol% $BaTiO_3$ templates (PMN-32.5PT-5BT) annealed at 1150°C for 0 h.

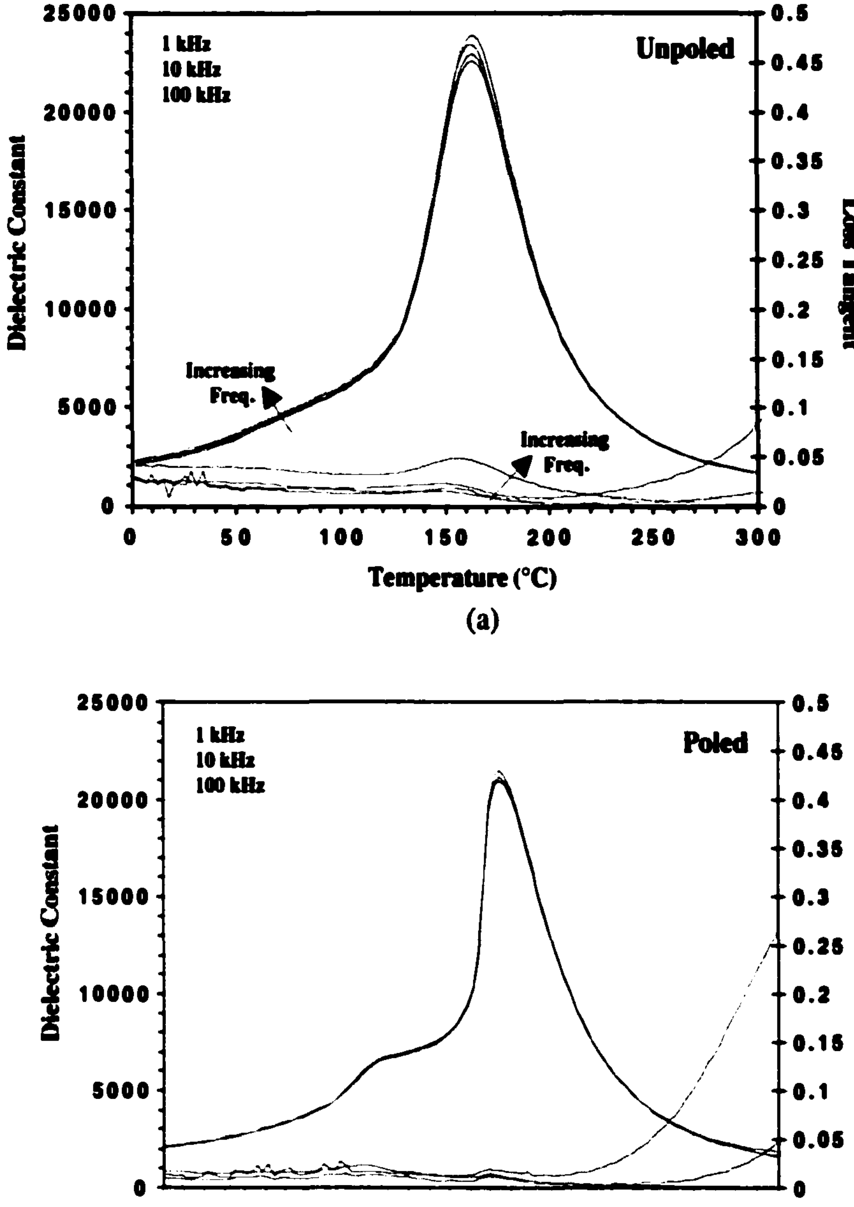

Figure 6.11: Dielectric constant and loss as a function of temperature for an a) unpoled and b) poled PMN-32.5PT ceramic containing 5 vol% $BaTiO_3$ templates (PMN-32.5PT-5BT) annealed at 1150°C for 5 h.

Table 6.5: Dielectric properties of textured PMN-32.5PT ceramics containing 5 vol% $BaTiO_3$ templates.

Unpoled

Texture Fraction	ε_{rt}	$Tan\delta_{rt}$	ε_{max}	$Tan\delta_{max}$	T_{max} (°C)
0	2760	0.033	14460	0.020	164
0.80	2270	0.022	22800	0.020	164
0.90	2750	0.021	23350	0.016	164

Poled

Texture Fraction	ε_{rt}	$Tan\delta_{rt}$	ε_{max}	$Tan\delta_{max}$	T_{max} (°C)
0	2750	0.028	13700	0.020	166
0.80	2120	0.015	21300	0.018	167
0.90	2440	0.013	21400	0.017	165

sample displayed a more diffuse transition, as well as more frequency dispersion than the samples without $BaTiO_3$ for the same PbO content. The rhombohedral-tetragonal transition at T_{r-t} (~95-105°C for random 1 wt% excess PbO samples) could not be identified which may indicate the limited ability to efficiently pole the sample due to the presence of the $BaTiO_3$ second phase. The T_{max} (~163°C) was not affected by the addition of the $BaTiO_3$ templates. This indicates that little Ba homogenization (i.e. solid solution formation) occurs at this temperature and time.(39-43) Although $BaTiO_3$ did not affect the ferroelectric-paraelectric transition temperature, it did have a large affect on the magnitude of the dielectric constant. The PMN-32.5PT-5BT ceramic showed a lower ε_{max} (~14,460 at 1 kHz) possibly due to the minor $BaTiO_3$ phase, which possesses a lower dielectric constant. By utilizing dielectric series and logarithmic mixing laws, it was calculated that a 5 vol% $BaTiO_3$ addition to PMN-32.5PT (1 wt% excess PbO) ceramic would cause a decrease of <2100 in the effective dielectric constant.(17,18,23) Therefore, the addition of the $BaTiO_3$ phase could not account completely for the decrease in the dielectric response. Chu *et al.* reported that Pb-vacancies in $Pb(Sc_{1/2}Nb_{1/2})O_3$ (PSN) ceramics resulted in a decrease in the transition temperature and dielectric constant.(44) The Pb-vacancies were reported to inhibit dipole coupling and broaden the ferroelectric transformation. The presence of Pb-vacancies remaining in the PMN-PT templated samples after the hot-pressing and annealing treatment may have influenced the dielectric behavior in a similar manner.

With an increase in texture fraction to ~0.80 for higher processing temperatures (1150°C, 0 h), the diffuseness of the permittivity peak decreased (γ=1.75 and C/ε_{max}=536) and the overall constant increased, especially at T_{max} (Fig. 6.10(a)). T_{max} did not change, remaining at a temperature ~164°C. The rhombohedral-tetragonal transition was visible in the dielectric data for the poled sample (Fig. 6.10(b)), and the transition temperature was consistent with that of that of the random, $BaTiO_3$-free samples ($T_{r\text{-}t}$≈95-105°C). The stability of the transition temperatures indicates that the $BaTiO_3$ templates remained stable within the PMN-PT matrix without the formation of a solid solution between the two phases.(39-43) The increase in the dielectric constant may have been influenced by the high temperature processing which could have eliminated Pb and oxygen vacancies which remained within the ceramic after hot-pressing.(44) While the dielectric constant values increased with an increase in texture fraction, the maximum permittivity was still dominated by the presence of the intergranular low-ε phase.

It is also clear that further texture development (~10% increase in texture, f≈0.90) with subsequent annealing at 1150°C for 5 h does not significantly alter the dielectric behavior (Fig. 6.11). The magnitude and diffuseness (γ=1.74 and C/ε_{max}=342) of the dielectric-temperature curve for both the unpoled (Fig. 6.11(a)) and poled (Fig. 6.11(b)) samples remained virtually unchanged. Again, the transition temperatures were also retained, suggesting the high stability and low dissolution rate of $BaTiO_3$ in the PMN-PT/PbO matrix composition.

Figures 6.12 and 6.13 show the dielectric constant versus temperature curves (1-100 kHz) for unpoled and poled PMN-32.5PT ceramic sample containing 10 vol% <001>-aligned $BaTiO_3$ templates (PMN-32.5PT-10BT). One sample set was only reoxidized (800°C, 10 h in O_2) after hot-pressing (Fig. 6.12) and the other sample set was

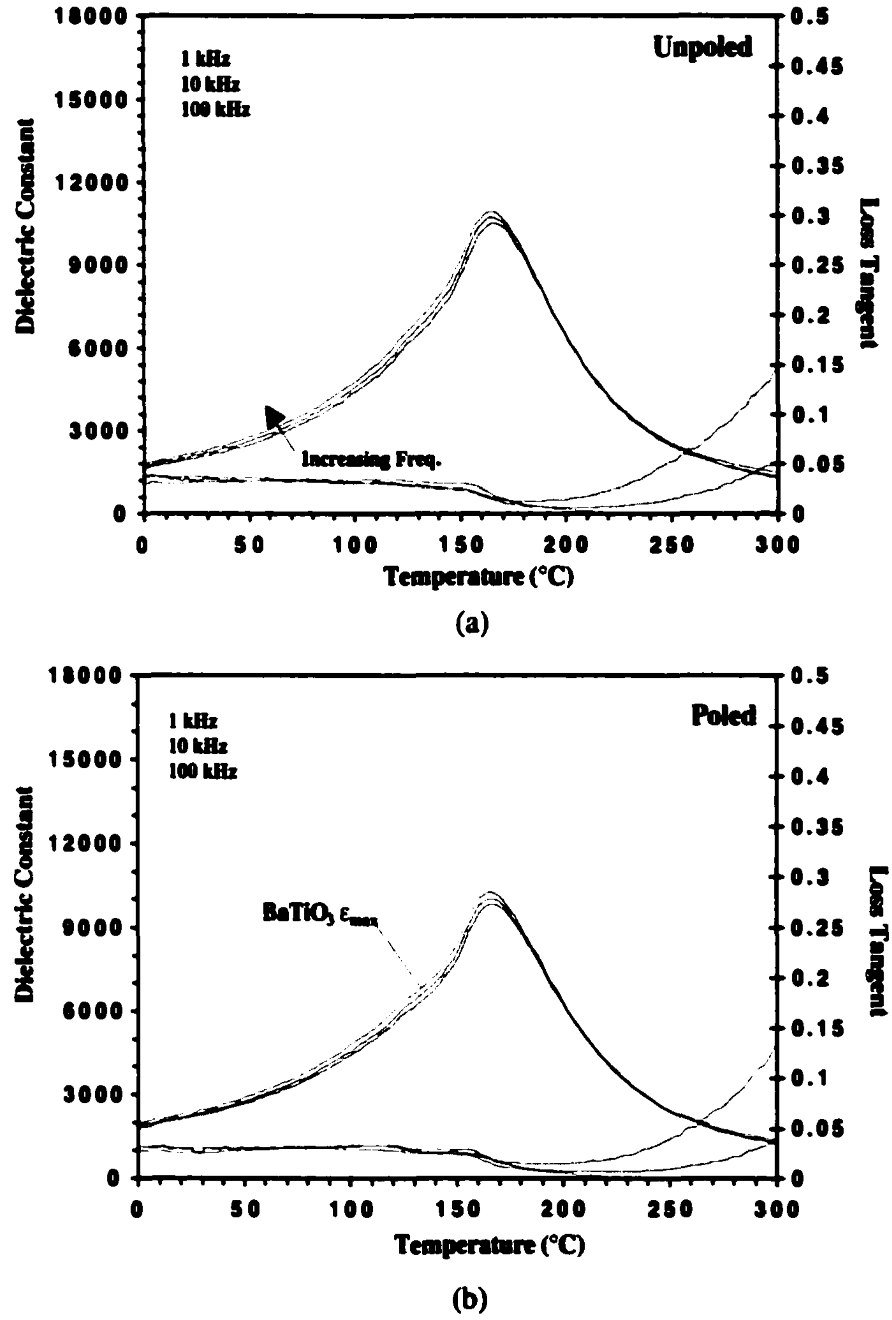

Figure 6.12: Dielectric constant and loss as a function of temperature for an a) unpoled and b) poled PMN-32.5PT ceramic containing 10 vol% $BaTiO_3$ templates (PMN-32.5PT-10BT) annealed at 800°C for 10 h.

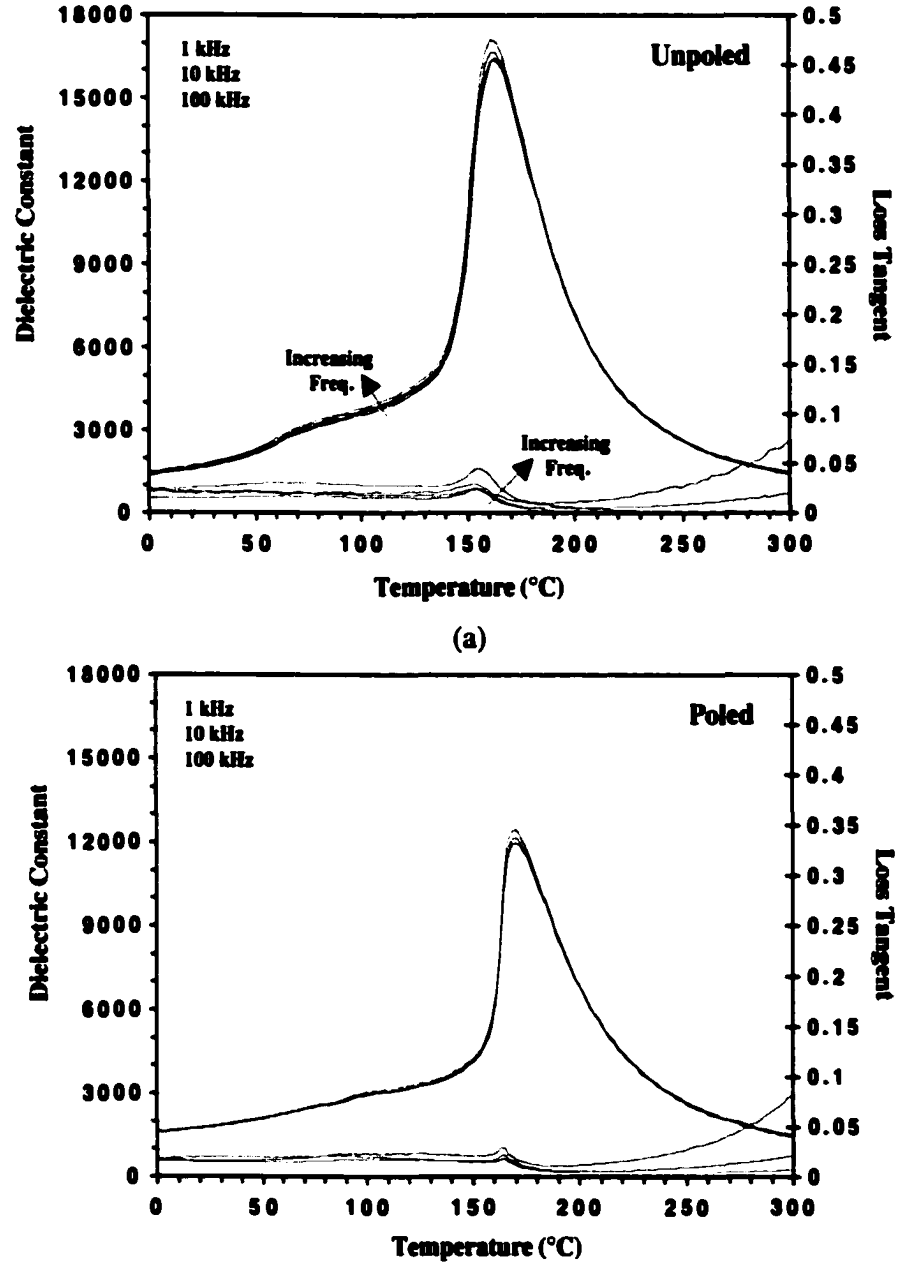

Figure 6.13: Dielectric constant and loss as a function of temperature for an a) unpoled and b) poled PMN-32.5PT ceramic containing 10 vol% $BaTiO_3$ templates (PMN-32.5PT-10BT) annealed at 1150°C for 5 h.

annealed at 1150°C for 5 h in O_2 (Fig. 6.13) in order to increase the texture fraction of the samples. After the 5 h thermal treatment at 1150°C, the PMN-32.5PT-10BT samples were textured to a fraction of ~0.95. The unpoled and poled dielectric behavior of the untextured PMN-32.5PT-10BT samples were found to show a similar diffuse ferroelectric-paraelectric transition (T_{max}=164°C) as the untextured PMN-32.5PT-5BT samples (~γ=1.78 and C/ε_{max}=939). Like the untextured PMN-32.5PT-5BT samples, the untextured, poled PMN-32.5PT-10BT samples did not clearly display the rhombohedral-tetragonal transition, probably because of the interference of a shoulder in the dielectric curve at 130°C associated with the $BaTiO_3$ paraelectric-ferroelectric phase transition (Fig. 6.12). The magnitude of the dielectric constant was suppressed beyond that displayed by the PMN-32.5PT-5BT samples due to the addition of the extra 5 vol% $BaTiO_3$. But again, the additional $BaTiO_3$ could not completely account for the lower dielectric constant. Dielectric mixing laws predict a decrease of <3800 in the maximum dielectric constant for PMN-32.5PT (1 wt% excess PbO) ceramics containing 10 vol% $BaTiO_3$.(17,18,23)

After a 5 h annealing time at 1150°C, the overall permittivity of the PMN-32.5PT-10BT ceramics increased with an increase in texture fraction, but the peak permittivity was still ~5000 less than that achieved in the 90%-textured PMN-32.5PT-5BT samples (Fig. 6.13). The T_{max} remained unchanged for both the unpoled and poled samples and the rhombohedral-tetragonal transition at $T_{r\text{-}t}$≈95-105°C was apparent, but the shoulder in the permittivity at $T_{r\text{-}t}$ was lower than that shown by the PMN-32.5PT-5PT samples. The diffuseness of the ferroelectric-paraelectric transition was decreased

($\sim\gamma$=1.69 and C/ε_{max}=418) with the additional texture as a result of the extended 1150°C anneal.

The stability of the transition temperatures for both the PMN-32.5PT-5BT and PMN-32.5PT-10BT samples suggested the high stability of the $BaTiO_3$ templates. Since the $BaTiO_3$ does not seem to diffuse into the matrix, then the apparent increase in the transition breadth can not be attributed to dissolution, as has been reported for PMN and PZN solid solutions.(34,39,42) Some of the broadening of the dielectric peak can be attributed to the presence of intergranular PbO acting as a Curie point depressor.(21) The diffuse transition can also be related to the possible distribution of space-charge in the material. Space-charge may also develop along the grain boundaries due the intergranular low-ε phase.(23,24) Therefore, the decrease in diffuseness may not be the result of texturing, but a result of the high temperature annealing which can diminish the residual space-charges by eliminating the Pb and oxygen vacancies and increasing grain boundary uniformity.(23,24,44) The diffuseness may also originate from the combined contributions of both the $BaTiO_3$ and the PMN-PT which have transition temperatures that are ~40-50°C apart. This is suggested by the appearance of the additional shoulder in the permittivity plot.

6.3.8 Ferroelectric Hysteresis of <001>-Textured PMN-32.5PT Ceramics

The dielectric polarization as a function of bipolar electric field measured in the textured <001> for both the PMN-32.5PT-5BT and PMN-32.5PT-10BT is displayed in Fig. 6.14 and Fig. 6.15, respectively. The maximum polarization for the PMN-32.5PT-5BT and PMN-32.5PT-10BT compositions were similar for both the untextured and

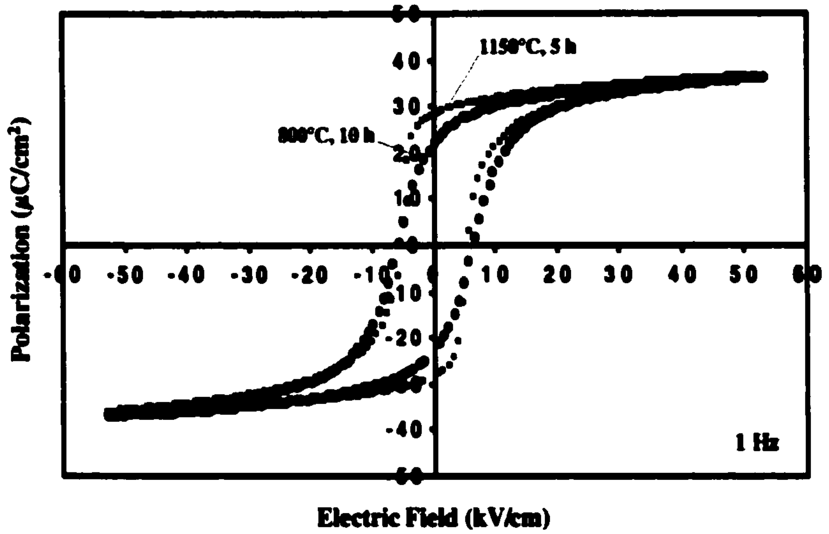

Figure 6.14: Polarization-electric field hysteresis for PMN-32.5PT ceramic containing 5 vol% $BaTiO_3$ templates (PMN-32.5PT-5BT) annealed at 800°C for 10 h and 1150°C for 5 h.

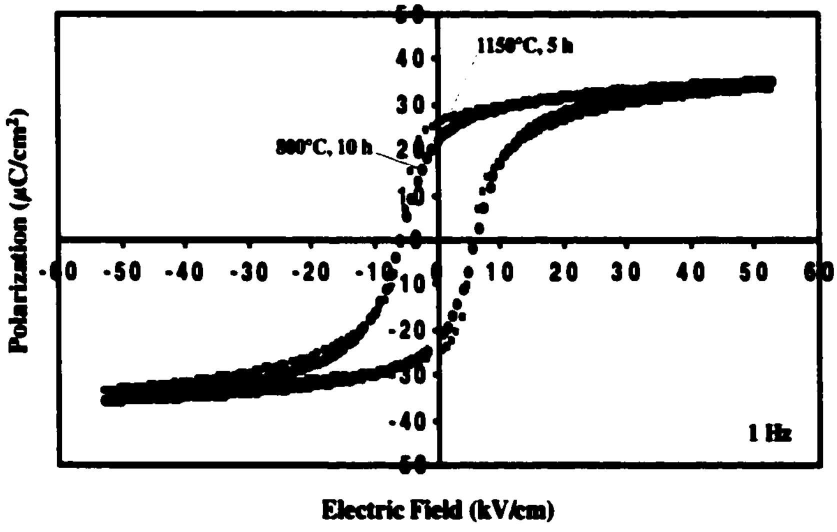

Figure 6.15: Polarization-electric field hysteresis for PMN-32.5PT ceramic containing 10 vol% $BaTiO_3$ templates (PMN-32.5PT-10BT) annealed at 800°C for 10 h and 1150°C for 5 h.

textured samples, although the loop was more square in the textured materials. The untextured PMN-32.5PT-5BT composition showed a $P_r \approx 22\ \mu C/cm^2$ and $E_c \approx 5.9$ kV/cm (Table 6.6). With an increase of texture fraction to ~0.90, the polarization increased and the coercive field remained relatively unchanged ($P_r \approx 28\ \mu C/cm^2$, $E_c \approx 5.6$ kV/cm) (Fig. 6.14). The remanent polarization of the highly textured sample was lower than that displayed by the random sample (~32.4 $\mu C/cm^2$). This is understandable since 90% of the ceramic is textured in the non-polar direction. Due to the additional 5 vol% $BaTiO_3$ templates in the PMN-32.5PT-10BT samples, the polarization decreased and the coercive field increased (Fig. 6.15). The increase in the coercive field, $E_c \approx 5.95$ kV/cm (untextured) and $E_c \approx 5.78$ kV/cm (95%-textured), indicates that the additional $BaTiO_3$ templates either restrict the movement of the domain walls or perturb the internal electric field distribution. Similar to the untextured PMN-32.5PT-5BT samples, the remanent polarization of the untextured PMN-32.5PT-10BT was $P_r \approx 21.9\ \mu C/cm^2$ and increased with the increase in texture fraction ($P_r \approx 25.4\ \mu C/cm^2$).

6.3.9 Piezoelectric Properties of <001>-Textured PMN-32.5PT Ceramics from Berlincourt and Strain-Field Measurements

The d_{33} coefficients of the PMN-32.5PT-5BT and PMN-32.5PT-10BT samples with various degrees of <001>-texture were measured using the Berlincourt d_{33} meter. Reliable d_{33} values could not be obtained, since the d_{33} values for all samples decreased below 200 pC/N in less than a minute. This may be because the textured samples, which possesses both a ferroelectric and ferroelastic nature, have a low coercive stress allowing the samples to depole under the induced stress.

Table 6.6: E_c and P_r of textured PMN-32.5PT ceramics containing 5 vol% $BaTiO_3$ templates.

Texture Fraction	E_c (kV /cm)	P_r ($\mu C/cm^2$)
0	5.9	22.0
0.80	5.7	25.0
0.90	5.6	28.0

The unipolar strain-field behavior of the PMN-32.5PT-5BT samples possessing different degrees of <001>-texture were collected by a linear variable differential transducer in conjunction with the Sawyer-Tower circuit (Fig. 6.16). The d_{33} coefficients were measured from the slope of the strain-field plots for fields under <5 kV/cm and <10 kV/cm in the same manner as the random PMN-32.5PT ceramics (Table 6.7). The plot shows that increasing the <001>-texture increased the maximum strain output of the samples. The improvement in strain performance was enhanced up to an annealing time of 1-5 h, where it began to saturate along with the rate of texturing (Chapter 5). A random sample containing oriented $BaTiO_3$ templates showed a maximum strain of 0.161% at 50 kV/cm, and with ~90% texture, the maximum strain increased to 0.279%. The low-field d_{33} coefficients (<5 kV/cm) for samples with ~90% texture (d_{33}≈1150 pC/N) were 1.5 times greater than that measured for randomly oriented PMN-32.5PT samples containing 0 wt% excess PbO (Fig. 6.5). The d_{33} coefficients of this magnitude are approximately 40-50% that measured for PMN-PT single crystals (30-35% $PbTiO_3$) in the <001>.(1,2,45,46) The textured samples showed relatively little opening in the strain curves (0.02-0.03%), but the hysteresis of the textured samples was above that measured for random PMN-32.5PT samples (Table 6.3).

The effect of the hysteresis on the d_{33} coefficient is made even more evident by observing the relationship between the magnitude of the maximum applied unipolar field and the strain-field curve. Fig. 6.17(a) shows the strain-field plots of a ~90%-textured PMN-32.5PT-5BT sample with progressively increasing maximum applied fields from 1-50 kV/cm. At maximum applied fields <5 kV/cm (<E_c), the magnitude of hysteresis and the slope of the plot (d_{33} coefficient) rapidly increased with an increase in maximum

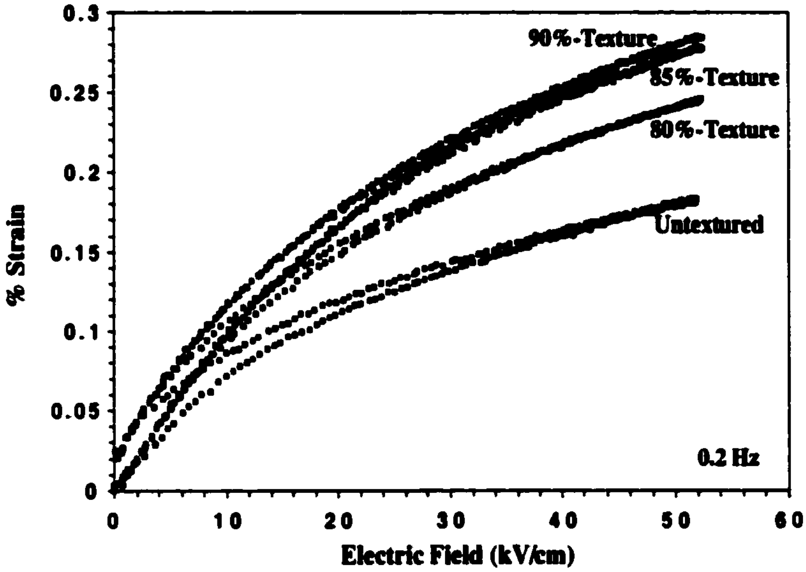

Figure 6.16: Unipolar strain-electric field curves of PMN-32.5PT ceramic containing 5 vol% $BaTiO_3$ templates (PMN-32.5PT-5BT) displaying various degrees of texture.

Table 6.7: Piezoelectric properties of textured PMN-32.5PT ceramics containing 5 vol% $BaTiO_3$ templates measured from the strain-field plots.

Texture Fraction	d_{33} (pC/N) (<5 kV/cm)	d_{33} (pC/N) (<10 kV/cm)	% Strain (50 kV/cm)	Max. Opening in Curve (%)
0	590	500	0.161	0.0170
0.80	975	808	0.235	0.0150
0.85	990	820	0.240	0.0220
0.90	1150	953	0.279	0.0239

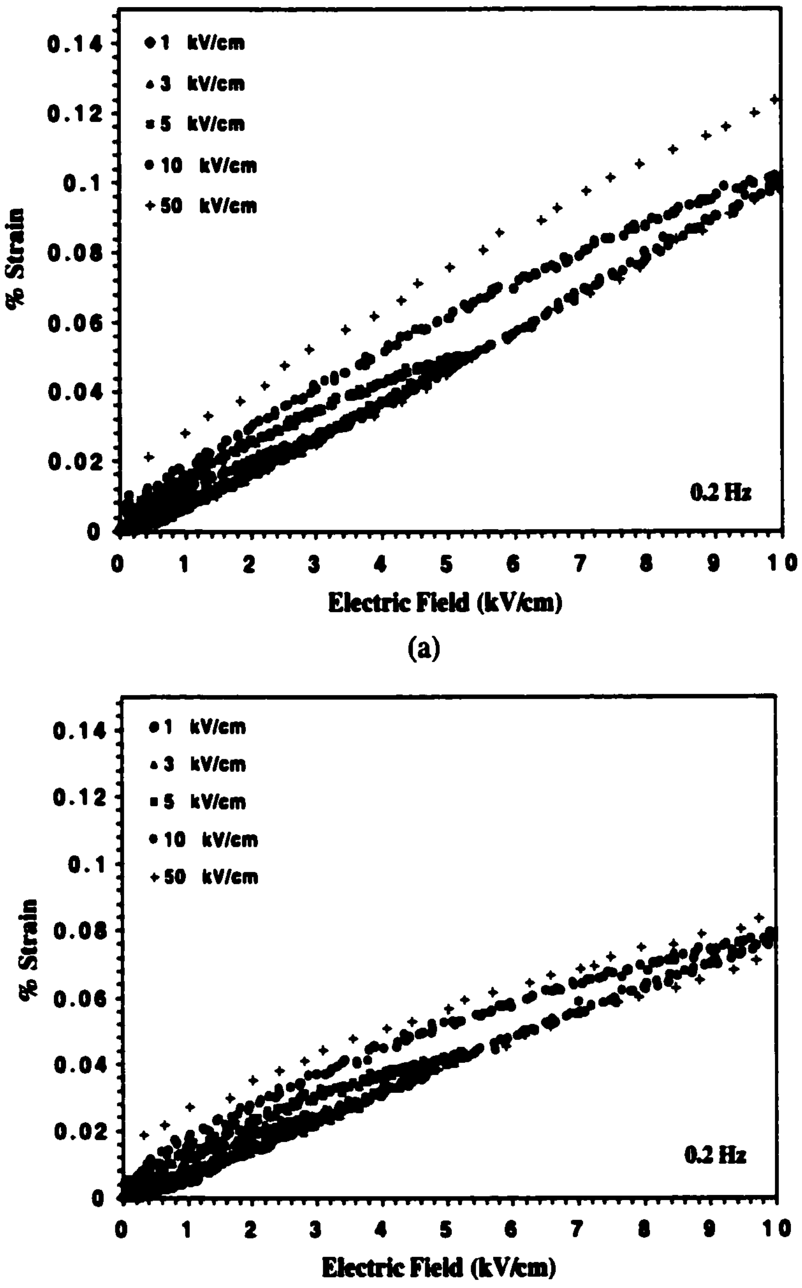

(a)

(b)

Figure 6.17: Unipolar strain-electric field curves of a (a) ~90%-textured PMN-32.5PT-5BT ceramic and a (b) random PMN-32.5PT ceramic measured to maximum unipolar fields between 1-50 kV/cm.

field. The rate of increasing slope and hysteresis began to subside at fields >5 kV/cm. A similar trend was observed for randomly-oriented PMN-32.5PT ceramics (0 wt% excess PbO), but the slope and hysteresis quickly saturated at maximum applied fields >5 kV/cm (Fig. 6.17(b)). The d_{33} values were measured from the slope of the curves for fields <5 kV/cm. The plot of the d_{33} coefficients as a function of maximum applied field for the random ceramic shows that the d_{33} coefficient is most strongly influenced by the hysteresis for AC drive fields greater than the coercive field (~5 kV/cm) (Fig. 6.18). This was not the case for the textured sample where effective d_{33} coefficient continued to rise even at fields much greater than the coercive field.

As previously described, the degree of irreversible domain wall contribution to the piezoelectric coefficient is presented in the strain-field plot by a large degree of piezoelectric hysteresis. Rhombohedral single crystal PMN-PT poled and measured in the <001> show nearly anhysteritic strain-field response indicating the absence of extrinsic contribution due to the stable domain configuration.(2)

There are several plausible reasons for the hysteresis in the textured samples. The splitting in the (200) XRD peaks shown in Chapter 5 suggested a possible presence of tetragonal domain states in the textured samples.(47) The presence of the tetragonal domain structure would increase the hysteresis. The origin of the hysteresis can also result from porosity and internal stresses developing during texturing, which would impede domain wall movement.(26,27,31,37) Internal stresses may result from the remnant $BaTiO_3$ templates embedded within the oriented grains. This would produce an internal stress field within the grains which might, for example, contribute to locally stabilizing

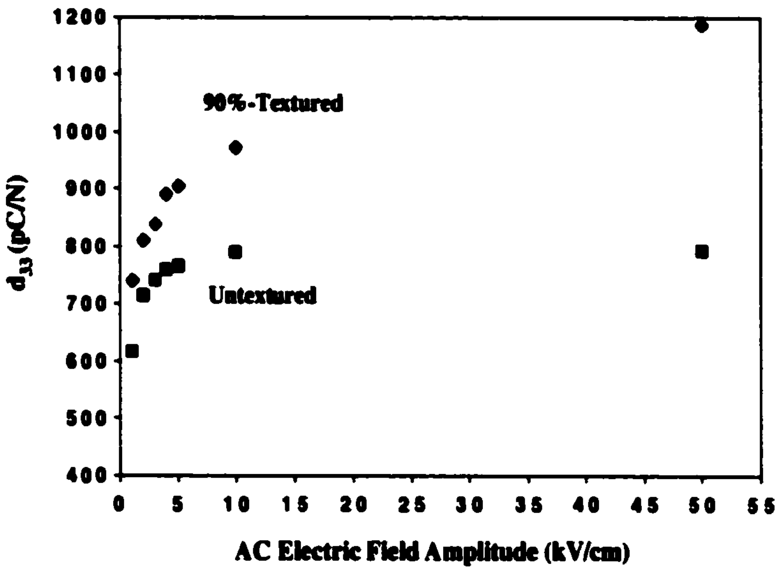

Figure 6.18: Low-field (<5 kV/cm) d_{33} coefficients measured from unipolar strain-electric field curves of a (a) ~90%-textured PMN-32.5PT -5BT ceramic and a (b) random PMN-32.5PT ceramic measured to maximum unipolar fields between 1-50 kV/cm.

the tetragonal PMN-PT. Any of these factors would alter the domain wall response to electrical fields and mechanical stresses.

The effect of porosity on the strain behavior was shown in a PMN-32.5PT-5BT sample that was textured to ~85% by sintering at 1150°C for 5 h without hot-pressing. Without hot-pressing, the sample contained ~8-10% porosity. The sample showed an increase in maximum strain and inflated piezoelectric coefficients (>1300 pC/N) due to the influence of the large hysteresis (>0.035%) (Fig. 6.19). The strain-field plot never "pinched off" for the porous sample, showing that extrinsic contributions were activated at various field levels.

A similar strain response was shown for samples containing a greater concentration of $BaTiO_3$ templates (10 vol%). Fig. 6.20 displays the strain-field curve of a PMN-32.5PT-10BT sample which was hot-pressed and then annealed at 1150°C for 1 h. Comparing the PMN-32.5PT-10BT to the PMN-32.5PT-5BT sample having the same texture fraction (~0.90), the PMN-32.5PT-10BT sample showed a higher degree of hysteresis (>0.03% opening in the strain-field plot). The resultant hysteresis amplified the strain levels, and therefore, increased the d_{33} coefficients (>1200 pC/N) measured from the strain-field plots at <5 kV/cm.

Overall, it is clear that the highly textured PMN-32.5PT samples prepared here showed a comparatively small enhancement in piezoelectric response relative to random samples. There are a number of factors which could effect the piezoelectric response of the textured samples. The piezoelectric behavior would be affected by the intergranular PbO, orientation distribution, and residual porosity. The piezoelectric response may also be limited by the remaining randomly-oriented matrix between the textured grains. The

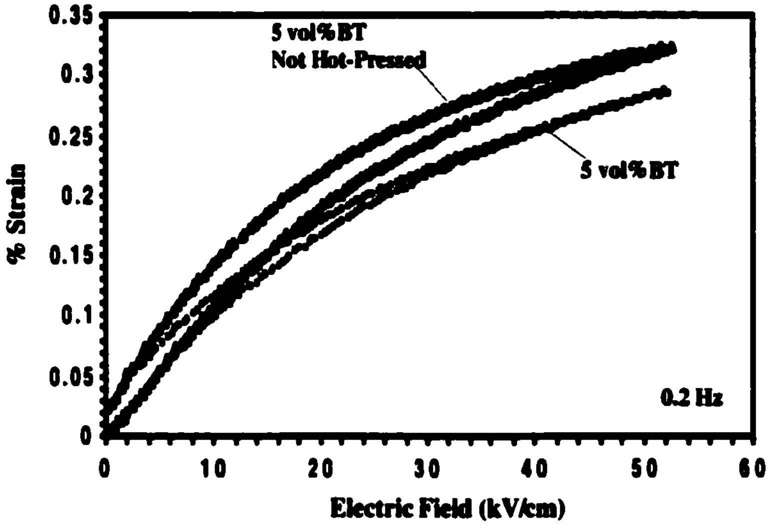

Figure 6.19: Unipolar strain-electric field curves of hot-pressed and non-hot-pressed PMN-32.5PT ceramics containing 5 vol% $BaTiO_3$ templates (PMN-32.5PT-5BT)

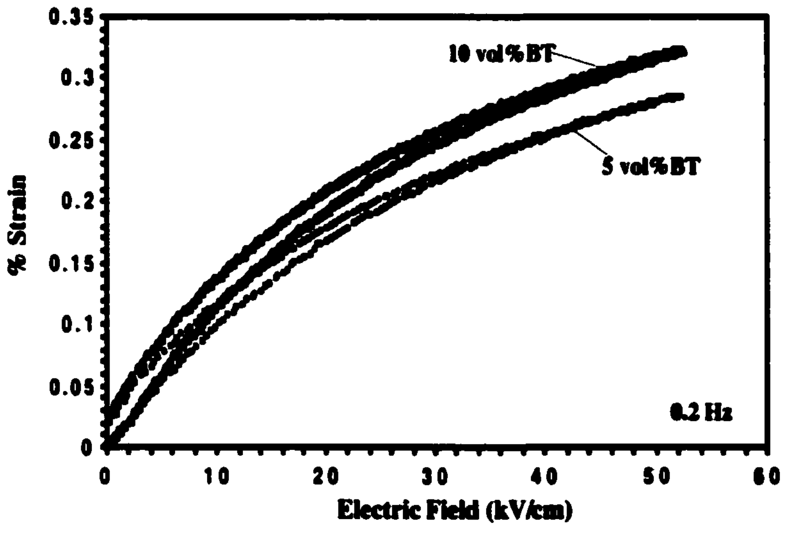

Figure 6.20: Unipolar strain-electric field curves of ~90%-textured PMN -32.5PT ceramics containing 5 vol% $BaTiO_3$ (PMN-32.5PT-5BT) and 10 vol% $BaTiO_3$ (PMN-32.5PT-5BT) templates.

matrix grains could clamp the piezoelectric response between the templated grains. Lateral clamping may also arise due to the nature of the texture. A fiber-textured ceramic would not experience the same lateral response as a well-poled crystal. The random nature of the orientation perpendicular to the textured direction may complicate the polarization rotation responsible for the large single crystal strain. This lateral clamping of the textured grains would restrain the longitudinal response of the templated grains.

The strain-field plots of the textured PMN-32.5PT ceramics did not show the field induced rhombohedral to tetragonal phase transformation (~15-30 kV/cm) which is present in the <001> single crystals.(2,3,48) In addition to the above mentioned variables which may clamp the oriented grains, the residual $BaTiO_3$ templates could internally clamp the grains, restricting both the piezoelectric response and phase transformation. The d_{33} and d_{31} coefficients for single crystal PMN-33PT ($d_{33}\approx2500$ pC/N, $d_{31}\approx-1075$ pC/N)(1,2,45,46) are, respectively, 20-40 times greater than single crystal $BaTiO_3$ ($d_{33}=140$ pC/N, $d_{31}=-34-60$ pC/N).(49) Therefore, the $BaTiO_3$ core would restrict the expected strain of the PMN-PT grain.

6.3.10 *In situ* Observation of Domain Movement in <001>-Oriented PMN-32.5PT Grains Templated by $BaTiO_3$

In order to observe the effect of the template particles on the domain movement in the templated PMN-PT grains, a highly textured PMN-32.5PT-5BT sample was polished perpendicular to the <001>-texture direction to 0.1 μm with diamond paste, and the sample was mounted in the center of a Teflon frame. Two windows on either side of the frame were centered on the sample, and the windows were filled with tap water. The water acted as transparent electrode for the sample. Wire leads were set into the water and connected to a high voltage amplifier (IRCO Model C12K-20, Columbia, MD). The macroscopic domain wall movement was observed *in situ* through an optical microscope (Axioplan 2, Carl Zeiss, Inc, Thornwood, NY) fitted with a video camera (Sony CCD-Iris) while applying a bipolar electric field. The macroscopic domain wall movement was observed in a optical reflection mode with cross-polarizers while a field <10 kV/cm was applied across the sample parallel to the textured <001>. Distinct domain walls were difficult to image in reflection mode at a magnification of 20× due to the complex, superimposed domain structure known for PMN-PT compositions close to the MPB.(48,50,51) Fig. 6.21 shows micrographs of oriented single crystal containing a $BaTiO_3$ template crystal. The $BaTiO_3$ template lies below the surface of the sample, therefore, the template crystal remains completely surrounded by the grown PMN-PT crystal layer. With increasing field, a change in the domain orientation initiated at the edge of the crystal and moved inward towards the $BaTiO_3$ core. This was displayed by the change of brightness and contrast due to the realignment of the dipoles which altered the strain and birefringence.(48,50-52) No domain reorientation was visible at fields <4.5 kV/cm (Fig. 6.21(a)). The applied field direction was in the <001> of the templated grain, which is perpendicular to the micrograph. Visible domain wall movement was activated at a field ~5 kV/cm (Fig. 6.21(b)) and the contrast front accelerated inward towards the template as the field was increased from 5-6 kV/cm at a rate of ~0.01 kV/cm·sec (Fig.6.21(c-f)). The arrows in the figures are indicating the position of the domain walls at various field levels. An area around and above the $BaTiO_3$ template crystal was not apparently altered with the increase of field, even at fields as high as 7 kV/cm (Fig. 6.22). This may

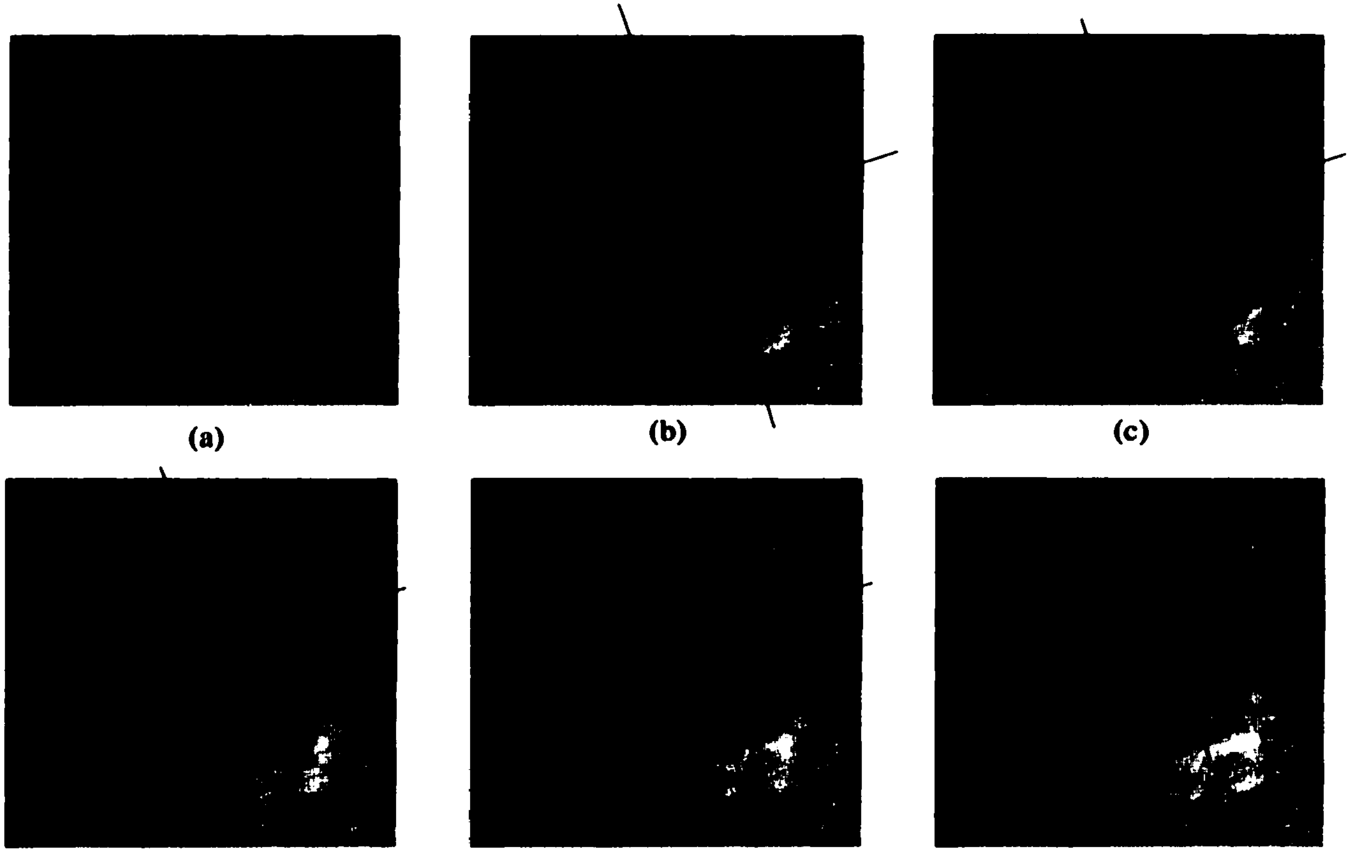

(a) (b) (c)

(d) (e) (f)

Figure 6.21: Optical micrographs (20×) of macroscopic domain wall movement in a templated grain oriented in the <001> (⊥ to micrograph) during poling at (a) 4.5 kV/cm, (b) 5.0 kV/cm, (c) 5.25 kV/cm, (d) 5.5 kV/cm, (e) 5.75 kV/cm, and (f) 6-7 kV/cm. The field was increased at a rate of ~0.01 kV/cm·sec.

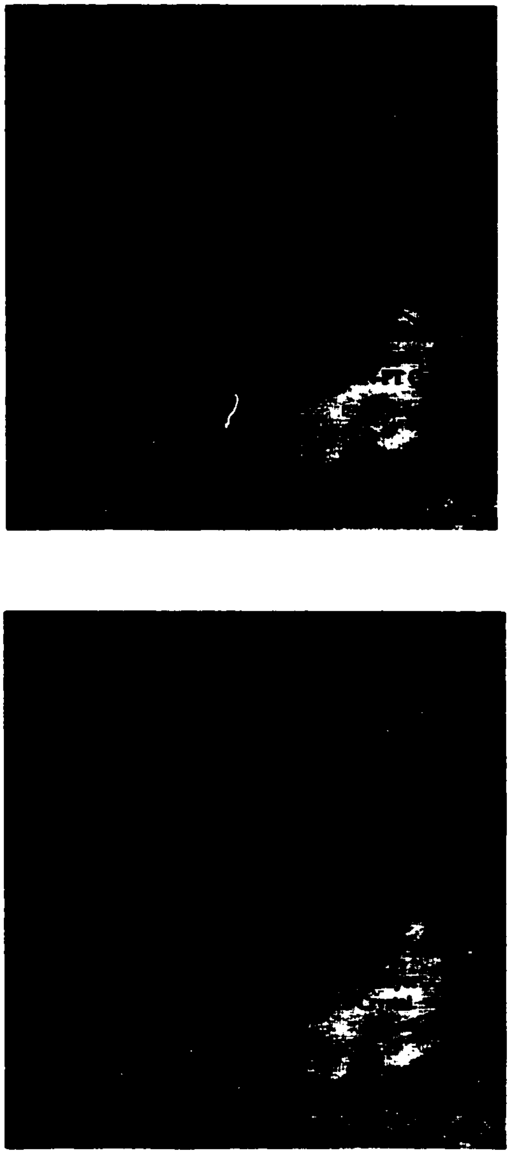

Figure 6.22: Optical micrograph (20x) showing a stable domain layer surrounding the $BaTiO_3$ template in an <001>-oriented grain at fields ≥7 kV/cm.

indicate that the domains are pinned in an area surrounding the $BaTiO_3$ crystal. A stress field at the template/crystal interface may decrease the domain wall mobility and the activation energy to liberate the domain walls would then require fields >7 kV/cm. Therefore, it is plausible that the residual $BaTiO_3$ templates within the oriented grains contribute to the internal clamping of the dielectric and piezoelectric properties, and this clamping could also obscure the field-induced phase rhombohedral-tetragonal transformation identified for single crystal PMN-PT.

6.3.11 Piezoelectric Properties of <001>-Textured PMN-32.5PT Ceramics from IEEE Resonance Measurements

The piezoelectric coefficients (d_{33}, d_{31}), mechanical compliances (s_{33}^E, s_{33}^D, s_{11}^E, s_{11}^D), and the electromechanical coupling coefficients (k_{33}, k_{31}) were also measured for the textured PMN-32.5PT-5BT and PMN-32.5PT-10BT samples by the IEEE resonance technique. The experimental setup was the same as that used for the randomly oriented samples. The longitudinal coefficients were measured from samples which were cut to the dimensional ratio of 4:1:1 (4×1×1 mm) and the lateral coefficients were obtained from samples with the dimensional ratio of 4:1:0.4 (4×1×0.4 mm)(Fig. 6.23). Fig. 6.24(a) shows a representative resonance pattern of an untextured longitudinal PMN-32.5PT-5BT sample where the relative resonance difference ($(f_a-f_r)/f_r$) produced a $k_{33}\approx0.600$. This k_{33} coefficient is far below that observed for random PMN-32.5PT ceramics, indicating that the initial addition of the $BaTiO_3$ templates reduced the coupling of the samples. By increasing the texture fraction to ~0.90, the electromechanical coupling increases to a value above that observed for random PMN-PT and PZT ceramics

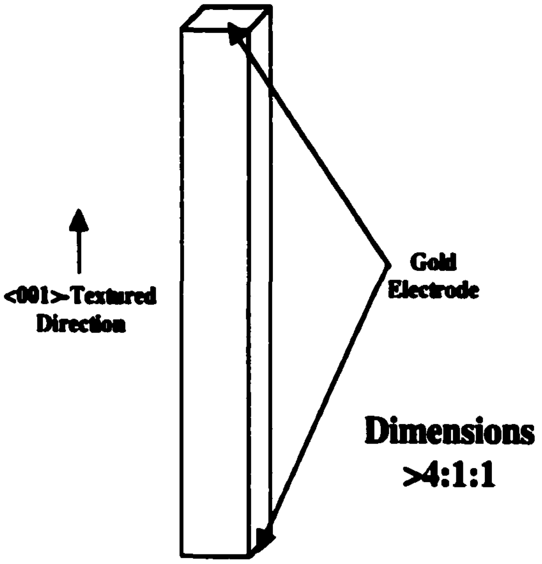

Longitudinal Resonance Sample (k_{33}, s_{33},d_{33})

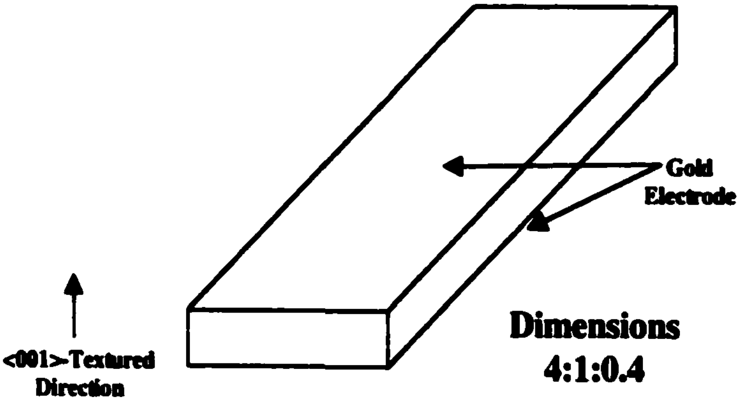

Transverse Resonance Sample (k_{31}, s_{11},d_{31})

Figure 6.23: Schematic of the longitudinal and transverse textured, resonance sample dimensions.

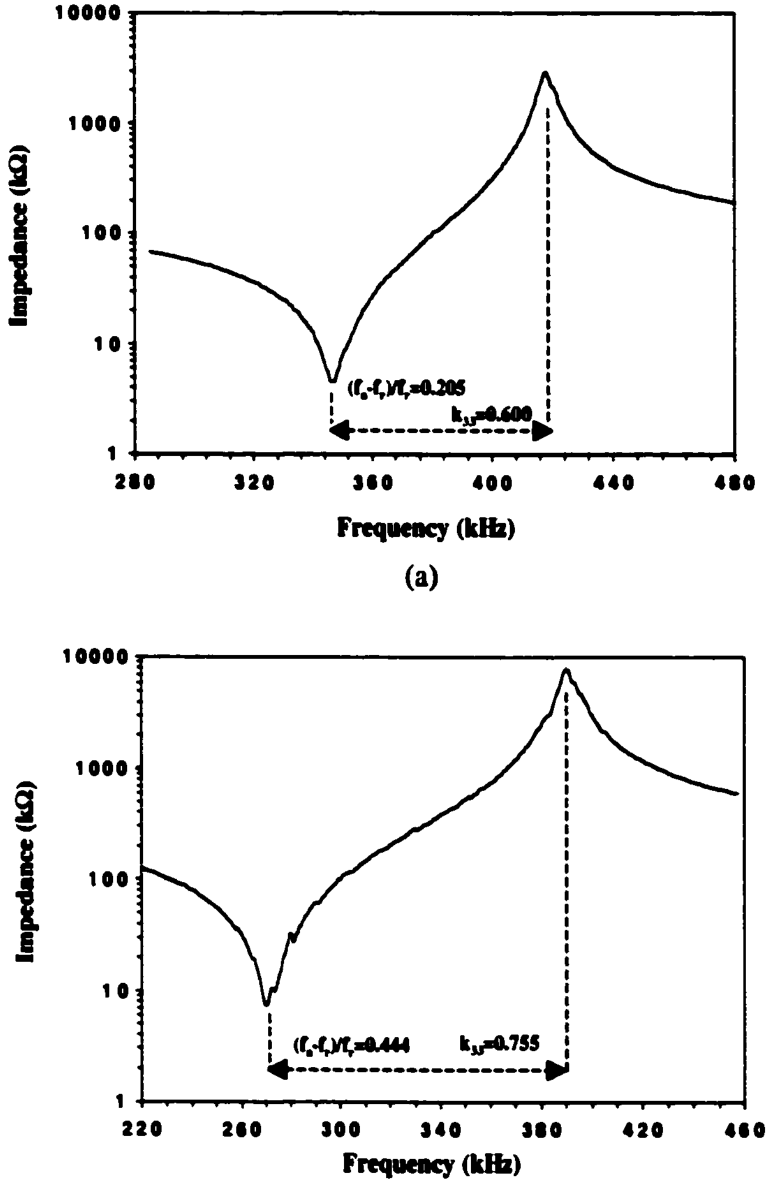

(a)

(b)

Figure 6.24: Impedance as a function of frequency near resonance of (a) 0%- and (b) ~90%-textured PMN-32.5PT ceramics containing 5 vol% $BaTiO_3$ templates (longitudinal measurement).

(0.755±0.006) (Fig. 6.24(b)).(53) The resonance and anti-resonance peaks of the textured samples showed some additional features, but the frequency of the minimum and maximum impedance were still reasonably well-defined. These features may have originated from grain pull-out or crack formation due to sample preparation. These defects would have a significant effect on the resonance patterns, especially since the longitudinal resonance samples had a low number of textured grains and a relatively small electrode area (~ 1 mm^2).

The calculated values for the material constants for the PMN-32.5PT-5BT and PMN-32.5PT-10BT samples are listed in Table 6.8 and Table 6.9, respectively. The PMN-32.5PT-5BT samples generally showed slightly higher values for all of the material constants. All of the constants increased with texturing. The compliances of the samples in the longitudinal and lateral directions showed greater anisotropy with additional texturing. The d_{33}/d_{31} ratio declined with texturing (~2.35 to 1.85), but the average d_{33}/d_{31} ratio remained the same as the random PMN-32.5PT ceramics (~2.1). The discrepancy in the d_{33}/d_{31} ratio may originate from the difference in poling efficiency between the textured longitudinal and transverse resonance samples.

The d_{33} coefficients measured by the resonance technique for the highly textured PMN-32.5PT-5BT samples were ~1.2 times greater than that measured for randomly oriented PMN-32.5PT ceramics (0 wt% excess PbO). A better comparison would be to associate the textured samples with the PMN-32.5PT composition containing 1 wt% excess PbO. The 90%-textured sample was at least 1.4 times greater than its random ceramic counterpart. Therefore, the resonance measurements concur with strain-field results indicating that fiber-texturing PMN-PT in the <001> with a low volume fraction

Table 6.8: Piezoelectric, electromechanical coupling, and compliance coefficients of textured PMN-32.5PT ceramics containing 5 vol% $BaTiO_3$ templates measured by the resonance technique.

Texture Fraction	d_{33} (pC/N)	d_{31} (pC/N)	k_{33}	k_{31}	s_{33}^E ($\times 10^{-12}$ m^2/N)	s_{11}^E ($\times 10^{-12}$ m^2/N)
0	370 ±1	-162 ±6	0.600 ±0.006	0.287 ±0.007	16.7 ±0.4	12.1 ±0.9
0.80	518 ±10	-254 ±22	0.744 ±0.007	0.448 ±0.020	26.2 ±1.0	16.4 ±0.7
0.90	525 ±35	-282 ±18	0.755 ±0.006	0.484 ±0.007	27.6 ±1.7	16.5 ±0.14

Table 6.9: Piezoelectric, electromechanical coupling, and compliance coefficients of textured PMN-32.5PT ceramics containing 10 vol% $BaTiO_3$ templates measured by the resonance technique.

Texture Fraction	d_{33} (pC/N)	d_{31} (pC/N)	k_{33}	k_{31}	s_{33}^E ($\times 10^{-12}$ m^2/N)	s_{11}^E ($\times 10^{-12}$ m^2/N)
0	439 ±7	-179 ±4	0.646 ±0.005	0.310 ±0.009	18.6 ±0.3	12.5 ±0.01
0.85- 0.90	478 ±3	-252 ±15	0.682 ±0.026	0.456 ±0.017	23.8 ±0.3	15.9 ±0.01
0.95	480 ±5	-266 ±20	0.705 ±0.002	0.460 ±0.016	25.2 ±0.6	16.4 ±0.1

of $BaTiO_3$ templates increases the piezoelectric response. The difference in the degree of enhancement between the two measurement techniques may be the result of extrinsic contributions to the piezoelectric coefficients which were evident in the strain-field measurements.

Similar to the low-field piezoelectric coefficients measured for the random PMN-32.5PT ceramics, the resonance measured piezoelectric coefficients for the highly textured PMN-32.5PT-5BT samples were low. It is evident that the additions of the $BaTiO_3$ initially degraded the properties, but with an increase in the <001> orientation fraction, the electromechanical coupling, and compliance values increased. This resulted in an increase in the overall piezoelectric response. It was identified that the dielectric constant was not significantly altered with texturing, and the magnitude of the dielectric constant was primarily dominated by the intergranular PbO-based phase. Therefore, the calculated piezoelectric coefficients were dictated by the low dielectric constant of the textured PMN-32.5PT ceramics (ε_{33}^T <3000).

The important detail identified in this work was that the textured samples consistently displayed strains, piezoelectric coefficients, electromechanical coupling coefficients, and compliances greater than its randomly-oriented counterpart. This comparison was based on standard random ceramics which were synthesized with same materials and measured with the same techniques as the textured ceramics.

6.3.12 Effect of DC Bias on the Resonance Measurements of Textured PMN-32.5PT Ceramics

The d_{31}, k_{31}, and ε_{33}^T coefficients as a function of an applied DC bias were measured by the AC resonance technique. A DC bias ≤10 kV/cm was applied to PMN-32.5PT-5BT k_{31} resonant samples during the impedance sweep. The measurement produced the same trend that was observed for the random PMN-32.5PT ceramic. The k_{31} decreased from 0.504 to 0.478 with the increasing applied DC field (Fig. 6.25). The ε_{33}^T coefficient decreased monotonically at a relatively higher rate than the k_{31} over the same field range (Fig. 6.26). The pronounced reduction in these constants with the increasing bias resulted in lower d_{31} values (Fig. 6.25). The DC bias clamped the polarization resulting in lower dielectric coefficients, coupling coefficients, and compliances.

6.3.13 Piezoelectric Degradation Under Unipolar Testing of <001>-Textured PMN32.5PT Ceramics

Unipolar strain-field measurements were completed on highly textured PMN-32.5PT-5BT samples (~90%-texture) in the <001> from 1-50,000 cycles (5 Hz) at maximum fields of 5 and 10 kV/cm. The intent of the piezoelectric degradation experiments was to identify the stability of the textured samples at various usable field levels. Fig. 6.27 shows a slight increase in piezoelectric hysteresis with increasing cycles at a maximum DC field of 5 kV/cm, but the overall strain-field plot opening remained <0.01%. Comparing the initial high strain-field plot (<50 kV/cm) with the plot after 50,000 cycles (Fig. 6.28), it can be seen that the general strain behavior remained consistent. By increasing the maximum applied voltage above the coercive field (~10

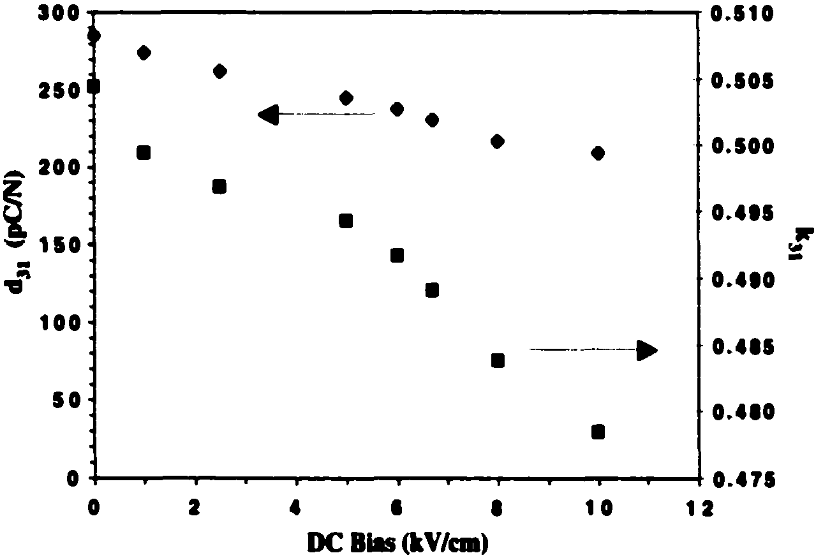

Figure 6.25: d_{31} and k_{31} as a function of DC bias for ~90%-textured PMN-32.5PT ceramics containing 5 vol% $BaTiO_3$ templates (PMN-32.5PT-5BT).

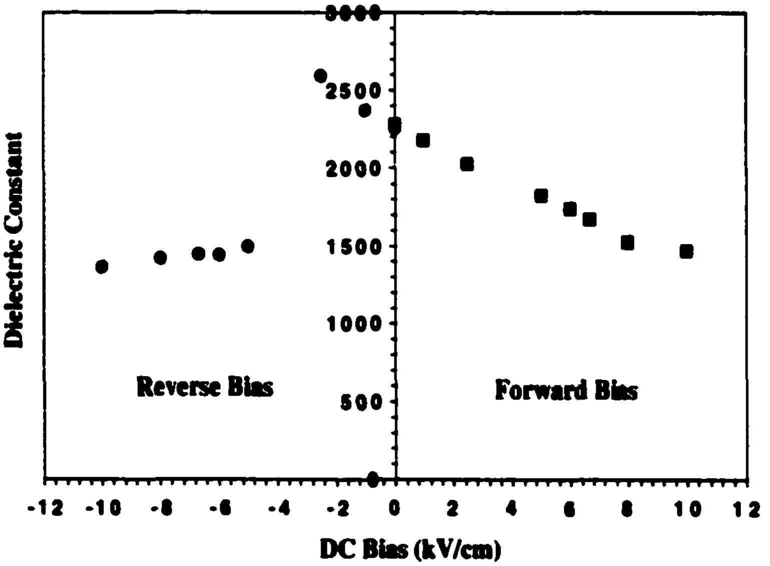

Figure 6.26: Dielectric constant (ε_{33}^T) as a function of DC bias for ~90%-textured PMN-32.5PT ceramics containing 5 vol% $BaTiO_3$ templates (PMN-32.5PT-5BT).

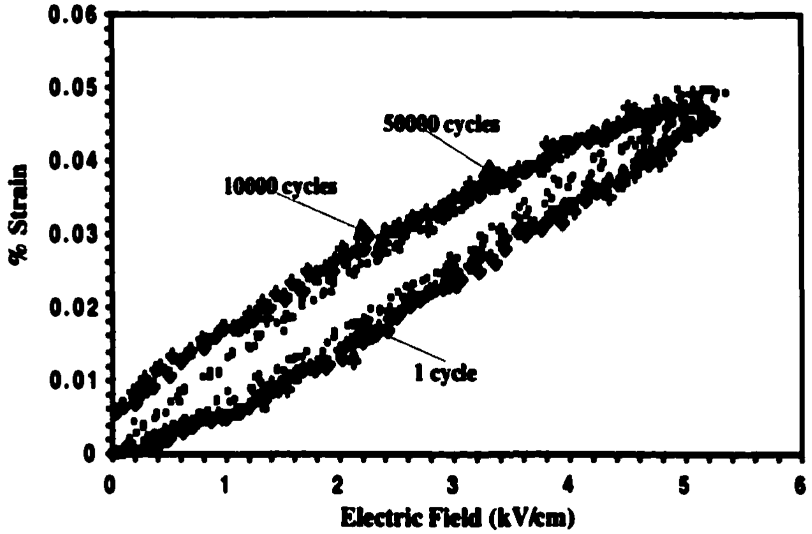

Figure 6.27: Strain-electric field curves for a ~90%-textured PMN-32.5PT ceramic containing 5 vol% $BaTiO_3$ templates (PMN-32.5PT-5BT) measured to a maximum field of 5 kV/cm after 50,000 cycles.

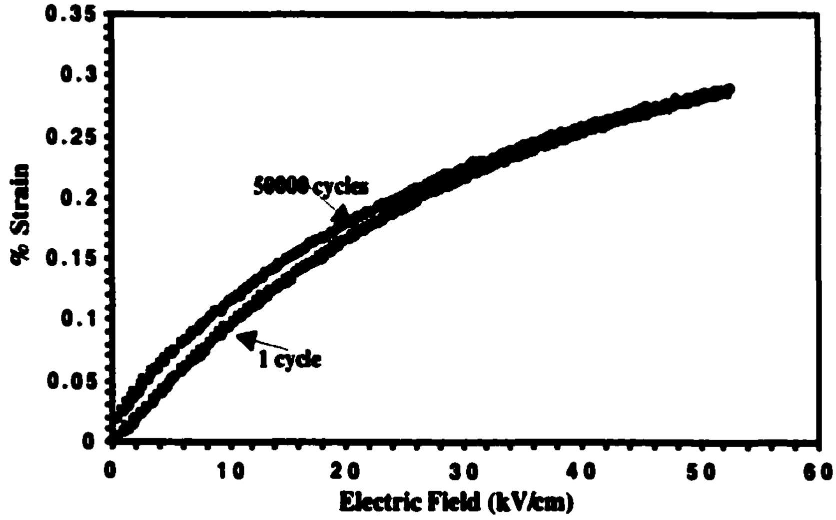

Figure 6.28: Strain-electric field curves for a ~90%-textured PMN-32.5PT ceramic containing 5 vol% $BaTiO_3$ templates (PMN-32.5PT-5BT) measured to a maximum field of 50 kV/cm after 50,000 cycles at 5 kV/cm.

kV/cm), the textured material began to display progressive degradation (Fig. 6.29). The comparison of the initial and final (after 50,000 cycles) strain-field plot of the fatigued ceramic showed a large increase in the opening of the strain-field response (>0.04%) (Fig. 6.30). The increase in hysteresis may be either due to the activation of various domain walls above the coercive field or possibly heating, microcracking, or space-charge buildup.

6.4 CONCLUSIONS

PMN-32.5PT ceramics were fiber-textured in the <001> by the TGG process using {001}-$BaTiO_3$ template particles. With an increase in texture, the PMN-32.5PT ceramic samples showed increased piezoelectric, electromechanical coupling, and compliance coefficients. The d_{33} piezoelectric coefficients of highly textured PMN-32.5PT ceramics were shown to be 1.2-1.5 times greater than randomly-oriented samples. The enhancement in the electromechanical response was limited by their relatively lower dielectric constant (ε_{33}^T<3000) due to the presence of the residual intergranular PbO-phase which was intentionally added to enhance the texturing kinetics. The piezoelectric response of the textured samples showed hysteresis when measured in the textured direction. This differs from the behavior identified for domain engineered PMN-32PT single crystals which show little to no piezoelectric hysteresis in the <001>. The hysteresis suggests some extrinsic contribution to the piezoelectric coefficient of the textured samples. Partial clamping by the residual intragranular $BaTiO_3$ template particles was identified to limit the mobility of the domain walls. Mechanical clamping

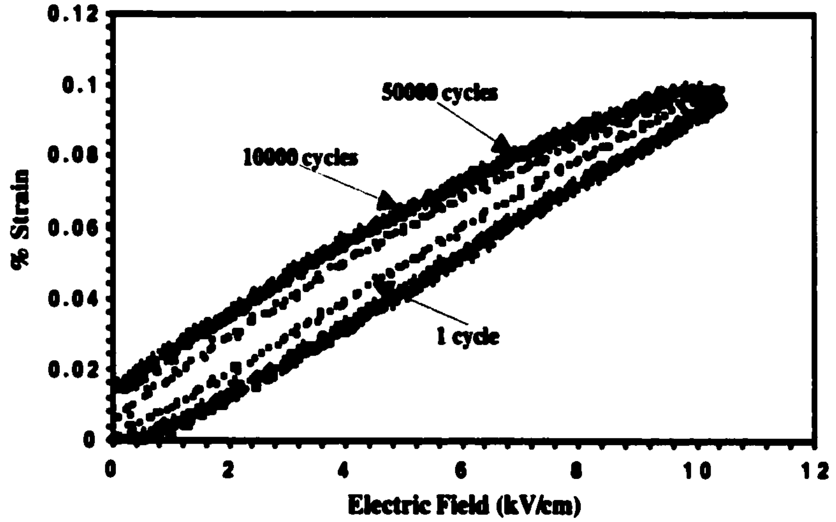

Figure 6.29: Strain-electric field curves for a ~90%-textured PMN-32.5PT ceramic containing 5 vol% BaTiO$_3$ templates (PMN-32.5PT-5BT) measured to a maximum field of 10 kV/cm after 50,000 cycles.

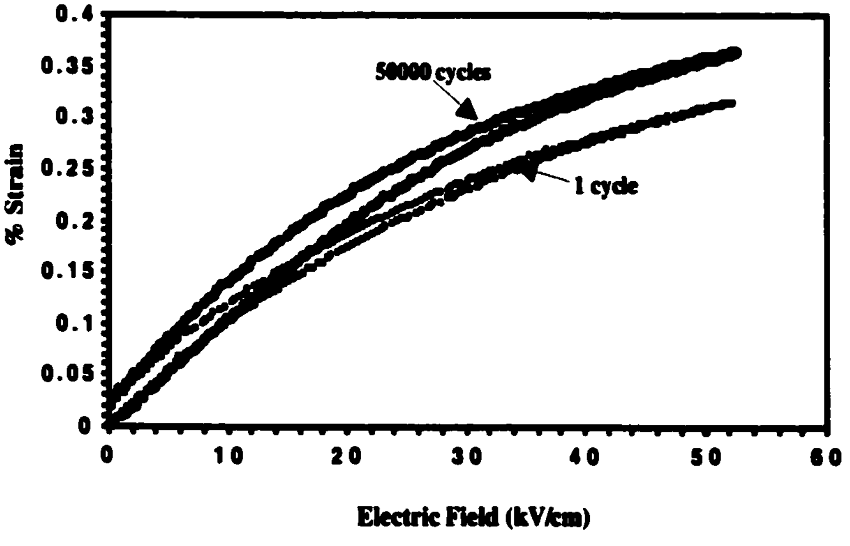

Figure 6.30: Strain-electric field curves for a ~90%-textured PMN-32.5PT ceramic containing 5 vol% BaTiO$_3$ templates (PMN-32.5PT-5BT) measured to a maximum field of 50 kV/cm after 50,000 cycles at 10 kV/cm.

by unoriented grains, intergranular PbO, and porosity may also limit the poling efficiency and the polarization rotation.

6.5 REFERENCES

1) S.-E. Park and T.R. Shrout, "Characteristics of Relaxor-Based Piezoelectric Single Crystals for Ultrasonic Transducers," *IEEE Trans. on Ultrasonics, Ferroelectrics, and Frequency Control*, **44** [5] (1997).

2) S-E. Park and T.R. Shrout, "Ultrahigh Strain and Piezoelectric Behavior in Relaxor Based Ferroelectric Single Crystals," *J. Appl. Phys.*, **82** [4] 1804-11 (1997).

3) J. Yin and W. Cao, "Domain Configuration in Domain Engineered $0.955Pb(Zn_{1/3}Nb_{2/3})O_3$-$0.045PbTiO_3$ Single Crystals," *J. Appl. Phys.*, **87** [10] 7438-41 (2000).

4) S-E Park, S. Wada, L.E. Cross, and T.R. Shrout, "Crystallographically Engineered $BaTiO_3$ Single Crystals for High-Performance Piezoelectrics," *J. Appl. Phys.*, **86** [5] 2746-50 (1999).

5) P.W. Rehrig, S.-E. Park, S. Trolier-McKinstry, G.L. Messing, B. Jones, and T.R. Shrout, "Piezoelectric Properties of Zirconium-Doped Barium Titanate Single Crystals Grown by Templated Grain Growth," *J. Appl. Phys.*, **86** [3] 1657-61 (1999).

6) J.-P. Maria, W. Hackenberger, and S. Trolier-McKinstry, "Phase Development and Electrical Property Analysis of Pulsed Laser Deposited $Pb(Mg_{1/3}Nb_{2/3})O_3$-$PbTiO_3$ (70/30) Epitaxial Thin Films," *J. Appl. Phys.*, **84** [9] 5147-54 (1998).

7) J.H. Park, F. Xu, and S. Trolier-McKinstry, "Dielectric and Piezoelectric Properties of Sol-gel Derived Lead Magnesium Niobium Films with Different Textures," *J. Appl. Phys.*, **89** [1] 568-74 (2001).

8) F.K. Lotgering, "Topotactical Reactions with Ferrimagnetic Oxides Having Hexagonal Crystal Structures-I," *J. Inorg. Nucl. Chem.*, **9** 113-23 (1959).

9) S.W. Choi, T.R. Shrout, S.J. Jang, and A.S. Bhalla, "Morphotropic Phase Boundary in $Pb(Mg_{1/3}Nb_{2/3})O_3$-$PbTiO_3$ System," *Mater. Lett.*, **8** [6,7] 253-55 (1989).

10) S.W. Choi, T.R. Shrout, S.J. Jang, and A.S. Bhalla, "Dielectric and Pyroelectric Properties I: The $Pb(Mg_{1/3}Nb_{2/3})O_3$-$PbTiO_3$ System," *Ferroelectrics*, **100** 29-38 (1989).

11) J. Zhao, Q.M. Zhang, N. Kim, and T. Shrout, "Electromechanical Properties of Relaxor Ferroelectric Lead Magnesium Niobate- Lead Titanate Ceramics," *Jpn. J. Appl. Phys., Part I*, **34** [10] 5658-63 (1995).

12) A.D. Hilton, C.A. Randall, D.J. Barber, and T.R. Shrout, "TEM Studies of $Pb(Mg_{1/3}Nb_{2/3})O_3$-$PbTiO_3$ Ferroelectric Relaxors," *Ferroelectrics*, **93** 379-86 (1989).

13) J. Kelly, M. Leonard, C. Tantigate, and A. Safari, "Effect of Composition on the Electromechanical Properties of (1-x)$Pb(Mg_{1/3}Nb_{2/3})O_3$-x$PbTiO_3$ Ceramics," *J. Am. Ceram. Soc.*, **80** [4] 957-64 (1997).

14) X. Zhang and F. Fang, "Study of the Structure and Dielectric Relaxation Behavior of $Pb(Mg_{1/3}Nb_{2/3})O_3$-$PbTiO_3$ Ferroelectric Ceramics," *J. Mater. Res.*, **14** [12] 4581-86 (1999).

15) S. Li, W. Cao, and L.E. Cross, "The Extrinsic Nature of Nonlinear Behavior Observed in Lead Zirconate Titanate Ferroelectric Ceramic," *J. Appl. Phys.*, **69** [10] 7219-24 (1991).

16) Q.M. Zhang, H. Wang, N. Kim, and L.E. Cross, "Direct Evaluation of Domain-wall and Intrinsic Contributions to the Dielectric and Piezoelectric Response and Their Temperature Dependence on Lead Zirconate-Titanate Ceramics," *J. Appl. Phys.*, **75** [1] 454-59 (1994).

17) S.L. Swartz, T.R. Shrout, W.A. Schulze, and L.E. Cross, "Dielectric Properties of Lead-Magnesium Niobate Ceramics," *J. Am. Ceram. Soc.*, **67** [5] 311-15 (1984).

18) J. Chen and M.P. Harmer, "Microstructure and Dielectric Properties of Lead Magnesium Niobate-Pyrochlore Diphasic Mixtures," *J. Am. Ceram. Soc.*, **73** [1] 68-73 (1990).

19) H.C. Ling, A.M. Jackson, M.F. Yan, and W.W. Rhodes, "Effect of PbO Evaporation on the Composition and Dielectric Properties of PbO-MgO-Nb_2O_5 Based Dielectrics," *J. Mater. Res.*, **5** [3] 629-39 (1990).

20) H.-C. Wang and W.A. Schulze, "The Role of Excess Magnesium Oxide or Lead Oxide in Determining the Microstructure and Properties of Lead Magnesium Niobate," *J. Am. Ceram. Soc.*, **73** [4] 825-32 (1990).

21) M. Villegas, A.C. Caballero, M. Kosec, C. Moure, P. Duran, and J.F. Fernandez, "Effects of PbO Excess in $Pb(Mg_{1/3}Nb_{2/3})O_3$-$PbTiO_3$ Ceramics: Part I. Sintering and Dielectric Properties," *J. Mater. Res.*, **14** [3] 891-97 (1999).

22) M.H. Frey, Z. Xu, P. Han, and D.A. Payne, "The Role of Interfaces on an Apparent Grain Size Effect on the Dielectric Properties for Ferroelectric Barium Titanate Ceramics," *Ferroelectrics*, **206/207** 337-53 (1998).

23) P. Papet, J.P. Dougherty, and T.R. Shrout, "Particle and Grain Size Effects on the Dieletric Behavior of the Relaxor Ferroelectric $Pb(Mg_{1/3}Nb_{2/3})O_3$," *J. Mater. Res.*, **12** [5] 2902-09 (1990).

24) C.A. Randall, A.D. Hilton, D.J. Barber, and T.R. Shrout, "Extrinsic Contributions to the Grain Size Dependence of Relaxor Ferroelectric $Pb(Mg_{1/3}Nb_{2/3})O_3$:$PbTiO_3$ Ceramics," *J. Mater. Res.*, **8** [4] 880-84 (1993).

25) R.A. Fry, *The Effects of Lead Oxide Volatility During Processing of Lead Magnesium Niobate Ceramics Upon Pyrochlore Formation and Dielectric Properties*. M.S. thesis at Penn State University (1992).

26) K. Okazaki and K. Nagata, "Effects of Grain Size and Porosity on Electrical and Optical Properties of PLZT Ceramics," *J. Am. Ceram. Soc.*, **56** [2] 82-6 (1973).

27) M. Kiyohara, K. Katoh, and K. Nagata, "Impurity Doping Effect on Piezoelectricity and Strain Induced by Electric Field in Piezoelectric Ceramics," *J. Ceram. Soc. Jpn., Int. Edition*, **104** 201-06 (1996).

28) J.C. Ho, K.S. Liu, and I.N. Lin, "Study of Ferroelectricity in the PMN-PT System Near the Morphotropic Phase Boundary," *J. Mater. Sci.*, **28** 4497-502 (1993).

29) E.G. Lee, J.K. Lee, J.-Y. Kim, J.G. Lee, H.M. Jang, and S.J. Kim, "Zr/Ti Ratio Dependence of the Deformation in the Hysteresis Loop of $Pb(Zr,Ti)_3$ Thin Films," *J. Mater. Sci. Lett.*, **18** 2025-28 (1999).

30) E.G. Lee, J.K. Lee, J.G. Lee, J.-Y. Kim, and H.M. Jang, "Deformation in the Hysteresis Loop of Pt/Pb(Zr,Ti)O3/Pt Thin-Film Capacitors," *J. Mater. Sci. Lett.*, **18** 1033-35 (1999).

31) S.C. Hwang and G. Arlt, "Switching in Ferroelectric Polycrystals," *J. Appl. Phys.*, **87** [2] 869-75 (2000).

32) G.A. Smolenskii, "Physical Phenomena in Ferroelectrics with Diffused Phase Transition," *J. Phys. Soc. Jpn.*, **28** 26-37 (1970).

33) K. Uchino, S. Nomura, L.E. Cross, S.J. Jang, and R.E. Newnham, "Electrostrictive Effect in Lead Magnesium Niobate Single Crystals," *J. Appl. Phys.*, **51** [2] 1142-45 (1980).

34) B.-Y. Ahn and N.-K. Kim, "Effects of Barium Substitution on Perovskite Formation, Dielectric Properties, and Diffuseness Characteristics of Lead Zinc Niobate Ceramics," *J. Am. Ceram. Soc.*, **83** [7] 1720-26 (2000).

35) F. Xia and X. Yao, "Piezoelectric Properties of Lead-Based Relaxor Ferroelectric Ceramics," *Ferroelectrics*, **231** 121-26 (1999).

36) F. Xia, X. Wang, L. Zhang, and X. Yao, "Dielectric and Piezoelectric Properties of PMN-PT Ceramics Prepared by Molten Salt Synthesis," *Ferroelectrics*, **215** 181-86 (1998).

37) F. Xu, S. Trolier-McKinstry, W. Ren, B. Xu, Z.-L. Xie, and K.J. Hemker, "Domain Wall Motion and its Contribution to the Dielectric and Piezoelectric Properties of Lead Zirconate Titanate Films," *J. Appl. Phys.*, **89** [2] 1336-48 (2001).

38) Y. Zhang, L. Li, Z. Gui, and J. Tian, "Dielectric Response of PMZNT Relaxor Ferroelectric Ceramics Under Various External Field," *Mater. Lett.*, **43** 230-33 (2000).

39) S.-Y. Chen, S.-Y. Cheng, and S.-M. Wang, "Effect of Barium Titanate on Microstructural Evolution and Properties of Lead Zinc Magnesium Niobate Ceramics," *J. Am. Ceram. Soc.*, **74** [2] 400-405 (1991).

40) Y.S. Cho, S.M. Pilgrim, H. Giesche, and K. Bridger, "Dielectric and Electomechanical Properties of Chemically Modified PMN-PT-BT Ceramics," *J. Am. Ceram. Soc.*, **83** [10] 2473-80 (2000).

41) O. Sakurai, M. Katsumoto, K. Shinozaki, and N. Mizutani, "Preparation and Dielectric Properties of $BaTiO_3$-$Pb(Mg_{1/3}Nb_{2/3})O_3$ Solid Solutions," *J. Ceram. Soc, Jpn., Int. Ed.*, **101** 594-596 (1993).

42) A. Halliyal, U. Kumar, R.E. Newnham, and L.E. Cross, "Stabilization of the Perovskite Phase and Dielectric Properties of Ceramics in the $Pb(Zn_{1/3}Nb_{2/3})O_3$-$BaTiO_3$ System," *Am. Ceram. Soc. Bull.*, **66** [4] 671-676 (1987).

43) J.R. Belsick, A. Halliyal, U. Kumar, and R.E. Newnham, "Phase Relations and Dielectric Properties of Ceramics in the System $Pb(Zn_{1/3}Nb_{2/3})O_3$-$SrTiO_3$-$PbTiO_3$," *Am. Ceram. Soc. Bull.*, **66** [4] 664-667 (1987).

44) F. Chu, I.M. Reaney, and N. Setter, "Spontaneous (Zero-Field) Relaxor-to-Ferroelectric-Phase Transition in Disordered $Pb(Sc_{1/2}Nb_{1/2})O_3$," *J. Appl. Phys.*, **77** [4] 1671-76 (1995).

45) W. Cao, Associate Professor of Mathematics and Materials Science, Penn State University, personal communication (2001).

46) T.R. Shrout, Z.P. Chang, N. Kim, and S. Markgraf, "Dielectric Behavior of Single Crystals Near the (1-x)$Pb(Mg_{1/3}Nb_{2/3})O_3$-(x)$PbTiO_3$ Morphotropic Phase Boundary," *Ferro. Lett.*, **12** 63-9 (1990).

47) M.K. Durbin, J.C. Hicks, S.-E. Park, and T.R. Shrout, "X-ray Diffraction and Phenomenological Studies of the Engineered Monoclinic Crystal Domains in Single Crystal Relaxor Ferroelectrics," *J. Appl. Phys.*, **87** [11] 8159-64 (2000).

48) D.-S. Paik, S.-E. Park, S. Wada, S.-F. Liu, and T.R. Shrout, "E-field Induced Phase Transition in <001>-Oriented Rhombohedral $0.92Pb(Zn_{1/3}Nb_{2/3})$-$0.08PbTiO_3$ Crystals," *J. Appl. Phys.*, **85** [2] 1080-83 (1999).

49) N.A. Pertsev, A.G. Zembilgotov, and R. Waser, "Aggregate Linear Properties of Ferroelectric Ceramics and Polycrystalline Thin Films: Calculation by the Method of Effective Piezoelectric Medium," *J. Appl. Phys.*, **84** [3] 1524-29 (1998).

50) C.-S. Tu, C.-L. Tsai, V.H. Schmidt, H. Luo, and Z. Yin, "Dielectric, Hypersonic, and Domain Anomalies of $(PbMg_{1/3}Nb_{2/3})_{1-x}(PbTiO_3)_x$ Single Crystals," *J. Appl. Phys.*, **89** [12] 7908-16 (2001).

51) Z.-G. Ye and M. Dong, "Morphotropic Domain Structure and Phase Transition in Relaxor-Based Piezo-/Ferroelectric $(1-x)Pb(Mg_{1/3}Nb_{2/3})O_3$-$xPbTiO_3$ Single Crystals," *J. Appl. Phys.*, **87** [5] 2312-19 (2000).

52) J. Yin and W. Cao, "Domain Configurations in Domain Engineered $0.955Pb(Zn_{1/3}Nb_{2/3})O_3$-$0.045PbTiO_3$ Single Crystals," *J. Appl. Phys.*, **87** [10] 7438-41 (2000).

53) B. Jaffe, W.R. Cook, and H. Jaffe, *Piezoelectric Ceramics*. Academic Press, New York (1971).

Chapter 7

SUMMARY AND FUTURE WORK

7.1 SUMMARY

7.1.1 Template Selection for TGG of PMN-PT

Highly anisometric particles of $Bi_4Ti_3O_{12}$, $Sr_3Ti_2O_7$, $KSr_2Nb_5O_{15}$, and $Sr_2Nb_2O_7$ were fabricated by molten salt synthesis. $Bi_4Ti_3O_{12}$, $Sr_3Ti_2O_7$, and $Sr_2Nb_2O_7$ possess a layered-perovskite crystal structure and $KSr_2Nb_5O_{15}$ has a tungsten-bronze structure. All were potential templates for the TGG of PMN-35PT. These particles were shown to be unstable in the PMN-35PT matrix regardless of the excess PbO content. All four compositions reacted with the PMN-35PT matrix, either dissolving or forming the cubic-pyrochlore phase with the matrix at temperatures >900°C. Molten salt and hydrothermal processes were also used to synthesize tabular or whisker $PbTiO_3$, $SrTiO_3$, and $BaTiO_3$ particles. These compositions all possess the perovskite crystal structure. The {001}-$BaTiO_3$ crystals made by the Remeika process were shown to be stable within the PMN-35PT matrix even in the presence of excess PbO. The other perovskite templates dissolved into the matrix composition during the sintering/growth step utilized in this work.

Templated growth of single crystal PMN-PT layers was observed from the surface of the {001}-$BaTiO_3$ crystals at various sintering conditions and matrix compositions, and therefore, the Remeika $BaTiO_3$ crystals were selected as the most suitable templates for the TGG of PMN-PT. This work clearly demonstrated the importance of physical and compositional stability of the template particles at the desired growth temperature and environment. Other factors like template size, shape, epitaxial relation, and effect on physical properties were all identified as criteria which will limit template usage.

7.1.2 Kinetics of Templated Grain Growth of PMN-35PT Crystals from $BaTiO_3$ Template Crystals

PMN-35PT single crystal layers were grown heteroepitaxially on {001}-, {110}-, and {111}-$BaTiO_3$ template crystals. Crystal growth kinetics were also found to differ for various crystallographic orientations with the <111>-direction being the fastest and the <001>-direction the slowest. Excess PbO within the matrix composition was found to affect the growth kinetics of both the matrix grains and the TGG single crystal layer. The Lay model which describes diffusion-controlled grain growth in the presence of a liquid phase was found to fit the matrix grain growth for <1 h at temperatures between 950-1150°C, although, deviations were observed for sintering times exceeding 1 h. The deviation from the model for longer sintering times was attributed to the development of intergranular porosity and the suggested {001}-habit formation of the matrix grains. The TGG kinetics for all template orientations was described as diffusion-limited for the growth process of a single crystal within a polycrystalline matrix, with a non-constant driving force due to the coarsening matrix during growth. Therefore, the extent of the PMN-PT crystal layer growth was shown to be limited by the decrease in the driving force due to the coarsening matrix grains.

7.1.3 Fiber-Textured PMN-32.5PT Ceramics by Templated Grain Growth

PMN-32.5PT ceramics were fiber-textured in the <001> by the TGG process by initially aligning {001}-$BaTiO_3$ platelets in the matrix by tapecasting. The {001}-$BaTiO_3$ template crystals (~75-150 μm in diameter) were synthesized by the Remeika process. Laminated samples of approximately 1 mm in thickness were hot-pressed in argon at 900°C for 30 min to alleviate any problems with constrained sintering. Samples which contained a 5 vol% template concentration without an excess PbO concentration were shown not to texture to a high fraction (f≈0.45) when annealed at 1150°C for >10 h. The growth kinetics were increased with the addition of 1 wt% excess PbO to the matrix composition and the ceramic could be textured to as high as f≈0.90 at 1150°C for 5 h with a template concentration of 5 vol%. The saturation in the rate of template growth, and therefore the texturing, was found to result from a decrease in the driving force for growth by the coarsening matrix. The increase in boundaries between templated-grains was identified as the cause of the decreasing rate of template growth. The rate of texturing was further accelerated by increasing the template concentration (to 10 vol%). In this case, the ceramic would texture to f≈0.90-0.95 at 1150°C for annealing times >1 h. The texture fraction was again limited by the coarsening matrix, impingement of the templated grains, porosity, and intergranular void formation with further growth time.

7.1.4 Dielectric and Piezoelectric Properties of <001> Fiber-Textured PMN-32.5PTCeramics

PMN-32.5PT ceramics were fiber-textured in the <001> by the TGG process using the {001}-$BaTiO_3$ platelet templates formed by the Remeika process. The fiber-textured PMN-32.5PT ceramic samples showed an increase in the piezoelectric, electromechanical coupling, and compliance coefficients when poled and measured in the <001>-textured direction. All of these coefficients exceeded the values displayed by randomly-oriented ceramics of the same composition. The low drive field (<5 kV/cm) d_{33} piezoelectric coefficients of the highly textured (>90%-textured) PMN-32.5PT ceramics were shown to be ~1.2-1.5 times greater than randomly-oriented samples. The piezoelectric response of the textured samples showed some piezoelectric hysteresis when measured in the textured direction. The hysteresis suggests a degree of extrinsic contribution to the piezoelectric coefficient of the textured samples. Partial clamping by the residual intragranular $BaTiO_3$ template particles affected the domain stability, which may contribute to the hysteresis. XRD of the textured ceramics suggests the stabilization of the PMN-PT tetragonal phase due to the remnant $BaTiO_3$ templates which would also increase the hysteresis. Mechanical clamping by misoriented templated-grains, unoriented grains, intergranular PbO, and porosity were also suggested to contribute to a lower poling efficiency and the piezoelectric activity.

Excess PbO and $BaTiO_3$ templates which remained in the textured ceramics resulted in lowering and broadening of the permittivity-temperature curves compared to the randomly-oriented PMN-32.5PT ceramic. The poled ε_{max} and ε_{rt} for a ~90%-textured PMN-32.5PT ceramic (5 vol% $BaTiO_3$ templates) were approximately 21500 and 2450, respectively. The inverse permittivity versus temperature response of the textured ceramics was fit to an empirical power law (a modification of the Curie-Weiss relationship). This relationship showed that the highly textured ceramics had a diffuse nature similar to that displayed by the randomly-oriented PMN-32.5PT ceramic containing excess PbO. Therefore, the dielectric data suggested that the excess PbO intentionally added to accelerate the TGG process was dominating the dielectric behavior of the textured samples. The paraelectric-ferroelectric transition temperature remained unchanged (~165°C) for the highly textured samples annealed at 1150°C for >1 h. This further indicates the stability, and the low dissolution rate, of the $BaTiO_3$ templates in PMN-PT.

7.2 FUTURE WORK

7.2.1 Template Synthesis and Selection

The quality and degree of texturing by TGG is primarily dependent upon the characteristics of the template particle. Chapter 3 reviewed some of the important traits a template particle must have in order to produce a highly textured ceramic. Four essential variables are shape, size, epitaxial relationship, and stability. The templates must display the proper shape, so that a high degree of alignment can be achieved by an applied shear force during consolidation and forming. Template size is important since the driving force for growth is supplied by the difference in size between the template and matrix grains. The size of the template is also important, since the final grain size of the templated grains will be determined by the initial size of the template. The crystal structure determines the epitaxial relationship between the template and the growing crystal layer. Thermodynamic stability was shown to be a very important issue, especially in the case of heteroepitaxial TGG where the matrix may react with the template of a different composition.

Currently, the Remeika $BaTiO_3$ crystals are the best and most consistently reproducible templates available for texturing PMN-PT and possibly other lead-based relaxor-$PbTiO_3$ materials. The stability of the crystal is high, and the PMN-PT composition readily grows from the $BaTiO_3$ surface, but these crystals due not fit all of the criteria well. The negative qualities of the Remeika crystals include their shape and size. Since the Remeika crystals used in this study were >75 µm in diameter, the final grain size after growth exceeded >150 µm. These final grain sizes result in ceramics which are prone to mechanical and thermal cracking. This ceramic would be unacceptable for use in many actuator or transducer applications. Fully-crystalline {001}-$BaTiO_3$ platelets that have a high aspect ratio and a size between ~10-30 µm should be synthesized in order to produce a high quality textured PMN-PT ceramic. With templates in this size regime, there would be a high number frequency of templates for the same volume, resulting in smaller growth distance required to fully texture the ceramic. These templates would also be more homogeneously distributed throughout the volume of the ceramic resulting in a higher uniformity of texture. In addition, these templates will produce a ceramic with a reasonable final grain size that would have higher strength and fracture toughness.

It would be especially interesting from the standpoint of understanding the role of the template in controlling the domain structures to compare the properties of a tetragonal $BaTiO_3$ templated PMN-PT ceramic with that of a textured PMN-PT ceramic templated with rhombohedrally distorted $Ba(Zr,Ti)O_3$. By adjusting the Zr concentration, the mechanical constraints imposed on the templated PMN-PT grains would change. This might change the stability of the domain state, as well as the propensity towards stabilizing tetragonal distortions in the PMN-PT grains. Synthesis of such compounds would be a first step towards distinguishing the relative importance of the orientation distribution and mechanical clamping induced by template particles of a different composition on controlling the piezoelectric coefficients and the hysteresis.

The work presented in Chapter 3 showed that it may be impossible to template PMN-PT from compositions which have a layered-perovskite or tungsten-bronze structure due to the inevitable formation of the cubic-pyrochlore phase at high temperatures. The same work suggested that the template compositions like $PbTiO_3$ and $SrTiO_3$, which have the perovskite structure, were limited by dissolution into the excess PbO and/or the PMN-PT matrix. The $PbTiO_3$ whiskers were shown to be morphologically unstable in the matrix due to their non-perovskite, $PbTiO_3$ structure. Therefore, well-crystallized perovskite, $PbTiO_3$ whiskers or platelets with the proper size and shape may provide a better template for the TGG of PMN-PT. $PbTiO_3$ would be advantageous relative to either $BaTiO_3$ and $SrTiO_3$, since additions of these compositions lower the T_c and the dielectric permittivity as they dissolve into the PMN-PT structure.(1-5) The incorporation of the $PbTiO_3$ templates into the PMN-PT ceramic will alter the composition, but this can be compensated by changing the original matrix composition, so that the final $PbTiO_3$ concentration will lie along the MPB. Stable $PbTiO_3$ platelets have been successfully formed by Moon *et al.*, but the aspect ratio is low (<3) and the particles show the tendency to form multiple growth islands which further decreases the aspect ratio.(6,7)

7.2.2 Matrix Composition and Reactive Templated Grain Growth (RTGG)

Due to the relatively large $BaTiO_3$ template size used in this study, an excess of PbO was required in the matrix to increase the TGG kinetics. As discussed in Chapter 5, at a low template concentration, these large templates had a large inter-template distance to grow in order to fully texture the ceramic. By synthesizing alternative template particles of the proper size and shape, as discussed in the previous subsection, the use of excess PbO in the PMN-PT matrix will not be required. This will eliminate many of the processing and property problems related to the presence of excess PbO. Also, the problem with template instability and dissolution may be circumvented by eliminating the excess PbO.

Recently, Sabolsky *et al.*(8) showed that by using an Reactive Templated Grain Growth (RTGG) approach, PMN-32PT could be fiber-textured with the {001}-$SrTiO_3$ platelets synthesized by the Watari *et al.*(9) procedure. In Chapter 3, it was shown that the {001}-$SrTiO_3$ crystal was unstable in the presence of excess PbO. As a result, the Pb-based liquid at the crystal interface complicated the potential nucleation of the PMN-PT phase. Sabolsky *et al.* showed that when a $SrTiO_3$ templated ceramic was fired in an uncalcined PMN-PT matrix below the melting temperature of PbO, the PMN-PT phase could nucleate and form a stable crystal layer on the template before reacting with the liquid phase.(8) The same approach may be utilized with other stable perovskite templates when they come available.

7.2.3 Texture Characterization

The texture fraction for the grain-oriented PMN-PT ceramics produced in this work was characterized by applying the Lotgering method to the acquired XRD patterns. This texture characterization was appropriate, since the texture was the result of a few large oriented grains inhomogeneously distributed throughout the ceramic. Rocking curves, pole figures, and stereology were inappropriate, since the population of oriented grains was small. When a better template particle becomes available, the above texture characterization techniques would more applicable. These techniques may be useful to compare the texture quality and achievable properties limitations between highly symmetric systems like PMN-PT and systems which possess a higher anisotropy.

7.2.4 TEM Characterization of the Heteroepitaxial TGG of PMN-PT

This work showed that the TGG kinetics fit the Seabaugh *et al.* model, which is based on the premise that the growth mechanism is diffusion-controlled. Most systems in which the growth is diffusion-limited show non-faceted grain structures.(10) The morphology of both the PMN-PT crystal and matrix distinctly showed a preference for habit formation. With transmission electron microscopy (TEM), it may be possible to distinguish the nature of the crystal-liquid or crystal-matrix interface and the degree of "roughness." TEM could help determine the atomic smoothness of the {001}-habit, and the possible origin of the kinks and steps which allow for the diffusion-limited growth. The appearance of growth islands or spirals would indicate a change in the proposed growth mechanism. Observation of the crystal-solution interface at different stages of growth may show the extinction and coalescence of nuclei leading to the final {001}-habit formation for both the templated crystal and the matrix.

Through the use of a TEM fitted with electron energy-loss spectroscopy (EELS), the compositional evolution of the crystal could be monitored for samples at different stages of growth. The high resolution, quantitative character of EELS may be able to distinguish the composition of the first nucleation sites, and how the composition is altered with further growth and high temperature annealing. It would be especially important to monitor whether there is any Ti gradient in the templated grains, as has been observed in melt-grown PMN-PT single crystals.

7.2.5 Property Characterization and the Effect of the Remnant $BaTiO_3$ Templates

Fiber-texturing the rhombohedral PMN-PT composition in the <001> results in an enhancement of the piezoelectric response over that displayed by the randomly-oriented ceramic. This work reinforced the domain engineering concept and showed that it is applicable to perovskite ferroelectric ceramics with the rhombohedral-tetragonal MPB. Although, the fraction of single crystal properties was lower than that identified for other highly textured systems, some of this can be attributed to the less-than-ideal quality of the textured ceramics formed in this study. With better templates, the quality of the textured PMN-PT ceramics will increase, therefore, increasing the degree of orientation, uniformity, and density, and decreasing the excess PbO content and final grain size.

The effect of the residual $BaTiO_3$ within the templated grains on the piezoelectric properties must be further investigated. The $BaTiO_3$ inclusion may restrict the full potential of domain engineering on textured PMN-PT ceramics, therefore, further characterization of the pinned domain walls around the $BaTiO_3$ inclusion must be completed. Also, this work implied that the remnant $BaTiO_3$ templates may stabilize the PMN-PT tetragonal form within the templated grains. Structural characterization of the $BaTiO_3$/PMN-PT crystal interface by TEM may give a better understanding of the domain state along the interface and across the templated grain. EELS preformed at various locations along and radiating from this interface would give a better understanding of the degree of interdiffusion (Ba and Pb movement) between the crystals and further assist in explaining the issues relating to the tetragonal stabilization.

The complete understanding of the effect of the remnant $BaTiO_3$ on the piezoelectric and dielectric properties will dictate the future applicability of certain template compositions for the TGG of PMN-PT. If it is found that the effect of the residual $BaTiO_3$ template is large and cannot be corrected for, then the use of this template must be discontinued. Transient templates, which will completely dissolve into the templated grains, will then be the only viable template option for PMN-PT.

7.2.6 Dielectric and Piezoelectric Models for Textured PMN-PT

The relation between the dielectric and piezoelectric properties with the degree of texture was shown in Chapter 6. This work indicated that with an increase in texture, there was an increase in the dielectric and piezoelectric coefficients. Due to the large grain size and the resulting texture inhomogeneity, it was inappropriate to make any generalized model comparing the texture fraction and the texture distribution with the observed properties. The texture/property relationship should be modeled for highly textured PMN-PT ceramics that are formed with a more ideal template, and thus, a more uniform and oriented grain structure. Previously reported effective-medium models, which describe the effect of various orientation distributions on the piezoelectric coefficients of ceramic $BaTiO_3$ and $PbTiO_3$, may be applied to such a PMN-PT textured ceramic.(11-13) By comparing the effective-medium model to the collected piezoelectric data, the contribution of excess PbO, porosity, and template clamping may be resolved for the textured samples.

7.3 REFERENCES

1) S.-Y. Chen, S.-Y. Cheng, and S.-M. Wang, "Effect of Barium Titanate on Microstructural Evolution and Properties of Lead Zinc Magnesium Niobate Ceramics," *J. Am. Ceram. Soc.*, **74** [2] 400-405 (1991).

2) Y.S. Cho, S.M. Pilgrim, H. Giesche, and K. Bridger, "Dielectric and Electomechanical Properties of Chemically Modified PMN-PT-BT Ceramics," *J. Am. Ceram. Soc.*, **83** [10] 2473-80 (2000).

3) O. Sakurai, M. Katsumoto, K. Shinozaki, and N. Mizutani, "Preparation and Dielectric Properties of $BaTiO_3$-$Pb(Mg_{1/3}Nb_{2/3})O_3$ Solid Solutions," *J. Ceram. Soc, Jpn., Int. Ed.*, **101** 594-596 (1993).

4) A. Halliyal, U. Kumar, R.E. Newnham, and L.E. Cross, "Stabilization of the Perovskite Phase and Dielectric Properties of Ceramics in the $Pb(Zn_{1/3}Nb_{2/3})O_3$-$BaTiO_3$ System," *Am. Ceram. Soc. Bull.*, **66** [4] 671-676 (1987).

5) J.R. Belsick, A. Halliyal, U. Kumar, and R.E. Newnham, "Phase Relations and Dielectric Properties of Ceramics in the System $Pb(Zn_{1/3}Nb_{2/3})O_3$-$SrTiO_3$-$PbTiO_3$," *Am. Ceram. Soc. Bull.*, **66** [4] 664-667 (1987).

6) J. Moon, T. Li, C. Randall, and J.H. Adair, "Low Temperature Synthesis of Lead Titantate by a Hydrothermal Method," *J. Mater. Res.*, **12** [1] 189-97 (1997).

7) J. Moon, M.L. Carasso, H.G. Krarup, J.A. Kerchner, and J.H. Adair, "Particle-shape Control and Formation Mechanisms of Hydrothermally Derived Lead Titanate," *J. Mater. Res.*, **14** [3] 866-75 (1999).

8) E.M. Sabolsky, S. Kwon, E. Suvaci, A.R. James, G.L. Messing, and S. Trolier-McKinstry, "Dielectric and Electromechanical Properties of <001>-Textured (0.68)$Pb(Mg_{1/3}Nb_{2/3})O_3$-(0.32)$PbTiO_3$,"; pp. 393-96, Vol. 1, *Proceedings of the Twelfth International Symposium on the Applications of Ferroelectrics*. Edited by S.K. Streiffer, B.J. Gibbons, and T. Tsurumi. IEEE, Piscataway, NJ, 2000.

9) K. Watari, B. Brahmaroutu, G.L. Messing, S. Trolier-McKinstry, and S.-C. Cheng, "Epitaxial Growth of Anisotropically Shaped, Single-Crystal Particles of Cubic $SrTiO_3$," *J. Mater. Res.*, **15** [4] 846-49 (2000).

10) S.-K Kwon, S.-H. Hong, D.-Y. Kim, and N.M. Hwang, "Coarsening Behavior of Tricalcium Silicate (C_3S) and Dicalcium Silicate (C_2S) Grains Dispersed in a Clinker Melt," *J. Am. Ceram. Soc.*, **83** [5] 1247-52 (2000).

11) C.-W. Nan, "Effective-Medium Theory of Piezoelectric Composites," *J. Appl. Phys.*, **76** [2] (1994).

12) C.-W. Nan, and D.R. Clarke, "Piezoelectric Moduli of Piezoelectric Ceramics," *J. Am. Ceram. Soc.*, **79** [10] 2563-66 (1996).

13) N.A. Pertsev, A.G. Zembilgotov, and R. Waser, "Aggregate Linear Properties of Ferroelectric Ceramics and Polycrystalline Thin Films: Calculations by the Method of Effective Piezoelectric Medium," *J. Appl. Phys.*, **84** [3] 1524-29 (1998).

VITA

Edward Michael Sabolsky was born in Parma, Ohio on January 26, 1973. He graduated from Normandy High School in Parma, Ohio in June 1991. Mr. Sabolsky studied for his B.S. degree in Ceramic Science and Engineering with a minor in Metallurgical Engineering at The Ohio State University. While at Ohio State, Mr. Sabolsky completed a two year co-op term with Oak Ridge National Laboratory and the Y-12 Nuclear Facility in Oak Ridge, Tennessee. He graduated Cum Laude with Honors Distinction from Ohio State in June 1996. Mr. Sabolsky began his Ph.D. studies with Prof. Gary L. Messing and Prof. Susan Trolier-McKinstry at The Pennsylvania State University in August 1996. At Penn State, he worked on the processing and properties of high strain, grain-oriented $Pb(Mg_{1/3}Nb_{2/3})O_3$-$PbTiO_3$ piezoelectric ceramics. His research has been presented in numerous conferences which include the Annual Meeting of the American Ceramic Society, the International Symposium on the Application of Ferroelectrics (ISAF), the International Conference on Ceramic Processing Science, and the U.S. Navy Workshop on Acoustic Transduction Materials and Devices. He is a member of the American Ceramic Society and the Materials Research Society.